Multifunctional Wireless Gut-Brain Neurotechnology

by

ATHARVA SAHASRABUDHE

B.S, Chemical Sciences, Indian Institute of Science Education and Research-Kolkata, 2015

M.S, Chemical Sciences, Indian Institute of Science Education and Research-Kolkata, 2015

Submitted to the Department of Chemistry

in Partial Fulfillment of the Requirements for the Degree of

DOCTOR OF PHILOSOPHY IN CHEMISTRY

at the

MASSACHUSETTS INSTITUTE OF TECHNOLOGY

MAY 2024

Author . . . . . .
Department of Chemistry
May 8, 2024

Certified by. . . . . .
Polina Anikeeva
Matoula S. Salapatas Professor of Materials Science and Engineering
Thesis Supervisor

Accepted by . . . . . .
Adam Willard
Associate Professor of Chemistry
Graduate officer

This doctoral thesis has been examined by a Committee of the Department of Chemistry as follows

Prof. Alex K. Shalek…….

Chairman, Thesis Committee
J. W. Kieckhefer Professor in the Institute for Medical Engineering and Science and the Department of Chemistry

Prof. Jeremiah A. Johnson…….

Member, Thesis Committee
A. Thomas Guertin Professor of Chemistry

Prof. Polina Anikeeva……

Thesis Supervisor
Matoula S. Salapatas Professor of Materials Science and Engineering

Multifunctional Wireless Gut-Brain Neurotechnology

by

Atharva B. Sahasrabudhe

Abstract

The complexity of the brain is well known, in that it uses specially organized neural circuits to interact with the external world. Besides external stimuli, the brain also receives, integrates, and responds to sensory signals emerging from internal organs of the body through the network of the peripheral nervous system. Although these nerve signals are subliminal and cannot be consciously detected or controlled, they play a profound role in maintaining a homeostatic state. Recent evidence also suggests that interoceptive signals can impact higher level cognitive functions. The anatomical, functional, and molecular details about these brain-body pathways are beginning to be deciphered, but a lot remains to be uncovered. Cutting edge neurobiological tools like optogenetics, chemogenetics, and activity-based sensors have revolutionized studies of the brain. However, application of these methodologies for studies of brain-body circuits is reliant on engineered devices that support these sophisticated functions in peripheral organs too. Studying interoceptive circuits in a causal fashion in behaving animals, thus, requires advanced multifunctional implantable neurotechnologies that can be deployed at multiple sites spanning regions in the brain and the peripheral organ of interest. This thesis aims to bridge this unmet technological need.

This work presents a collection of advances that overcome thermomechanical constraints of fiber drawing and allow processing of traditionally non-drawable components. These advances yielded multifunctional probes that allow depth specific optical, electrical, and pharmacological probing of neural circuits in the brain, while also being compatible with brain-wide functional magnetic resonance imaging techniques. The same underlying design principles have also made possible fiber-based miniaturized electrochemical probes for performing electrocatalytic reactions in the brain to deliver transient, gaseous neurotransmitters, such as NO, through controlled generation and delivery in-vivo. Finally, wireless microelectronic fibers that combine the scalability and mechanical versatility of thermally drawn polymer fibers with the sophistication of microelectronic chips for organs as diverse as the brain and the gut were developed. This approach produces meters-long continuous fibers that can integrate light sources, electrodes, thermal sensors, and microfluidic channels in a miniature footprint. Paired with custom-fabricated control module, the fibers wirelessly deliver light for optogenetics and transfer data for physiological recording. This technology was validated by modulating the mesolimbic reward pathway in the mouse brain and the anatomically challenging intestinal lumen to demonstrate wireless control of sensory epithelial cells and vagal afferents that guide animal’s feeding and reward behaviors.

Acknowledgments

First and foremost, I would like to express my deepest gratitude to my advisor Prof. Polina Anikeeva without whose unwavering support, constant encouragement, and critical guidance none of this would have been remotely possible! I deeply appreciate the intellectual freedom that she granted during this journey as well as her patience with me over all these years. Polina's accepting me into her group and introducing me to the fascinating world of cutting-edge neuroscience and neurotechnology research will undoubtedly remain a life-changing event for me, something I could not have even dreamed about just a few years ago sitting in a remote, rural college-town of eastern India. For all this (and much more) I cannot thank her enough!

I arrived in the Bioelectronics lab with absolutely no exposure to engineering research or neuroscience fundamentals. The entire Bioelectronics team (and our friends) has immensely helped me in navigating this steep learning curve! A big thank you and forever grateful to Dr. Tural Khudiyev who taught me fiber drawing and tolerated my incessant requests to shadow him and witness his crazy preforms and mind-blowing draws. I was blessed to learn mouse brain surgeries, animal behavior, transcardial perfusion, and histology from the experts Dr. Po-han Chiang, Dr. Siyuan Rao, and Dr. M.J. Antonini. I fondly recall countless animated discussions, brainstorming ideas, long midnight walks back to the dorm with my amazing friend Dr. Jimin Park. I have learned so much from you and thank you for patiently listening to my frustrations about failed experiments and philosophical musings on life in general!!

I consider myself extremely lucky to have had a chance to collaborate with Prof. Diego Bohorquez's lab on aspects of gut-brain biology! Words may not be enough to thank Diego, Dr. Kelly Buchanan, and Dr. Laura Rupprecht for teaching whatever little I know about fundamentals of gut-brain biology, GI experimental techniques, and hypothesis driven research framework. Laura's constant encouragement and guidance, even though I continuously bothered her with my naïve questions over text messages even at odd hours is something I will be forever be grateful to Laura for! During my Ph.D. I got exposed to advanced low-power wireless circuits through fruitful collaborations with Prof. Anantha Chandrakasan and Dr. Sirma Orguc. Working and collaborating with Sirma was an absolute pleasure and I cannot wait to see all the great things that she goes on to accomplish in her independent career! I am also very grateful to Harrison Allen who did his MEng in our group and elevated our wireless controllers to another level! Thank you so much for all your hard work and being so patient, kind, and understanding during this process.

I had the absolute privilege to mentor several wildly-talented undergraduates at MIT through the UROP and MSRP programs. Jorge, Jesse, Maggie, Neha, Stuti, Viktor – thank you from the bottom of my heart for being such amazingly motivated and dedicated researcher at such a young age, you guys have taught me so much about mentorship and I have zero doubts about the stellar careers that each one of you will carve out in the near future! To all the present members of the Bioelectronics team (if I describe you all individually, this section will turn into an autobiography) - I have to literally pinch myself everyday to be surrounded by such a knowledgeable, driven, supportive, and kind bunch of scientists that allow me to continuously elevate my skills and together push the boundaries of human knowledge.

My amazing friends from college – Shashank, Bibudha, Manjunath, and Sandipan - who kept me sane through some of the most trying times of personal grief and Ph.D. struggles. You know I am as least expressive as they come and almost entirely incapable of saying this to you in person – but your emotional support during this journey will not be ever forgotten!! Lastly, my family – Mom, Abhishek, Dnyanada, Sameehan – you are all too close to me to say a formal thank you! Without you guys none of this would have been possible in the first place. Cannot wait to spend some quality time with you guys soon. Love you all!

I am sure my late Father would have been immensely proud to witness my research journey, and there is not a single day or a single moment that I do not miss your presence! Your own personal journey of resounding triumph over personal struggles, beginning from extremely humble roots to make sure we got the best of education has and will always remain an eternal source of inspiration and boundless motivation. Dedicating this Ph.D. thesis in your loving memory, Pappa!

Contents

CHAPTER 1. INTRODUCTION 9
1.1 Overview of Interoception 9
1.2 Sensory innervation of the gut 12
1.3 Sympathetic and Parasympathetic innervation of the gut 13
1.4 Disorders of aberrant interoceptive signaling 14
1.5 Bio-integrated devices to study brain-body circuits 14
1.6 The need for multifunctional devices 15
1.7 Scalable and integrated fabrication of multimodal neurotechnology using fiber drawing 19
CHAPTER 2. MULTIFUNCTIONAL FIBERS FOR DEPTH-SPECIFIC INTERROGATION AND DELIVERY OF GASEOUS NEUROMDULATORS TO THE BRAIN 22
2.1 Motivation 22
2.2 Fabrication of multifunctional neural probes through iterative and convergence thermal drawing 24
2.3 Characterization of optical, electrical, mechanical, and fluidic properties of fiber probes 28
2.4 Recording and stimulation of neural activity *in vivo* using two-step and converged fiber probes 31
2.5 Coupling fibers to microdrives: Fabrication and characterization 35
2.6 Coupling fibers to the microdrive for depth specific *in vivo* electrophysiology 37
2.6 *In vivo* MRI imaging in the presence of the multifunctional fibers 38
2.7 Immunohistochemical evaluation of biocompatibility of the fiber probes 40
2.8 Conclusion 40
2.9 Experimental Methods 41
2.10 Neural probes that deliver transient gaseous neuromodulators to the brain 51
2.11 Design and characterization of implantable NO-delivery probes. 51
2.12 NO-mediated neuronal stimulation *in vivo*. 54
2.13 Experimental methods for NO delivering neural probes 57
CHAPTER 3. FIBER DEVICES FOR PROBING THE GUT-BRAIN AXIS 62
3.1 Post-ingestive sugar sensing 62
3.2 Need for a flexible fiber for gut optogenetics 63
3.3 Wireless microelectronics fibers for probing gut-brain signaling 68

3.4 Multifunctional microelectronic fibers for the brain 72
3.5 Characterization of brain fibers 72
3.6 Microelectronic fibers for the gut 75
3.7 Characterization of gut fibers 75
3.8 Wireless operation of microelectronic fibers 78
3.9 Multimodal interrogation of midbrain dopaminergic neurons 81
3.10 Multimodal interrogation of gut-brain communication 84
3.11 Discussion 91
3.12 Experimental methods 92
CHAPTER 4. CONCLUSIONS AND OUTLOOK 105
APPENDIX A 107
APPENDIX B 124
References 173

CHAPTER 1. INTRODUCTION

1.1 Overview of Interoception

The highly sophisticated mammalian nervous system is composed of billions of neurons that form complex information networks through trillions of synapses in the brain and the spinal cord. Evolutionarily, such a nervous system has emerged to optimize for our survival. To facilitate this, the brain and the spinal cord interact and integrate streams of sensory information ascending from the peripheral nerve endings that are distributed throughout the body and form a part of the peripheral nervous system (PNS). This bidirectional cross-talk allows us to perceive, make sense of, and respond to the environmental signals such as the visual, auditory, and tactile stimuli. The process of conscious emergence of sensory awareness of our environment is termed as Exteroception. Besides these consciously perceived environmentally triggered exteroceptive signals, the brain and the spinal cord are also continuously bombarded by multiple sensory signals from visceral organs of the body[1]. However, unlike the exteroceptive signals, the sensory cues emerging from the peripheral organs are subliminal and are not consciously detected[2]. Nonetheless, they are extremely important for the brain to develop a sense of body's internal physiological state and maintain homeostasis[3]. For example, as you are sipping on a chai latte and reading this sentence using consciously detected visual cues emerging from your computer screen, somewhere in the background your brain is also sensing and regulating the exact blood pressure in the arteries at the tip of your toe and detecting sugar from your ingested chai drink at the duodenum– all of this without you consciously knowing or thinking about it! This process through which the brain detects and integrates the consciously imperceptible ascending signals emerging from visceral organs of the body and develops an appropriate cognitive, affective or physiological response is termed as Interoception (Fig. 1)[2]. The sensory (ascending) and regulatory (descending) interoceptive signals can be transmitted by both neuronal (vagal, spinal) and non-neuronal (endocrine, vascular, immune) pathways. The neuronal pathway, which is central to the work presented in this thesis, has two major afferent (i.e. ascending) branches that host their cell bodies in two distinct peripheral ganglia: Nodose/jugular ganglia (NG) and the dorsal root ganglia (DRG). The NG sends pseudo bipolar projections to the Nucleus Tractus Solitarius (NTS) in the brainstem

while DRG projects to the brain through the spinal cord. Broadly, the visceral afferents emerging from NG (vagal afferents or parasympathetic afferents) are thought to transmit mechanosensory and chemosensory signals to the brain, while those from the DRG (spinal afferents or sympathetic afferents) are believed to signal pain, temperature, and

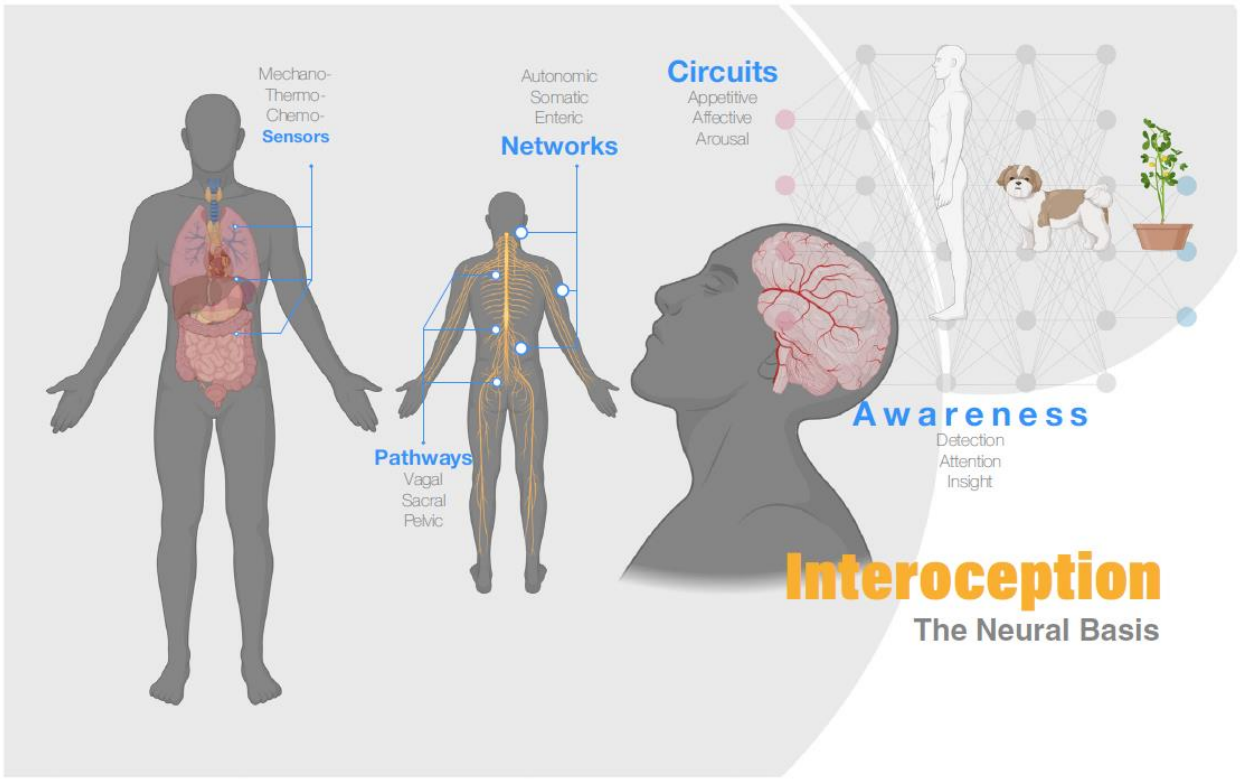

Figure 1.1. The neural basis of interoception spans across sensors (mechano-, thermos-, chemo-), pathways (vagal, somatosensory, sympathetic, parasympathetic), networks (autonomic, somatic, enteric), and circuits (such as arousal, appetitive, nociceptive, social, cognitive etc.). The processing and integration of these signals occurs at a subliminal level and helps create a circuit-based representation of internal body. Figure adapted from Ref. 2 (Berntson and Khalsa, 2022)

tissue injury. The central integration sites of these or other non-neuronal signals are often located in the subcortical structures of the brain such as the NTS and Parabrachial Nucleus (PBN). These integration hubs then subsequently project to higher brain regions such as the insula, somatosensory cortex, and the hypothalamus for further signal decoding. The descending or regulatory branches of the interoceptive circuits can similarly be of neuronal or non-neuronal origins. In the neuronal pathway, the parasympathetic and sympathetic-chain/prevertebral ganglia receive direct innervation from the brain through the vagal or spinal efferent nerves and in-turn

directly synapse onto the non-neuronal cells inside the end-organ for regulating organ function. Thus, to summarize the anatomical organization of the brain-body neural circuits: The peripheral nervous system, that is composed of somatic and autonomic branches, forms an information highway between peripheral organs and the brain. Physiological signals from organs can be processed by both somatosensory (DRG originating) and/or vagal (NG originating) nerves. The signals are predominantly processed in the brain-stem nuclei (NTS, PBN) and then regulatory signals are relayed back to the end-organs through the sympathetic and/or parasympathetic branches of the efferent arm to complete the interoceptive neural circuit[4] (Fig. 2).

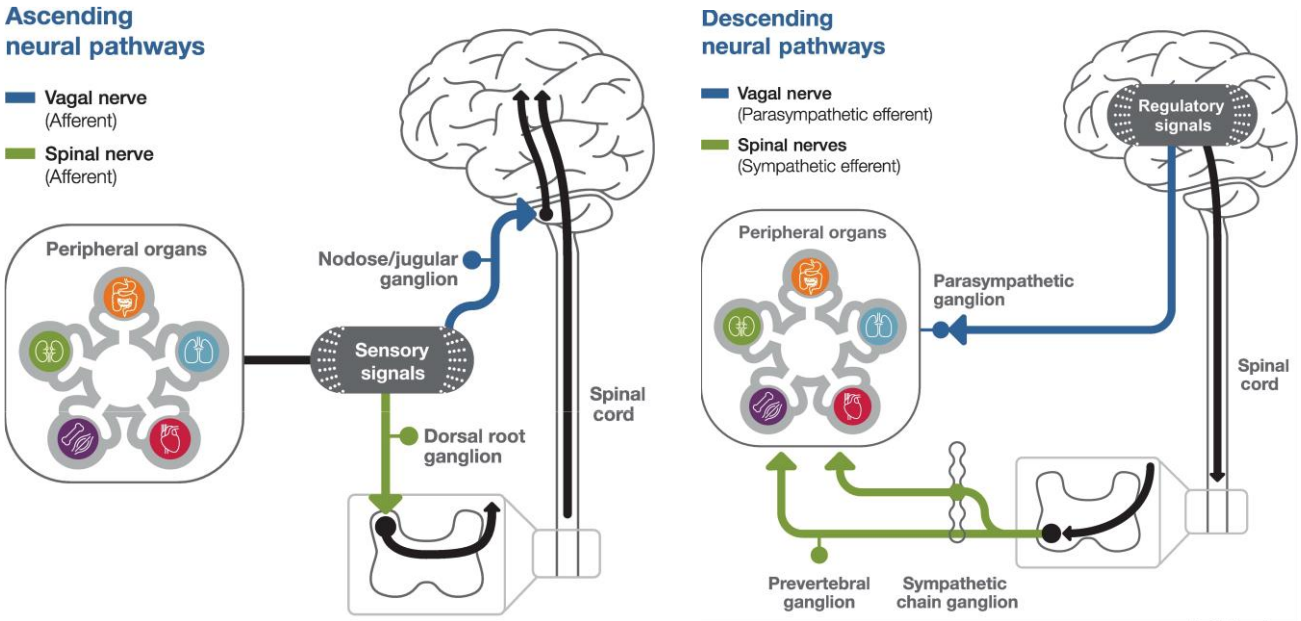

Figure 1.2. Schematic depiction of sensory (ascending) and motor (descending) neural pathways that innervate the peripheral organs. Figure adapted from Ref. 4

As the interoceptive circuits that connect the gastrointestinal (GI) tract to the brain are central to the work presented in this thesis, I will briefly discuss the neuroanatomical and functional atlas of sensory innervation of the gut (GI tract and gut are used interchangeably throughout this work) to illustrate the neurobiological basis of gut-brain interaction[5,6].

The gut presents a vast interface between the host and the external environment in the form of ingested food and pathogens. As such, to regulate the functioning of this complex organ, an equally complex nervous system has evolved which comprises of both intrinsic and extrinsic nerves. The intrinsic innervation of the gut (cell bodies residing in gut wall) is composed of the Enteric nervous

system (ENS), which largely operates autonomously and spans the entire length of the gut. The extrinsic innervation of the gut (cell bodies in ganglia outside the gut) is composed of both vagal sensory and somatosensory nerve terminals as well as sympathetic and parasympathetic efferent branches of the autonomic nervous system.

1.2 Sensory innervation of the gut

The gut lumen is a hollow tubular structure which is composed of several delicate layers, namely the epithelium, lamina propria, submucosal plexus, circular muscle, myenteric plexus, longitudinal muscle, and the serosa. The vagal sensory nerves terminate at several of these layers in the gut wall, specifically right below the epithelium (called as mucosal endings), in the circular muscle (intramuscular arrays, IMAs), and in the myenteric plexus (intra-ganglionic laminar endings, IGLEs). These extrinsic vagal nerves are known to encode both mechanical and chemical information emerging from the gut lumen. Molecularly distinct vagal subtypes such as the Oxtr1+ and Glp1r+ that form IGLEs in the small intestine and the stomach, respectively, were recently shown to selectively respond to gut distention[7,8] and a subset of vagal IGLEs have been found to express the mechanosensitive ion channel PIEZO2. The vagal sensory afferents (e.g. Gpr65+ subtype) also play a key role in detecting the chemical contents passing through the gut lumen, such as sugars, fats, pH, and amino acids. This role is largely thought to be performed by the mucosal endings[7]. For example, through electrophysiology and imaging at the NG, it has been shown that highly specific glucose chemoreceptors are distributed in the duodenum and upper jejunum that robustly respond to intestinal glucose perfusion, but not to perfusion of other macronutrients, mechanical distention or perfusion of glucose in the blood stream. At the same time, there also exist vagal polymodal chemoreceptors that are responsive to a wide range of luminal stimuli such as acid, alkali, hypertonic saline, and water. The somatosensory innervation of the gut emerging from the DRGs mediate visceral pain and form nociceptive terminals that detect temperature and noxious stimuli. Moreover, the spinal and vagal afferents in distal gut are also believed to sense microbial metabolites and thereby coordinate the host response to gut microbiota[9].

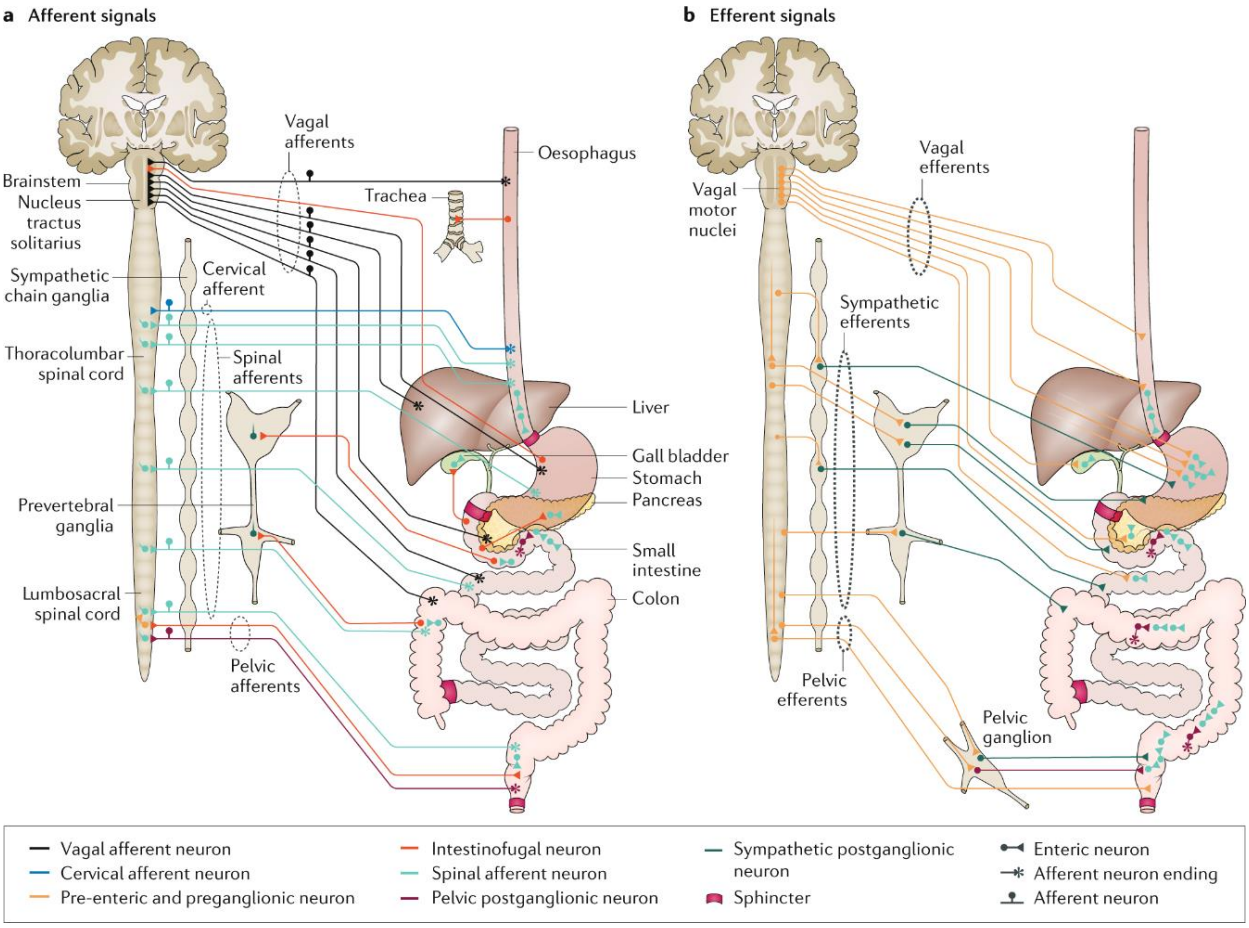

Figure 1.4. Detailed neuroanatomical map of innervation of the gastrointestinal tract starting from the esophagus to the colon[10]. Figure adapted from Ref. 10.

1.3 Sympathetic and Parasympathetic innervation of the gut

The sympathetic preganglionic neurons originate in the thoracic and lumbar regions of the spinal cord and project to the superior mesenteric, inferior mesenteric, and celiac ganglion. The postganglionic nor-adrenergic parasympathetic nerve fibers innervate the myenteric and submucosal plexus in the gut wall where they regulate intestinal blood flow, motility, and secretion of digestive enzymes. On the other hand, the parasympathetic gut innervation originates in the brain-stem region of the dorsal motor nucleus of the vagus (DMV) and the lumbosacral spinal cord. These nerve fibers regulate gut function through a combination of excitatory cholinergic pathway (smooth muscle contraction) and a non-adrenergic, non-cholinergic pathway (relaxation of smooth muscles)[9].

1.4 Disorders of aberrant interoceptive signaling

Since the brain-body communication is extremely vital to maintaining a homeostatic state, any aberrations or breakdown in this cross-talk at any node (central or peripheral) can lead to emergence of neurological, neuropsychiatric, and metabolic disorders and comorbidities. This is exemplified in disorders of the brain-gut interactions (represented by irritable bowel syndrome and chronic stress), non-cardiac chest pain, urological chronic pelvic pain, autism spectrum disorder and metabolic disorders such as obesity and diabetes, among others. Activation of the immune system in the periphery is signaled to the brain through both neuronal and humoral interoceptive signaling. A maladaptive recruitment of these pathways can put an individual at a greater risk to psychiatric disorders, affective disorders (i.e. mood disorders), and depressive disorders[11].

1.5 Bio-integrated devices to study brain-body circuits

Despite the significance of brain-body interoceptive signaling in understanding fundamental neurobiological processes as well as its clinical relevance, studying these circuits in causal fashion in model organisms such as rodents in their freely behaving states is extremely challenging. Engineered neurobiological tools such as optogenetics and chemogenetics for cell-type specific interrogation of neural circuits in the brain have become cornerstones of modern neuroscience research[12,13]. However, the application of these methodologies to causally investigate peripheral organ functions has not seen much progress[14,15]. The reason for that is largely technological, since, unlike the brain, the peripheral organs are extremely fragile, soft, mobile, show macroscale deformations, and have complex 3-D shapes. These features preclude direct extension of traditional neurotechnology devices that are developed for studying the brain to the periphery. Besides silencing and exciting cells with high spatiotemporal specificity, another vital function required for deciphering interoceptive signaling is recording of high-quality physiological activity from the brain as well as peripheral organs, either independently or simultaneously. Thus ideally, one needs devices that can seamlessly interface with the brain as well as a peripheral organ of interest while allowing cell-type specific stimulation and recording from regions of interest, while at the same time seeing the effects of these manipulations on animal behavior and physiology over chronic time scales. Developing such biomedical devices has been the focus of my PhD thesis. Before I delve into the specifics of how I went about developing this technology for the

gastrointestinal tract in mice[16], I would like to introduce and discuss the essential building blocks of this technology that are required for a complete systems level integration.

1.6 The need for multifunctional devices

The complexity of the brain can be estimated from the fact that it harbors billions of neurons that can be further classified into several hundred (at least) of molecularly defined distinct cell types. Neurons in the brain are organized into different neural circuits and communicate with each other by sending pulses of electrical activity, or action potentials, along their axons. As such recording the electrical activity from neurons has become one of the key techniques in neuroscience. Conventionally, this has been achieved by developing probes in the form of multielectrode arrays and shanks that allow integration of 1000s of channels using the sophisticated complimentary metal-oxide semiconductor (CMOS) technology[12,17]. While probes of this class undoubtedly benefit from a very high channel count, they are often made from hard, brittle, and rigid substrates such as elemental Silicon that exhibit a large mechanical mismatch (~ GPa) when compared to the modulus of the brain tissue itself (~kPa). This mismatch in mechanical properties between the device and interfacing tissue as well as the constant micromotion of the implanted probe with respect to the tissue generates a cascade of immune response in the brain, whereby the brain fully isolates the implanted probe by creating a thick, insulating glial scar (~100 μm thick) around the device[17]. This often results in lowering of the signal-to-noise ratio, in the best case, and complete loss of activity in the worst-case scenarios. More recently, the neural engineering community has tackled this challenge by aggressively reducing the probe thickness and by using soft, flexible substrates (plastic sheets, viscoelastic hydrogels) and electrode coatings (conducting polymers). Notable device geometries and thicknesses that allow fabrication of ultra-thin mesh like form factors of electrode arrays with bending stiffnesses approaching that of the brain tissue itself have successfully enabled long-term tracking (several years) of electrical activity in rodents[17,18].

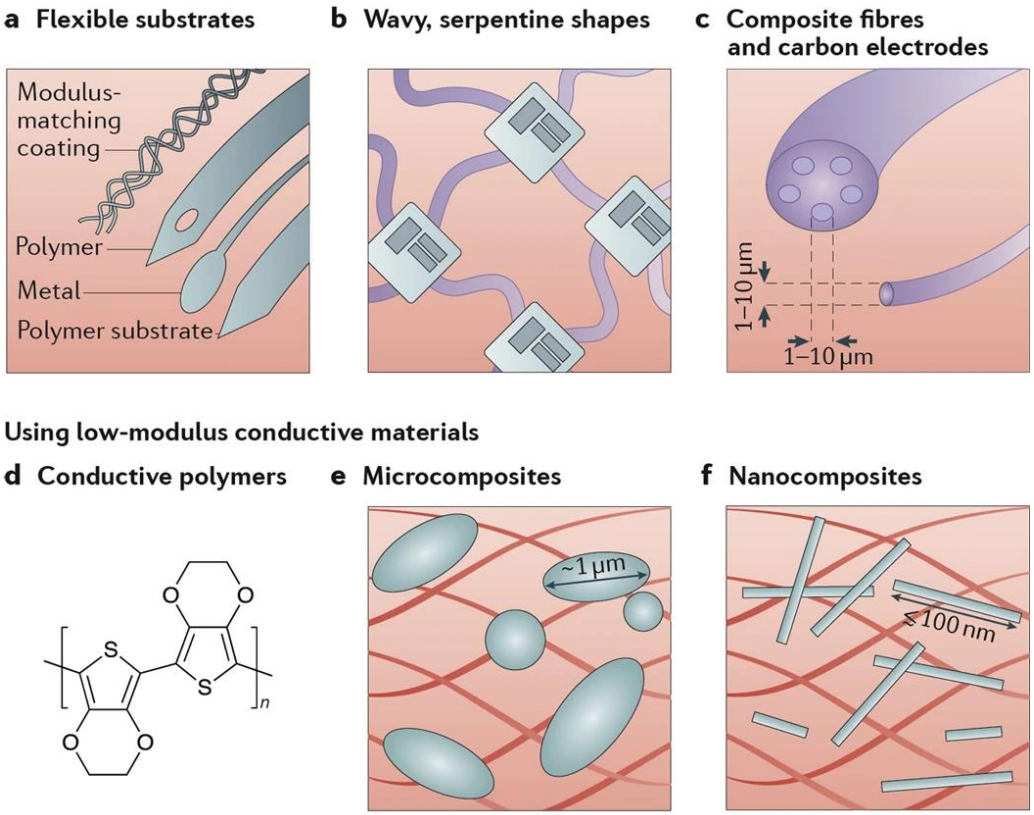

Figure 1.5. Summary of common approaches used to reduce the mechanical mismatch between implanted device and brain tissue. (a) Use of thin plastic substrates with soft encapsulation coatings; (b) Use of serpentine shaped tracks of thin deposited metal layers for interconnects; (c) Probes shaped like a cylindrical plastic fiber with microscale features; (d-f) Use of conductive polymer coatings, micro- and nano-composites of conductive fillers with soft, stretchable elastomers or hydrogels. Figure adapted from Ref. 12[12]

While these are indeed promising trends and have clinical relevance, especially for the emerging space of brain-machine interfaces, the large channel count devices lack the ability to bidirectionally interrogate the brain. More specifically, parallel advances in genetic engineering have resulted in powerful neurobiology tools in the form of optogenetics and chemogenetics that now allow cell-type specific stimulation of neurons with a high spatiotemporal precision[19]. This should be contrasted with the previous non-specific ways of neuronal stimulation such as electrical stimulation or approaches with limited specificity such as pharmacology. Techniques like optogenetics instead rely on expression of a light sensitive opsin (cation channel) such as Channelrhodopsin-2 (ChR2) in the cell membrane of pre-defined neuronal populations which then can be activated by short pulses of light. Opening of these ion channels depolarizes the cell through

influx of Ca^{2+} ions and kickstarts an action potential. Similar opsin variants (proton or chloride pumps) have also been developed to hyperpolarize the cell membrane and silence the neurons. Thus, with this approach, short and low intensity pulses of light delivered into brain regions of interest can switch-ON or switch-OFF genetically homogenous cellular populations.

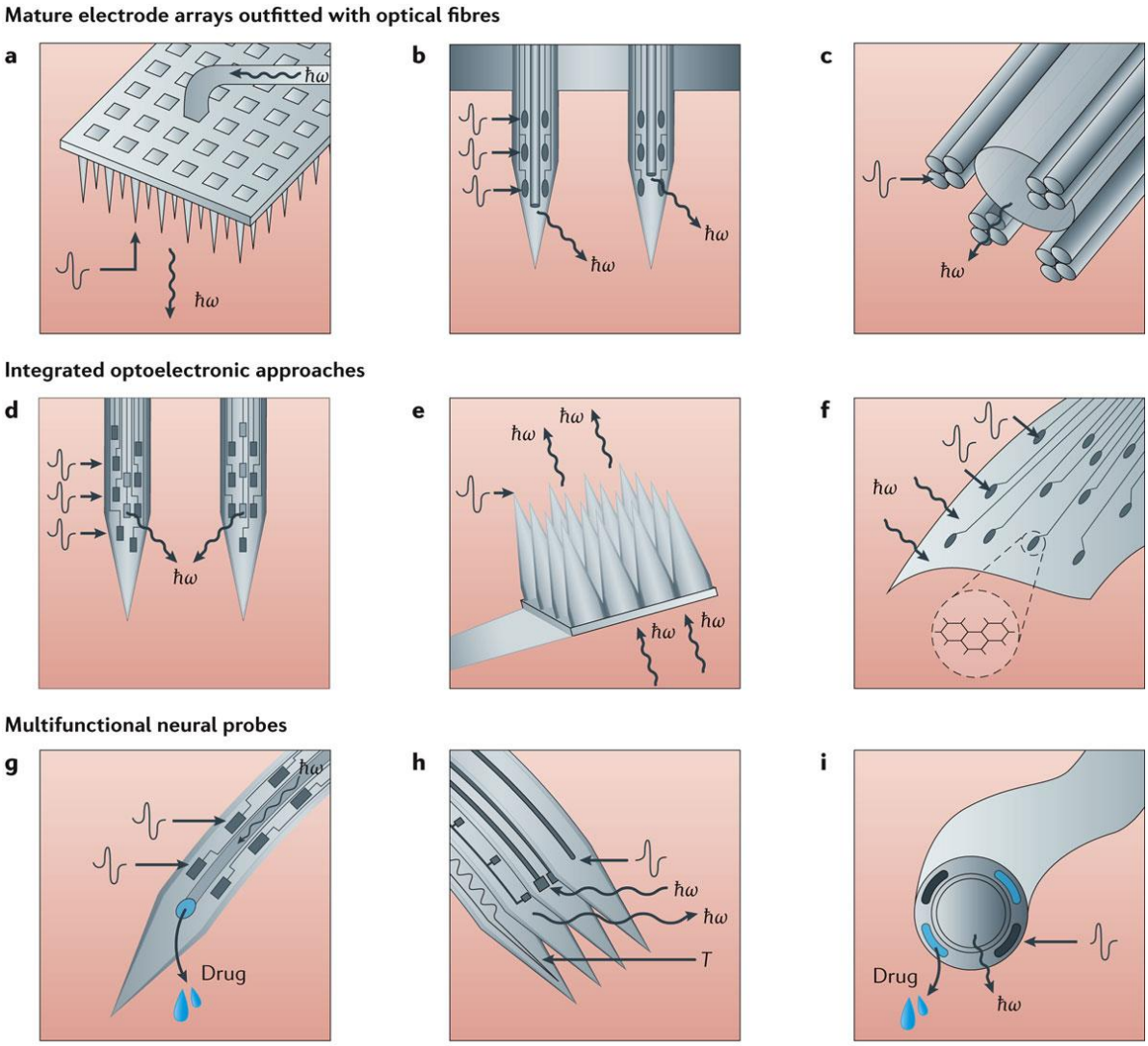

Figure 1.6. Summary of multimodal neural probes for bidirectional interfacing with the brain. Integration of light emitting optical waveguide with (a) Utah arrays; (b) Michigan style shanks; (c) tetrode arrays; (d) Electrode arrays on Silicon shanks monolithically integrated microscale light emitting diodes; Transparent yet conducting materials such as (e) ZnO arrays, and (f) ultrathin graphene electrode array permit delivery of light through an externally coupled source. (g-i) Examples of multifunctional and polymer based flexible neural probes. Figure adapted from Ref. 12[12].

To take full advantage of these powerful neurobiological tools for disentangling neural circuits in the brain, thus, requires implantable devices that can both record as well as modulate neural activity. When such bidirectional features are integrated in soft, flexible, and miniature probes that produce minimal inflammatory response in the brain they create powerful paradigm for chronic interrogation of brain circuits in a causal fashion in behaving animals. Several groups, including ours, have developed strategies that allow fabrication of such advanced multimodal integrated brain probes for fundamental neuroscience research[20].

While devices that allow causal modulation of neural circuits in the brain have received significant attention, commensurate progress in systems with similar capabilities that can be deployed in peripheral organs is severely lacking. As such causal studies of neural circuits of interoception which span across the brain, brain-stem, and visceral organs are not widely performed in the neuroscience community. Unlike the brain, which is encased in a rigid skull that provides an ideal anchorage site for an implanted device, peripheral organs in the abdominal cavity are predominantly composed of fragile and soft tissue that undergo large scale deformations (macromotion in organs versus micromotion in brain). I will illustrate this with the example of the GI tract which forms a major focus of my work. In the previous chapter I described the complexity of the nervous system of the gut that harbors both intrinsic neurons (ENS) and receives extrinsic innervation. The entirety of this complex nervous system resides in only ~300 μm thin fragile gut wall and spans almost ~5 times the body length in rodents. Moreover, the gut constantly undergoes motion in the form of giant peristaltic pressure waves to pass and digest ingested food and fecal matter. Such a complex physiology and anatomy makes it very challenging to study the nervous system of the GI tract in mice that are chronically carrying a device in their gut and moving freely in a behavior setting. Moreover, unlike the brain, most of the peripheral organs are not immune privileged and any rupture of the tissue can lead to sepsis and death. Recently, some progress has been made in modulating nerve activity in peripheral organs such as the bladder and kidney wherein soft and thin microfabricated devices which carry light sources in the form microscale light emitting diodes and thermal sensors were laminated onto the surface of these organs [21,22]. However, devices tuned for modulation of large lengths of luminal organs such as the intestine are non-existent.

1.7 Scalable and integrated fabrication of multimodal neurotechnology using fiber drawing

Fabrication of multifunctional neurotechnology comes with its own set of challenges. The most common approach that researchers have adopted for fabricating such devices is that of traditional optical lithography-based microfabrication. While this approach provides some compelling advantages in the form of mature process flows borrowed from the semiconductor industry and sub-micron precision of patterned features, it nonetheless relies on layer-by-layer development of a multifunctional device. Specifically, the individual device layers are produced independently and then the whole probe is put together through careful (and often laborious) manual alignment and bonding of the fabricated layers through several transfer-printing steps[23].

Recently work from our lab has introduced a rather non-traditional technique for scalable and monolithic fabrication of multimodal neurotechnology. This method, termed as fiber drawing, begins with fabrication of the macroscale scaled-up version (cm scale) of the desired device through machining of blocks of thermoplastic polymers[24]. This scaled-up template, called the preform, is then drawn into several hundred kilometers of fiber device by controlled application of heat and stress and simultaneous size reduction (10 to 100 times with deterministic control), such that the embedded functionalities in the parent preform are preserved throughout the entire length of the drawn fiber. As compared to traditional photolithographic methods, this approach provides two clear advantages: Scaled up production (~ 1000s of rodent scale devices from single successful fabrication) and monolithic integration of multiple modalities in a one-step fabrication scheme. Our group first demonstrated the utility of this approach by producing a first-of-its-kind multifunctional microscale polymeric device for the brain that was capable of recording single-unit neural activity in upto 8 channels through embedded Sn based microelectrodes, deliver light through an embedded polymeric core/clad waveguide, and deliver pharmacological compounds through a microfluidic channel[25]. In subsequent iterations our group successfully developed versions of this device that integrated low-modulus (~MPa) polymer-based conducting electrodes that replaced high moduli Sn microelectrodes (~GPa) and engineered ways to process thermoplastic elastomers that permitted fabrication of stretchable fiber for interfacing with the spinal cord in mice[26,27].

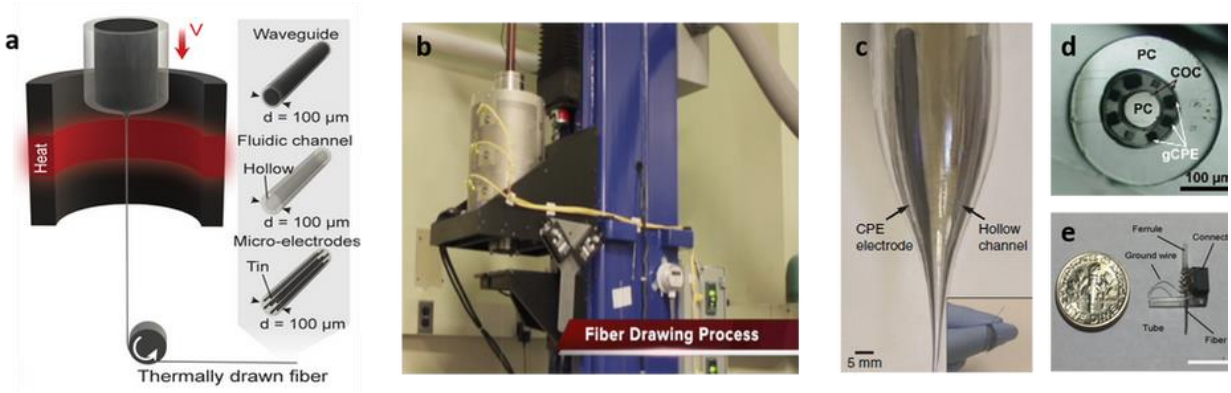

Figure 1.7. (a) Schematic illustration of the thermal drawing process that shows a preform that is predominantly composed of thermoplastic polymers being heated in 3-zone furnace and drawn into several kilometers long fibers with microscale features that remain conserved in the entire length, figure reproduced from Ref. 28[28]; (b) Photograph of the thermal drawing tower that I used for all of my draws; (c) Pictures showing the necking-zone of an all-polymer preform, figure reproduced from Ref.26[26]; (d) Cross-sectional micrograph showing the embedded features in the corresponding fiber that results from this preform, figure reproduced from Ref.26[26]; (e) Fully assembled device, figure reproduced from Ref.26[26].

In this thesis I have developed new device integration schemes that enable development of wireless fiber technology to study neural circuits in the brain as well as peripheral organs exemplified by the different regions of the gut such as the duodenum, ileum, and the proximal colon in awake behaving mice. To achieve this, several current limitations of fiber drawing as a neurotechnology fabrication method had to be overcome. I began by developing an approach that overcomes thermomechanical constraints of fiber drawing and allows us to process traditionally non-drawable components such as metal microwires, carbon nanotube yarns, and semiconductor based microelectronic chips. These advances have yielded probes that allow depth specific probing of neural circuits in the brain, while also being compatible with functional magnetic resonance imaging (fMRI) scans[29]. Subsequently, the same underlying design principles have led me to develop fiber-based miniaturized electrochemical probes for performing electrocatalytic reactions in the brain tissue. This platform device has made possible, for the very first time, the investigation of transient, gaseous neurotransmitters such as NO and CO in awake behaving animals through controlled generation and delivery in-vivo, which is otherwise intractable with existing technology[30]. With an eye on developing technology for modulating neural circuits embedded within organs, I designed a flexible, low-loss polymer waveguide to enable, for the very first time, optogenetic control of neuroepithelial cells lining the gut wall in behaving mice. These probes not

only allowed a new chronically viable paradigm of intraluminal gut optogenetics and introduced me to the possibility of designing advanced fibers for the GI tract, but it was also instrumental in the discovery of CCK neuropod cells as specialized sensory cells that discern sugar from artificial sweetener and relay this information to the brain within milliseconds[16]. All these advances in device designs, fabrication routes, and new surgical approaches finally led me, along with my amazing collaborators, to develop wireless microelectronic fibers to modulate and record gut-to-brain neural circuits[31]. I hope that the ideas, devices, and systematic validation in rodent studies presented in this thesis serve as useful examples and inspire future application of these principles to study other currently intractable brain-organ neural circuits.

CHAPTER 2. MULTIFUNCTIONAL FIBERS FOR DEPTH-SPECIFIC INTERROGATION AND DELIVERY OF GASEOUS NEUROMDULATORS TO THE BRAIN

Note: The material presented in this chapter was first published as M. Antonini, A. Sahasrabudhe* et. al. Adv. Funct. Mater.2021, 31, 2104857 (Ref. 29) and J. Park*, K. Jin*, A. Sahasrabudhe et. al. Nat. Nanotechnol. 15, 690–697, 2020 (Ref. 30). Work on delivery of gaseous neuromodulator (sections 2.10 – 2.13) was also presented in Jimin Park, PhD Thesis 2022.*

2.1 Motivation

Signaling complexity within the nervous system suggests the need for integration of bi-directional electrical, optical and chemical interfaces within neural probes.[32] Over the past decade, thermal drawing has enabled fabrication of versatile neural probes in the form of flexible miniature fibers that permitted multimodal neural interrogation while minimizing impact on local tissues.[24,30,33–35] A typical fiber fabrication workflow begins with a centimeter-scale model, termed preform, which is produced by standard machining methods. The preform is then heated in a furnace above the glass transition temperature (T_g) and melting temperature (T_m) of its constituent materials and drawn into meters long microscale fibers.[36] During this process, the preform dimensions are scaled down by several orders of magnitude, while preserving the overall cross-sectional geometry of the final fiber.[37] This approach permits integration of multiple functionalities such as electrodes for recording of extracellular neuronal potentials, optical waveguides for optogenetic neuromodulation, and microfluidic channels for drug and gene delivery. This one-step, top-down fabrication process can yield hundreds of probes from a single preform, and is a cost-efficient and scalable alternative to lithographic approaches that require resource-intensive cleanroom microfabrication techniques.[23,38] Despite these advantages, widespread adoption of fiber-based probes by the neuroscience community has been hindered by several limitations.

Although thermal drawing is compatible with a wide range of metals, semiconductors, and polymers, recording electrodes previously incorporated into fibers were limited to either carbon-based polymer composites or drawable metals such as tin.[33,39] Polymer composites exhibit limited conductivity due to the constraints on the weight fraction of conducting additives that can be incorporated into a polymer matrix without adversely modifying its T_g and viscosity.[35,39] This poor conductivity restricts the electrode lateral dimensions (>~20 μm) and fiber lengths (<~4 mm), which in turn limits the spatial resolution of extracellular electrophysiology [17] and increases device footprint.[35,39] Moreover, the heterogeneous volumetric distribution of filler particles in carbon composites introduces additional variability in the conductivity of polymer electrodes.[35,39] Although metals can be thermally drawn, their T_m dictates the need for comparable T_g of the polymer cladding. For instance, while tin permitted integration of 5 μm electrodes into fiber-based probes, the necessary use of high T_g polymers such as polyetherimide and polyphenylsulfone precluded integration of low-loss optical waveguides due to the strong absorption of visible light in those materials.[33] In addition to the materials limitations, the labor-intensive interfacing of each functional feature embedded within a fiber to fiber backend hardware has been the rate-limiting fabrication step and a barrier for broad adoption of fiber-based neural probes.

To overcome materials selection and interface challenges associated with fiber-based probes, we have implemented two approaches: 1) iterative thermal drawing with a soft, low T_m metal (indium); 2) convergence-drawing with a traditionally non-drawable metal (tungsten). These methods deliver multifunctional polymer fibers with low-impedance metal electrodes, low-loss polymer waveguides and microfluidic channels, while substantially reducing the complexity of back-end connectorization. We characterize the electrical, optical, fluidic and mechanical properties of these fibers and validate them *in vivo* for studies in mice and rats. Furthermore, we integrate multifunctional fibers into a light-weight and compact mechanical microdrive that allows fine electrode positioning post-implantation to maintain high-fidelity, single-neuron depth-specific recordings in freely moving mice. Finally, we demonstrate that these fibers elicit negligible artifacts in magnetic resonance imaging (MRI), and couple them with functional MRI (fMRI) to track the spatiotemporal kinetics of fluid delivery in rat brain. This suggests that that fiber-based multifunctional probes could in future be leveraged for mapping global brain-wide activity to local neuromodulation.[40–42]

Results and Discussion

2.2 Fabrication of multifunctional neural probes through iterative and convergence thermal drawing

To enable scalable fabrication of neural probes with customizable functionalities & geometries, we developed two approaches: (1) Two-step iterative thermal drawing with soft, low T_m metal indium; and (2) convergence drawing with tungsten microwires. A two-step iterative thermal drawing approach is schematically illustrated in Figure 2.1a. The macroscale preforms of each modality (electrodes, optical waveguides, and microfluidic channels), termed here as the *first-step preforms*, are separately drawn into millimeter-scale *first-step fibers*. These first-step fibers are then arranged within the *second-step preform*. Drawing this second-step preform yields the microscale *second-step fiber*. This iterative size reduction approach using multi-step drawing enables the fabrication of microscale electrodes while preventing emergence of capillary instabilities.[33,43,44]

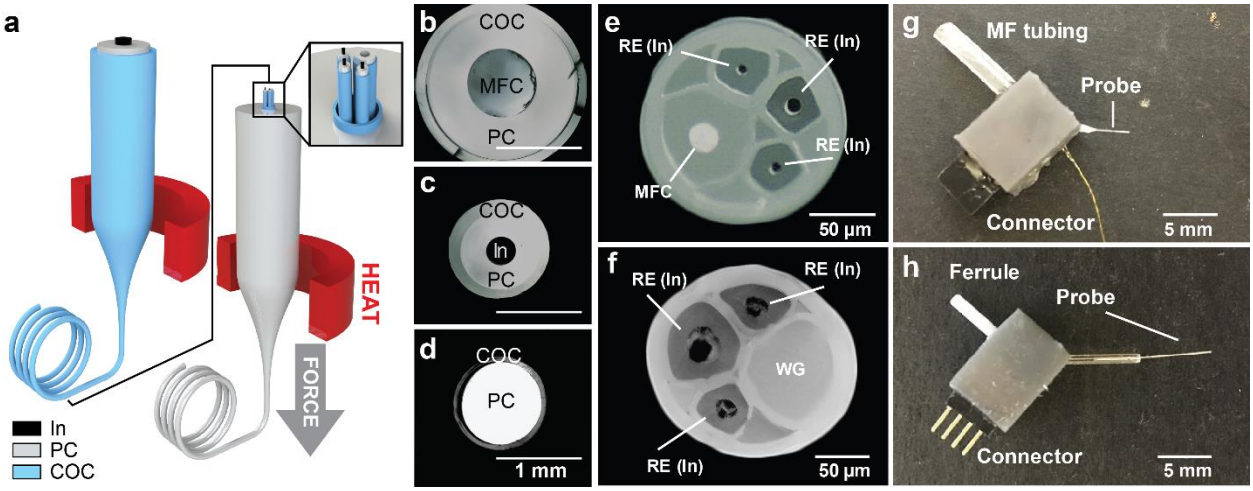

Figure 2.1. Multifunctional neural probe fabrication through the two-step thermal drawing process. (a) Schematic of the two-step TDP. (b-d) Cross-sectional microscope image of the fibers produced by the first iteration of the TDP. (e-f) Cross-sectional microscope image of the fibers produced by the second iteration of the TDP. (g-h) Final connectorized device. COC: cyclic olefin copolymer, MFC: microfluidic channel, PC: polycarbonate, In: indium, RE: Recording electrode. *From Antonini*, Sahasrabudhe* et. al., Ref. 29.*

Here, the first-step fibers consist of a recording electrode made of indium (In) encapsulated in polycarbonate (PC) and cyclic olefin copolymer (COC) cladding (Figure 2.1b), an optical waveguide with a PC core and COC cladding (Figure 2.1c), and a microfluidic channel made of a hollow PC/COC cladding (Figure 2.1d). Unlike other high T_m metals/alloys[33,45], a low T_m of ~156 °C enables indium to be co-drawn with an optically transparent PC/COC waveguide (PC refractive index n_{PC}= 1.59, T_g = 150 °C; COC n_{COC} = 1.53, T_g = 158 °C).[33,35,46] The macroscale first step fibers are then arranged inside a COC/PC polymer cladding to form the second-step preform which is then drawn into a microscale fiber. As these first-step fibers can be arranged into any desired configuration, this "mix-and-match" approach enables straightforward customization of fibers for a given application. We illustrate this concept in two fiber designs: i) an electro-fluidic fiber; and ii) an opto-electric fiber. Figure 2.1e shows the cross-section of the electro-fluidic fiber (~141.8 ± 7.4 μm) which comprises three indium electrodes (~9.3 ± 2.1 μm) for electrophysiological recording and a hollow channel for concomitant delivery of fluids (19.1 ± 0.8 μm). Similarly, Figure 2.1f depicts the cross-section of the opto-electric fiber (~162.2 ± 6.1 μm) that enables simultaneous light delivery and electrical recording and features three indium electrodes (~21.6 ± 7.8 μm) and a (~67.3 ± 5.5 μm) PC/COC optical waveguide. Figure B1 demonstrates another example of the iterative drawing method to achieve a more complex fiber geometry. Here, multifunctional first-step fibers are fabricated (Figure B1a,b), and stacked into a linear pattern before being drawn again into a microscale fiber (Figure B1c,d). By cutting the second-step fiber at an angle (Figure B1e), or in a step-wise manner (Figure B1f,g), depth specific recording and modulation can potentially be achieved with this design.

The iterative fiber drawing approach not only enables customized fiber design, but also facilitates the back-end connectorization process which transforms a fiber segment into a fully functional neural probe. Drawing of the second step preform without prior consolidation allows for facile separation of individual components in a second step fiber upon removal of its outer COC cladding due to strain (Figure B2). Figure B2 illustrates the connectorization workflow of a two-step fiber. The mechanical etching of the outermost sacrificial cladding exposes individual functional components (electrodes, waveguides, channels) in the fiber and provides independent access to each component. The electrode microfibers are then connected to header-pins using a conductive adhesive, the waveguide is coupled to a ceramic ferrule, and the hollow channel is connected to the plastic tubing for fluid delivery. The sacrificial PC cladding from the remaining exposed fiber

(implantable front end) is chemically etched. Encapsulation of the backend input/output (I/O) hardware inside a 3D printed microdrive shuttle completes the overall fabrication process. Figure 2.1g, h show images of a fully connected fiber-based device using this approach. Thus, the connectorization process has been reduced to 9 steps (~1h per device), compared to 18 steps (~4h per device) used in previous designs.[35]

Another approach to overcome materials constraints in multifunctional fiber-probe design relies on recently demonstrated convergence drawing.[47] This approach overcomes constraints on the preform components to have similar glass transition temperatures (T_g) and melt viscosities at the drawing temperature.[24,37] During convergence drawing, a microwire of a material with T_m (or T_g) significantly higher than the drawing temperature is fed into a hollow channel within the preform which collapses and converges the wire into the polymer cladding of the resulting fiber (Figure 2.2a). This approach enables incorporation of high conductivity metallic electrodes independent of their T_m and thereby widens the palette of functional materials that can be integrated into fiber probes.[24,37] To illustrate the versatility of this fiber drawing method we fabricate two different fiber designs: i) a tetrode-like fiber; ii) a multifunctional fiber with electrical, optical, and microfluidic features.

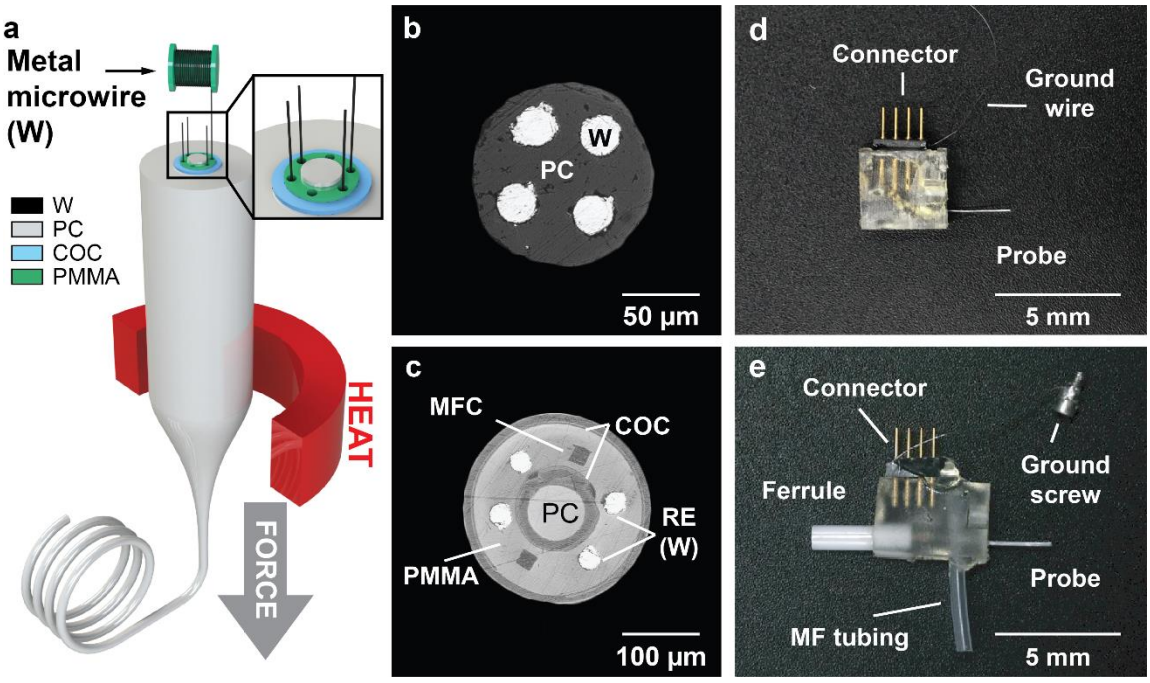

Figure 2.2. Multifunctional neural probe fabrication through the convergence thermal drawing process. (a) Schematic of the convergence drawing process. (b-c) Cross-sectional microscope

image of the fibers produced by the convergence TDP. (d-e) Final connectorized device. COC: cyclic olefin copolymer, PMMA: Polymethyl methacrylate, PC: polycarbonate, W: tungsten, MFC: microfluidic channel, RE: Recording electrode. *From Antonini*, Sahasrabudhe* et. al., Ref. 29.*

First, we fabricate a 108.94 ± 9.4 μm PC (T_g = 150 °C) fiber comprising four tungsten electrodes arranged in a tetrode like configuration (Figure 2.2b). The preform is produced by machining four grooves (1 mm) onto a PC rod (1/8 inch in diameter), which is then wrapped with PC sheets and consolidated in a vacuum oven (Methods section) to obtain a final diameter of ~4 mm. The preform is then drawn into ~50 m long fiber while simultaneously feeding tungsten microwires into the hollow channels. The resulting microscale fiber has four closely packed 25 μm electrodes that are separated by 10-12 μm (Figure 2.2b). This process can be easily extended to a higher number of electrodes, either through a convergence of N electrodes (N>4) or a subsequent convergence of multiple tetrode fibers (N × 4-electrodes) akin to iterative thermal drawing described above.

Following demonstration of integrating tungsten electrodes into a transparent polymer PC, we apply convergence drawing to create a multifunctional probe that features four tungsten recording electrodes, a PC/COC optical waveguide, and two microfluidic channels (Figure 2.2c). The preform for this fiber was produced by standard machining, like fibers described above, and then drawn into ~100 m long fiber with a 40-45-fold reduction in its cross-sectional dimensions. Four 25μm tungsten microwires were simultaneously fed into the fiber during drawing. The overall cross-sectional diameter of the fiber was 225.50 ± 8.7 μm (~350 μm prior to etching of the sacrificial layers). The final linear dimensions of the waveguide core and microfluidic channels were 108 ± 4.9 μm and 19.27 ± 1.5μm, respectively. (Figure 2.2c).

Like the iterative drawing, convergence drawing simplifies the interfacing to the back-end connectors. Figure B3 schematically depicts a typical process flow, wherein solvent etching exposes metal microwires and/or the PC/COC waveguide which are subsequently connected to electrical pins and optical ferrules, respectively. The microfluidic channels are accessed through an orthogonal T-connection and the entire assembly is encapsulated into a 3D printed shuttle drive. Complete and ready for implantation tetrode-like and multifunctional fibers (Figure 2.2c, d) can be produced in 4-6 steps (30 min). Thus, the iterative drawing and convergence drawing approaches presented in this work not only expand the array of materials used in fiber-based probes, but also address the bottleneck associated with back-end interfacing of these devices.

2.3 Characterization of optical, electrical, mechanical, and fluidic properties of fiber probes

We next characterized electrical, optical, fluidic, and mechanical properties which will dictate the performance of the fiber-based probes *in vivo*. Electrochemical impedance spectroscopy (Figure 2.3a) was employed to assess the utility of the integrated tungsten and indium microelectrodes for neural recording. The average electrode impedance was found to be in the range of 71.8 ± 29.8 kΩ for tungsten and 338.1 ± 167.8 kΩ for indium at 1 kHz, which is comparable to state-of-the-art recording probes featuring metallic electrodes with similar dimensions.[17,32] Moreover, the inter-electrode impedance through the polymer cladding was found to be >2 MΩ at 1 kHz which indicates negligible inter-electrode cross talk (Figure B4).[48] Tungsten electrodes are routinely used for *in vivo* electrophysiology and are known to form stable interfaces with the surrounding tissue.[49,50] However, little is known about the nature of the electrochemical interface between indium and the neural tissue. From the established Pourbaix diagram for indium (Figure B5a),[51] we hypothesized the presence of a self-passivating native oxide layer on the surface of indium microelectrodes at physiological conditions (pH 7.4, E= 0V). This was indeed corroborated by the the presence of a reversible In^{2+}/In^{3+} redox peak in the –0.9 to –0.8V potential window (vs. Ag/AgCl) which is observed for both macro- and microscale indium electrodes (Figure 2.3b and inset). This self-passivating native oxide layer on the electrode surface can be beneficial to establishing a capacitively dominant electrochemical interface that minimizes faradaic charge transfer reactions.[52] To further quantify this observation, the Nyquist plot for indium was fitted to a Randle's equivalent circuit (Figure 2.3c) and the corresponding charge transfer resistance (R_{ct}) value was calculated. A high value of R_{ct} (4.68 MΩ) suggests slow charge-transfer reactions at the metal/electrolyte interface and thus a predominantly capacitive interface for indium electrodes.

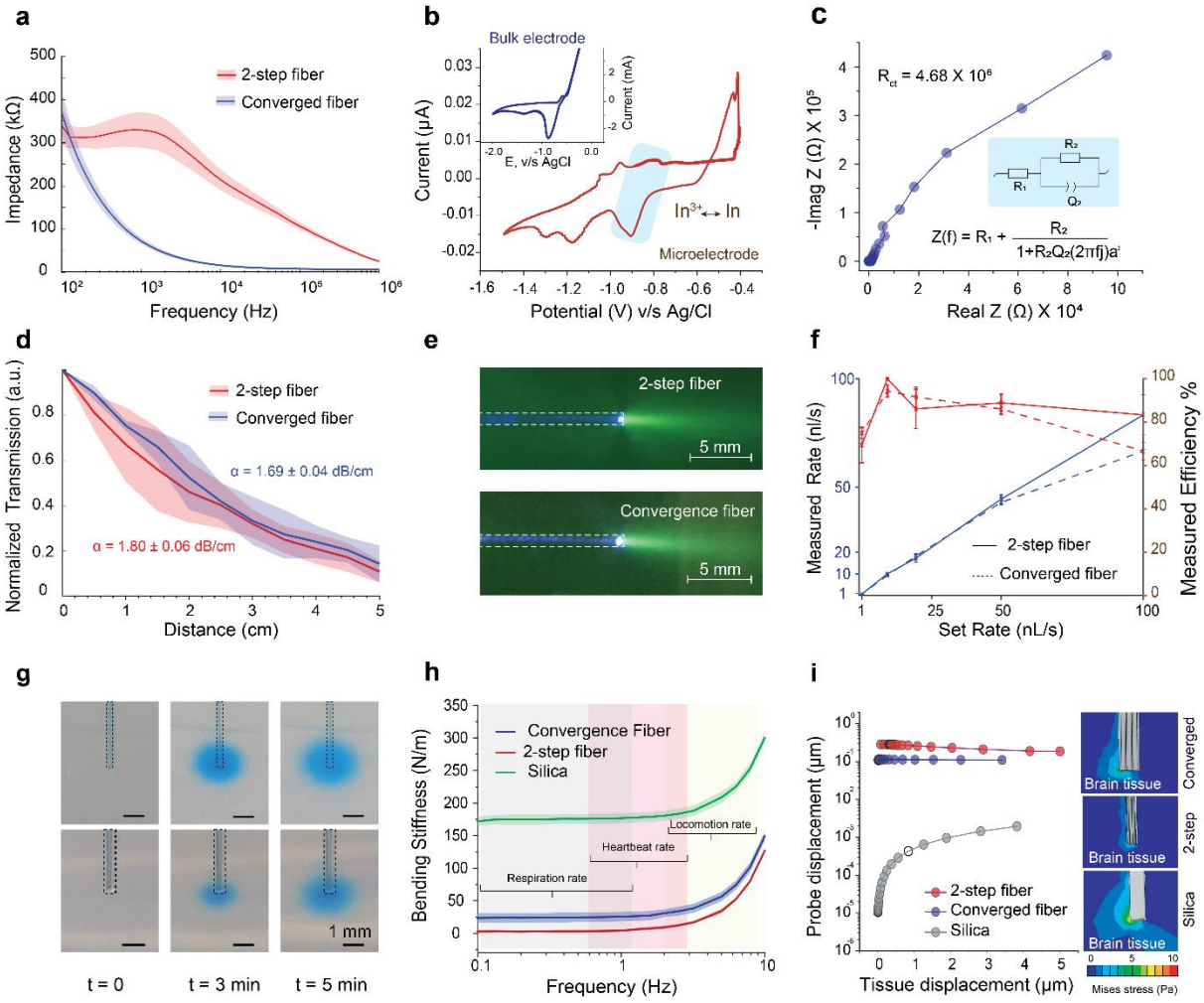

Figure 2.3. Characterization of the two-step and converged multifunctional fibers. (a) Electrochemical impedance spectroscopy of the two-step and converged fiber probes. (b) Cyclic voltammogram in 1xPBS of bulk indium and indium microelectrode from neural probe of fig. 1e. (c) Nyquist plot and equivalent circuit model for indium electrode in PBS (d) Optical loss characterization of the two-step and converged fiber probes. Shaded areas represent s.d (n=3). (e) Illustration of light emission profiles of waveguides via coupling of 473nm laser in a diluted fluorescein solution. (f) Output injection rate and injection efficiency of the microfluidic channel of two-step and converged fiber probes. (n = 4, 2 cm long). (g) Illustration of microfluidic capabilities via infusion of a blue dye at 100nl/min into a phantom brain (0.6% agarose gel). (h) Bending stiffness measured for two-step fiber, convergence fiber, and a 300 μm silica optical fiber . Shaded areas represent s.d (n=3). (i) The displacement for two-step fibers, converged fibers and 300μm silica fibers during 0-5 μm lateral displacement of the brain tissue (left); Mises stress profile within the brain tissue for two-step fibers, converged fibers and 300 μm silica fibers at 5 μm lateral deformation of the brain tissue. *From Antonini*, Sahasrabudhe* et. al., Ref. 29.*

We then characterized the integrated waveguides with the two-step and converged fibers. A transmission loss coefficient (α) of 1.8 ± 0.06 and 1.69 ± 0.04 dB/cm at 473 nm was determined for the opto-electric and the multifunctional fibers, respectively (Figure 2.3d). The obtained values are comparable to those of previously reported multifunctional fibers, and indicate that these integrated polymer waveguides are suitable for optogenetic modulation mediated by blue-light activated opsins *in vivo.*[33,35,53] Figure 2.3e shows typical illumination profiles from the waveguides for fibers produced via iterative and convergence methods immersed in a solution of 0.01 mM Fluorescein dye.

Next, we quantified the efficiency of fluid delivery by infusing an Evans' Blue dye solution at injection rates that are commonly used for intracerebral injections (Figure 2.3f). An efficiency between 65 –100% was observed for injection rates between 1-100 nL/s for both the electro-fluidic and multifunctional fibers. Figure 2.3g shows a typical time-course of dye injection in a phantom brain (0.6% agarose gel).

Finally, we characterized the mechanical properties of both fibers by quantifying their bending stiffness in a single cantilever mode (Figure 2.3h). We found that fibers produced by two-step and convergence drawing showed substantially lower bending stiffness than a conventional silica fiber of comparable dimensions (300μm) across the entire frequency spectrum corresponding to respiration, heartbeat and locomotion rates (0.1–10 Hz). A decrease in bending stiffness positively correlates with reduced relative micromotion between brain tissue and implanted probes, which is anticipated to reduce the tissue damage and facilitate their chronic use.[54] The two-step fibers were found to have 10-12 times lower stiffness values compared to converged multifunctional fibers due to their smaller dimensions (140 μm vs 225 μm) and substantially lower Young's modulus for indium (12.74 GPa) as compared to tungsten (340 GPa).[55] The stress distribution in the polymer cladding visualized with finite elemental analysis (FEA) for a single cantilever bending mode qualitatively corroborates the experimentally observed trends of stiffness values (Figure B5b). We next evaluated the relative micromotion between the implanted fiber probes and the brain tissue using FEA. From the displacement plots, it is apparent that relative micromotion between the implant and the tissue is higher for mechanically rigid silica fibers as compared to compliant polymer fibers (Fig. 2.3i (left)). The deflection at the implant tip for rigid silica fibers is predicted to be ~2 – 4 orders of magnitude lower than that for the flexible polymer fibers. The FEA also captures the difference in micromotion between the two-step and converged fibers, wherein the

soft and low stiffness indium-containing fibers experience larger displacement (and hence smaller relative motion) than the stiffer converged fibers. The distribution of von-Mises stress profiles around the implant tips produced by this relative micromotion agrees with the bending-stiffness trends experimentally observed for the respective probes (Fig. 2.3i, right). Note, that depending on the application, the bending stiffness can be further minimized/tuned by reducing the fiber dimensions and selecting softer polymers as cladding.

2.4 Recording and stimulation of neural activity *in vivo* using two-step and converged fiber probes

To evaluate our probes' ability to chronically record endogenous neuronal activity, we implanted the two-step electro-fluidic fibers (Figure 2.1e) and the converged multifunctional fibers (Figure 2.2c) into the medial prefrontal cortex (mPFC) of wild type (WT) C57BL/6 mice. The central role that mPFC plays in cognitive and executive processes has made this brain region a target of numerous neuromodulation studies, offering a rich field for comparison of our probes' performance to prior observations.[56–58] Both designs reliably recorded extracellular potentials for at least four weeks following implantation surgeries, and single unit activity was reliably detected over this time period. Similar to previous studies with Sn microelectrodes,[33] electrophysiological recording with indium electrodes in the two-step fibers had a signal to noise ratio (SNR) of 7.4 ± 0.7 and a noise floor of 114.4 ± 39.3 μV at one week (Figure 2.4a), and a SNR of 10.9 ± 2.8 and noise floor of 94.5 ± 21.1 μV at four weeks post-implantation (Figure 2.4e). Principal component analysis (PCA) followed by gaussian mixture model (GMM) clustering [59] isolated 2 putative single units at week 1 (Figure 2.4b,c). For these units, cluster quality was confirmed as intermediate by calculating L-ratio (<0.1) and isolation distance (>50).[60] Although one of the isolated units was lost during subsequent recordings, the second unit was preserved up to week 4 (Figure 2.4e,f,g) and likely up to week 8 (Figure B6) as indicated by its stable average waveform (Figure 2.4c,g) and inter-spike interval (ISI) (Figure 2.4d,h). [61]

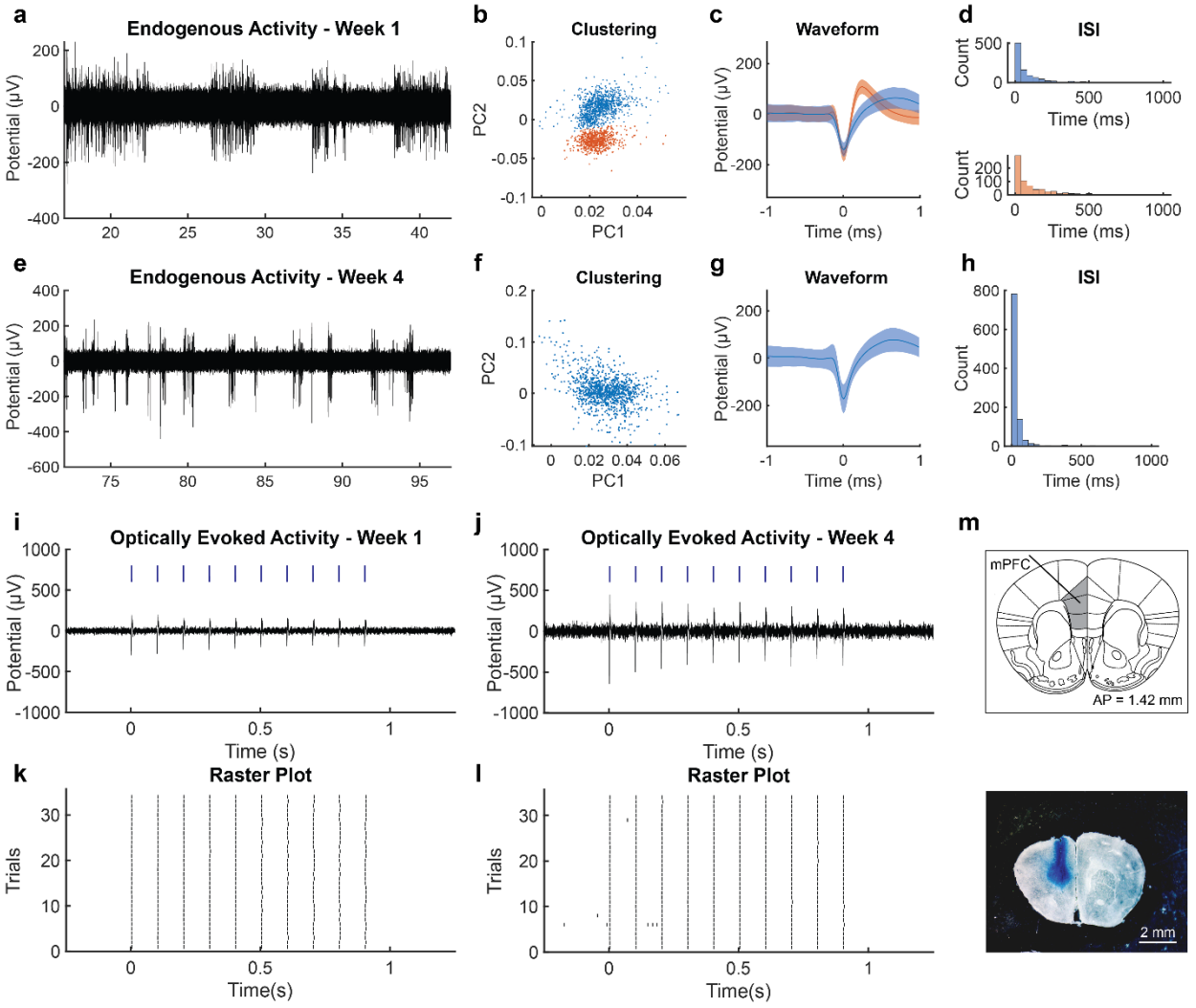

Figure 2.4. Two-step opto-electric and electro-fluidic neural probes enables chronic recording of endogenous and optically-evoked neural activity *in vivo***.** (a) (a-h) Endogenous activity recorded using the two-step fiber. (a) endogenous activity 1 week after implantation containing 2 separable single-unit activity. (SNR = 6.88, noise floor = 89 μV) (b) Principal-component analysis (PCA) of the putative unit detected in (a). (c) Average waveform (STA) shows the waveform of the separated units. (d) Interspike interval of each separated unit. (e-h) similar to (a-d) endogenous activity, PCA, waveform and ISI for week 4 after implantation. (SNR = 12.91, noise floor = 80 μV) A single unit detected and is similar to the one of the units from week one. (i-l) Simultaneous optogenetic stimulation (wavelength λ=473 nm, 5 ms pulse width, 10 Hz, 1s-long pulse train, power density 10 mW/mm^2, blue markers indicate laser pulse. Activity recorded 1 week (i) and 4 weeks (j) post implantation. raster plot of detected evoked potentials over 31 stimulation trials (k,l) highlight the reproducibility of the optically-evoked activity. (m) micrograph of brain slices following Evans' Blue dye injection (2% in NaCl, 2μl over 20mn) through the microfluidic channels and transcardial perfusion of the animal. *From Antonini*, Sahasrabudhe* et. al., Ref. 29.*

Similarly, tungsten electrodes in the converged multifunctional fibers also enabled weeks-long tracking of single units. These recordings yielded a SNR values of 15.6 ± 5.2 and 12.4 ± 2.4 and a noise floor 36.2 ± 8.4 µV and 41.5 ± 2.4 µV at weeks 2 and 3, respectively (Figure 2.5c,g). Two single units were isolated and tracked from week 2 (Figure 2.5a,b,c,d) to week 3 (Figure 2.5e,f,g,h) (L-ratio $<10^{-9}$, isolation distance >105), as indicated by the stable waveform and ISI.

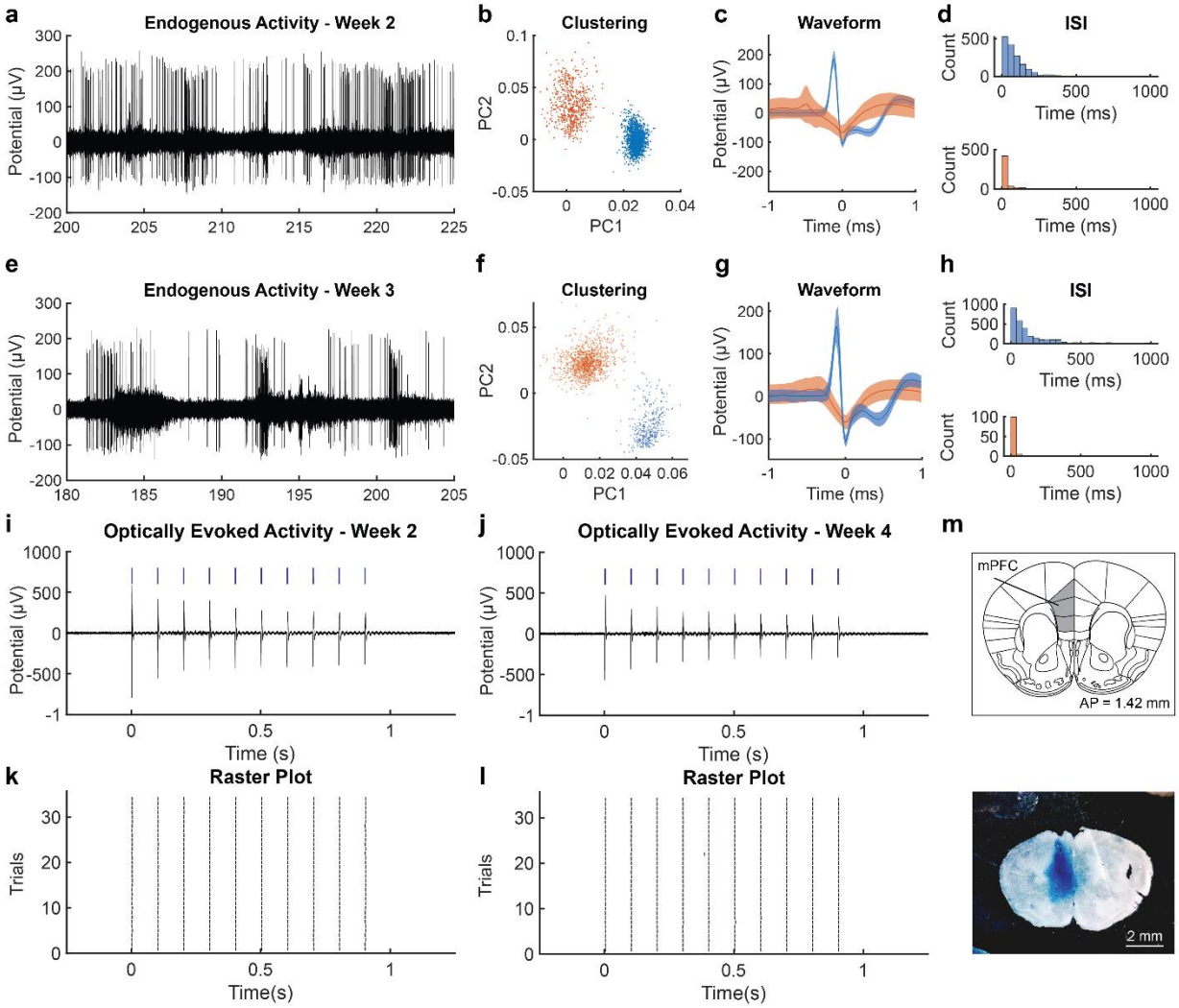

Figure 2.5. Converged multifunctional neural probes enables chronic recording of endogenous and optically-evoked neural activity *in vivo***.** (a) (a-h) Endogenous activity recorded using the convergence fiber. (a) endogenous activity 2 week after implantation containing one separable single-unit activity and one multi-unit activity. (SNR = 21.26, noise floor = 46 µV) (b) Principal-component analysis (PCA) of the putative unit detected in (a). (c) Average waveform of the separated units. (d) Interspike interval of each separated units. (e-h) similar to (a-d) endogenous activity, PCA, waveform and ISI for 3 weeks after implantation (SNR = 14.07, noise floor = 40 µV). Both multi-unit and single unit detected appear similar to week 2. (i-j) Simultaneous optogenetic stimulation (wavelength λ=473 nm, 5 ms pulse width, 10 Hz, 1s-long pulse train,

power density 10 mW/mm^2, blue markers indicate laser pulse. Activity recorded 2 weeks (i) and 4 weeks (j) post implantation. Raster plot of detected evoked potentials over 31 stimulation trials (k,l) highlight the reproducibility of the optically-evoked activity. (m) micrograph of brain slices following Evans' Blue dye injection (2% in NaCl, 2 µl over 20mn) through the microfluidic channels and transcardial perfusion of the animal. *From Antonini*, Sahasrabudhe* et. al., Ref. 186.*

Next, we tested the ability of the two-step and converged probes to record neural activity during optical stimulation. To sensitize the neurons to light, we first injected a viral vector carrying a transgene that encodes for a blue light-sensitive cation channel channelrhodopsin-2 (ChR2) under the excitatory neuronal promoter calmodulin kinase II α-subunit (*AAV5-CaMKIIα::ChR2-EYFP)*[62] into the mPFC of WT mice. Following a four weeks incubation period, we implanted either the opto-electronic two-step fiber (Figure 2.1f) or the converged multifunctional fiber (Figure 2.2c) at the injection coordinates (Methods). For both designs, we reliably recorded electrophysiological activity evoked by optogenetic stimulation (λ = 473 nm, 10 Hz, 10 mW/mm^2, 5 ms pulse width) (Figure 2.4i,j and Figure 2.5i,j). The recorded activity was well correlated with the onset of the laser stimulation (Jitter = 0.6 ms, peak latency = 3.7 ms), and reproducibility of the response was qualitatively assessed with the spike raster plot (32 stimulation trials, 5-s inter trial interval) (Figure 2.4k,l and Figure 2.5k,l). To further confirm the physiological origin of the optically-evoked potentials and to rule out photo-electrochemical artifacts,[63] we performed an array of control experiments. We observed that violet light (λ = 420 nm, 4 mW/mm^2, 10 Hz, 5 ms pulse width) pulses (Figure B7a,c) and but not green light (λ = 565 nm, 4 mW/mm^2, 10 Hz, 5 ms pulse width) pulses (Figure B7b,d) elicited an electrophysiological response. Additionally, contrary to mice transduced to express ChR2 (Figure B7e,g), mice transduced with *AAV-CamKIIα::EYFP* (a control virus carrying an enhanced yellow fluorescent protein) did not exhibit any optically-evoked activity (Figure B7f,h). We also observed that 100 Hz stimulation pulse train (Figure B7j,l) evoked neuronal activity that was uncorrelated with the optical pulses, which is consistent with the ChR2 kinetics.[64]

The neuronal activity was further correlated to a previously observed behavioral response to optical stimulation in the M2 area of the mPFC.[35,65] The mice were subjected to an open field test (OFT) divided into three epochs OFF/ON/OFF, each lasting 3 mins. During the ON epochs, mice received optical stimulation (473nm, 20Hz, 10ms, 30mW/mm^2) and no stimulation was applied during OFF epochs (Figure B8a,b). Mice expressing ChR2 exhibited a higher locomotor activity

during stimulation epochs as compared to pre- and post-stimulation epochs, while the control group showed no effect of optical stimulation (Figure B8c).

Finally, the ability of our probes to deliver chemical cargo *in vivo* through the integrated microfluidic channels was evaluated by delivering a bolus of Evans's blue dye (2% in sterile NaCl solution, 2 µL, 20 nL/s) into the mPFC of WT mice. Delivery of the dye was then confirmed *via* optical microscopy of the extracted brain slices (Figure 2.4m and Figure 2.5m).

Together, these findings illustrate that the two-step and convergence techniques extend the utility of thermal drawing to additional classes of materials and permit fabrication of neural probes that record and stimulate neuronal activity across multiple modalities. While indium has not commonly been used in neural recording devices, our findings demonstrate its utility for recording endogenous as well as optically-evoked activity *in vivo* for at least eight weeks. Note that, indium electrodes exhibited higher impedances and lower SNRs compared to their tungsten counterparts integrated via convergence into polymer fibers. However, surface coating strategies such as electrochemical deposition of conducting polymers or noble metals could potentially further optimize their performance.[66] Convergence drawing can also be extended beyond tungsten to microwires composed of platinum-iridium or gold that can potentially enable additional features including electrical stimulation via multifunctional fibers.

2.5 Coupling fibers to microdrives: Fabrication and characterization

To enable depth-resolved interrogation of neural circuits, we adapted the custom-screw and shuttle drive mechanism developed by Voigts and colleagues [67] to a microdrive compatible with our flexible polymer fibers. Like the prior design, our microdrive is composed of four functional elements: the drive body, the shuttle that carries the neural probe, a ceramic retaining collar and a custom screw (Figure 2.6a). Vertical translation of the shuttle is actuated by rotating the screw (Figure B9a-b). Step-by-step assembly of the microdrive is illustrated in Figure B10.

The resulting drive enables controlled linear motion with a travel range of 4 mm (Figure B9c,d,e) sufficient to probe the majority of the dorsoventral span in multiple regions in a mouse brain.[68] The assembled microdrive has an overall maximum volume of 25 × 15 × 8 mm^3 (excluding the implanted fiber), and a weight of 1g ± 0.02g (Figure 2.6b,c,d). Using an open-field test of the locomotor activity, no differences in speed and track length were identified between microdrive-carrying mice and naïve counterparts. As expected, tethering the drives to external hardware

produces modest yet significant decrease in locomotion motivating future implementation of wireless interfaces (Figure B11).

To characterize the linear displacement of the fiber probes via the microdrives, we lowered them into a phantom brain (0.6% agarose) while tracking the position of the fiber tip under a microscope. The custom screw which has a thread pitch of 150 μm is expected to produce ~150 μm fiber displacement for each counterclockwise turn.[67] We found that the observed displacement of the fiber tip was consistently higher than the targeted value (Figure B9d). This tracking error could be attributed to the imprecision of the manual rotation of the screw. Conversely, the observed lateral deflection was found to be less than 30 μm per millimeter of vertical displacement, ensuring precise targeting in the brain (Figure B9e). We additionally validated the depth-specific microfluidic injection of the microdrive-fiber assembly by delivering a bolus of Evans' Blue dye (2% into water, 500 nL, 100 nL/min) at 3 different drive positions (Figure B9f).

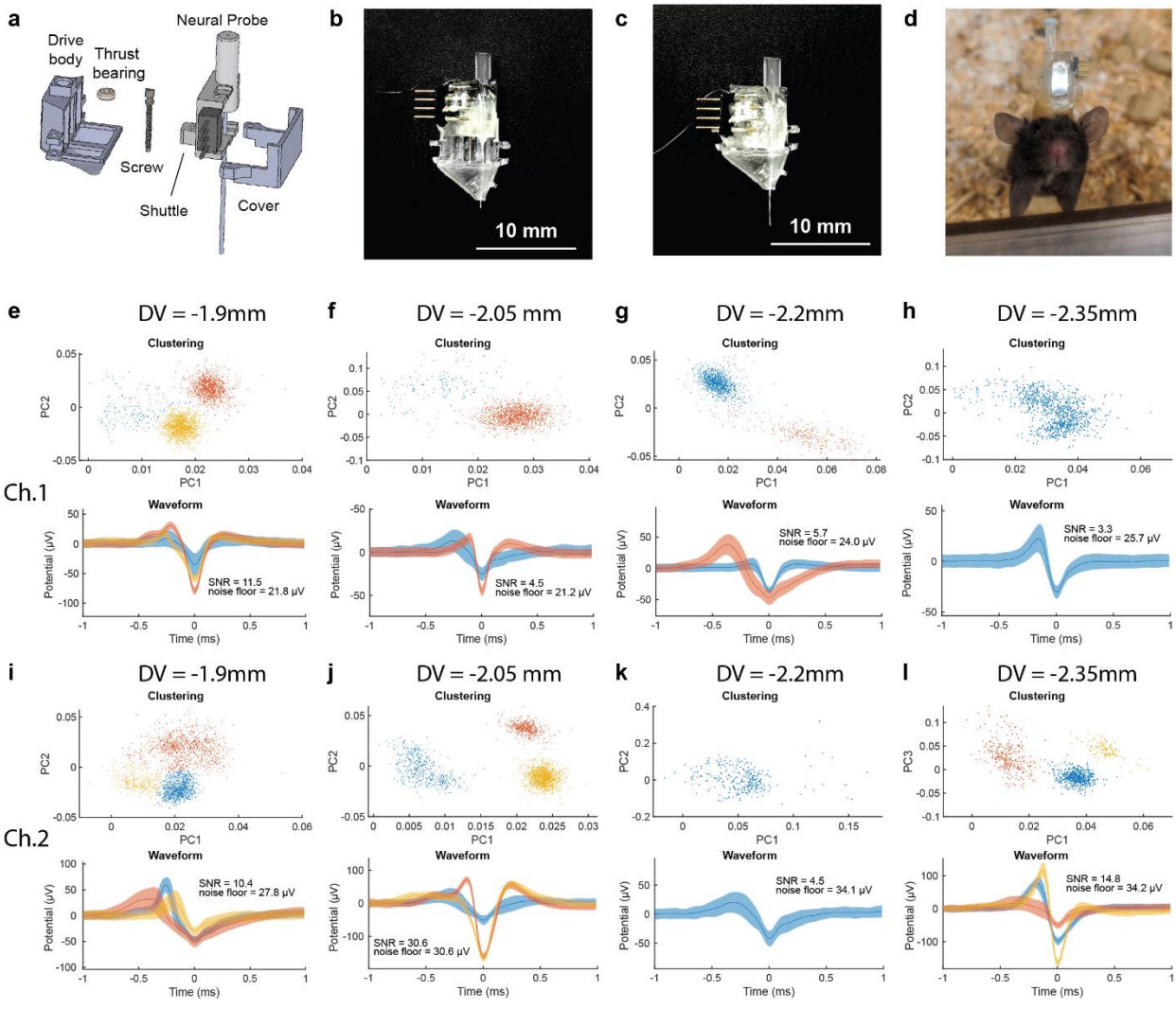

Figure 2.6. Microdrive assembly enables depth-specific recording of endogenous neural activity *in vivo*. (a) Exploded view of the microdrive assembly composed of a drive body, a dental cement thrust bearing, a custom-made screw, a neural probe mounted on a shuttle, and a cover. (b-c) neural probe assembly onto the microdrive on the up (b) and down (c) position. (d) Picture of the assembly implanted into the mPFC of a C57BL/6 wild type mice. The implant was placed at AP= +1.7 mm, ML= 0.4 mm, DV= -1.9 mm during the first day, and was lowered by 150 µm (1 turn) every day for 3 days. Endogenous neural activity was successfully recorded at each depth for channel 1 (e-h) and 2 (i-l) and putative single unit activity were isolated by principal-component analysis (top), and the average trace illustrates the waveform of the separated units (bottom). *From Antonini*, Sahasrabudhe* et. al., Ref. 186.*

2.6 Coupling fibers to the microdrive for depth specific *in vivo* electrophysiology

To test the utility of the microdrive-coupled multifunctional fibers to probe neural activity along the dorsoventral (DV) axis, we implanted the tetrode-like converged fiber (Figure 2b) into the mPFC of wild type mice. Fibers including tungsten electrodes were chosen over those employing indium due to the lower impedance and higher SNR associated with these probes. During implantation, the assembly was positioned slightly above the mPFC (AP +1.7 mm, DV -1.9 mm, ML ± 0.4 mm). Following a 3-day recovery period, we recorded endogenous electrophysiological activity under isoflurane anesthesia every day for 4 days. After each recording session, the microdrive screw was turned counterclockwise (1 turn) to advance the implant by 150 µm. The tissue was allowed to recover for a full day prior to the next recording session. Given that 150 µm distance exceeds the typical single-unit recording range of an electrode,[69] each recording session was anticipated to yield a different set of units. We recorded spiking activity with SNR=10.7 ± 9.0 and noise floor = 27.4 ± 5.2 µV each day on two of the four channels (#1 - Figure 2.6e-h, #2 - Figure 2.6i-l) , while the other two channels recorded little to no endogenous activity and were used as reference. Following spike sorting, we found that potentials could be isolated, and clustered into putative single units and multi-unit activity (Figure 2.6e-l). For each isolated cluster, we measured its average firing rate, inter-spike interval (ISI), L-ratio, and isolation distance [60,61,70] (Figure B12). The differences in these parameters observed for each unit indicate that electrophysiological activity was recorded from distinct neurons upon daily advancement of the probes, while the L-ratio and isolation distance illustrate an intermediate to good quality of clustering for 10 out of 16 clustered units (L-ratio <0.01, isolation distance >20). Similar results were obtained for electrophysiological recording sessions in freely moving mice (Figure B13).

While on average the SNR was lower and noise floor was higher than the values observed for recordings in anesthetized subjects (SNR = 8.3 ± 6.1, noise floor = 28.8 ± 5.4 μV), the majority of putative single-unit and multi-unit activity were recovered (15/18 units), with an additional unit being detected in the awake but not in the anesthetized animals (Figure B13h).

This proof-of principle study highlights how thermally-drawn neural probes can be integrated with compact and light-weight microdrives to enable recordings from several different loci along the DV axis, in both anesthetized and freely moving mice. Given that a similar design can be applied to any multifunctional fiber-based probe, this approach can be further exploited to perform multimodal depth specific interrogation of neural circuits using optical and chemical functionalities.

2.6 *In vivo* MRI imaging in the presence of the multifunctional fibers

Pairing neural probes with magnetic resonance imaging (MRI) enables simultaneous local interrogation of neural ensembles and anatomical and functional characterization across the entire brain. This approach has been leveraged to understand neurophysiological correlates of functional MRI (fMRI) signals,[40] brain wide circuit activation patterns in response to deep brain stimulation,[42] or to verify an implant placement.[71] However, the mismatch in the magnetic susceptibility between the typical neural recording electrodes and brain tissue manifests in large image artifacts making it challenging to visualize the surrounding brain structures. Here we evaluated the compatibility of both two-step and converged multifunctional fibers with MRI in a 9.4T small animal scanner. We apply fiber-based probes implanted in a deep brain structure, the ventral tegmental area (VTA), of rats to focally deliver a Gd^{3+}-based MRI contrast agent ProHance (0.01mM) through the integrated microfluidic channels. During an imaging session, the implanted rat was placed in the MR scanner and the microfluidic channel was connected to an external infusion pump (Figure 2.7a,b). The first two panels of Figure 2.7c show the anatomical scans of the implanted fibers using a T1-weighted scanning sequence. We observed that the converged fibers produced a minimal tissue distortion artifact, while the two-step fiber exhibited an almost artifact-free profile. Artifact sizes of ~400 μm and ~200 μm were measured for converged and two-step fibers, respectively, which is comparable to their actual diameters of (225 ± 8.7 μm and 141.8 ± 7.4 μm respectively), indicating negligible loss of functional response visualization during MRI (Figure B14). We note that the artifacts created by polymer fibers are substantially smaller than those produced by standard

monopolar stimulation electrodes, such as 200 µm Ag microwires (artifact size of ~1mm), which are routinely used in functional MRI experiments.[72,73]

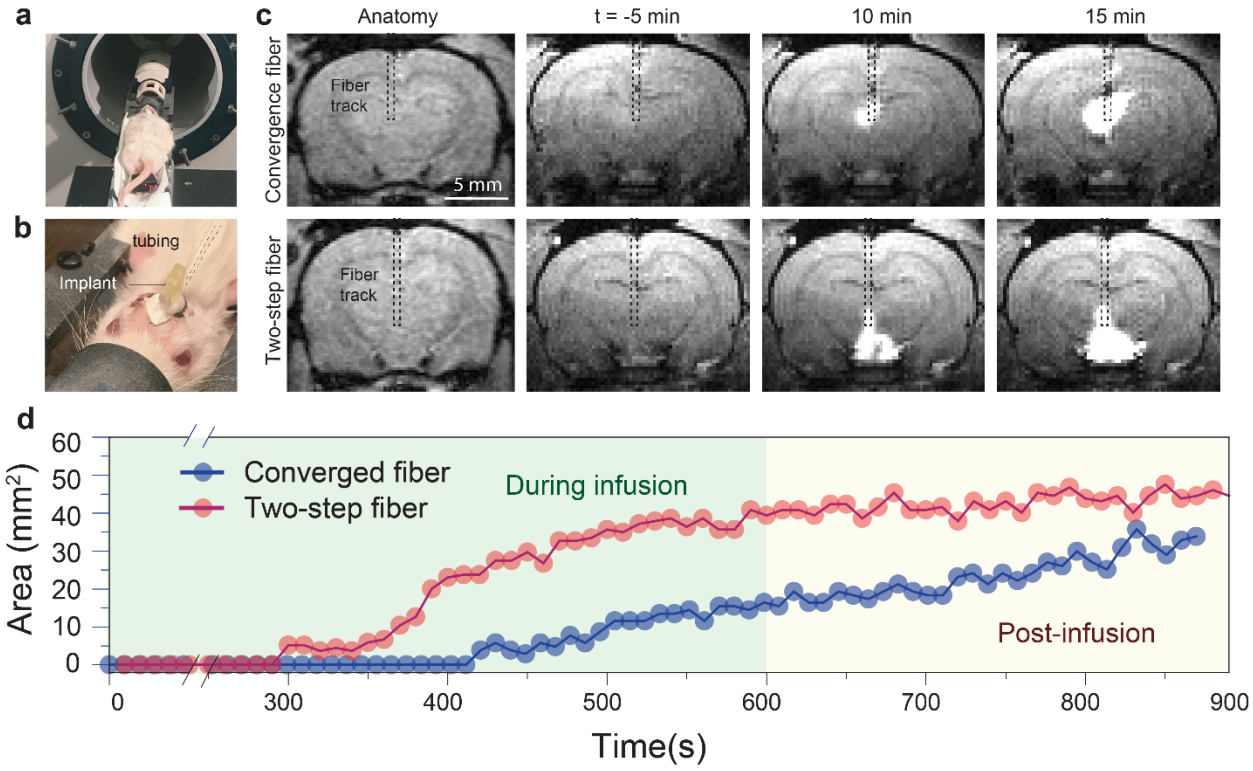

Figure 2.7. MRI in the presence of fiber-based probes. (a) Rat in MRI bore with surface coil placed over fiber implant. (b) Rat with fiber implant attached to infusion tubing. (c,d) T1-weighted fast low angle shot MRI images were acquired to evaluate the placement of both fiber implants (convergence (c) and two-step (d) fiber). (e-g) Images of T1-weighted rapid acquisition with refocused echoes (RARE) pulse sequence pre (e), during (f) and post (g) injection of contrast agent for convergence fiber. (h-j) similar as (e-g) for two-step fiber implant. (k) Infusion profile showing contrast changing area over time as a measurement of infusion efficiency of the two fiber types over the course of a 20 min scan. *From Antonini*, Sahasrabudhe* et. al., Ref. 29.*

Although chemical neuromodulation methods are common in basic and translational research, the real-time visualization of neuromodulatory agents *in vivo* remains challenging.[74] For example, imaging of the intracerebral fluid injection (as described above) is typically performed postmortem using standard histology techniques. This approach, however, is not suitable for tracking the delivery of fluid cargo in real time, nor can it ascertain the spatiotemporal kinetics of the infusion in intact animals.[74] Here, we leverage the MRI compatibility of our multifunctional fibers to visualize in real-time microliter scale infusions of a Gd^{3+}-based contrast agent ProHance (0.01

mM) in the VTA of rats. We infuse this contrast agent at a rate of 20 nL/s over a 10 min period while MRI images are captured at a sampling rate of 0.1 Hz. Figure 7c shows T1-weighted rapid acquisition with refocused echoes (T1-RARE) images of implanted fibers of both types before, during, and following infusion. The bolus of the Gd^{3+} agent is clearly visible as an enhanced contrast around the fiber tip. As expected, the delivered fluid continues to diffuse out and away from the fiber tip following active infusion. Figure 2.7d illustrates the spatiotemporal kinetics profile of the contrast agent infusion by tracking the gradual increase of affected tissue area over time. Figure B15 and Figure B16 depict the portfolio of snapshots captured every 10s. These experiments validate the MRI-compatibility of the multifunctional fibers for both anatomical and functional neuroimaging scans. They also motivate future studies aimed at coupling the local multimodal interrogation of neural circuits with global brain-wide activity mapping with MRI.

2.7 Immunohistochemical evaluation of biocompatibility of the fiber probes

To assess the tissue response of the two-step fibers containing indium and converged multifunctional fibers containing tungsten, we performed immunohistochemical analysis in 50 µm thick coronal brain slices two and twelve weeks following implantations into mPFC. Similarly sized silica fibers (200 µm diameter, Thorlabs) were used as for comparison given their prevalence in systems neuroscience studies (Figure B17). Analysis of markers associated astrocytic response (glial fibrillary acidic protein, GFAP) and microglial activation (activated macrophage marker ionized calcium-binding adaptor molecule 1, Iba1)[75,76] at two weeks following implantation revealed substantially lower tissue responses for the polymer fibers compared to silica fibers, which is consistent with prior reports of polymer based fibers.[33,35] This trend persisted for microglial activation twelve weeks following implantation, while we observed a significant lower glial accumulation around the fiber-based probes as compared to silica (GFAP - $P<0.01$).

2.8 Conclusion

Multimaterial fiber fabrication has enabled straightforward integration of neural recording, optogenetics, and drug delivery within miniature and flexible probes. However, previously thermomechanical compatibility at drawing conditions limited electrodes materials in fiber-based probes to either metals incompatible with low-loss waveguides, or polymer composites with high impedance. Through the use of an iterative thermal drawing with low T_m metal indium and convergence drawing of tungsten microwires, we produced an array of flexible multifunctional

neural probes with low-impedance metal electrodes, low-loss polymer optical waveguides, and microfluidic channels. Notably, these fabrication advances led to a streamlined back-end interfacing of multifunctional probes.

We demonstrated the utility of fibers drawn using both approaches *in vivo* through chronic recording of endogenous and optically-evoked electrophysiological activity in mice. Moreover, we showed for that this class of fiber-based probes can be combined with a mechanical microdrive to interrogate multiple clusters of neurons along the dorso-ventral axis in awake, freely moving mice. Finally, we found that our fiber probes were MRI-compatible and could be coupled with anatomical and functional brain wide imaging while causing minimal tissue distortion artifacts.

This study expands the palette of available materials for fiber-based neural probes. By highlighting a streamlined connectorization process, the coupling of fiber-probes with mechanical microdrives, and their compatibility wih MRI, this work will facilitate dissemination and widespread adoption of fiber-based multifunctional neural probes within the neuroscience community.

2.9 Experimental Methods

Fabrication of the Two-step neural probes: The two-step fibers implants were fabricated using a combination of polycarbonate films (PC film, 50 μm thick, Ajedium; PC rod, McMaster-Carr) and cyclic-olefin-copolyer (COC 6015, 0.003" thick; TOPAS) for the waveguide and the microfluidic channel, and indium (In; 99.999% pure indium shot, Indium Corporation) as the electrode material. Two iterations of the thermal drawing process were used to obtain the final device. During the first iteration, optical waveguide, insulated electrode and microfluidic channel were individually fabricated and drawn. To fabricate the optical waveguide, 0.003" COC films were rolled around a 1" polycarbonate rod PC until the assembly reached 1.25" thickness. The microfluidic channel was fabricated by drilling a 1/2" hole through an 8" long, 1" thick PC rod. 0.003" COC was then wrapped onto the rod until it reached 1.25". To fabricate the insulated electrode, a 3/8" hole was drilled into a 1" thick, 8" long PC rod, which was also wrapped in 25 μm COC sheets to reach 1.5" in thickness. All three preforms were consolidated at 175°C under vacuum for 40 min. The electrode channel was then filled with indium pellet, and all three preform were drawn at 275°C using a custom-built fiber drawing tower as described in previous work.[33] The microfluidic channel was drawn with a draw-down ratio of 15 to obtain ~2 mm fibers, the optical waveguide with a ratio of 30 and the electrodes a ratio of ~40 to obtain ~1 mm fibers. To fabricate the preform

for the second iteration of the thermal drawing process. A COC/PC cylinder was fabricated by first rolling 1 layer of 0.001" fluorinated ethylene propylene (FEP) teflon (McMaster-Carr) around a 4.5mm steel mandrel (McMaster-Carr), followed by several sheets of COC sheets to reach a thickness of 5.25mm. It was then wrapped into PC films to reach 1" in thickness, this sacrificial cladding is necessary to enable stable drawing conditions. The assembly was consolidated under vacuum at 175°C for 40 min. The FEP wrapped steel mandrel was then removed, and optical, microfluidic and insulated electrode fiber were inserted. To eliminate air pockets between individual fiber strands, PC fibers were added, and the assembly was annealed in a vacuum oven at 110°C for 1 hr, before being drawn at 275°C with a draw down ratio of 35 to obtain the 2nd step fibers.

Assembly of the two-step neural probes: Connectorization refers to the process of interfacing the individual modalities of neural probes (electrodes, microfluidic channel and optical waveguide) with input/output electric pins, inlet tube and optical ferrules. The fiber was first cut into 7 cm long sections, and the proximal end of each fiber was scored with a razor blade, snapped and pulled apart to expose the COC-wrapped first-step fibers. The COC layer was scored and pulled apart, releasing the individual first-step fibers. Once exposed, each individual fiber was connected to the corresponding hardware. The neural probe was placed on a 3D-printed box (microdrive shuttle), and individual fibers were connected to the corresponding hardware. Individual electrodes were connected and fixed to the male pin connectors (Digi-Key, #1212-1328-ND) using silver epoxy (Epo-Tek, #H20E). An insulated stainless-steel ground/reference wire (A-M systems, #790500) was soldered to one of the pins. EVA tube (0.03" ID, 0.09" OD, McMaster #18883T2) was placed around the microfluidic channel, and affixed to the fiber using UV epoxy (NO68; Norland). The optical waveguide was placed into a 10.5 mm long, 2.5 mm diameter ceramic ferrule, with a 270 µm bore size (Thorlabs, #CF270) and affixed it using optical epoxy (NO68; Norland). The silver epoxy was cured by placing the assembly onto a hot plate at 80 °C for 2 hr. UV-epoxy was added onto the box cavity to submerge the assembly for additional mechanical stability and electrical insulation. The ferrule was then polished using a Thorlabs fiber polishing kit, and the distal end of the implant was immersed into dichloromethane (Sigma, #270997) for 4 min to remove the sacrificial PC layer.

Fabrication of the converged neural probes: Multifunctional fibers using the convergence approach were fabricated as follows. A macroscopic preform was assembled by rolling multiple layers of COC thin films (COC 6015, 0.003" thick; TOPAS) around a 1/8" PC rod that defined the central PC/COC waveguide scaffold. Subsequently an additional layer of PC was added by rolling PC films (film, 50 μm thick, Ajedium; PC rod, McMaster-Carr) until a diameter of ~6.2 mm was reached. At this step the rolled preform was consolidated in a vaccum oven at 185 °C for 30 min. Next, six square slots of 1mm each were machined in a symmetrical pattern in the outermost PC layer which overall defined the four convergence channels and two microfluidic channels. Teflon spacers were inserted into these channels and additional PC sheets were rolled until a diameter of ~9 mm was reached. Finally, alternate layers of COC films (0.003" thickness) and PC films (50 μm thickness) were rolled that defined the stopping layer and the cladding layer respectively. The assembled preform was again consolidated in a vacuum oven at 185 °C for 40 min. All the fiber drawing processes were conducted using a custom-built fiber drawing tower. The fibers were drawn by placing the preform in a three-zone heating furnace, where the top, middle, and bottom zones were heated to 150 °C, 285 °C, and 110 °C, respectively. The preform was fed into the furnace at a rate of 1 mm/min and drawn at a speed of 1600 mm/min, which resulted in a draw-down ratio of 40. Four tungsten microwire spools (25 μm diameter, 99.95%, Goodfellow) were continuously fed into the preform during the draw that defined the convergence process.
Tetrode-type electrophysiology fibers were fabricated as follows. A macroscopic preform was assembled by machining four grooves (1 mm) along the length of mm PC rod (1/8") that defined the convergence channels. Teflon spacers were inserted into the hollow channels and layers of PC films (50 μm thin) were rolled until a final diameter of ~4 mm was reached. The assembled preform was consolidated in a vacuum oven at 185°C for 20 min and drawn into meters long fibers using identical draw parameters as described above.

Assembly of the converged neural probes: In a typical connectorization protocol for multifunctional fibers, the sacrificial cladding (PC) and the stopping layer (COC) were dissolved by subsequently submerging the fibers in dichloromethane (DCM) and cyclohexane for 5 and 10 min respectively. An intermediate wash cycle with IPA was performed before switching between the solvents. After etching the cladding layers, the fibers were dipped in DCM for 5 min to expose the individual metal microwires and PC/COC waveguide. The microwires were soldered to header

pins (Digi-Key, #1212-1328-ND) and the waveguide was affixed into a ceramic ferrule (Thorlabs, #CF270) using UV epoxy (NO68; Norland) and subsequently polished with Thorlabs polishing kit. The microfluidic channels in the fiber were connected to an external EVA tubing (0.03" ID, 0.09" OD, McMaster #18883T2) by mechanically etching the polymer cladding on the fiber with a razor blade and then threading through the fiber into the tubing to form a T-junction. The assembly was made watertight using copious amounts of UV epoxy. The device assembly was finished off by soldering a ground screw to a reference wire on of the header pins and securing all the I/O hardware (pins, ferrules, tubes) inside a 3D printed Microdrive shuttle with copious amounts of UV epoxy. The tetrode type fibers were connectorized in a series of almost identical steps. To begin with, the fibers were etched in DCM for 5 min to expose all microwires. These electrodes were soldered to header pins. A reference wire connected to a ground screw was attached to one of the header pins and the whole backend assembly was supported inside a microdrive shuttle using copious amounts of UV curable epoxy.

Characterization of two-step and converged neural probes: To image the neural implants, we embedded the fiber samples in an epoxy matrix (EMSFix Epoxy Resin) and grinded the sample with a series of sandpapers with decreasing grain sizes (Struers Tegrapol) before polishing with a 0.3 µm alumina particle solution (Buehler AutoMet 250 Polisher). Images were acquired using a metallurgical microscope. To highlight the functional part of the fiber and mask the sacrificial cladding, morphological image processing was performed by segmenting foreground and background pixels using a region-growing algorithm in Mathematica 12.0. Bending stiffness of the fibers were measured using a dynamical mechanical analyzer (Q800, TA Instruments). We used a single cantilever mode with 20 µm deformation within the frequency range of 0.1-10 Hz. Electrical impedance spectroscopy of fiber integrated electrodes was measured using a LCR meter (HP4284A, Agilent Technologies) with a sinusoidal voltage input (10 mV, 20 Hz-10 kHz). Microfluidic capability of the channel was characterized by implanting the fiber tip into a phantom brain (0.6 % wt/vol agarose in distilled H_2O). The microfluidic inlet was connected to a syringe pump (WPI Micro4, UMC4) and controller (WPImUMP3) via a Hamilton syringe and EVA tubing (0.03"ID, 0.09"OD, McMaster #18883T2). Tryptan blue (3 µl) was injected at a speed of 750 nl/min, and images were captured at t=0, t=3 and t=5 following the start of the injection using a phone camera. To further characterize the microfluidic capabilities of the implants, 9 µl of water was injected at infusion speeds of 1, 10, 20, 50, 80 and 100 nl/s through the microfluidic channel,

measuring injection output by weight. Output injection rate was calculated by dividing the injection output by the time required to inject it. Injection efficiency was computed as the ratio of input and output injection rate. To image the light emission profile of polymer waveguides, 5 cm long fiber probes were connected to a diode-pumped solid state (DPSS) laser (50 mW maximum output, wavelength λ=473 nm, Laserglow) via optical cable and a zirconia ferrule. The fiber tip was placed into a fluorescein solution (0.01mM), light was delivered through the fiber and images were captured. Transmission losses for waveguides were measured by varying the fiber lengths from 1 to10 cm using the cut-back method. The absolute output power was measured using a digital power meter (Thorlabs, PM100D) with a photodiode sensor (S121C). All the electrochemical measurements were performed with a potentiostat (Solartron, SI 1280B) at room temperature. The bulk indium rods (In; 99.999% pure indium shot, Indium Corporation) or two-step indium fibers were utilized as working electrodes. Pt wire (MW-1032, BAsi) and Ag/AgCl electrode (BASi, 3 M NaCl) were used as the counter and reference electrodes, respectively. Phosphate buffer saline (PBS, Fisher Scientific) was used as the electrolyte, and cyclic voltammetry curves for the indium working electrodes were obtained at the scan rate of 20mV/s. Potentiostatic electrochemical impedance spectroscopy (PEIS) was performed at the open circuit potential (OCV) with a Biologic VMP3 potentiostat on first-step indium fibers in a PBS electrolyte. The working electrode was held at open circuit for 2 sec, followed by scanning frequencies from 1 MHz to 10 Hz at six points per decade. An amplitude of 5 mV was used, and an average of 10 points was performed at each frequency. A leak-free Ag/AgCl reference electrode (Innovative Instruments) and a platinum foil counter electrode (99.99% trace metals basis, Beantown Chemical) were used. Equivalent circuit fitting was performed with Z Fit, an EIS fitting tool in EC-Lab with 5,000 iterations using a randomize + simplex algorithm. A simplified Randles circuit model, consisting of a solution resistance in series with a parallel combination of a charge-transfer resistance and a double-layer capacitance, was used to fit the data; the double-layer capacitance was modeled both as an ideal capacitor and as a constant phase element, although the ideal-capacitor model was chosen for its simplicity and lower uncertainty in its fitted parameters. The finite element modelling software, Abaqus, is used for the simulation of the bending of the different fibers as well as the fiber displacement in moving tissue. The element used for the materials in the fiber, such as the polymer, silica, and metal wires, is C3D8H with a HEX element shape. The element used for the tissue is C3D10H with a TET element shape. For the bending fiber

simulation, the fiber is held fixed at one end and is displaced with a fixed distance at the other end. The amount of displacement is 0.1 mm. For the simulation for the fiber in the brain tissue, the tissue at its bottom is displaced sidewards with a distance of 3.5 um, while the exposed end of the fiber, which is not in the tissue, is fixed.

Microdrive fabrication and characterization: The microdrive body, shuttle and cover were designed on Solidworks (Dassault System) and 3D printed on a Form 2+ (Formlabs) using a clear resin (Formlabs, RS-F2-GPCL-04), at a 25 μm resolution. Following 3D printing, each element was cleaned using the FormWash for 30 min, then cured for 180min into the FormCure. Due to the imprecision of 3d printing at this scale, screw channels onto the body and the shuttle were widened to the designed 0.5mm using a handheld drill. Following connectorization of the fiber onto the shuttle. Microdrive body, shuttle carrying the fiber, and custom-made screw were assembled. The drive body and shuttle were assembled by placing the shuttle into the guide channel, and using a custom screw described in Voigts et al.[67] The shuttle was then place to its uppermost position, and linear motion of the screw was prevented by filling the retaining pocked with light-hardened dental cement (Vivadent Tetric EvoFlow). The screw was then slightly turned counterclockwise to delaminate the screw from the cement that now acts as a thrust bearing.

Quantitative microdrive characterization was performed by fixing the stationary part of the device to a glass slide. A rectangular cuvette filled with 0.6% agarose was fixed to another glass slide. The fiber was introduced into the agarose gel, and the slides were both fixed into place under a light microscope. The microdrive was then advanced one turn at a time, and microscope images were acquired after each turn. The distance traveled by each turn was analyzed by measuring the number of pixels between the end of the fiber and a reference point on the cuvette. Pixels were converted to micrometers by measuring the diameter of the fiber. To illustrate the performance of the microdrive, the device was fixed to the top of a glass vial filled with 0.6% agarose. Three injections of 500 nl of Evans Blue (2% in PBS) were delivered at a rate of 100 nl/min at depths of 0, 1 and ~2 mm (7 and 14 turns).

Surgical procedures: All animal procedures were approved by the MIT Committee on Animal Care and performed in accordance with the IACUC protocol 0121-002-24 (Implantation of Neural Recording and Stimulation Devices into Adult Mice and Rats). WT mice (Jacskon, 000064) aged 8 weeks, were used for the study, and housed in a normal 12h light/dark cycle and fed a standard rodent chow and water diet *ad libitum*. All surgeries were performed under aseptic conditions.

Mice were anesthetized with 1-2% isoflurane and placed on a heat pad in a stereotaxic head frame (Kopf Instrument), and were injected subcutaneously with slow-release buprenorphine (ZooPharm, 1.0 mg/kg). Following a midline incision along the scalp, the skull was repositioned by aligning and leveling Lambda and Bregma landmarks with respect to the Mouse Brain Atlas. Adeno associated viruses serotype 5 (AAV5) carrying CaMKIIα::hChR2(H134R)-eYFP and CaMKIIα::EYFP plasmids were purchased from University of North Carolina Vector Core at concentrations of 3×10^{12} particles/ml and 2×10^{12} particles/ml, respectively. Implantation and injection coordinates were established following the mouse brain atlas. A craniotomy was performed using a rotary tool (Dremel Micro 8050) and a carbon steel burr (Heisinger, 19007-05). The animal was then either injected with virus or implanted with the neural probes. Virus injection was performed using a standard NanoFil Syringe and UMP3 Syringe pump (World Precision Instruments), 0.5 µl of virus was injected using a at a rate of 100nl/min. Prior insertion, implants were flushed with sterile PBS, fastened to the stereotaxic cannula holder, and were connected to a RZ5D (TDT) recording system using a PZ2-32 head-stage with a 16-channel zero insertion force-clip headstage. Probes were lowered into the medial prefrontal cortex (mPFC; ML = 0.4mm; AP = +1.7mm; DV= 2.5mm). Following insertion, a stainless steel screw (McMaster-Carr, # 92196A051) was inserted into the skull above the cerebellum as a ground and reference. The device was then cemented to the skull using 3 layers C&B-Metabond adhesive acrylic (Parkell) then dental cement (Jet Set-4) to cover both the screw and the base of the device. The incision was then closed with 5-0 suture in a simple interrupted pattern, and the mouse was subcutaneously injected with carprofen (5mg/kg) and sterile Ringer's solution (0.6 mL) prior to be returned to their home cage, partially placed on a heat pad. Post-implantation, the mice were provided food and water *ad libitum*, were monitored for 3 days for signs of overall health, and were given carprofen injection (0.6 mL, 0.25mg/ml in sterile Ringer's solution) as necessary.

In vivo electrophysiology: Neural implants were attached to a PZ2-32 head-stage with a 16-channel zero insertion force-clip connector which was in turn connected to a RZ5D recording system. Electrophysiological signals were filtered in the frequency range 0.3 - 5 kHz and digitized at a sampling frequency of 50kHz. Subsequent signals processing and analysis was done with Matlab (Mathworks). Spiking activity was detected using threshold detection with a threshold set at 5 standards deviation from the mean of the signals, with a downtime of 2ms to reject double detections. lustering and classification of spikes were performed by principal component analysis

and Gaussian Mixture Model clustering (with full and independent covariance matrices). We assessed the quality of the clustered data by calculating the L-ratio and the isolation distance of the classified clusters.[60]

During optogenetic stimulation, a 500mW 473nm diode-pumped solid-state laser (OEM Laser Systems) was coupled to the implant through a silica fiber (200μm core, Thorlabs #RJPFF2) using a rotary joint optical fiber and a ceramic mating sleeve. Waveform generation was delivered by the RZ5D acquisition system with a stimulation frequency as set at 10 or 100hz, 5-ms pulse width, 1s trial duration and 4 s intertrial interval. During the control experiment with violet (λ = 420 nm) and green (λ = 565 nm) light emitting devices (LEDs), the optical stimulation was generated using fiber-coupled LEDs (Thorlabs, M420F2, M565F3) driven by a LED driver (Thorlabs, LEDD1b, 1.2A current limit) and a waveform generator (Agilent 33500B).

During chemical delivery, the implants were connected to a Nanofil syringe (10 μl, World precision Instruments) using an EVA tube (0.03" ID, 0.09" OD, McMaster) and a Nanofil beveled needle (33G, WPI). 2 μl of Evans Blue (2% in sterile NaCl) was injected at a speed 100 nl/min through the implants' microfluidic channels.

In vivo MRI imaging: Adult male Sprague–Dawley rats (350–450 g) were purchased from Charles River Laboratories (Wilmington, MA). After arrival, animals were housed and maintained on a 12-hr light/dark cycle and permitted ad libitum access to food and water. All procedures were carried out in strict compliance with National Institutes of Health guidelines, under oversight of the Committee on Animal Care at the Massachusetts Institute of Technology. Animals were anesthetized with isoflurane (3% for induction, 2% for maintenance) and placed on a water heating pad from Braintree Scientific (Braintree, MA) to keep body temperature at 37 °C. Animals were then fixed in a stereotaxic frame, and topical lidocaine was applied before a 3 cm lateral incision extending from bregma to lambda was made, exposing the skull. Craniotomies (0.5 mm) were drilled unilaterally over the ventral tegmental area (VTA), 6.0 mm posterior and 0.5 mm lateral to bregma. Fiber implants (two step or convergence) were preloaded with a gadolinium-based contrast agent (ProHance, Bracco Diagnostics; 0.01mM), lowered to 8.0 mm below the surface of the skull through the craniotomy and held in place by the stereotactic arm. The implants were fixed to the skull with dental cement (Secure Resin Cement, Parkell). Animals were then transferred into a custom rat imaging cradle, fixed with ear bars and bite bar, maintained under 2% isoflurane anesthesia, and kept warm using a recirculating water heating pad for the duration of imaging.

MRI was performed on a Bruker 9.4 T BioSpec small animal scanner (Billerica, MA) using a transmit-only 70 cm inner diameter linear volume coil made by Bruker (Billerica, MA) and a receive-only 3x1 array-coil with openings through which the implant and connected tubing was led through to then be connected to an infusion pump. Scanner operation was controlled using the ParaVision 6.01 software from Bruker (Billerica, MA).

Multislice T1-weighted fast low-angle-shot MRI images with TE = 4 ms, TR = 200 ms, field of view (FOV) = 30 × 18 mm, in-plane resolution 200 × 200 μm, and four to six coronal slices with slice thickness = 1 mm and T2-weighted TurboRARE images with TE = 30 ms, TR = 1000 ms, Rare Factor 8, Matrix size 256 × 256, FOV = 25.6 × 25.6 and in-plane resolution of 100 × 100 μm were used to evaluate the location of the implants.

Rapid acquisition with refocused echoes (RARE) pulse sequences were used for functional scans with the following parameters: FOV = 30 × 18 mm, slice thickness = 1 mm, matrix size = 128 × 64, and RARE factor = 4 (with 5 ms echo spacing). Functional scans of 20 min length were performed during the infusion of contrast agent over the course of 10 min (20nl/s), starting 5 min after the start of the scan.

Behavior assays: Locomotor tests were performed with virally transfected mice, in a 30 × 30 × 30 cm^3 white acrylic chamber. Optical stimulation was generated by blue laser (λ = 473 nm) controlled by a waveform generator (Agilent). The laser was collimated and coupled into a silica patch cord with a rotary joint optical fiber and were attached to the implant using a ceramic mating sleeve. Prior to the start of the behavioral experiment, mice were restrained while the patch cord was attached to their implant, and were placed in the center of the chamber for 10 min to recover from handling stress. Each session consisted of three 3-min epochs, wherein baseline locomotor activity was assessed in the first and third epoch (OFF stimulation) and optical stimulation with 20hz frequency (5ms pulse width) was delivered during the second epoch (ON stimulation). The locomotor activity was tracked and analyzed using Ethovision software. The ability of mice to carry light-weight microdrive implants was measured using an Open-field assay in a 30 × 30 × 30 cm^3 white acrylic chamber. Mice were acclimatized to the OFT chamber for 10 min before recording their activity. The OFT test session lasted for 10 min during which the overall distance travelled and locomotion velocity was tracked and analyzed using Ethovision software.

Immunohistochemical evaluation of foreign body response: Animals were anesthetized with isoflurane, injected with fatal plus (100 mg/kg IP), and transcardially perfused with 50 mL of ice-cold phosphate buffered saline (PBS) followed by 50 mL of ice-cold 4% paraformaldehyde (PFA) in PBS. The devices were carefully explanted and the brains were removed and fixed in 4% PFA in PBS for 24 hr at 4 °C, then stored in PBS afterwards.

Coronal slices (50 μm thickness) were prepared using a vibratome (Leica VT1000S) and a razor blade (Electron Microscopy Sciences, 72002) in ice-cold PBS. The slices were then stored in PBS at 4 °C in the dark until staining.

Slices were permeabilized with 0.3% (vol/vol) Triton X-100 and blocked with 2.5% donkey serum in PBS for 30 min. Slices were incubated overnight at 4 °C in a solution of primary antibody and 2.5% donkey serum in PBS. Following incubation, slices were washed three times with PBS. The slices were then incubated with secondary antibody (Donkey anti-Goat Alexa Fluor 488, A11055, 1:1000, Thermofischer) for 2 hr in room temperature on a shaker followed by additional three washes with PBS. Slices were then incubated with DAPI (4'6-diamidino-2-phenylindole) (1:50,000) for another 20 min, and washed three times with PBS. Fluoromount-G® (SouthernBiotech) was used for mounting slices onto glass microscope slides. A laser scanning confocal microscope (Fluoview FV1000, Olympus) was used for imaging with 20× objectives. A laser scanning confocal microscope (Fluoview FV1000, Olympus) was used for imaging with 20× objective, with z-stack images across the slice thickness. Region of interest was chosen based on the fiber location, imaging the immune response in the fiber surrounding.

The following primary antibodies were used:

Target	**Antibody**	**Dilution**
Iba1	Goat anti- Iba1 (ab107159, Abcam)	1:500
GFAP	Goat anti- GFAP (ab53554, Abcam)	1:1000

Statistical Analysis: All data is presented as mean ± S.E.M. Statistical significance was assessed using Matlab (Mathworks), by first confirming a normal distribution using a Lilliefors test, and then by 2-sided t-test, with significance threshold placed at *P<0.05, **P < 0.01, ***P < 0.001.

2.10 Neural probes that deliver transient gaseous neuromodulators to the brain

Nitric oxide (NO) is a gaseous signaling molecule involved in multiple biological processes, including neurotransmission, cardiovascular homeostasis, and immune response[77–81]. In the central nervous system, NO is involved in mediating synaptic plasticity and neurosecretion[82]. The essential role of NO across multiple signaling pathways has evoked a demand for regulating its levels *in vitro* and *in vivo*. Early studies have targeted endogenous NO synthase enzymes via genetic knock-out strategies or via systemic delivery of pharmacological inhibitors[83–85]. These strategies resulted in organism-wide changes in NO levels with limited spatiotemporal specificity. More recently, NO-releasing materials (NORMs), triggered by non-enzymatic or enzymatic processes, have been designed to achieve a more controlled and localized delivery of this molecule[86–88]. However, as tuning of the NO-release kinetics in a single NORM has been challenging[86,89], multiple injections of different NORMs were necessary to study the biological effects of NO[89,90]. Furthermore, degradation of NORMs during delivery has often resulted in off-target release of this molecule[91,92]. Consequently, there remains a need for techniques to deliver NO to the targeted cells and tissues with spatiotemporal precision.

To address this need, we propose an electrocatalytic approach to NO generation (Fig. 1a). Our approach is inspired by the catalytic reduction of nitrite (NO_2^-) into NO by the iron sulfide containing enzyme, xanthine oxidoreductase[80]. We mimic this biological NO generation by employing nanoscale iron sulfide-based catalysts for the electrochemical denitrification reaction (Eq. 1)[93],

$$NO_{2\ (aq)}^{-} + 2H^{+} + e^{-} \leftrightarrow NO_{(g)} + H_2O_{(aq)} \quad E_0 = 1.202\ \text{V vs NHE} \quad (1)$$

Where NHE indicates normal hydrogen electrode.

In the presence of an external voltage, NO_2^- can be reduced by iron sulfide-based catalysts at the cathode allowing for spatially and temporally restricted generation of NO. We applied this bio-inspired strategy to control NO-dependent neuronal signaling *in vitro* and in the mouse brain.

2.11 Design and characterization of implantable NO-delivery probes.

To investigate the utility of our NO-delivery approach for applications *in vivo*, I designed miniature electrocatalytic probes suitable for chronic implantation into the mouse brain. We adopted thermal drawing process that has previously enabled fabrication of multifunctional, miniature fibers for

neural interfaces (Fig. 2.8a-d)[26,33]. A macroscopic polycarbonate preform (12 mm in diameter) containing three hollow channels was fabricated by standard machining (Fig. 2.8b)[26]. One of the channels was intended for delivery of $NaNO_2$ solution and the remaining two channels were designed to host microelectrodes forming the electrocatalytic cell for reduction of the delivered $NaNO_2$ into NO. During the draw (Fig. 2.8a), the preform (Fig. 2.8b) was heated above the polycarbonate glass transition temperature and stretched into a 5 m-long fiber with a diameter of ~ 400 µm (Fig. 2.8c, d). Tungsten and gold-coated tungsten microwires (50 µm in diameter) were directly converged into the preform from the wire spools (Fig. 2.8a), resulting in a probe featuring two microelectrodes and a microfluidic channel.

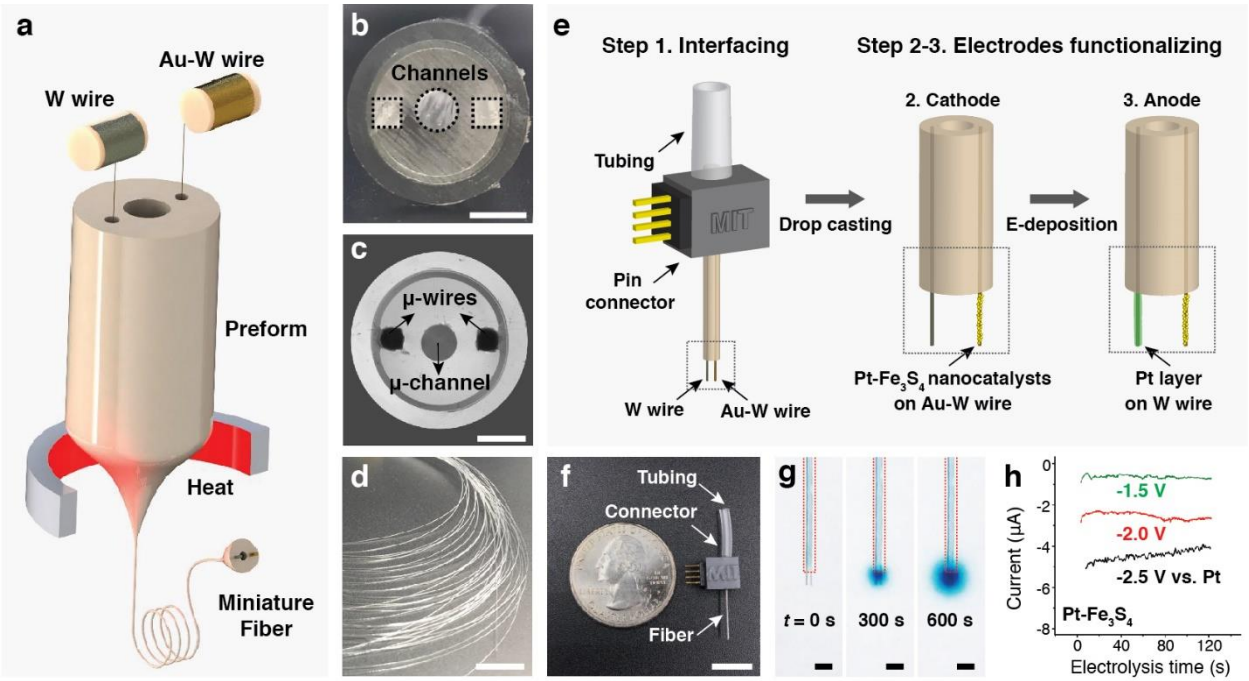

Fig. 2.8. Fabrication and characterization of the NO-delivery fiber. (a) An illustration of the fiber drawing process. Tungsten and gold-plated tungsten wires were converged into the preform during the draw. (b) Cross-sectional image of the preform containing three hollow channels. Scale bar: 3 mm. (c) Cross-sectional microscope image of the resulting fiber. Scale bar: 100 µm. (d) A photograph of a bundle of fiber produced during the draw. Scale bar: 10 cm. (e) An illustration of fiber connectorization, followed by functionalization of the cathode and anode microwires with Pt-Fe_3S_4 nanocatalysts and Pt layer, respectively. (f) A photograph of a fully assembled NO-delivery fiber. Scale bar: 10 mm. (g) Infusion of Tyrode's solution containing 0.1 M $NaNO_2$ and a dye (BlueJuice) into a brain phantom (0.6% agarose gel) through the microfluidic channel. Images were taken at 0, 300 and 600 s after the infusion at a rate of 100 nL/min. Scale bar: 500

μm. (h) Chronoamperometry profiles of the NO-delivery fiber in the Tyrode's solution containing 0.1 M $NaNO_2$. *From Park*, Jin*, Sahasrabudhe et. al., Ref. 30.*

Following fiber connectorization to external tubing and electrical pin connectors, 300 μm lengths of the embedded microwires were exposed from the fiber tips for further functionalization (Please refer Ref. 30[30] for detailed discussion on synthesis, characterization, and *in-vitro* validation of NO generating electrocatalysts that was co-developed by my colleagues Dr. Jimin Park and Dr. Kyoungsuk Jin). Pt-Fe_3S_4 nanoclusters, which exhibited greater electrocatalytic activity as compared to Fe_3S_4 counterparts, were deposited onto the exposed gold-coated tungsten microwire cathodes. The tungsten microwires were electroplated with Pt and used as the anodes (Fig. 2.8e)[94]. The fully assembled NO-delivery fibers exhibited height and weight of ~25 mm and 0.3-0.4 g, respectively (Fig. 2.8f). The microfluidic capabilities of the probes were corroborated by passing the solution of a blue dye and $NaNO_2$ into agarose brain phantoms (Fig. 2.8g). Electrocatalytic conversion of the delivered $NaNO_2$ into NO was characterized via chronoamperometry. The current density at the integrated electrodes was 4 mA/cm^2 at –2.0 V vs Pt, which was similar to that of the bulk electrochemical cells used for *in vitro* studies (Fig. 2.8h). Akin to the bulk cells, the electrocatalytic fibers were capable of NO generation at the cathodes, which mediated Ca^{2+} influx in $TRPV1^+$ cells *in vitro* (Fig. 2.9 a-f).

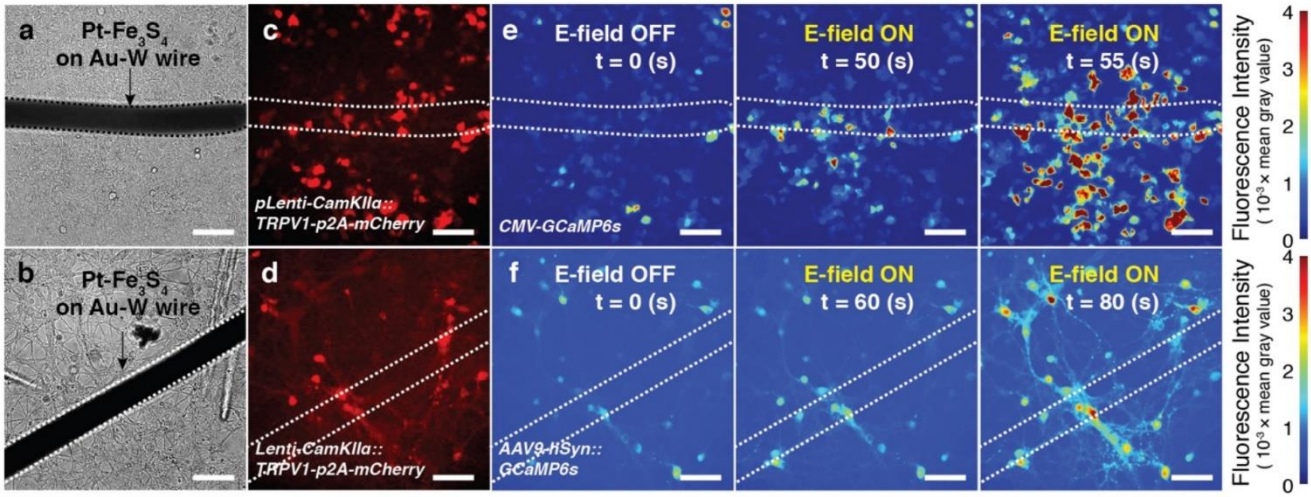

Figure 2.9. In vitro neuronal responses induced by NO-delivery fiber a-b, Optical images of Pt Fe3S4 nanocatalysts coated microwires of the NO-delivery fiber, positioned above the TRPV1+ HEK293FT cells (a) or TRPV1+ hippocampal neurons (b). c-d, Fluorescent images of TRPV1+ cells (c) and neurons (d), positioned below the microwires in a and b, respectively. White dotted lines indicate the positions of microwires onto cells and neurons. e-f, Representative time-lapse

images of Ca2+ responses in TRPV1+ HEK293FT cells (e) and neurons (f) elicited by Pt-Fe3S4 electrocatalyzed NO generation at –2.0 V vs Pt, indicating the localized activation of TRPV1 in the proximity of the microwires. Scale bar: 50 μm. *From Park*, Jin*, Sahasrabudhe et. al., Ref. 187.*

2.12 NO-mediated neuronal stimulation *in vivo*.

We next applied the electrocatalytic fibers to drive NO-mediated responses *in vivo*. We chose mouse ventral tegmental area (VTA) as our target brain region due to its low endogenous TRPV1 expression levels and well-characterized projection circuits[95–97]. The mice were transduced in the VTA with *Lenti-CaMKIIα::TRPV1-p2A-mCherry* ($TRPV1^+$) or a control virus (*Lenti-CaMKIIα::mCherry*, $TRPV1^-$) to account for potential effects of NO on the endogenously expressed channels. Following a 6-8 weeks incubation period, the mice were implanted with NO-generation fibers in the same region[98,99]. To locally generate NO with the implanted fibers, Tyrode's solution containing 0.1 M $NaNO_2$ was infused into the VTA via the microfluidic channels and –2.5 V was applied to the integrated Pt-Fe_3S_4 coated cathodes vs the integrated Pt-coated anodes (Fig. 2.10a).

The extent of NO-mediated neuronal excitation in the VTA was first investigated via the immunofluorescence analysis of the expression of an immediate early gene c-fos[100]. Significantly higher percentage of c-fos positive cells relative to all cells as marked by nuclear stain DAPI was found in the VTA of $TRPV1^+$ mice subjected to NO generation as compared to control groups, which included $TRPV1^+$ mice where voltage was not applied following $NaNO_2$ delivery and $TRPV1^-$ mice subjected to NO generation (Fig. 2.10 b, c). We also observed upregulation of c-fos expression in the nucleus accumbens (NAc) and medial prefrontal cortex (mPFC) of $TRPV1^+$ mice subjected to NO generation (Fig. 2.10 d-g). The NAc and mPFC receive excitatory projections from the VTA[95–97].

Consistent with c-fos expression analyses, fiber photometry recordings of GCaMP6s fluorescence showed that NO released from the implanted fibers could trigger neuronal activity in the VTA (Fig. 2.10 h-k). In these experiments, a cocktail of *Lenti-CaMKIIα::TRPV1-p2A-mCherry* (or *Lenti-CaMKIIα::mCherry*) and *AAV9-hSyn::GCaMP6s* was injected into the mouse VTA (Fig. 2.10 i). Following a 6-8-week incubation period, the mice were implanted with the NO delivery

fibers in the VTA and the conventional silica optical fibers the NAc, respectively (Fig. 2.10 j). Consistent with prior studies that have shown that neuronal stimulation in the VTA can be photometrically detected in their excitatory projections in the NAc[97], we found that in $TRPV1^+$ mice NO-mediated excitation of the VTA neurons yields an increase in the GCaMP6s fluorescence in their terminals in the NAc. A modest increase in intracellular Ca^{2+} was observed following a 60 s long application of –2.0 V to the fiber cathodes in the presence of $NaNO_2$. Applying –2.5 V has resulted in a rapid rise in GCaMP6s fluorescence consistent with accelerated NO generation kinetics. No significant GCaMP6s fluorescence change was observed in $TRPV1^-$ mice under the same stimulation conditions (Fig. 2.10 k). These results demonstrated that the interplay between NO and over-expressed TRPV1 in the VTA dominated over other endogenous processes potentially elicited by NO. Similarly, application of the cathode voltage alone was insufficient to evoke neural activity (Fig. 2.10 k). This is expected as the current elicited by –2.5 V was ~ 5 μA, which was significantly lower than the values (≥50 μA) typically used for direct electric neural stimulation[101,102].

To evaluate the biocompatibility of our NO-delivery strategy *in vivo*, we investigated the interfaces between the brain tissue and the implanted fibers. No noticeable differences in cytotoxicity (and no observable deleterious effects on the tissue) were observed between the mice subjected vs not subjected to NO generation, likely due to the intermittent nature of NO release exclusively in the presence of applied voltage and rapid decay of NO [103]. Furthermore, we confirmed that the Pt-Fe_3S_4 nanocatalysts, which did not evoke any observable cytotoxic responses *in vitro* and *in vivo*, remained stable at the surfaces of the cathodes two months following implantation into the mouse brain.

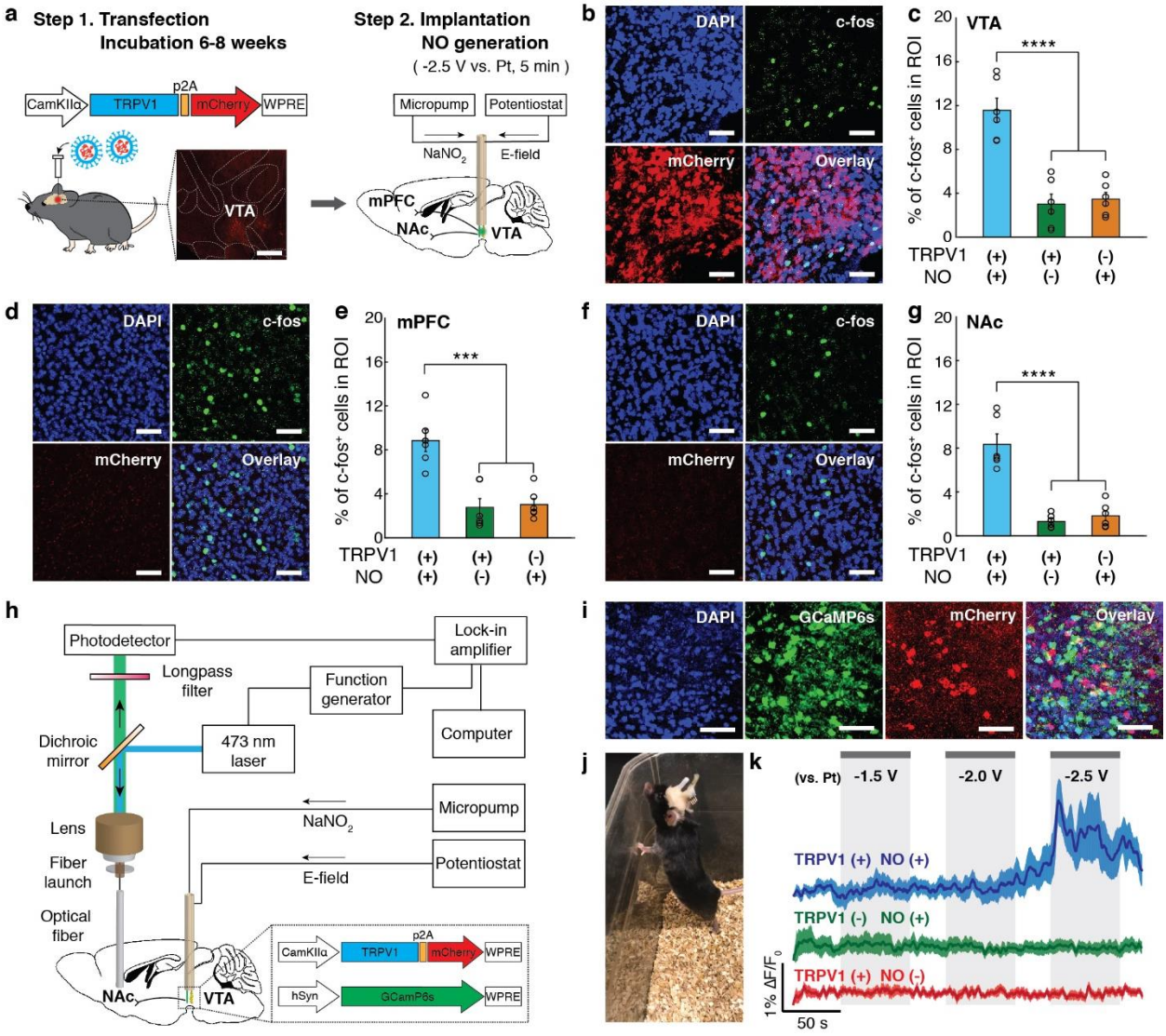

Figure 2.10. Neuronal stimulation mediated by NO-delivery via implanted fibers *in vivo*. (a) An illustration of the virus-assisted gene delivery, fiber implantation, and NO generation in the mouse brain. Inset: A confocal image of TRPV1-p2A-mCherry expression in the mouse VTA. Scale bar: 500 µm. (b-g) Confocal images (in TRPV1$^+$ mice) and percentages of the c-fos expressing neurons among DAPI-labelled cells (mean ± s.e.m.) in the region of interest (ROI) in the VTA (b, c), mPFC (d, e), and NAc (f, g) following electrocatalytic NO generation in the VTA. Scale bar: 50 µm. Statistical significance of an increase in c-fos expression after NO generation in TRPV1$^+$ mice as compared to controls was confirmed by one-way ANOVA and Tukey's multiple comparison tests (n = 6 mice, VTA $F_{2,15}$ = 28.27, mPFC $F_{2,15}$ = 18.10, NAc $F_{2,15}$ = 38,08, *** p <0.001, **** p < 0.0001). (h) An illustration of the fiber photometry setup integrated with the micropump and potentiostat for NO generation. (i) Representative confocal microscope images of a mouse VTA co-expressing GCaMP6s and TRPV1-p2A-mCherry. Scale bar: 50 µm. (j) A mouse implanted with a NO-delivery fiber in the VTA and an optical fiber in the NAc. (k) Normalized GCaMP6s

fluorescence traces in the NAc of the anesthetized TRPV1$^+$ (blue) and TRPV1$^-$ (green) mice in the presence of NO generation and in the NAc of TRPV1$^+$ mice in the presence of voltage alone (no $NaNO_2$ infusion, red). Solid lines and shaded areas indicate the mean and s.e.m., respectively (n = 5 mice per condition). F_0 indicates the mean of the fluorescence intensity during the initial 10 s of measurement. *From Park*, Jin*, Sahasrabudhe et. al., Ref. 30.*

2.13 Experimental methods for NO delivering neural probes

Preform fabrication and fiber drawing.

The macroscopic preforms were developed by machining two rectangular grooves of 1.5 mm × 1.5 mm on polycarbonate (PC; Ajedium Films) tube with inner and outer diameter of 3.175 mm and 9.525 mm respectively. This was followed by sequentially rolling additional sheets of PC, cyclic olefin copolymer (COC; TOPAS) and PC to yield a final overall preform diameter of ~ 12 mm. The preform was consolidated in a vacuum oven at 175 °C for 30 min. All the fiber drawing processes was conducted using a custom-built fiber drawing tower[33]. The fibers were drawn by placing the preform in a three-zone heating furnace, where the top, middle, and bottom zones were heated to 150 °C, 285 °C, and 110 °C, respectively. The preform was fed into the furnace at a rate of 1 mm/min and drawn at a speed of 900 mm/min, which resulted in a draw-down ratio of 30. A tungsten microwire (50 μm diameter, 99.95%, Goodfellow) and a gold-coated tungsten microwire (50 μm diameter, 0.5 μm Au coating, 99.95%, Goodfellow) were continuously fed into the preform during the draw.

Device connection.

To establish electrical interfacing with embedded electrodes, the electrodes were exposed from the PC cladding with a sharp razor blade and then bonded to copper wires (40 AWG) with a two-part silver epoxy (Epotek). Connections to anode and cathode electrodes were established at different locations along the fiber probe to avoid cross-talk. The wires were then soldered to Mill-Max male pin connectors. For interfacing with the central microfluidic channel, the fiber was inserted into a 0.5 mm diameter ethylene-vinyl acetate tubing and sealed with UV-curable epoxy. Finally, the entire pin connector and fluidic interface region of the fiber probe was coated with 5-min epoxy (Devcon) for mechanical stability and electrical insulation. Then, 300 μm of embedded microwire was exposed from the tip of the fiber with a sharp razor blade. Pt-Fe_3S_4 nanocatalysts were then deposited onto the exposed gold-coated tungsten microwire utilizing the same method for

depositing the nanocatalysts onto FTO electrode. Lastly, we coated platinum through a cyclic-electrodeposition method on the tungsten microwire anode. The working electrolyte was 2 mM K_2PtCl_6 in aqueous solution. Platinum wire was used as the anode and reference electrode during deposition. Platinum was electrodeposited on the tungsten microwire by continuous cycling the voltage from –1.2 V to 0 V vs Pt (Supplementary Fig. 11)[94]. After ten consecutive scans, the fiber was gently rinsed with de-ionized water and then dried in an oven. The thickness of the deposited Pt layer is approximately a fraction of a micron.

Injection of virus solutions into mouse brain.

All *in vivo* studies were approved by the MIT Committee on Animal Care and performed according to the National Institutes of Health Guide for the Care and Use of Laboratory Animals. Male C57BL/6 mice (Jackson Laboratory) aged 8 weeks were utilized and all surgeries were conducted under aseptic conditions. Mice were anesthetized with isoflurane (0.5-2.5 % in O_2) with a rodent anesthesia machine (VET EQUIP). Anesthetized mice were positioned in a stereotaxic frame (David Kopf Instruments) and ophthalmic ointment was applied to the eyes. Skin incisions were then performed to expose and align the skull. Coordinates for the injection and implantation were established based on the Mouse Brain Atlas[104]. For c-fos quantification assays, 1.5 µL of Lentivirus solution (>10^9 transducing units/mL) (*Lenti-CaMKIIα::TRPV1-p2A-mCherry* or *Lenti-CaMKIIα::mCherry*) was injected into VTA (coordinates relative to bregma; -3.3 mm anteriorposterior (AP); -0.5 mm mediolateral (ML); and -4.4 mm dorsoventral (DV)[104]) using a microinjection apparatus (10 µL NanoFil Syringe, beveled 33-gauge needles facing the dorso-lateral side, UMP-3 Syringe pump, and controller Micro4, World Precision Instruments) at an infusion rate of 80 nL/min. For fiber photometry experiments, a mixture of 1.4 µL of Lentivirus solution (>10^9 transducing units/mL) (*Lenti-CaMKIIα::TRPV1-p2A-mCherry* or *Lenti-CaMKIIα::mCherry*) and 0.7 µL of AAV solution (>10^{12} transducing units/mL) (*AAV9-hSyn::GCaMP6s*) were injected into the VTA. After injection, the syringe was lifted up by 0.1 mm from the initial coordinates and remained at least 10 min before a slow withdrawal. After injection, skin tissue was sutured and the mice recovered on a heat pad. During surgery, all the mice were given a subcutaneous injection of buprenorphine (0.05 mg/kg). Recovered mice were maintained at a 12-h light/dark cycle and provided with water and food *ad libitum*.

Implantation of NO-delivery fiber and fiber optic cannula into mouse brain

Implantation of the NO-delivery fiber was conducted after 6-8 weeks of virus injection to allow for sufficient viral expression. Mice were anesthetized and positioned in a stereotaxic frame as described previously[26]. For c-fos quantification assays, NO-delivery fibers were implanted into the VTA coordinates. The fibers were firmly fixed to the skull with three layers of adhesive (C&B Metabond; Parkell) and dental cement (Jet-Set 4, Lang Dental). For fiber photometry experiments, fiber optic cannula (Ø 2.5 mm ceramic ferrule, Ø 400 µm core, 0.50 NA, length = 10 mm, Thorlabs) was additionally implanted into NAc coordinates (1.25 mm AP; -0.75 mm ML, -3.9 mm DV[104]) after the implantation of the NO-delivery fibers in VTA. The cannula was also fixed to the skull with the adhesive and dental cement. After implantation and fixation, remaining exposed skull was fully covered with the adhesive and dental cement. All the mice were given a subcutaneous injection of buprenorphine (0.05 mg/kg) during surgery, followed by the recovery process on a heat pad.

Immunohistochemistry analyses

After implantation and recovery processes, mice were anesthetized through an intraperitoneal (IP) injection of ketamine (100mg/kg) and xylazine (10mg/kg) mixture in saline and transferred to NO generation setup. First, to mimic *in vitro* experimental conditions, 3 µL of $NaNO_2$ containing Tyrode's solution was injected through microfluidic channels into the mouse brain at an infusion rate of 500 nL/min. Then, the mice were subjected to the NO generation by applying –2.5 V vs Pt to the cathode for 5 min with the Bipotentiostat SP-300 from Biologic. To ensure sufficient delivery of $NaNO_2$ to the electrode, 3 µL of the same $NaNO_2$ solution was additionally injected during the NO generation at an infusion rate of 500 nL/min. The mice then kept in their home cages for 60 min to allow for c-fos expression. In the case of the control group with $TRPV1^-$ mice, an identical NO generation method was used. For another control group without NO generation, only an injection of the $NaNO_2$ solution was performed to $TRPV1^+$ mice without applying the voltages. Mice were then euthanized by IP injection of Fetal Plus solution (100 mg/kg in saline) before performing transcranial perfusion with 4 % paraformaldehyde (PFA) in PBS. Extracted brains were then fixed in a 4 % PFA solution overnight at 4 °C. The fixed brains were washed with PBS three times and then sliced into 60 µm sagittal sections using a vibrating blade microtome (Leica VT1000S) with a FEATHER razor blade (Electron Microscopy Sciences, 72002). The slices were then placed in a Netwell insert (Corning, 3478) in a standard 12-well plate and incubated with 2.5 mL of the blocking buffer (0.3 % triton + 3 % normal goat serum (NGS) in

PBS) for 1 hour at room temperature in the dark on an orbital shaker. The slices were then transferred to 2.5 mL of the primary antibody solution (500× dilution primary antibody + 3 % NGS in PBS) and incubated for 1 hour at room temperature in the dark on an orbital shaker. The slices were further incubated in the primary antibody solution overnight at 4°C. Following three washes with PBS, slices were transferred to the secondary antibody solution (500x dilution secondary antibody in PBS) and incubated for 3 hours at room temperature in the dark on an orbital shaker. Following another three washes with PBS, the slices were then transferred onto glass slides, and covered with mounting solution containing DAPI (Vectashield mounting medium with DAPI, H-1200, Vector Laboratories). Finally, the slides were covered with a coverglass, and sealed with nail-polish. A laser scanning confocal microscope (Fluoview FV1000, Olympus) with 20× (oil, 0.85 NA) objective was used for imaging. The c-fos quantification and biocompatibility analyses were conducted with z-stack images with a depth of 5 µm. Rabbit anti-c-fos (Cell Signaling technology, 2250s), rat anti-mCherry (Invitrogen, M-11217), and rabbit anti-cleaved caspase-3 (Cell Signaling technology, 9661s) were used as primary antibodies. Goat anti-rabbit labeled with Alexa Fluor 488 (Invitrogen, A-27034), goat anti-rat labeled with Alexa Fluor 633 (Invitrogen, A-21094), and goat anti-rabbit labeled with Alexa Fluor 633 (Invitrogen, A-21070) were used as secondary antibodies.

Fiber photometry analyses

In order to establish the fiber photometry setup, a 473 nm diode laser (OEM Laser Systems, 50 mW peak power) was coupled to a ferrule rotary joint patch cable (Ø 400 µm core and Ø 1.25 mm ferrules, Thorlabs) utilizing a 20× microscope objective (0.45 NA, Olympus) integrated with the fiber launch (Thorlabs, MBT610D). The laser was then controlled by a function generator (400 Hz, square wave, Agilent) and the laser intensity out of the fiber tip was controlled to be approximately 100-200 µW. Before fiber photometry recordings, mice were anesthetized through an IP injection of ketamine (100 mg/kg) and xylazine (10 mg/kg) mixture in saline and transferred to photometry setup integrated with potentiostat and micropump for NO generation. Then, a fiber optic cannula implanted into mice was connected to the photometry patchcord, which is linked to the fiber launch, with a ceramic split mating sleeve (Ø 2.5 mm, Thorlabs). Before NO generation, 3 µL of $NaNO_2$ containing Tyrode's solution was injected through microfluidic channels into the mouse brain at an infusion rate of 500 nL/min. To identify a threshold voltage for evoking Ca^{2+} responses in $TRPV1^+$ mice, the following applied voltages and electrolysis times were applied to

the cathode in a sequential manner; –1.5 V for 60 s, 0 V for 30 s, –2.0 V for 60 s, 0 V for 30 s, –2.5 V for 60 s, 0 V vs Pt for 30 s. At the same time, 3 μL of the same $NaNO_2$ solution was additionally injected during the NO generation at an infusion rate of 500 nL/min. The GCaMP6s fluorescence from NAc during the NO generation was collected by the implanted fiber optic cannula. The collected fluorescence was transmitted through a dichroic mirror (Thorlabs) and then filtered to avoid the remaining laser background with a longpass filter (Semrock) on a femtowatt silicon photoreceiver (NewFocus). The photoreceiver connected to a lock-in amplifier (8 ms time constant, Stanford Research Systems) was recorded by custom software written in Labview (acquisition frequency: 8.5 Hz). All the fiber photometry recordings were performed in the dark.

CHAPTER 3. FIBER DEVICES FOR PROBING THE GUT-BRAIN AXIS

Note: The content presented in this chapter was first published as A. Sahasrabudhe, L. Rupprecht* et. al. Nat Biotechnol (2023) https://doi.org/10.1038/s41587-023-01833-5 (Ref. 31) and K. Buchanan*, L. Rupprecht*, M. Kaelberer*, A. Sahasrabudhe et. al. Nat Neurosci 25, 191–200, 2022 (Ref. 16).*

3.1 Post-ingestive sugar sensing

Both sugar and artificial sweeteners elicit a sweet taste, but sugar is preferred by animals and humans. Even mice lacking taste receptors can distinguish sugar from sweetener or water[105,106]. Although sensing sweetness depends on the tongue, flavor-conditioning tests show that the duodenum is needed to discern sugar from sweeteners.

Table sugar, or sucrose, is a disaccharide made of D-glucose and D-fructose. Unlike D-fructose or the sweetener sucralose, D-glucose conditions a robust preference when infused into the duodenal lumen[107,108]. In fact, animals with prior D-glucose exposure identify the sugar entering the intestine within minutes[109]. This ability to identify D-glucose vanishes when the small intestine is bypassed[110], suggesting that the duodenal epithelium is where the 'sugar transducer' cell resides. But up until now, the identity of these cells has remained elusive because of the lack of tools to control gut sensory processing with temporal and spatial precision.

In other epithelial surfaces, electrically excitable cells use molecular receptors to detect and transduce sensory stimuli onto a cranial nerve to guide behavior. In the nose, for instance, olfactory receptor cells transduce odorant stimuli through glutamatergic synapses onto second-order mitral cells to assist the animal in distinguishing odors. In the tongue, sweet, bitter or umami taste receptor cells form purinergic synapses with afferent nerve fibers to guide an animal in distinguishing tastants. In the gut, this function seems to be performed by neuropod cells[111,112].

Neuropod cells were first documented when enteroendocrine cells, known for their release of hormones such as CCK, were found to form synapses with underlying mucosal nerves. In 2018, CCK-labeled duodenal neuropod cells were shown to form glutamatergic synapses with the vagus

nerve. These cells use the neurotransmitter glutamate to transduce a D-glucose stimulus from the gut to the brain in milliseconds (see video https://youtu.be/3v92lRNOdlA).

We hypothesized that duodenal neuropod cells discern nutritive sugars from non-caloric artificial sweeteners to guide the animal's preference for sugar over sweetener.

3.2 Need for a flexible fiber for gut optogenetics

My collaborators at Duke University in the lab of Prof. Diego Bohorquez had established that neuropod cells discern sugar from sweetener through a series of elegant experiments involving vagal electrophysiology and NG imaging with simultaneous perfusion of nutrients in the small intestine (See Ref. 16[16] and 105[113] for additional details on these sections). A logical next experiment in this thread of investigation was to determine whether these epithelial transducers also guide the animal's preference for sugar over sweetener. To test the contribution of these cells to behavior, a method was needed to silence neuropod cells while the mouse's preference was recorded. In the brain, the contribution of specific neurons to behaviors has been uncovered using optogenetics34. This technique relies on light-gated channels activated by laser light traditionally delivered using rigid silica fiberoptic. In the gut, however, we found that rigid fiberoptics puncture and perforate the intestinal wall. Recently, some efforts have been made to stimulate the outer muscular wall of the intestine or a small portion of the stomach in vivo. But no tool existed to control a specific population of gut epithelial cells diffused along several centimeters of the intestinal lumen in a living animal. As such, we developed a new device to deliver laser light into the gut lumen.

The system required a flexible fiberoptic with the following properties: (1) thin diameter for minimal footprint within the intestinal lumen, (2) low optical loss coefficient to deliver light to the gut lumen, (3) efficient light transmission even when bent and (4) durability for months when flexed inside the churning gut. First, we engineered a fiber preform of a poly-methyl methacrylate (PMMA) cladding layer around an optical core of polycarbonate (PC). Then, the preform was thermally drawn at 270 °C into a final flexible fiber 230 μm in diameter (Fig. 3.1a, b). To determine optical loss, the fiber was cut in 0.5-cm increments, and light transmission was measured when the fiber was either straight or bent to 180°. Percent transmission was compared to transmission at the shortest length. The loss coefficients were determined to be 0.93 dB cm–1 and 1.30 dB cm–1 for straight and bent fibers, respectively (Fig. 3.1c). Light transmission had minimal loss when bent

at 90°, 180° and 270° angles compared to transmission when the fiber was held straight (Fig. 3.1d). Repeated 180° bending did not heavily influence light transmission (Fig. 3.1e). In addition, the device transmitted light with a 1.2-dB cm–1 loss and tolerated rapid bending at 10 Hz, which is above the physiological frequency of gut motility (Fig. 3.1f). Compared to rigid silica, the flexible fiberoptic did not pierce through a soft layer of 1.5% agarose, which is similar in consistency to the gut wall (Fig. 3.1g). The flexible fiberoptic was opacified to restrict light to the first 1.5 cm of the mouse small intestine (Fig. 3.1h).

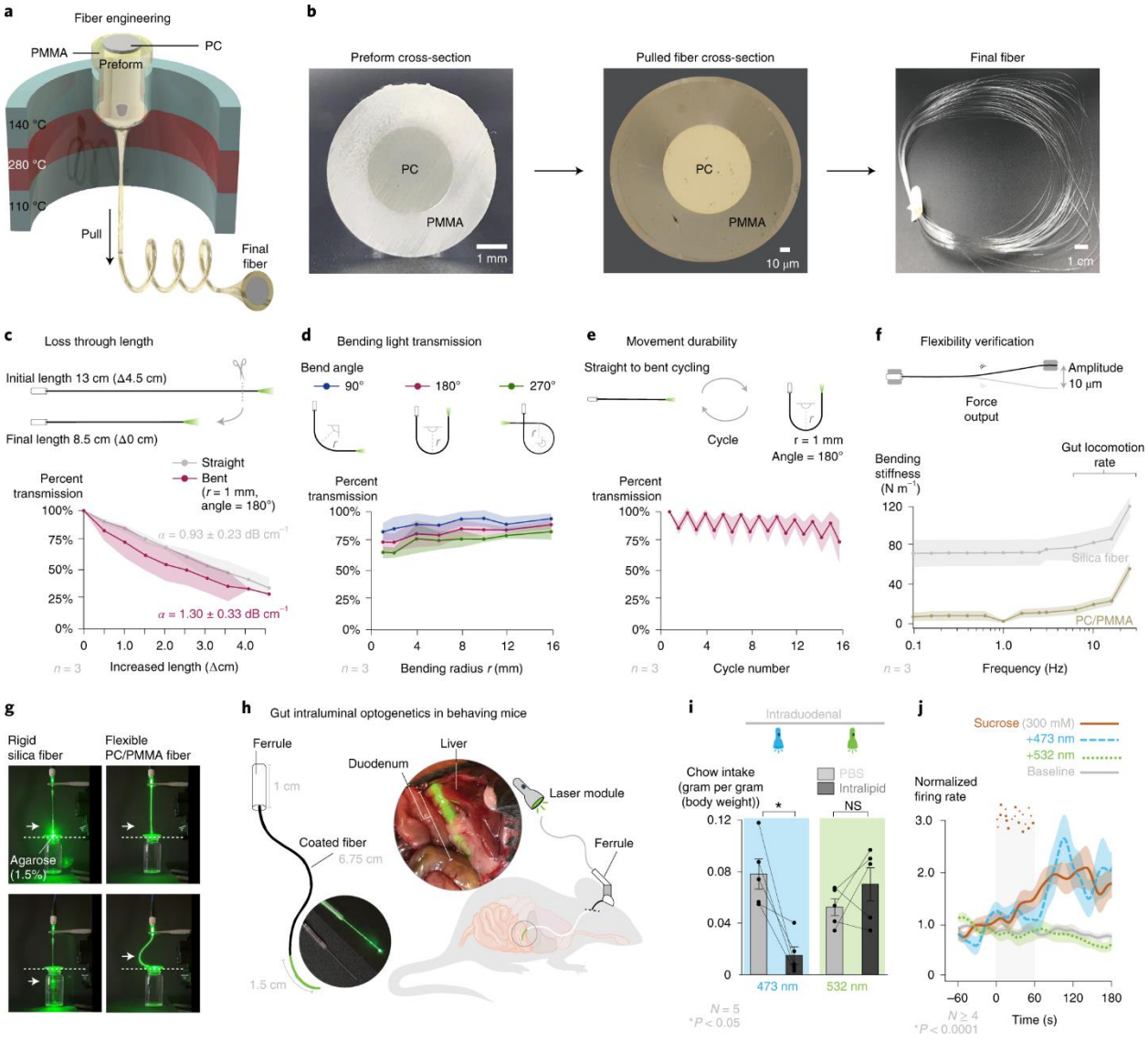

Figure 3.1. Development of a flexible fiberoptic device for optogenetic targeting of gut neuropod cells. (a) Model of the thermal drawing process to obtain a flexible PC/PMMA fiber. (b) Cross-

section of the PC/PMMA preform (left), pulled PC/PMMA fiber (middle) and ~50-m fiber bundle (right). (c) Light transmission for straight and bent flexible fibers using the cut-back method plotted as percentage of light output (y axis) from shortest length (Δ0 cm). Loss coefficients (α) were determined as 0.93 dB cm–1 and 1.30 dB cm–1 for straight and bent fibers, respectively; r, radius. (d) Light transmission for fibers bent at 90°, 180° and 270° at different radii of curvature (x axis) plotted as percentage of light output from a straight fiber (y axis). (e) Light transmission for fibers during cyclic bending at 180° (odd cycles, straight; even, bent) plotted as percentage of light output from initial position (cycle = 0). (f) The flexibility of silica and PC/PMMA fiber was measured by a dynamic mechanical analyzer at physiologic frequencies. For c–f, n = 3 fibers, the bold line indicates the mean, and the shaded regions indicate s.d. (g) A conventional silica fiber pierces an agarose (1.5%) membrane, while the PC/PMMA flexible fiber bends and does not pierce the membrane. (h) The flexible fiber was implanted into mice to target the lumen of the proximal duodenum. (i) To validate the device in a known function of CCK-labeled neuropod cells, CckCRE_Halo mice received intragastric gavage of intralipid (7%, 0.1 ml per 10 g) with control 473-nm light, which reduced chow intake. This effect was reversed when CCK-labeled neuropod cells were silenced with 532-nm light (N = 5 mice; *P = 0.0193 by analysis of variance (ANOVA) with post hoc two-tailed paired Student's t-test; error bars indicate s.e.m.); NS, not significant. (j) To validate device longevity, vagal responses to baseline (PBS), sucrose without light, sucrose with control 473-nm light and sucrose with silencing 532-nm light were recorded in CckCRE_Halo mice 4 weeks after fiber implantation (N ≥ 4 mice per group; the bold line indicates the mean, and the shaded region indicates s.e.m.). *From Buchanan*, Rupprecht*, Kaelberer*, Sahasrabudhe et. al., Ref. 16.*

To validate the device for gut optogenetics in freely moving mice, we investigated if silencing CCK-labeled neuropod cells eliminated the anorectic effect of a lipid gavage, an established physiological effect of CCK. A fat solution (intralipid, 7%) was delivered to CckCRE_Halo mice by gavage with simultaneous silencing (532-nm) or control (473-nm) light. Total food intake was significantly suppressed in mice with fat gavage and control light but not in mice with fat gavage and silencing light (Fig. 3.1i). We then confirmed the device's durability by implanting it in the intestine of CckCRE_Halo mice. Four weeks later, control 473-nm light emitted from the device did not affect the vagal response to intraduodenal sucrose (Fig. 3.1j), whereas 532-nm light eliminated the response. These results corroborated the sustained functionality of the device to optogenetically modulate CCK-labeled neuropod cells in vivo.

Sugar preference depends on duodenal neuropod cells

We then determined if CCK-labeled neuropod cells are necessary for mice to discern sucrose from sucralose. Mice were implanted with the flexible fiberoptic, acclimated to the phenotyping cage

and tested for side preference. Each mouse was exposed to sucrose and sucralose until they demonstrated a stable preference for sucrose (see Methods). The location and power of the implanted device was corroborated at the end of the study. On each experimental day, implanted mice were given the choice between sucrose (300 mM) and sucralose (15 mM) for 1 h while receiving light stimulation to inhibit CCK-labeled neuropod cells (1 min on/2 min off, 5 V, 40 Hz, 20% duty cycle).

In the presence of 532-nm light, control littermates showed 90.8% (±3.7%) sucrose preference (Extended Data Fig. 6a,b Ref. 16[16]), whereas in CckCRE_Halo mice, sucrose preference was only 58.9% (±3.9%) ($N = 8$ mice; $P < 0.01$ compared to controls; Fig. 3.2a,b). In control experiments, silencing duodenal CCK-labeled neuropod cells with 532-nm light did not cause malaise, as neither locomotor activity during the assay (Extended Data Fig. 6d, Ref. 16[16]) nor chow or water intake in the following 24 h (Extended Data Fig. 6e,f, Ref. 16[16]) were affected. Additional experiments showed that laser inhibition with 532-nm light did not affect gastric emptying of sucrose, total gut transit time or glucose absorption compared to 473-nm control light (Extended Data Fig. 6g–j, Ref. 16[16]). Of importance, silencing CCK-labeled neuropod cells decreased sucrose intake and increased sucralose intake, but the total consumption of liquid during the 1-h test was not affected ($P < 0.05$; Fig. 3.2c and Extended Data Fig. 6c, Ref. 16[16]). In other words, silencing duodenal neuropod cells eliminated preference for sucrose over sucralose. In posttest controls without laser treatment, mice displayed the same pretest preference for sucrose (Fig. 3.2b), indicating that the animals did not lose their preference for sucrose but rather their ability to discern the preferred sugar from the sweetener.

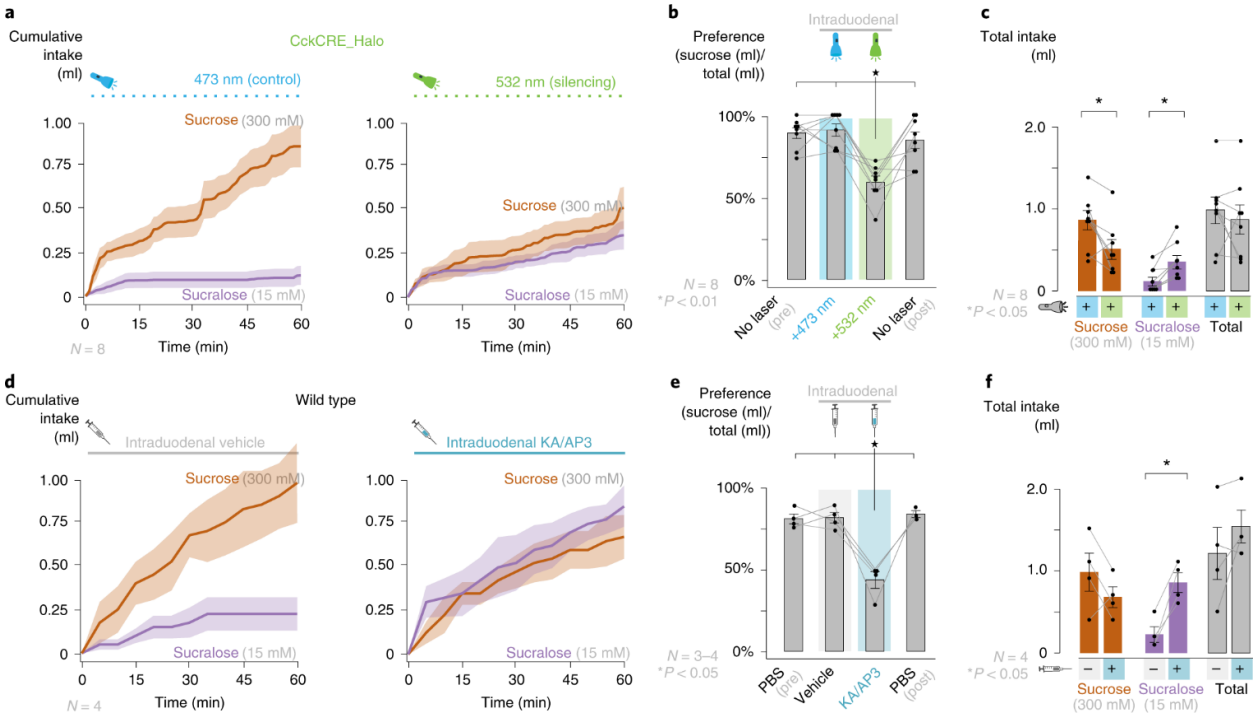

Figure 3.2. Sugar preference depends on duodenal neuropod cells. Mice with a stable preference for sucrose over sucralose chose between the two solutions during optogenetic (a–c) or pharmacologic (d–f) inhibition in a 1-h two-bottle choice assay. a, In CckCRE_Halo mice implanted with a flexible fiberoptic, average traces show sucrose and sucralose consumption in the presence of intraduodenal control 473-nm (left) or silencing 532-nm (right) light. b, Quantification of preference at 1 h with no laser (pretest/posttest) and with control 473-nm light and silencing 532-nm light. Silencing 532-nm light significantly reduced sucrose preference compared to pretest ($P = 0.0012$), posttest ($P = 0.0057$) and control 473-nm light ($P = 0.0003$). c, Quantification of total intake during optogenetic silencing at 1 h. Silencing 532-nm light significantly decreased sucrose intake ($P = 0.0224$) and increased sucralose intake ($P = 0.048$) with no change in total intake ($P = 0.4347$). For a–c, $N = 8$ CckCRE_Halo mice; $^*P < 0.05$ by repeated measures ANOVA with post hoc two-tailed paired *t*-test. d, In wild-type mice with intraduodenal catheters, average traces show sucrose and sucralose consumption in the presence of vehicle (PBS + NaOH, pH 7.4; left) or local dose of ionotropic/metabotropic glutamate receptor inhibitors KA/AP3 (15 ng per 0.1 µg in 0.4 ml delivered over 1 h; right). e, Quantification of preference at 1 h with PBS (pretest/posttest), vehicle and glutamate receptor inhibitors KA/AP3. KA/AP3 significantly reduced sucrose preference compared to pretest ($P = 0.0294$), posttest ($P = 0.0497$) and vehicle ($P = 0.0294$). f, Quantification of total intake during glutamatergic inhibition at 1 h. KA/AP3 significantly reduced sucralose intake ($P = 0.0090$). For d–f, $N = 4$ wild-type mice; $^*P < 0.05$ by Kruskal–Wallis test with non-parametric comparisons using the Wilcoxon method. Shaded regions/error bars indicate s.e.m. *From Buchanan*, Rupprecht*, Kaelberer*, Sahasrabudhe et. al., Ref. 16.*

To determine whether activating duodenal neuropod cells would increase an animal's consumption of the non-preferred solution, sucralose, we bred mice in which CCK-labeled neuropod cells expressed channelrhodopsin 2 (CckCRE_ChR2). This excitatory opsin is activated by blue light (473 nm). The mice were presented with one bottle containing sucralose (15 mM), and intake of 0.01 ml triggered a 5-s laser stimulation (5 V, 40 Hz, 20% duty cycle) (Extended Data Fig. 7a, Ref. 16[16]). In this assay, 473 nm light had no effect on the intake of wild-type littermates ($N = 4$; not significant compared to 532-nm control; Extended Data Fig. 7b,c, Ref. 16[16]). However, in CckCRE_ChR2 mice, exciting CCK-labeled neuropod cells with 473-nm light significantly increased sucralose intake ($N = 4$; $P < 0.05$ compared to 532-nm control; Extended Data Fig. 7b,c, Ref. 16[16]). These results indicate that stimulating duodenal neuropod cells drives mice to consume sweetener as if it were sugar.

Thus, we demonstrate that an animal's preference for sugar over sweetener depends on duodenal neuropod cells. These cells rapidly transduce such stimuli onto the vagus nerve using two receptors and two neurotransmitters; whereas sweetener activates T1R3 to cause the release of ATP, the entry of sugar into the cell stimulates the release of glutamate. By developing a flexible fiber for gut optogenetics, we discovered that sugar preference depends on neuropod cell glutamatergic signaling. Uncoupling the synapses between neuropod cells and vagal neurons will inform how appetitive functions beyond choice are continuously modulated by fast neurotransmission from the gut epithelium.

3.3 Wireless microelectronics fibers for probing gut-brain signaling

The extensive lines of bidirectional communication between the brain and visceral organs facilitate integration of internally arising interoceptive cues that are critical for survival. The gut-brain communication exemplifies one such important pathway wherein humoral and neural signals emerging from the abdominal viscera relay metabolic information to the brain for maintaining energy balance. Besides the well-known homeostatic functions, recent evidence suggests that the consciously imperceptible gut-to-brain signals can also modulate higher-level cognitive processes such as motivation, affect, learning, and memory[1,114–117]. These findings create opportunities for co-opting such brain-organ neural circuits to develop minimally invasive autonomic neuromodulation therapies for otherwise intractable metabolic and neurological disorders such as treatment-resistant depression, obesity, or diabetes[118,119]. However, identification of mechanisms underlying brain-viscera communication that influence neurocognitive states has remained

challenging, which is at least in part due to the dearth of implantable bio-integrated multifunctional devices that allow safe, long-term deployment in anatomically and physiologically disparate organs of behaving animals. Traditionally the fabrication of biontegrated devices has relied on the use of resource intensive lithographic techniques adapted from the semiconductor industry that require specialized cleanroom environments[21,120–126]. The thin film processing nature of lithography necessitates independent fabrication of individual modalities of the device stack, followed by careful manual assembly thereby making this approach unsuitable for rapid customization[23,127–132]. Consequently, there remains a need for monolithic and scalable fabrication approaches that do not compromise the design flexibility, multimodality, functional sophistication, and long-term biocompatibility of bioelectronic interfaces. Here we introduce a strategy that bridges this technological gap and demonstrate its potential in experiments spanning neural circuits in the brain and the gut.

We develop multifunctional bioelectronic interfaces based on polymer fibers embedded with solid-state microelectronic components using thermal drawing[133] (Fig. 3.3a). We leverage the top-down nature of thermal drawing to produce, in a single step, several tens of meters of microscale fibers (~1000 rodent-scale probes) that can host: a) surface localized microscale light emitting diodes (μLEDs) for optogenetics; b) microscale thermal sensors for precision thermometry; c) microelectrodes for electrophysiology, and d) microfluidic channels for drug and gene delivery (Fig. 3.3b). We demonstrate that mechanical properties of such fibers can be engineered to produce architectures compatible with implantation in the deep brain and the tortuous, mobile gastrointestinal (GI) tract. Furthermore, we also develop a modular wireless control circuit, NeuroStack, to interface with the microelectronic fibers (Fig. 3.3c)[134] that permits real-time, programmable light delivery across multiple independent channels and wireless data transfer for recording of local tissue temperature in untethered behaving mice.

We demonstrate that microelectronic fibers can be chronically implanted into the brain and the intestine of mice (Fig. 3.3d). The stiff, yet flexible fibers designed for the brain can accurately target deep-brain nuclei such as the ventral tegmental area (VTA) where we deliver a viral vector carrying channelrhodopsin-2 (ChR2) to dopaminergic neurons through the integrated microfluidic channel. The co-localized electrodes and μLEDs on the same fiber permit longitudinal recording of spontaneous and optically-evoked neural activity following delivery of genetic payload, while thermal sensors enable concomitant deep-brain thermometry. On the other hand, the soft and

compliant gut fibers capable of delivering light and nutrients in the intestinal lumen allow direct modulation of GI neural circuitry including epithelial sensory cells in the proximal and distal small intestine and the upper-gut innervating vagal afferents. Moreover, multi-site devices permit simultaneous implantation of multifunctional fibers in the gut and the brain allowing us to probe central neural representation of post-ingestive nutrient sensing. By coupling the VTA implanted fibers to NeuroStack, we show that wireless programmable optogenetic stimulation of dopaminergic neurons elicits a reward behavior. Similarly, the soft gut fibers enable wireless intraluminal gut optogenetics targeting the sparsely distributed enteroendocrine/neuropod cells in the duodenum and ileum that modulate feeding behavior. Finally, we uncover that optogenetic stimulation of vagal afferents from the gut lumen produces a rewarding phenotype, thereby demonstrating direct modulation of central nervous system function from the intestine in behaving mice. We anticipate that these illustrative applications will foreshadow widespread use of wireless multifunctional microelectronic fibers to study brain-viscera and multi-organ neural communication pathways.

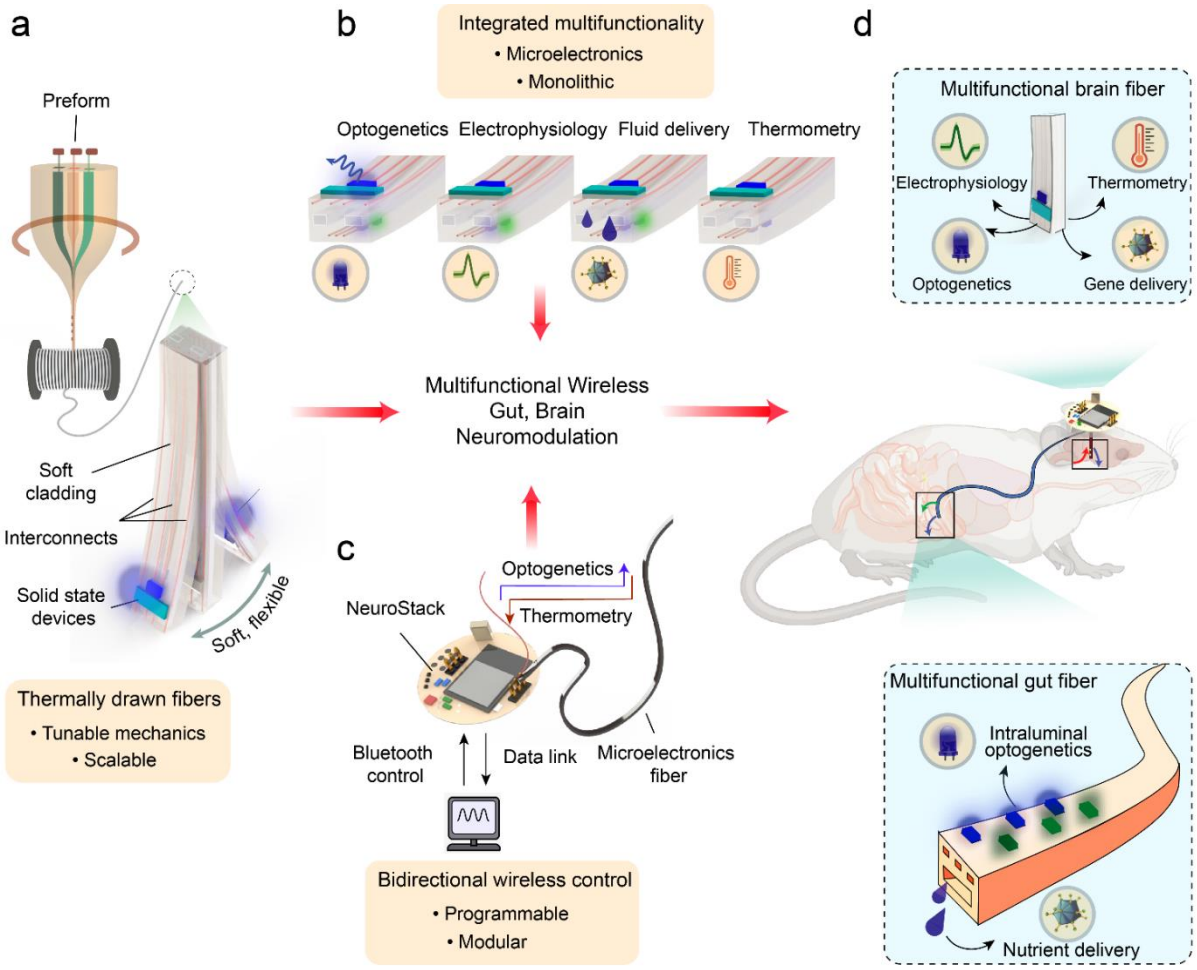

Figure 3.3. Schematic illustration of microelectronics integrated multifunctional fibers that enable wireless modulation of brain and gut neural circuits. (a) High throughput, monolithic fabrication of multifunctional polymer fibers using thermal drawing yields several meters long fibers (~1000 rodent scale probes) with tunable mechanics and solid state microelectronic components; (b) Such fibers can host multiple independently addressable μLEDs for optogenetics, microelectrodes for extracellular electrophysiology, microfluidics for gene/chemical delivery, and thermal sensors for tissue thermometry in a miniature footprint; (c) NeuroStack, a custom designed modular wireless control circuit, enables real time programmable optical stimulation and data transfer for recording of tissue temperature; (d) The multifunctional microelectronics fibers together with NeuroStack allow for wireless modulation of neural circuits in the deep-brain and in the small intestine of awake behaving mice. *From Sahasrabudhe*, Rupprecht* et. al., Ref. 31.*

3.4 Multifunctional microelectronic fibers for the brain

To produce multifunctional microelectronic fibers for interrogation of brain neural circuits we designed a multilayer polycarbonate preform (PC, T_g = 150 ºC, *E* = 1.8-3.2 GPa) (Fig. 3.4a) that was thermally drawn into a functional fiber (Fig. 3.4b, Supplementary Fig. B1 a-d), while simultaneously feeding spools of interconnect (Silver-Copper, Ag-Cu, 40 µm diameter) and recording electrode microwires (Tungsten, 25 µm diameter) (Supplemental Note-B1). The overall cross-sectional geometry of the preform (Fig. 3.4c) was conserved during the draw (Fig. 3.4d), yielding ~50 m of functional fiber (Fig. 3.4e) with dimensions of 370.7 ± 2.8 µm × 190.4 ± 3.4 µm (mean ± s.d., n=5 sections, Supplementary Fig. B1e). The fibers were assembled into implantable probes (Supplementary Fig. B2 a-f, Fig. 3.4f) by mounting blue (peak emission wavelength, λ = 470 nm) and green (λ = 527 nm) microscale light-emitting devices (µLEDs, $In_xGa_{1-x}N$, 270 µm × 210 µm × 50 µm) along the fiber surface followed by deposition of a thin layer of parylene-C as a biofluid barrier coating. Optical micrographs of independently addressable µLEDs and microfluidic infusion in the final fiber device are shown in Fig. 3.4 g-i. While the above approach shows integration of microelectronic components within the fibers post-draw, we also demonstrate embedding semiconductor devices inside multifunctional fibers during fiber drawing indicating further scalability of this platform (Supplemental Note-B2, Supplementary Fig. B3 a-k)[47].

3.5 Characterization of brain fibers

Incorporation of tungsten microwires in fibers afforded low impedance microelectrodes (|Z| = 46.3 ± 6 kΩ at 1 kHz) for electrophysiology without compromising device flexibility (Fig. 3.4j and inset). The electrode impedance exhibited a negligible increase upon immersion in phosphate buffered saline (PBS) over 7 weeks, and no leakage current was observed through the polymer cladding (Supplementary Fig. B4 a-b). The light intensity from the integrated blue µLEDs was tunable over a range between 0.6 mW/mm^2 to 70 mW/mm^2 (Fig. 3.4k), which is sufficient for optogenetic modulation of behavior mediated by microbial rhodopsins such as ChR2[135,136]. The robust bonding of µLEDs was corroborated by the stable light output even at large bending angles up to 90º, while long-term immersion tests in PBS demonstrated functionality for at least 7 weeks (Supplementary Fig. B4 c-d). We applied finite element modelling (FEM) to investigate how illumination intensity and volume varied with distance from the µLED at different input intensities

(Supplementary Fig. B5 a-d). We find that even a moderate intensity of 30 mW/mm^2 covers a tissue volume of ~0.75 mm^3 near the fiber surface, sufficient for optogenetic modulation of most brain nuclei in mice.

We leveraged the temperature dependent I-V characteristics of the diodes ($In_xGa_{1-x}N$ μLED, λ = 470 nm) to record heat dissipation in the tissue during operation of the neighboring μLED[137]. A linear dependence of diode current on temperature defined the sensor calibration curve (Fig. 3.4l). Consistent with the thermal FEM (Supplementary Fig. B6 a-d), the sensor detected a negligible temperature rise of 0.085 ºC from a co-located μLED (λ = 470 nm, ~30 mW/mm^2) operating at 40 Hz, which is well below the ~2 ºC heating that occurs during clinical electrical deep brain stimulation (Fig. 3.4m, Supplementary Fig. B7)[138]. To assess the microfluidic functionality, we measured the return rate of fluid infusion through the fiber (Fig. 3.4n) that was found to be in the range of 80-100% at physiologically relevant infusion speeds of 20-100 nl/s for intracranial injections. Since packaging of multiple functions in a neural probe can be at odds with achieving flexible device mechanics, we measured the bending stiffness of the fibers in the single cantilever mode to mimic their anchoring to the skull. The fiber stiffness ranged between 25-33 N/m, which is significantly lower than that of silica (132 N/m, 0.4 mm dia., 1 cm length) and stainless steel (792 N/m, 0.4 mm dia., 1 cm length) probes of similar dimensions (Supplementary Fig B8a). This was further corroborated through the mechanical FEM, which estimated a relative micromotion between the fiber tip and brain tissue that was ~2-4 orders of magnitude lower than silica and steel implants of similar dimensions (Fig. 3.4o, Supplementary Fig. B8 b-f)[139].

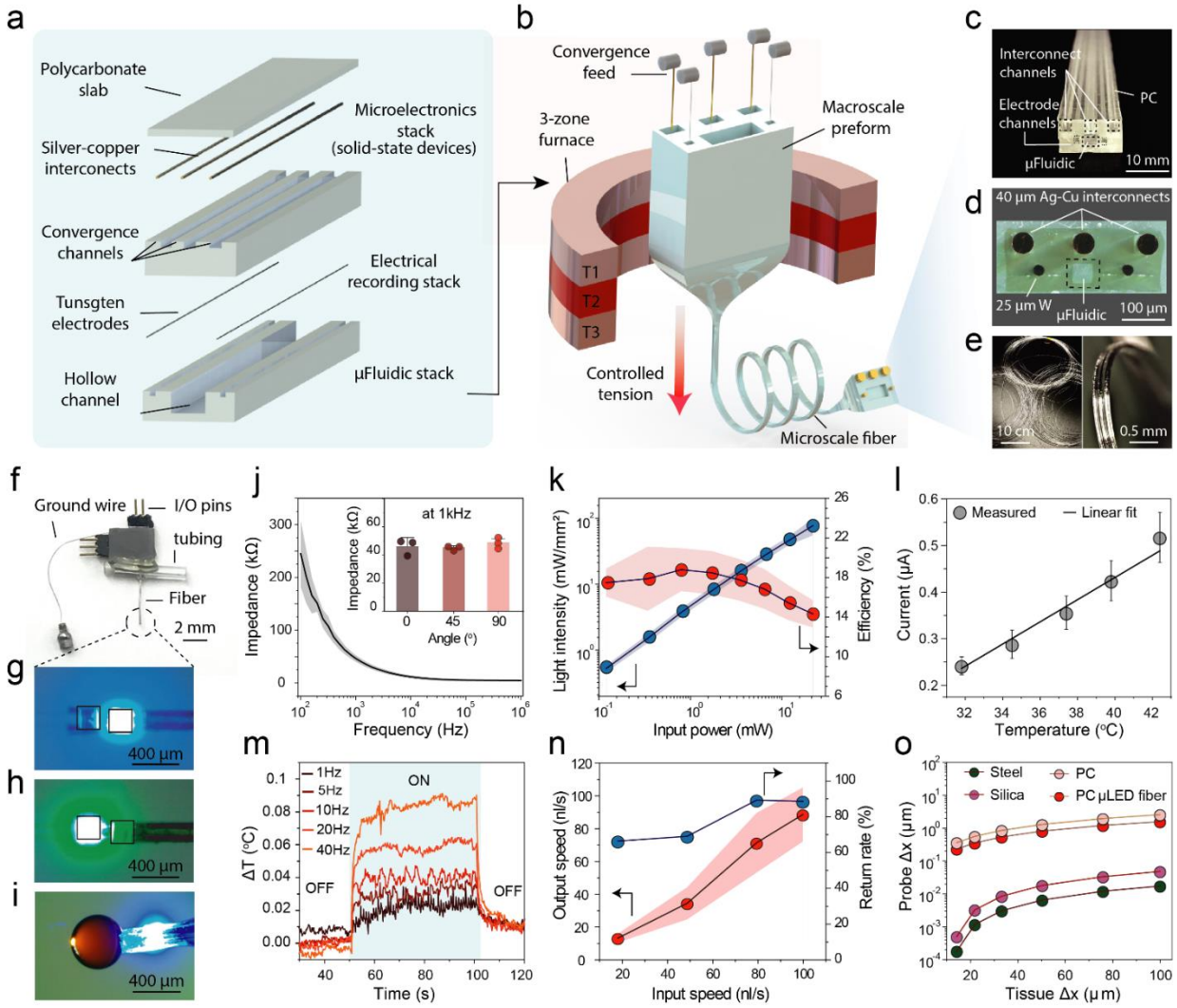

Figure 3.4. Fabrication and characterization of multifunctional brain fiber. (a) Preform layout and assembly of a multifunctional brain fiber that comprises of interconnect channels in the central poly(carbonate) (PC) layer and a precursor to microfluidic channel and recording electrodes in the bottom PC layer; (b) Schematic of the thermal drawing process with simultaneous feeding of metal microwires serving as interconnects (40µm silver-copper, Ag-Cu) and recording electrodes (25µm tungsten); (c) A photograph of a consolidated preform highlighting channels for interconnects, electrodes, and microfluidics; (d) An optical micrograph of a fiber cross-section showing conserved cross-sectional features; (e) Several meters of as-drawn fiber depicting the scalability of fabrication (left) and a close-up view of an acutely bent flexible fiber (right); (f) A fully assembled multifunctional fiber dveice with I/O pins for microelectrodes and µLEDs, access tubing for microfluidic channel, and a ground wire; (g-h) Independently addressable blue (g) and green (h) µLEDs at the distal end of the device; (i) Simultaneous microfluidic fluid delivery and blue µLED under operation; (j) Electrochemical impedance spectrum of the tungsten microelectrodes in 1×PBS (n=3). Inset shows variation of electrode impedance with bending deformation; (k) Optical intensity output (blue trace) and efficiency (red trace) of µLED (λ =

470nm) integrated within a fiber with varying input electrical power (n=6), where arrows indicate the y-axes for respective plots; (l) Steady-state calibration curve of the in-fiber thermal sensor between 32-42ºC (n=4); (m) Variation of local temperature as recorded by the thermal sensor during operation of an adjacently placed blue µLED on the same fiber at different stimulation frequencies (35.2 mW/mm^2, 10ms pulse); (n) Characterization of the fiber microfluidic channel showing output speed (red trace) and return rate (blue trace) at varying input injection speeds (n=4), where arrows indicate the y-axes for respective plots; (o) Mechanical finite element model compares the displacement of the probe tip for steel, silica, bare PC fiber, and a microelectronic PC fiber implant at displacements of the brain tissue between 10-100 µm; All shaded areas and error bars represent standard deviation (s.d.). *From Sahasrabudhe*, Rupprecht* et. al., Ref. 31*.

3.6 Microelectronic fibers for the gut

Unlike the brain, the GI tract precludes implantation of rigid devices owing to a tortuous anatomy of the lumen that is encased in a delicate tissue, through which ingested food and fluids must pass[140]. Hence, we created multifunctional microelectronic fibers that are 10-15 times more compliant than the brain interfaces described above. These fibers permitted site-specific delivery of light and nutrients in the intestinal lumen of behaving mice. As their cladding (Fig. 3.5a), these fibers leveraged thermoplastic triblock elastomer poly(styrene-*b*-ethylene-*co*-butylene-*b*-styrene) (SEBS, T_g = 140 ºC, E = 3-5 MPa)[141] which is ~10^3 times softer than the PC cladding used in microelectronic brain fiber. A flexible conductive polyethylene (CPE) composite was employed for integration of metallic interconnects within the elastomer cladding, and a thin layer of PC was applied to maintain structural integrity at the drawing conditions. The preform was drawn (Fig. 3.5b) into ~50 m of continuous microscale fiber (535 µm × 315 µm) with a largely conserved cross-sectional geometry (Fig. 3.5 c-e), while simultaneously incorporating interconnect microwires through convergence drawing. The fully assembled gut fiber devices (Fig. 3.5f) were ~8.5 cm long and hosted six µLEDs at the distal end that could be operated as two independently addressable sets of blue and green µLEDs (3 each, Fig. 3.5f inset) and a microfluidic outlet situated ~0.8-1 mm posterior to the first µLED pair.

3.7 Characterization of gut fibers

In the gut fibers, the surface mounted µLEDs enable a laterally directed illumination profile which allows spatial targeting of epithelial cells and vagal afferents from within the lumen. This illumination profile is in contrast to an anatomically mismatched dorsal-ventrally oriented light

cone of a typical silica fiber (Supplementary Fig. B9a). The cumulative light output from the three axially distributed µLEDs remained stable in PBS over at least 4 weeks (Supplementary Fig. B9 b-c), while the optical output on the outer surface of the intestinal wall was only modestly attenuated by the presence of the intestinal tissue (Supplementary Fig. B9d). Using FEM, the optical penetration depth in the gut wall was found to be in the range 0.15-1 mm, and the illumination volume was estimated to be between 0.9-8.8 mm^3 for input intensities ranging from 20-100 mW/mm^2 (Supplementary Fig. B10 a-f). This is sufficient to broadly illuminate the subepithelial mucosa layer 50-100 µm beneath the mucosal membrane that receives dense vagal innervation[142]. The corresponding temperature change in the gut wall was found to be negligible for input optical intensities between 20-100 mW/mm^2, while the µLED separation (~1 cm) was sufficient to prevent any co-operative heat buildup (Supplementary Fig. B11 a-e).

As the gut continuously undergoes peristaltic distortion, we performed cyclic buckling tests to assess the mechanical integrity of the fibers at deformations of 1 mm and 5 mm for up to 10^4 cycles which had no impact on device performance (Fig. 3.5g). The fiber robustness was further supported by negligible changes in light output during 90º and 180º bending deformation at radii between 2-10 cm, which corresponds to strains exceeding those experienced by devices during surgical implantation process (Fig. 3.5h). We hypothesized that the mechanical compliance of the gut fiber would minimize the force exerted on the intestinal lumen, which is critical for chronic bio-integration in behaving animals. To mimic a surgically implanted gut fiber affixed to the abdominal wall at one end, their stiffness was evaluated in a single-cantilever bending mode. The gut fibers exhibited stiffness between 2-5 N/m across frequency ranges of heartbeat, respiration, locomotion, and peristalsis (Fig. 3.5i), which is significantly lower than the stiffness of identical fibers composed entirely of stiffer plastic such as PC (70-75 N/m) and similarly sized commercial silica fibers (400 µm diameter, 132 N/m). FEM of stress distribution profiles also qualitatively captured these experimentally observed stiffness trends (Fig. 3.5j). Unsurprisingly, during an intraluminal implantation in a mouse small intestine, the rigid silica fiber punctured the mucosal membrane, and thus was unsuitable for *in vivo* use, whereas the soft gut fiber readily negotiated the lumen curvature without damaging the epithelial tissue (Fig. 3.5k). Since the surgical procedure requires bending of the gut fiber at acute radii, we simulated strain distribution in the copper interconnects which have the lowest yield strain among the fiber constituents and confirmed the strain to be below the elastic limit of 0.3% for radii >0.5 cm (Fig. 3.5 l-m). Finally,

fluid infusion through the microfluidic channel of gut fiber at injection speeds relevant to intestinal nutrient delivery (1-5 µl/s)[16] yielded a high return rate in the range of 60-90% under both straight and bent conditions (Fig. 3.5n).

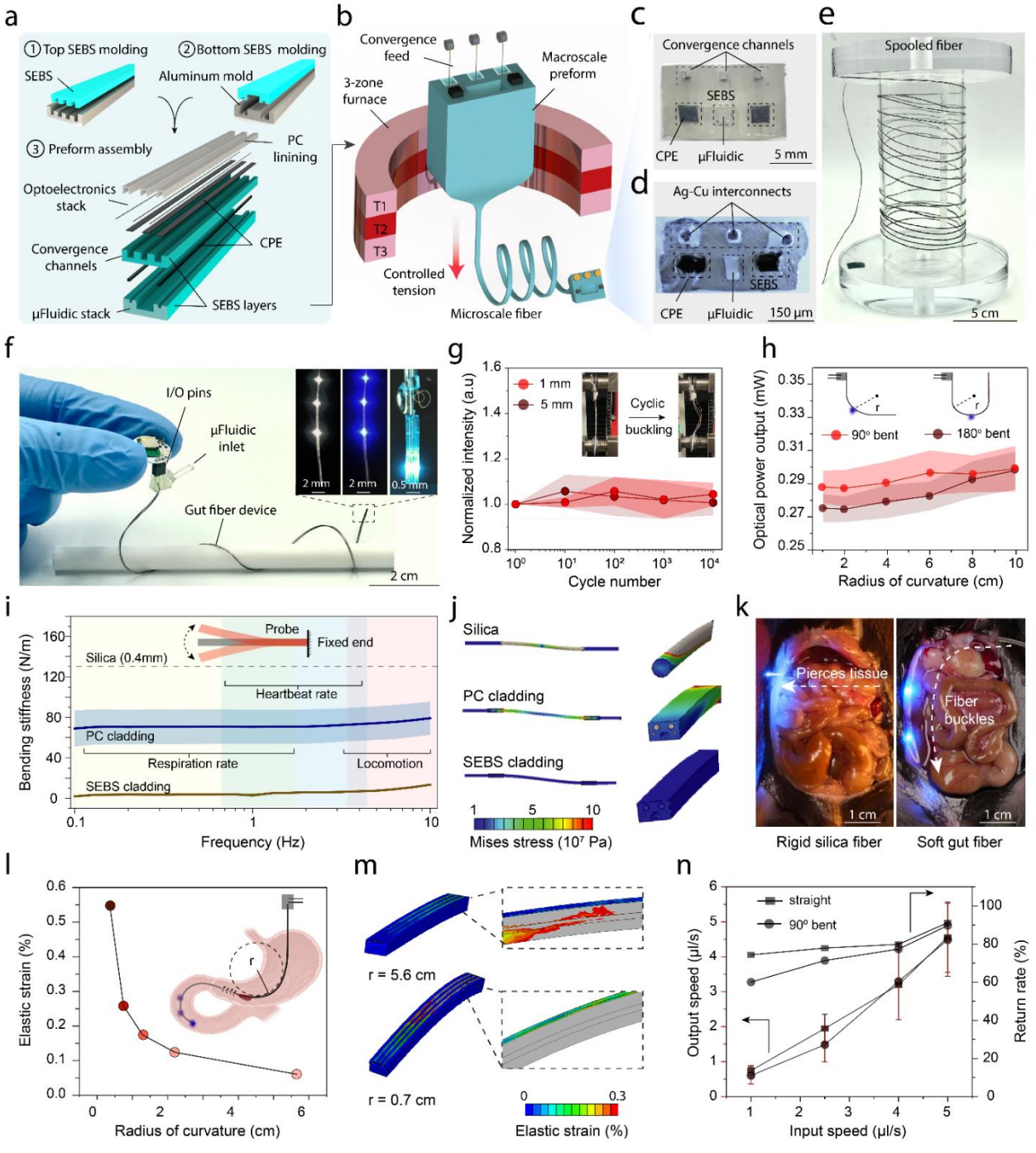

Figure 3.5. Fabrication and characterization of soft multifunctional GI fiber. (a) Layout of the multi-layered gut fiber preform, where triblock elastomer poly(styrene-*b*-ethylene-*co*-butylene-*b*-styrene) (SEBS) layers for convergence and microfluidics channels are molded from an inverse aluminum mold followed by preform assembly and thermal consolidation; CPE = conductive poly(ethylene); (b) The resultant preform was thermally drawn into several meters of soft gut fiber with simultaneous feeding of interconnect microwires (40μm Ag-Cu); (c) Digital image showing the cross-section of a fully assembled and consolidated preform; (d) Cross-sectional micrograph of the gut fiber highlighting conserved features; (e) Several meters of as-drawn fiber wrapped around a spooler demonstrating scalable fabrication; (f) Digital image of a fully assembled multifunctional gut fiber device highlighting the I/O pins and microfluidic access tubing. Inset shows three green (left) and blue μLEDs (middle) over the distal 2.5 cm of the fiber and dual optofluidic modality (right) where infusion of a PBS bolus is accompanied by operation of a blue μLED; (g) Cyclic buckling of the gut fiber over 10^4 cycles at 1mm (red trace) and 5mm (brown trace) displacements and corresponding normalized light output from an integrated μLED (n=3); (h) Light output from integrated μLEDs on the gut fiber subjected to deformations at varying radii of curvature at 90º (red race) and 180º angles (brown trace); (i) Bending stiffness of the fiber with SEBS cladding (red trace) and PC cladding (blue trace) with identical cross-sections in comparison to a 400 μm silica waveguide (dotted) in a single cantilever mode; (j) Mechanical FEM depicting stress distribution profiles in a rigid silica (top), stiff PC (middle), and soft SEBS (bottom) fiber mimicking a single cantilever mode; (k) Intraluminal implantation of a rigid silica fiber results in rupture and perforation of intestinal tissue (left) while soft gut fiber permits intestinal implantation that can negotiate the luminal curvature without tissue damage; (l) FEM simulated elastic strain in Ag-Cu interconnects at varying radii of curvature; (m) and corresponding spatial strain distribution profiles in a gut fiber bent at radii of curvature of 5.6 cm (top) and 0.7 cm (bottom); (n) Microfluidic return rate measurements through the gut fiber at injection speeds between 1-5 μl/s relevant to intraluminal nutrient infusion in a straight and bent geometry (n=3 fibers); All shaded areas and error bars represent s.d. *From Sahasrabudhe*, Rupprecht* et. al., Ref. 31.*

3.8 Wireless operation of microelectronic fibers

Incorporation of microelectronics in polymer fibers provides an opportunity for wireless bi-directional operation that can facilitate behavioral assays in untethered subjects. To realize this, we engineered a miniature (15.5 mm), lightweight (1.1 g) modular platform[134], NeuroStack, that enabled programmable wireless optical stimulation across two independent channels and data transfer for real time temperature recording (Fig. 3.6a). The circuit features a Bluetooth-low energy (BLE) communication protocol via a 2.4 GHz wireless link and an on-board miniature rechargeable battery for stable operation. This not only allows easy deployment in animal behavior studies with minimal user intervention, but also permits real time programming of up to 4 devices

across independent channels without any specialized equipment from a computer connected to a nRF52840 Development Kit that acts as a base station. The modular design of the circuit enables straightforward customization of experiments and allows integration of additional functions (Fig. 3.6b) within the same areal footprint which is limited in small rodents. Similarly, the detachable architecture of the module obviates the need for the animals to carry subdermal electronics that are prone to misalignment and malfunction (see Supplemental Note-B3 for additional discussion).

The primary module of NeuroStack carries a MDBT42V wireless microcontroller (with Nordic nRF52832 chip) and a rechargeable battery for orientation-independent power supply (Fig. 3.6a, Supplementary Fig. B12 a-d). During operation, the primary module relies on the microcontroller's general-purpose input output (GPIO) pins to drive current through the fiber μLEDs (Fig. 3.6c-f), while the header pins at the top support attachment of an intensity module (Fig. 3.6b). The intensity module can control the intensity of optical stimulation through a digital-to-analog converter (DAC) that is programmed from the serial interface and allows transient shaping of optical stimulation pulses, a feature that is important for minimizing coupled electromagnetic artifacts in electrophysiological recordings during optical stimulation. The temperature sensing circuit uses one of the in-fiber μLEDs as a temperature sensor, whereas the other channel is assigned for optical stimulation via the second μLED. A constant voltage below the turn-on voltage is applied to the sensor diode using a low-dropout regulator to measure current variations. The sensed current is then amplified using a single-stage inverting differential amplifier. The internal analog-to-digital converter of the microcontroller then digitizes the amplified analog signal and transmits it wirelessly to the computer. The default sampling rate for temperature recording is set to 200 Hz and the temperature sensing function can also be turned off through the system software to save power when not needed. In addition to the main components, the module also hosts a 32 kHz crystal oscillator and inductors for power management. The device is programmed/debugged with a 6-pin J-link interface and controlled remotely through an intuitive software platform (see methods section for software details). The NeuroStack power breakdown (Supplementary Fig. B12 e-f) scales with the μLED duty cycle and other functions including temperature sensing and intensity control. Figures 3.6 c-f show wireless operation of the independently addressable μLEDs within the brain and gut fibers connected to NeuroStack. The complete electrical layout of the Primary Module, together with temperature sensing and intensity control circuits appears in Fig. 3.6g. We characterized the capability of NeuroStack to control the frequency, duty cycle, pulse

shape, and intensity of optical stimulation in real-time from the user interface. The creation of the stimulation pulse consists of two phases controlled by software timers. One of the timers manages the change in state between pulsing and resting period, thereby controlling frequency of optical stimulation (Fig. 3.6h), while the other timer sets the duty cycle during the pulsing period (Fig. 3.6i). The same principle is used for the intensity control to set the maximum intensity and rise/fall times of the pulses (Fig. 3.6 j-k). Wireless temperature recording function was evaluated via steady-state measurements on a hot plate that showed linear dependence of the measured current on the surrounding temperature (Fig. 3.6l), while the dynamic response upon successive immersions in a temperature-controlled water bath matched closely to that of wired recordings from a commercial thermocouple (Fig. 3.6m).

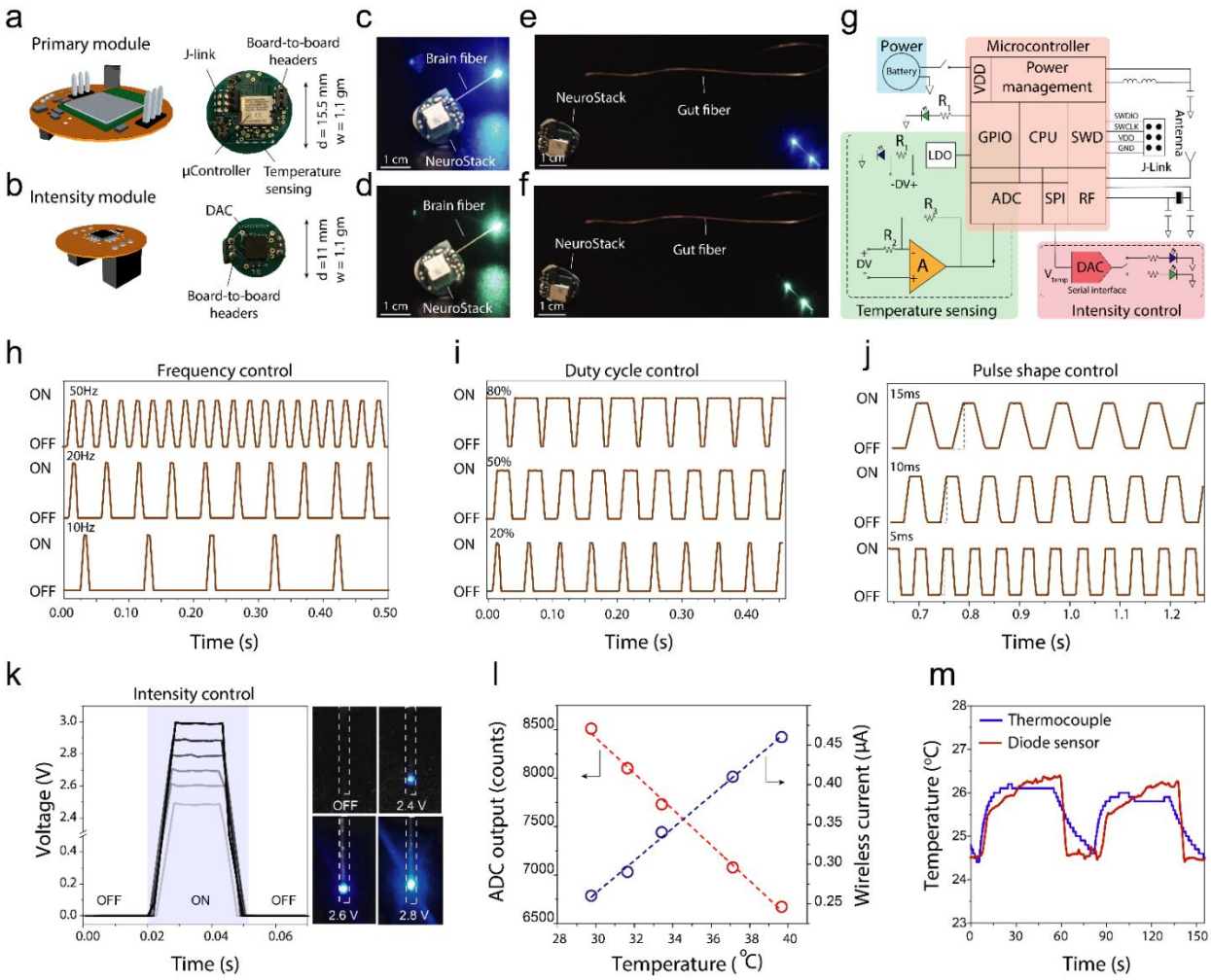

Figure 3.6. NeuroStack, a custom designed modular wireless circuit for microelectronic fibers, allows programmable light delivery and physiological recording. (a,b) Schematic illustration (left) and digital images (right) highlighting important circuit components of a primary module (a) and intensity module (b); (c-f) Images showing independent wireless control of blue and green µLEDs within a brain (c-d) and gut (e-f) fiber; (g) Circuit layout of NeuroStack highlighting power management block, temperature sensing block, and intensity control block; (h) Real time control of optical stimulation frequency between 10-50Hz; (i) Real time control of optical stimulation duty cycle between 20-80%; (j) Optical pulse shaping through control of pulse rise and fall times between 5-15 ms; (k) Intensity module permits real time control of µLED brightness with corresponding photographs at 2.4, 2.6, and 2.8 V bias voltage; (l) Calibration of the fiber thermal sensor using NeuroStack under steady-state conditions between 29-40 ºC; (m) Wireless recording of temperature transients with the thermal sensor in the microelectronics fiber, and its comparison to a commercial thermocouple in wired mode upon immersion in a water bath. *From Sahasrabudhe*, Rupprecht* et. al., Ref. 31.*

3.9 Multimodal interrogation of midbrain dopaminergic neurons

The combined optical, electrical, fluidic, and thermometry functions in the brain fibers enabled multiple experiments in mice for at least 2 months following implantation (Fig. 3.7a). As a validation study, we first targeted the dopaminergic (DA) neurons in the VTA, a key node of the reward and motivation pathways[143]. The fibers were stereotactically implanted in the VTA of DAT::Cre transgenic mice that express Cre-recombinase under the dopamine transporter (DAT) promoter. The integrated microfluidic channel within the fiber permitted delivery of an adeno-associated virus (AAV5) carrying ChR2 gene in a Cre-dependent construct (Ef1α::DIO-ChR2-mCherry) or a control construct (Ef1α::DIO-mCherry) to the VTA during a single-step surgery (Fig. 3.7b i-iii) [26] and robust expression of ChR2 was observed in the VTA sagittal sections (Fig. 3.7c). Emergence of electrophysiological potentials recorded through integrated microelectrodes in response to optical stimulation via fiber µLEDs revealed time course of Cre-dependent opsin expression in DA neurons (Fig. 3.7d, Supplementary Fig. B13). As it is known that recording electrodes may exhibit optical stimulation artifacts (e.g. Becquerel effect)[144], we confirmed the physiological origins of optically evoked signals and devised artifact mitigation strategy by transient pulse shaping (Supplementary Fig. B14 a-i, Fig. B15 a-h; Supplemental Note B4). Optically evoked multiunit neural activity was reliably recorded for at least 2 months in awake moving mice (Supplementary Fig. B16 a-o). We hypothesized that the flexible fibers could enable stable recording of spontaneous single neuron activity over extended periods due to their reduced

micromotion relative to brain tissue. After confirming the functional stability of implanted electrodes up to 6 months (Supplementary Fig. B17 a-b), we recorded the spontaneous single-unit activity from putative VTA neurons in chronically implanted mice for 4 weeks (Fig. 3.7e and Supplementary Fig. B18). Additional examples of single neuron electrophysiology at weeks 2 (n=3 mice) and 4 (n=3 mice) appear in Supplementary Fig. B19 a-i and Supplementary Fig. B20 a-i, respectively.

To confirm device safety, we wirelessly recorded intracranial temperature with the embedded thermal sensors in freely moving animals in an open field chamber and found no significant changes in tissue temperature during simultaneous wireless optical stimulation (Fig. 3.7f). The long-term biocompatibility of the fibers was assessed via immunohistochemical analysis (Supplementary Fig. B21 a-l) of markers characteristic of glial scarring (activated macrophage marker ionized calcium-binding adaptor molecule 1 (Iba1), astrocytic marker glial fibrillary acidic protein (GFAP)). As expected from FEM and experimentally measured lower bending stiffness, the immune response to microelectronic fibers was lower than that of silica fibers of comparable size (300 μm) across both inflammatory markers at week-2 [139].

We next evaluated the ability of the thermal sensors to detect physiologically evoked changes in intracranial temperature induced by an anesthetic drug mixture (Ketamine-Xylazine), which is known to trigger hypothermia by inhibiting thermoregulatory responses in a dose dependent manner[145]. In mice that were given intraperitoneal injections of Ketamine-Xylazine (9:1 ratio) at two concentrations (30 mg/kg and 60 mg/kg of Ketamine), the fibers reliably recorded a drop in the intracranial temperature (Fig. 3.7g, Supplementary Fig. B22 a-b). The temperature recovery to pre-anesthesia level was commensurate with the animals' gaining consciousness and ambulating in the home cage. The co-integration of thermal sensors and recording electrodes within same fiber may facilitate understanding of how changes in brain temperature alter neural dynamics under anesthesia[146].

To illustrate the wireless programmable photostimulation capability during behavioral studies, mice expressing ChR2 in the DA neurons in the VTA were subjected to a real-time place preference (RTPP) task (Fig. 3.7h) [143]. The use of BLE communication protocol allowed programming of optical parameters without any line-of-sight or angular orientation handicap. To illustrate this, we performed RTPP tasks at three different stimulation conditions that were updated in real-time: (1) Stimulation ON (λ = 470 nm, 25 Hz, 10 ms pulse, 1s ON, 2s OFF) v/s OFF; (2)

Phasic bursting (λ = 470 nm, 40 Hz, 5 ms pulse, 0.5 s ON, 4 s OFF) v/s Tonic stimulation (λ = 470 nm, 5 Hz, 5 ms pulse); (3) Blue light (λ = 470 nm, 25 Hz, 10 ms pulse, 1 s ON, 2 s OFF) v/s Green light stimulation (λ = 527 nm, 25 Hz, 10 ms pulse, 1 s ON, 2 s OFF). The mice expressing ChR2 in DA neurons in the VTA exhibited a significant preference (Fig. 3.7 i,k,m Supplementary Fig. B23 a-f) for the chamber paired with stimulation condition as compared to their baseline values (pre-test day) which was not observed in the control mice expressing mCherry alone. Fig. 3.7 j,l,n show the representative heatmaps of the animal positions in the RTPP arena in each experimental condition. Furthermore, we did not observe any significant differences in the average velocity and distance travelled by device-carrying mice as compared to naïve counterparts, and no significant changes in locomotor activity were observed in response to photostimulation of the VTA ChR2-expressing DA neurons (Supplementary Fig. B24 a-e). The µLEDs embedded in the fiber also remained functional for at least 9-months following implantation (Supplementary Fig. B24f).

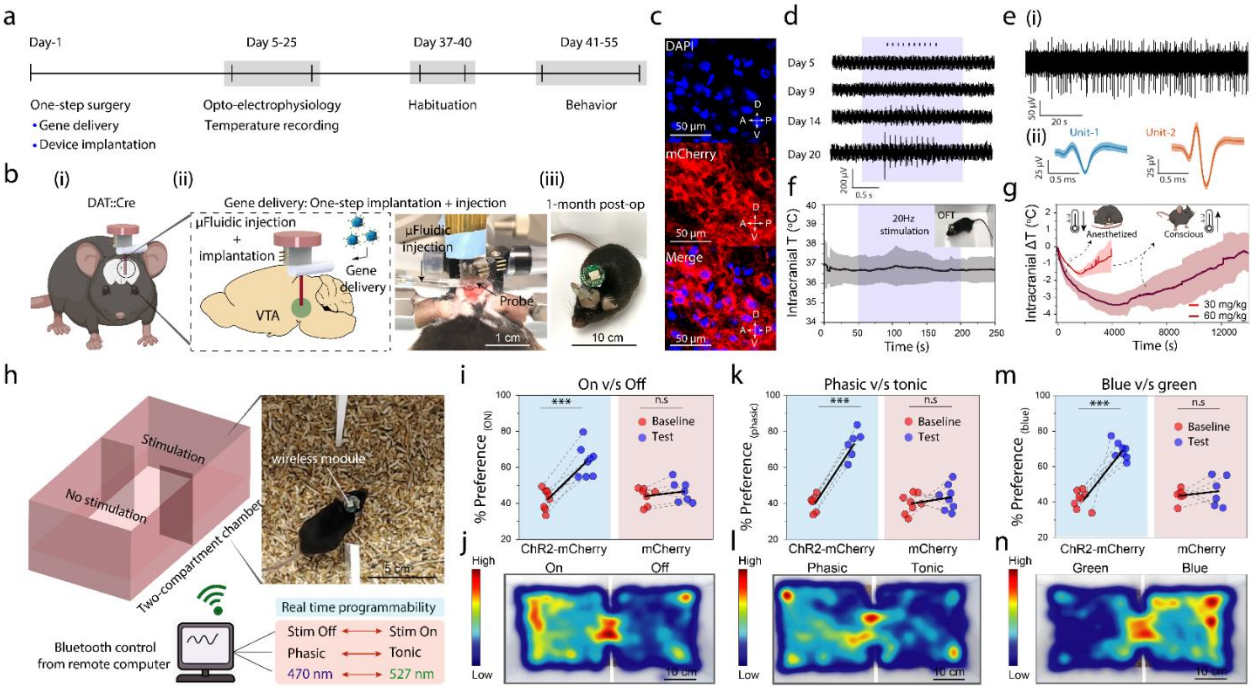

Figure 3.7. Microelectronic brain fibers enable multimodal interrogation of deep-brain neural circuits and wireless programmable optogenetics during behavior. (a) Experimental timeline for *in-vivo* validation of various fiber functionalities; (b) An illustration of gene delivery through the integrated microfluidic channel and fiber implantation in the same surgical procedure (i); A photograph of one-step surgery where arrows highlight the fluid injection setup connected to the microfluidic channel and the implanted fiber probe (ii); Fully recovered animal ~1 month post-

surgery connected to a wireless module (iii); (c) Expression of Cre-dependent ChR2-mCherry construct 4 weeks following microfluidic AAV5 delivery into the VTA of DAT::Cre mice; (top) Blue – DAPI; (middle) red - mCherry; (bottom) merge; (d) Electrophysiological recording of optically evoked neural activity in the VTA after 5, 9, 14 and 20 days following AAV5 delivery of Cre-dependent ChR2-mCherry construct where optical pulses (λ = 470 nm, 10 Hz, 5 ms pulse width) were delivered through the fiber μLEDs; (e) Spontaneous neural activity recorded from VTA neurons at week-4 post implantation (i); corresponding average action potential (spike) waveforms of two isolated neurons (units) from the recording in (j) (ii); (f) Wireless intracranial temperature recorded in mice (n=6) exploring an open field chamber during simultaneous wireless photostimulation (shaded region, 20 Hz, 10 ms pulse width, 1 s ON, 2 s OFF); (g) Integrated thermal sensors within fibers detect brain hypothermia in the VTA induced by intraperitoneal injection of an anesthetic drug mixture of Ketamine/Xylazine at 30 mg/kg (red) and 60mg/kg (brown) doses; (h) Schematic depiction of a place preference assay for validation of the real time programmable optical stimulation along with a representative image of a mouse undergoing the assay; (i,k,m) Percent (%) preference to the chamber coupled to the rewarding optical stimulation at baseline and on test-day for mice transduced with ChR2-mCherry or mCherry in the DA neurons in the VTA at three different wireless photostimulation conditions (top); (i) Stimulation ON (470 nm, 25 Hz, 10 ms pulse, 1 s ON, 2s OFF) vs OFF (No stimulation). ChR2-mCherry: $P = 4.16\times10^{-5}$, $t = -9.03$, $d.f = 7$; mCherry: $P = 0.183$, $t = -1.50$, $d.f = 6$; (k) Phasic (470 nm, 40 Hz, 5 ms pulse, 0.5s ON, 4 s OFF) v/s tonic stimulation (5 Hz, 5 ms pulse, continuous). ChR2-mCherry: $P = 2.02\times10^{-4}$, $t = -9.65$, $d.f = 5$; mCherry: $P = 0.403$, $t = -0.88$, $d.f = 7$; (m) Blue-light (470 nm, 25 Hz, 10 ms pulse, 1s ON, 2s OFF) v/s green light stimulation (λ = 527nm, 25 Hz, 10 ms pulse, 1s ON, 2 s OFF). ChR2-mCherry: $P = 3.58\times10^{-5}$, $t = -9.24$, $d.f = 7$; mCherry: $P = 0.55$; $t = -0.64$, $d.f = 5$; (j,l,n) Representative heat-maps tracing the animal position corresponding to the assays summarized in panels (i,k,m), respectively. All shaded areas and error bars represent s.d. (**$P < 0.01$, ***$P < 0.001$; n.s. $P > 0.05$, paired samples *t*-test). *From Sahasrabudhe*, Rupprecht* et. al., Ref. 31.*

3.10 Multimodal interrogation of gut-brain communication

Optogenetics and pharmacology have revolutionized studies of brain circuits. However, the extension of these methodologies to neural circuits in the gut has remained challenging. We hypothesized that our soft multifunctional, microelectronic gut fibers capable of targeted light and chemical delivery along the GI tract can address this challenge.

The sensory cell of the gut epithelium is the enteroendocrine cell, also known as the neuropod cell[147,148]. Although enteroendocrine cells have been historically studied in the context of hormone release in response to nutrient stimuli, it was recently shown that these cells synapse with the vagus nerve and transduce signals to the brain within milliseconds[16,147,149]. To acknowledge their

neurotransmission function, we refer to these cells as neuropod cells. In spite of the importance of these cells in providing critical inputs for driving behavior directly from the gut, there are only few studies subjecting them to targeted optogenetic and pharmacological manipulations to unravel their role in feeding behavior[16,150]. We first used these epithelial sensory cells as a testbed to evaluate the dual optofluidic modality of fibers using cervical vagus nerve electrophysiology as a readout (Fig. 3.8a, Supplementary Fig. B25a). In wild-type mice, we found that intestinal infusion of sucrose solution (300 mM, 0.2 ml, 3.3 µl/s) via the microfluidic channels of the implanted fibers resulted in a significant increase in the vagal firing rate as compared to baseline activity (Fig. 3.8 b-c). This effect of chemical stimulation was recapitulated in transgenic mice expressing ChR2 in cholecystokinin (Cck) cells (Cck::ChR2), where optogenetic excitation via the blue µLEDs (40 Hz, 10 ms pulse width) within gut fibers resulted in an increased vagal firing rate. Vagal responses remained unchanged in Cck::ChR2 mice upon illumination with the green µLEDs integrated within the same devices as well as in control littermates that lacked ChR2 in Cck cells (Fig. 3.8 d-e, Supplementary Fig. B25b). Since the gut is also innervated by nociceptive vagal afferents that harbor temperature-sensitive ion channels (e.g. transient receptor potential vanilloid family member 1)[151], it raises the concern that tissue heating during µLED operation in the gut lumen may lead to off-target activation of nociceptive terminals, thereby compromising the cell-type specificity afforded by intraluminal gut optogenetics. To address this concern, we performed wireless *in-vivo* temperature recordings during optical stimulation epoch in awake, chronically implanted mice and found no significant changes in local temperature as predicted by our FEM studies (Supplementary Fig. B25c).

Neuropod cells are present along the entire alimentary tract, where they release hormones and neurotransmitters to regulate food intake[148,152]. To evaluate the impact of neuropod cells on feeding behavior, we implanted the soft gut fibers in two distinct GI regions: the duodenum and the ileum. Since the proper function of the intestinal lumen is critical for survival, we first evaluated whether chronic implantation of the multifunctional fibers in the gut affected animals' food and water intake as well as locomotor activity. We found no significant changes in these measures before and after fiber implantation (Supplementary Fig. B26a-c), thereby confirming that the implanted fibers do not obstruct the passage of ingested food or fluids and do not interfere with physiological activity. The biocompatibility of chronically implanted gut fibers was also evaluated through histological analysis of the gut tissue, which did not show significant changes in the anatomical

characteristics of the epithelial layer (Supplementary Fig. B27 a-d). This indicates that, commensurate with their soft mechanics, the chronically implanted gut fibers do not compromise the integrity of the fragile epithelial barrier.

It is well known that exogenous administration of the satiety hormone cholecystokinin (CCK) produces robust anorexia in rodents and humans[153,154]. CCK is also released from the neuropod cells in the small intestine in response to nutrients entering the gut[155]. Thus, we hypothesized that optogenetic stimulation of duodenal Cck-expressing neuropod cells will produce an enduring anorectic effect that can be measured by alterations in food intake. To test this hypothesis, the soft gut fibers were implanted in the duodenum of Cck::ChR2 mice (Fig. 3.8 f-g). The multiple independently controlled stimulation channels on the gut fiber allowed a within-subject experimental design for these studies (Methods section). After an overnight fast, stimulation of duodenal Cck cells (Supplementary Fig. B28 a-b) with blue µLEDs (20 Hz, 10 ms pulse width, 0.5 s ON, 1 s OFF) significantly suppressed chow intake for three hours, compared to control green light stimulation (Fig. 3.8h). Blue light stimulation had no impact on food intake in mice lacking ChR2 expression compared to within-subject green illumination control (Fig. 3.8i).

In the ileum, the presence of fat and carbohydrates induces the ileal brake which is a neuro-hormonally mediated feedback loop that regulates GI emptying rates by decreasing food intake[156]. Prior studies employing nutrient infusion into the ileum or exogenous administration of neuropeptides indicated that Peptide YY (PYY) and glucagon-like-peptide 1 (GLP-1) mediate the effects of the ileal brake[157,158]. However, these findings were correlational as limited approaches were available to establish a causal link between specific cell types in the ileum to the physiological feedback loop[159,160]. We reasoned that direct optogenetic activation of Pyy+ cells in the ileum, which release PYY and GLP-1, through a chronically implanted gut fiber may further implicate these cells as mediators of the ileal brake. To ensure a stable optical power output from gut fibers during hour-long ileal feeding assays, the wireless circuit was modified to include a low drop-out voltage regulator which supports higher voltage, and higher capacity, light-weight rechargeable batteries (Supplementary Fig. B29 a-d). The soft gut fibers were implanted in the ileum of Pyy::ChR2 mice that were allowed to recover for 1-week post-surgery and fasted for 18 h prior to the experiment (Fig. 3.8 j-k, within-subject experimental design). Wireless stimulation of ileal Pyy neuropod cells (Supplementary Fig. B30 a-b) with blue µLEDs (20 Hz, 10 ms pulse width, 0.5 s ON, 1 s OFF) caused a significant suppression of consumption of the high fat and carbohydrate

solution (Fig. 3.8 l-m) compared to control green light, while blue light stimulation in mice lacking ChR2 in Pyy ileal cells had no impact on intake compared to within-subject controls (Fig. 3.8 n-o). We note that baseline intake is lower in mice lacking ChR2 (see Methods), but there was no effect of blue light on total intake in the within-subject designs. Together, the control of vagal activity as well as the feeding behavior upon intraluminal optofluidic stimulation in the proximal and distal small intestine highlight the efficacy of multifunctional gut fibers in modulating the sparsely distributed intestinal cells (~1% of epithelial cells)[152,161].

Food intake is regulated by bidirectional and coordinated gut-brain signaling[162]. While the effects of gut derived signals on satiety are extensively studied, their influence on neural populations driving food intake are not fully understood[163]. We reasoned that recording single-unit neural activity through the brain fibers during intestinal microfluidic delivery of nutrients via the gut fibers may open future possibilities in probing how nutrient detection in the gut is encoded in the brain. For instance, it was previously shown that feeding-induced DA release in the ventral striatum can be driven by post-ingestive feedback in a nutrient specific manner, independent of oro-sensory cues[106,107]. Since the ventral striatum receives dense innervation from the VTA DA neurons, we hypothesized that intra-intestinal delivery of sucrose can positively modulate firing rate of DA neurons in the VTA. To test this hypothesis, wild-type mice were implanted with brain fibers in the VTA and electrophysiological recordings were performed 1 week following surgery (Fig. 3.8p). The identity of putative DA neurons was corroborated by their sensitivity to the DA D2 autoreceptor agonist quinpirole (200 μg/kg, i.p.) (Fig. 3.8q, Supplementary Fig. B31a). After overnight fasting (18h), animals were implanted with a gut fiber in the proximal small intestine and received intra-intestinal microfluidic delivery of either sucrose solution (600 mM, 0.5 ml over 10 min) or saline (0.5 ml over 10 min) while concomitantly recording spiking activity in the VTA. Intestinal sucrose delivery produced a significant increase in the firing rate of DA neurons compared to the pre-infusion period, whereas no change in firing rate was observed following saline infusion (Fig. 3.8r, Supplementary Fig. B31 b-e). Since multi-organ implantation of wireless devices can be particularly appealing for functional studies of interoceptive neural circuits, we further established the efficacy of survival surgeries with multisite and multifunctional microelectronic fibers (Supplementary Fig. B32 a-h) through assays of feeding and locomotion (Supplemental Note B5 and Supplementary Fig. B33 a-h). These experiments highlight the utility

of wireless fiber neurotechnology for probing dynamics of circuits spanning multiple organs such as the gut and the brain in awake behaving mice.

Beyond satiety and food intake, gut signals reaching the brain also modulate motivation and reward. Optogenetic stimulation of upper-gut projecting vagal afferents at the level of the brainstem was shown to drive DA-dependent reward behaviors[164]. Motivated by these findings, we applied the gut fibers to test whether the central nervous system functions could be directly controlled from the intestine in behaving mice (Fig. 3.8s). Using Cre-loxP recombination we bred Phox2b::ChR2 mice, in which ChR2 fused to a fluorescent protein tdTomato was expressed under the Phox2b promoter broadly found in the viscerosensory nodose neurons (Supplementary Fig. B34a)[165]. Subsequently, the Phox2b::ChR2 mice chronically implanted with gut fibers in the duodenum (Supplementary Fig. S34 b-c) were subjected to an RTPP behavioral task during which intraluminal vagal stimulation with blue μLEDs (20 Hz, 10 ms pulse width, 0.5 s ON, 1 s OFF) caused a significant preference to the light-paired chamber, compared to their pre-test values (Fig. 3.8 t,u). No significant differences in preference for either chamber was observed in control mice lacking ChR2 expression that received identical optical stimulation (Fig. 3.8 v,w). Similarly, intraluminal stimulation in Phox2b::ChR2 mice with control green μLEDs (20 Hz, 10 ms pulse width, 0.5 s ON, 1 s OFF) also did not elicit significant preference for the light paired chamber as compared to their pre-test exploration (Supplementary Fig. B34 d-e). These findings illustrate the potential of wireless multifunctional microelectronic fibers to empower studies aimed at unraveling contributions of gut-brain signaling underlying complex motivated behaviors.

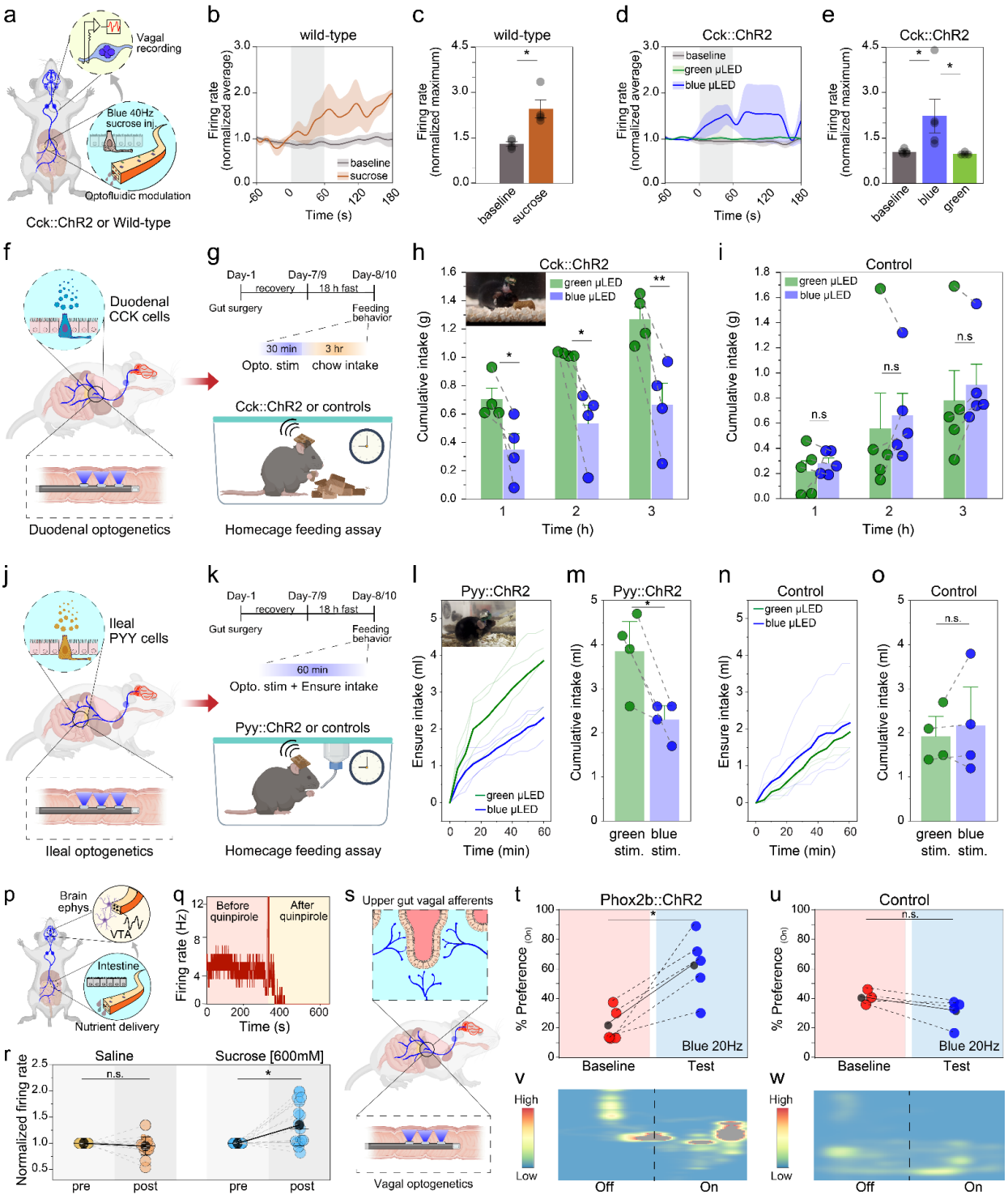

Figure 3.8. Soft gut fibers enable multimodal interrogation of intestinal neural circuits. (a) An illustration of vagal electrophysiology during optofluidic modulation of epithelial neuropod cells in the duodenum with a implanted gut fiber; (b) Chemical stimulation of Cck+ cells with microfluidic delivery of sucrose solution (300 mM, 0.2ml, 3.3 µl/s) increases mean vagal firing rate. Gray bar indicates stimulation epoch; (c) Quantification of peak vagal responses (n=4 mice

per group; *P < 0.0304 by Kruskal-Wallis test with non-parametric comparisons using Wilcoxon Method); (d) Optogenetic stimulation of Cck+ cells with implanted gut microelectronic fiber (λ = 470 nm, 40 Hz, 10 ms pulse width) increases vagal firing rate while stimulation with control green µLEDs (λ = 527 nm, 40 Hz, 10 ms pulse width) has no effect. Gray bar indicates stimulation epoch; (e) Quantification of peak vagal responses (n = 3-5 mice per group; *P < 0.0367 by Kruskal-Wallis test with non-parametric comparisons using Wilcoxon Method, baseline v/s blue µLED; P = 0.0367, baseline v/s green µLED; P = 0.1113, blue µLED v/s green µLED; P= 0.0200); (f) Schematic illustration depicting optogenetic control of duodenal Cck+ cells with implanted gut fiber in the duodenum in behaving mice; (g) Experimental timeline for evaluating feeding behavior in chronically implanted mice in a homecage feeding assay with ad-libitum access to standard chow during wireless intraluminal gut optogenetics; (h) Total chow intake measured over 3 hours for Cck::ChR2 mice that received wireless optical stimulation (20 Hz, 10 ms pulse, 0.5 s ON, 1s OFF) with a blue wavelength or control green wavelength (within-subject design, n=4 mice, significant effect of time [p = 0.0003], significant effect of stimulation [p < 0.0001], and significant time*stimulation interaction [p=0.0086], posthoc paired t-test between stimulation at each time point:1h – p = 0.0161, 2h – p = 0.0376, 3h – p = 0.0044). Inset shows digital photo of an implanted animal connected to wireless module consuming chow diet in home cage; (i) Total chow intake measured over 3 hours for control mice lacking ChR2 that received wireless optical stimulation (20 Hz, 10 ms pulse, 30 min) with a blue wavelength or control green wavelength (within-subject design, n=4 mice, significant effect of time [p = 0.0020], but no significant effect of stimulation [p = 0.4975] or time*stimulation interaction [0.8906]; (j) Schematic illustration depicting optogenetic control of ileal Pyy+ cells with implanted gut fiber in the ileum in behaving mice; (k) Experimental timeline for evaluating feeding behavior in chronically implanted mice in a homecage feeding assay with ad-libitum access to Ensure solution (high fat and carbohydrate solution) during wireless intraluminal gut optogenetics; (l) Ensure consumption monitored for 60 min at 5 min intervals for Pyy::ChR2 mice during concomitant wireless optical stimulation (20 Hz, 10 ms pulse, 0.5 s ON, 1 s OFF) with either blue wavelength or control green wavelength (within-subject design, n=4 mice, significant effect of time (p < 0.0001), stimulation (p < 0.0001), and time*stimulation interaction (p < 0.0001); (m) Cumulative ensure intake at the end of 60 min period for Pyy::ChR2 mice (within-subject design, n=4 mice, paired t-test, p = 0.0381); (n) Ensure consumption monitored for 60 min at 5 min intervals for control mice lacking ChR2 during concomitant wireless optical stimulation (20 Hz, 10 ms pulse, 0.5 s ON, 1 s OFF) with either blue wavelength or control green wavelength (within-subject design, n=4 mice, significant effect of time [p < 0.0001], significant effect of stimulation [p = 0.0160], but no significant time*stimulation interaction [p = 0.5796]); (o) Cumulative ensure intake at the end of 60 min period for control mice lacking ChR2 (within-subject design, n=4 mice, posthoc paired t-test, p = 0.4639); (p) Schematic illustration of *in vivo* brain electrophysiology of VTA DA neurons while stimulating the gut with nutrient infusion through microfluidic channel of a implanted gut fiber in the context of post-ingestive sucrose sensing; (q) Firing rate of a putative DA neuron is sensitive to quinpirole administration; (r) Intraluminal sucrose infusion positively modulates the firing rate of putative

DA neurons (Sucrose: P = 0.00242; t = -3.23743; $d.f.$ = 17, paired t-test) compared to saline controls (Saline: P = 0.49994; t = -0.68771; $d.f$ = 19, paired t-test); (s) Schematic illustration of optogenetic stimulation of vagal afferents in the proximal small intestine of Phox2b::ChR2 transgenic mice enabled by gut microelectronics fibers; (t,u) Percent (%) preference to the chamber coupled to rewarding optical stimulation in the intestine at baseline and on test day for Phox2b::ChR2 (t), and control mice lacking ChR2 (u) (λ = 470 nm 20 Hz, 10 ms pulse, 0.5 s stimulation, 1 s rest). Phox2b::ChR2: P = 0.014, t = 4.19, $d.f$ = 4. Control mice: P = 0.110, t = –2.25, $d.f$ = 3; (v,w) Representative heat-maps of animal position corresponding to the assays summarized in (t,u). All shaded areas and error bars represent s.d. *From Sahasrabudhe*, Rupprecht* et. al., Ref. 31.*

3.11 Discussion

The multifunctional and wirelessly capable microelectronic fibers enabled stable bioelectronic interfaces with the brain and GI tract in untethered behaving mice. We leveraged the scalability of fiber drawing to produce tens of meters of microscale polymer filaments that can integrate solid-state devices along their surfaces. Coupled with deterministic tunability of fiber mechanics, this approach offers unprecedented design flexibility which is demonstrated by producing stiff yet flexible multifunctional fibers to interface with the brain, and soft compliant fibers to interface with the gut. In doing so we also overcame outstanding challenges associated with fiber drawing. Thermally drawn fiber-based neural interfaces were limited to tip-localized functionality, used passive features, and were incompatible with untethered operation[25,26]. Embedded microelectronics within fiber-based neural probes break their axial redundancy and unlock new stimulation and sensing modes empowered by solid-state devices. By coupling these fibers with NeuroStack modules, we demonstrate their wirelessly programmed control in real time. Although, unlike a number of elegant fully implantable wireless platforms, the NeuroStack is mounted externally, it enables straightforward deployment using Bluetooth protocol without specialized antennas. It additionally invites mixing and matching of sensing and modulation capabilities by stacking light-weight customized backend circuits. Thus, the complete platform overcomes several limitations of current wireless bioelectronics technologies by delivering lithography-free scalable fabrication, multifunctionality in a single step process, stable wireless control without line-of-sight handicap or angular dependency, and intuitive operation commensurate with complex behavioral paradigms (Supplemental Note 6 and Supplementary Table S1). Future extensions of multifunctional microelectronic fibers and NeuroStack module will leverage continued progress

in low-power application specific integrated circuits, miniature batteries, and wireless communication protocols to enable closed-loop, fully implantable operation and on-the-fly recharging.

We apply our platform to sense and modulate neural activity in the brain and the gut of freely behaving animals. The brain fibers enable gene delivery, dynamic and chronic opto-electrophysiological monitoring of opsin expression in specific neurons, single neuron recording, sensing of anesthesia-induced brain hypothermia, and wireless programmable optical control of reward behavior. The soft gut fibers permit light and nutrient delivery to targeted sites spanning several centimeters in the mouse intestine enabling modulation of sensory enteroendocrine cells and vagal afferents – capabilities that remained out of reach with prior elegant tools that demonstrated optical modulation in small areas of the stomach fundus or outer colonic wall[16,129,166]. The ability of microelectronic fibers to deliver or sense multiple stimuli in the brain and the gut, and to interface with both organs simultaneously sets the stage for their applications in studies of gut-to-brain signaling. Future innovations in materials and fiber architectures mimicking tissue level mechanics may extend the application scope of microelectronic fibers to peripheral organs beyond the gut.

We anticipate that with the ever-increasing repertoire of transgenic animals, multifunctional wireless fiber-based tools will provide key insights into the roles of specific cells in bidirectional communication between the peripheral organs and the brain. These tools will empower the study of the enigmatic interoceptive networks in health and disease.

3.12 Experimental methods

Multifunctional brain fiber draw. The multifunctional brain fibers were produced by thermal drawing from a macroscopic preform which was produced through CNC machining of PC slabs (McMaster, 8574K43). The layer for convergence channels was obtained by milling three square channels of 1.6 mm × 1.6 mm with a pitch of 4 mm in a 14.8 mm × 3 mm × 30 cm slab. A top cover with dimensions of 14.8 mm × 0.8 mm fully defined the convergence channels. The subsequent layer had a central channel (3.2 mm × 2 mm × 30 cm) that defined the microfluidic functionality and was flanked by two additional channels (1 mm × 1 mm × 30 cm) on either side for recording electrodes. The tri-layered preform was thermally consolidated at 185 ºC for 1 hr and drawn into a functional fiber at a size reduction ratio of ~40-50 while simultaneously feeding

spools of Ag-Cu and tungsten microwires which serve as interconnects and recording electrodes, respectively.

Multifunctional gut fiber draw. The preform assembly for soft, multifunctional gut fibers began with molding SEBS pellets (Kraton, G1657) into desired geometrical patterns in a CNC machined inverse aluminum mold at 200 ºC for 12 hr under vaccum. The top layer defined the convergence channels (3.6 mm × 3.6 mm × 30 cm) with a pitch size of 4 mm for hosting interconnect microwires. The precursor to the microfluidic channel (2.8 mm × 2 mm × 30 cm) and soft conducting electrodes (2 mm × 2 mm × 30 cm) were incorporated in the bottom layer. The SEBS convergence channels were lined with a U-shaped PC layer that had a wall thickness of 1 mm and channel size of 1.6 mm × 1.6 mm. Finally, two slabs of carbon-loaded polyethylene (2 mm × 2 mm × 30 cm) were inserted in the bottom layer. The multilayered preform was consolidated at 130 ºC for 45 min and subsequently drawn into microscale fibers at a size reduction ratio of ~40-45 on a custom-built draw tower (LabView, version 18.0), while simultaneously feeding three spools of 40 μm Ag-Cu microwires that serve as interconnects.

Fiber device fabrication and characterization. Fabrication of implantable brain fiber device began with dissolving away the PC layer on distal ~1 cm length of the as drawn fiber in dichloromethane for 2-3 min which exposed the interconnect and electrode microwires. The microwires were subsequently soldered onto male header pins that were assembled inside a custom 3-D printed casing (5 mm × 7 mm × 0.5 mm) and secured using UV curable epoxy (NOA 61, Norland Products). ~0.5 cm of the Ag-Cu interconnect was exposed by low-end machining with a razor blade at the distal end of the fiber under an optical microscope, followed by mounting of blue and green μLEDs chips (Cree, TR2227 or SR2130) using reflow soldering (Chip Quik, TS391LT10) or thermally curable silver paste (Epo-Tek H20E). An insulated stainless-steel ground wire connected to the header pin was soldered onto a ground screw. Connection to microfluidic channel was established through a T-junction using a PVA access tubing. For this purpose, the microfluidic channel on the fiber was first exposed with a razor blade and subsequently the fiber was threaded into the access tubing through a metallic needle. The T-junction was made water-tight by flowing UV-epoxy at the tubing-polymer junction. The patency of microfluidic channel was confirmed by flowing a bolus of DI water. Finally, a 12-14 μm layer of vapor deposited parylene-C (SCS Labcoter2, Parylene deposition system) defined the bio-fluid barrier layer. The final device

assembled in this way had an overall length of ~6-6.5 mm for targeting the VTA. The fabrication of soft-gut fiber involved identical steps of exposing interconnects, soldering to I/O pins, mounting of μLEDs on the fiber, and connecting the microfluidic channel through a T-junction. The final gut fiber had an overall length of ~8.5 cm that hosted three green and three blue μLEDs on the distal 2 cm length of the fiber at a separation of ~1 cm each. The device was encapsulated in a ~4-6 μm thin layer of parylene-C, followed by encapsulation in a ~100 μm layer of medical grade silicone (MED-6215, Avantor Inc.) by inserting the fiber in a PTFE sacrificial mold. The silicone mixture was filled and thermally cured in the mold along with the fiber at 90-100 ^{o}C for 3 h and subsequently the tubing was cut open to yield the final coated devices for implantation. Details about fiber device characterization and finite element modelling studies appears in Supplementary methods.

NeuroStack hardware. The NeuroStack module is composed of a custom printed circuit board (PCB) that carries a MDBT42V wireless microcontroller (with Nordic nRF52832 chip and on-chip PCB antenna) for BLE communication with the central system (nRF52840 DK development kit) that is connected to a base station computer. A male header pin near the edge of the circular board allows the device to connect and disconnect from the implanted probe. Two vertical header pins on the base of the board allow for the attachment and removal of the optional modules. For this study, optional modules offer precise control of optical intensity. To prepare the individual devices and optional modules, components were mounted onto the custom PCBs using reflow soldering and software was loaded using J-Link programmers with an Arduino library. The μLEDs integrated with the fibers were driven by either a constant 3.3 V source or a programmable DAC (MAX5510), with a suitable current limiting series resistor in place to keep the brightness within the desired level. Validation of the device waveforms was done using an oscilloscope to compare measured frequencies and shapes to those specified in the interface. The current consumption patterns were characterized using a Keithley 100B source meter. A further test of battery life was conducted by leaving the system running with the desired stimulation parameters until the output voltage decreased below the optogenetic stimulation threshold. With a 11 mAh capacity rechargeable Lithium battery (MS920SE-FL27E, Seiko Instruments, 9.5 mm diameter coin cell, 3 mm thick, 0.47 gm), the brain devices can be operated for up to 1 hr on a single charge, while the first version of the gut devices can be operated for up to 30 min which is sufficient for most neuroscience behavioral studies. The modified wireless circuit developed in Fig. S28 for

performing longer term feeding studies with gut optogenetics provides up to 2 hr of continuous operation on a single charge (45 mAh capacity rechargeable battery, 4 x 12 x 15 mm, 1.1 gm, GM041215 PowerStream Inc.). The continuous operational duration of both brain and gut devices can be easily extended to several hours by adopting light weight, high-capacity batteries (eg. 62 mAh capacity, 3 x 10 x 30 mm, ~1.2 gm, GM 01030 PowerStream Inc). For testing the temperature recording function, the probe was placed on a hotplate with a commercial thermocouple and was left to settle for 30 seconds between each temperature reading. Recordings of the amplifier output voltage and the temperature from the commercial sensor were compared to allow for calibration. For wireless temperature recording, the transmitted data was collected using a 12-bit ADC of the NRF52 chip and sent over BLE to a central collection point. To improve the bandwidth and reduce packet overhead, the data was batched at the cost of latency in the recordings. The data received was transferred over a serial interface to the MATLAB (R2019b) program or saved for later analysis.

NeuroStack user interface. The control software supports the modularity that the hardware presents, provides flexibility to the user in terms of the system preferences, as well as plots and saves the recorded data on the computer. It allows enabling/disabling functionalities as desired and sends real time stimulation updates to the neuromodulation platform. The system relies on two pieces of software for communication and control of the neuromodulation platform. First is the firmware that is loaded on the neuromodulation board to send the stimulation updates, enable desired functionalities, and send data back to the computer if enabled. The peripheral portion of the code was developed in Arduino IDE. The system code was then loaded on the neuromodulation device using Adalink Tool Kit. The central portion of the code was developed using Nordic Software Development Kit and Segger Embedded Studio Software. This portion of the code is responsible for communicating and controlling the peripheral board. The second piece of code essential to the system operation is the graphical user interface (GUI), developed in MATLAB (R2019b) that allows the user to select functionalities and send updates to the neuromodulation device in real time.

Experiments involving animal subjects. All animal procedures were approved by the MIT Committee on Animal Care and Duke University Institutional Animal Care and Use Committee and carried out in accordance with the National Institutes of Health Guide for the Care and Use of

Laboratory Animals. Approximately equal number of male and female mice were used. Mice were group housed before surgery and single housed after surgery in cages maintained at 22 ºC, 12 h light/dark cycle, and 50% humidity with ad libitum access to food and water unless otherwise noted.

Surgical implantation of microelectronics fibers in the brain. Wild type mice (C57BL/6) aged 6–8 weeks (Jackson Laboratory, Strain #:000664) and transgenic DAT::Cre mice (breeding pairs obtained from Jackson Laboratory, Strain #:006660) aged 8-10 weeks were used for the study, and all surgeries were conducted under aseptic conditions. Mice were anaesthetized with isoflurane gas (0.5–2.5% in O_2, VET EQUIP) and subsequently positioned in a stereotaxic frame (David Kopf Instruments). After application of ophthalmic ointment to the eyes, a skin incision was made to expose the skull. Lambda and bregma points were used to align the skull with respect to the Mouse Brain Atlas (Franklin and Paxinos). All implantation and injection coordinates were established according to the brain atlas. A single step injection/implantation was performed in the VTA [coordinates relative to bregma; -3.2 mm anteroposterior (AP); 0.5 mm mediolateral (ML); -4.4 mm dorsoventral (DV)]. Adeno-associated viruses serotype 5 (AAV5) carrying *Ef1α::DIO-hChR2-mCherry* and *Ef1α::DIO-mCherry* plasmids were purchased from the University of North Carolina Vector Core at titers of 2×10^{12} particles/mL and 3×10^{12} particles/ml, respectively. Using a microinjection apparatus (NanoFil Syringe and UMP-3 Syringe pump, Word Precision Instruments) 1.2 µl of AAV virus was front-loaded into the fiber microfluidic channel. The fiber was lowered into the brain and 600 nl of viral payload was injected each at -4.6 mm and -4.2 mm DV sites at an infusion rate of ~150-300 nl/min. After each injection, the fiber was left undisturbed for further 10 min. The stainless-steel ground screw was affixed to the skull on the cerebellum of the contralateral hemisphere. Finally, the fiber backend connector was fixed to the skull with layers of adhesive (C&B Metabond; Parkell) and dental cement (Jet-Set 4, Lang Dental). Following the surgery, mice were individually housed at 22 °C, 12-h light/dark cycle, and food and water *ad libitum*. Inclusion criteria for different experiments were as follows: 1) spontaneous electrophysiology – low background noise (<400μV_{pp}); 2) opto-electrophysiology, thermometry – intact µLED as assessed from *in-vivo* and *ex-vivo* I-V curve; 3) behavior – intact µLED as assessed from *in-vivo* and *ex-vivo* I-V curve, expression of viral construct as assessed from optically evoked neural activity and/or histology.

Surgical implantation of fiber probes in the gut. Adult wild-type (Jackson Laboratory, Strain #:000664), Phox2b::ChR2 (breeding pairs obtained from Jackson Laboratory, Strain #: 016233; 012567), Pyy::ChR2 (Pyy::Cre mouse is courtesy of Andrew Leiter; Jackson Laboratory, Strain #: 012567), or Cck::ChR2mice (breeding pairs obtained from Jackson Laboratory, Strain #: 012706; 012567) (C57BL/6J background) or littermates were anesthetized with isoflurane (1-3% in oxygen). A 1 cm incision was made from the xiphoid process diagonally to the left-mid clavicular line. The peritoneal cavity was accessed, and the stomach extra-corporealized for implantation in wild-type, Phox2b::ChR2, and Cck::ChR2 mice. In these mice, the distal end of the gut fiber was introduced into the duodenum through the pylorus. To access the pylorus, a purse string suture was made in the gastric antrum, between which a small incision was made in the stomach wall. The distal end of the device was threaded into the proximal duodenum. The purse string stitch was then tied to secure the device in the intestine. In Pyy::ChR2 mice, a 1 cm incision was made 3 cm below the xiphoid process to access the cecum. The cecum was extra-corporealized and the distal end of the gut fiber was introduced into the distal ileum through a purse string suture, as in the duodenal surgeries. The purse string suture was tied to secure the device in the ileum. In all surgeries, the remaining length of the device was tunneled to the base of the skull by creating a subdermal pocket. The peritoneum and overlying skin were sutured closed at the abdominal site. The fiber exited the subdermal tunnel at the base of the skull. The skull was etched with a scalpel blade and a thin layer of Metabond cement (Clear L-powder S399 + catalyst; Metabond) was applied. Then, the Metabond layer was similarly etched with a blade, and the backend connector of the fiber was affixed to the skull using dental cement (Stoelting #51458). Mice recovered for at least 5 days during which they were fed wet mash and received appropriate post-operative care. Inclusion criteria at the end of each study were that the fibers were appropriately secured in the proximal small intestine and that the µLEDs were operational.

In-vivo electrophysiology/opto-electrophysiology. Implanted fibers were connected to RZ5D electrophysiology system through a PZ2-32 head stage (Tucker Davis Technologies, TDT). Following data accquisition, electrophysiological signal was digitized with 50-kHz sampling frequency and filtered in the frequency range 0.3–5 kHz. Subsequent signal processing and analysis was done in MATLAB (R2019b). Spiking activity was detected using threshold detection with a threshold of 5 standards deviation from the mean of the signals. A downtime of 2 ms was employed to reject double detections. Principle Component Analysis (PCA) and Gaussian Mixture

Model (GMM) clustering were used to perform spike classification and clustering (full and independent covariance matrices). L-ratio and the isolation distance of the classified clusters were used to assess the quality of the clustered data. For opto-electrophysiology experiments optogenetic stimulation pulses were delivered via integrated μLEDs on the fiber with rise/fall time between 1 to 15 ms to minimize capacitively coupled artiacts. Stimulation was delivered in 1-s stimulation epochs separated by 4-s rest epochs at a frequency of 10 Hz from the RZ5D acquisition system with a custom designed connector.

In-vivo impedance spectroscopy. To assess the *in-vivo* stability of the recording electrodes, we performed impedance spectroscopy on these electrodes v/s the ground screw in the VTA of wild-type implanted mice for up to 6 months (n=3 mice) with a portable BioLogic VMP3 potentiostat.

In-vivo brain temperature measurements. Wireless intracranial temperature measurements were performed in an open field arena. Wild-type mice (n=6) implanted in the VTA with the pre-calibrated microelectronic fibers were coupled to the NeuroStack module and allowed to explore an open field arena (30 cm × 30 cm) as they received wireless photostimulation (20 Hz, 10 ms pulse width) with blue μLED for 200 s. Anesthesia induced brain hypothermia was quantified following an intraperitoneal injection of an anesthetic drug mixture of Ketamine-Xylazine (9:1 dilution) at 30 mg/kg and 60 mg/kg dosage in wild-type mice implanted with pre-claibrated microelectronic fibers in the VTA (n=3 for each dosage). The current response from the fiber thermal sensor was measured with a potentiostat (Soalrtron, 1280C) in a two-electrode configuration until the animal gained consciousness and began freely ambulating in the home cage.

In-vivo gut temperature measurements. Wireless gut temperature measurements were performed in a clean home cage with food and water removed. A wild-type mouse was chronically implanted with a gut fiber in the duodenum as described above. Temperature was continually recorded while the animal received wireless photostimulation (20 Hz, 10 ms pulse width) with implanted blue μLED for 10 minutes in the homecage.

In-vivo gut optofluidic modulation with simultaneous vagal cuff electrophysiology. Whole nerve recordings were performed in Cck::ChR2 mice as previously[147]. A gut fiber with two connected tubes for PBS perfusion and stimulant delivery was surgically inserted through the stomach wall into the duodenum. A perfusion exit incision was made at the ligament of Treitz for the small intestine. To control for volume pressure and to act as a within subject baseline, PBS was

constantly perfused through the isolated intestinal region at ~400 µL/min. Stimulation conditions were applied after recording 2 min of baseline activity. During nutrient stimulation conditions, PBS perfusion was continuous and 200 µL of stimulant was perfused over 1 min using a syringe pump (Fusion 200, Chemyx). The 1-minute infusions of each compound were separated by at least 6 min, or the return to baseline firing rate, whichever came first. Sucrose (300 mM) was used as the nutrient, as it is known to stimulate vagal firing rate. Blue (λ = 470 nm, 20 Hz, 30.3 mW/mm^2, 10 ms pulse width) or green light (λ = 527 nm, 20 Hz, 45.6 mW/mm^2, 10 ms pulse width) was delivered via fiber µLEDs concomitant with the sucrose infusion through the microfluidic channel. Extracellular voltage was recorded as previously described[147]. The raw data were analyzed using SpikeTailor, a custom MATLAB (R2019b) software script[147]. Spikes were detected using a threshold of two standard deviations above the noise-floor determined by the root mean square (RMS) noise. The firing rate was calculated using a Gaussian kernel smoothing algorithm in 200-ms bins[147].

In-vivo intestinal nutrient delivery with simultaneous brain electrophysiology. C57BL/6J mice were chronically implanted with a brain fiber in the VTA and allowed to recover for 1 week. Subsequently, electrophysiological recordings were performed and analyzed as detailed in '*in-vivo* electrophysiology' section. The identity of putative DAergic neurons was assessed by their characteristic inhibitory response to dopamine D2 receptor agonist quinpirole (200-300 µg/kg, i.p.). Firing rate was computed for each recorded unit based on the peri stimulus time histogram with a wiondow size of 1s (moving average gaussian with a standard deviation of 200 ms). Animals that did not yield successful recordings from DAergic neurons (background noise >400 μV_{pp} or insensitive to quinpirole administration) were excluded from the experiment. Subsequently, the animals were fasted overnight for 18 h and underwent a second surgery for intraduodenal implantation of a gut fiber. Sucrose (0.6 M, 0.5 ml over 10 min) or saline infusions (0.5 ml over 10 min) were performed with a programmable infusion pump (New Era Pump Systems Inc.) while concomitantly recording VTA activity that also extended up to 10 min after the end of the infusion session. Average firing rate was computed for each putative DA unit over a 120 s recording window pre- and post-infusion based on the mean inter-stimulus-interval at a 40 ms bin size.

Real time place preference assays. Behavioral tests were performed by an investigator with knowledge of the identity of the experimental groups versus control groups.

Brain. DAT::Cre mice implanted with multifunctional microelectronics fibers and injected with viral vectors in the VTA were handled and acclimated to the investigator for 2 days prior to the behavioral test for 10 min each (n=8-10 per group). On third day animals were acclimated to the connection of NeuroStack module and allowed to explore their homecage for 15 min. On the following day (pre-test day) the NeuroStack module carrying mice were allowed to freely explore an unbiased two-compartment chamber (60 cm × 30 cm × 30 cm) for 30 min while being video recorded. The time spent by an animal in each chamber was calculated using a behavioral software (Ethovision XT, Noldus). Mice that showed >70 % preference to a chamber during pre-test were eliminated from the subsequent analyses. On the day of the test, the less preferred chamber for each animal was coupled to wireless photostimulation condition by controlling NeuroStack from a base computer positioned ~5 m away. The live video feed from a recording camera provided input on the animal location and the investigator controlled the status of the stimulation condition in real time. Three different photostimulation conditions were tested using the above procedure: (1) Stimulation ON (470 nm, 25 Hz, 10 ms pulse, 1s ON, 2 s OFF) v/s OFF (no stimulation); (2) Phasic bursting (470 nm, 40 Hz, 5 ms pulse, 0.5 s ON, 4 s OFF) v/s tonic stimulation (5 Hz, 5 ms pulse, ON); (3) Blue (470 nm, 25 Hz, 10 ms pulse, 1 s ON, 2s OFF) v/s green stimulation (527 nm, 25 Hz, 10 ms pulse, 1 s ON, 2 s OFF).

Gut. Phox2b::ChR2 mice and their negative genotype littermates were implanted with the gut fiber in the duodenum. Mice were acclimated to investigator handling and connection to the NeuroStack module akin to the brain experiments. On the pre-test day, the NeuroStack module was attached the I/O pins of the implanted fiber and mice were allowed to freely explore an unbiased chamber (Techniplast Greenline IVC cage for mice) for 20 minutes. Animal activity was determined by beams crossed in the x and y planes and was collected with a 100 Hz scan rate using the TSE PhenoMaster (Software version 7.3.3). On test day, the less preferred chamber for each animal was coupled to wireless photostimulation by controlling the wireless module from a base computer. The live activity feed provided input on mouse location and the investigator wirelessly controlled the stimulation status in real time. There were three different conditions: (1) the experimental group was Phox2b::ChR2 mice receiving blue-light stimulation (470 nm, 20 Hz, 10 ms pulse, ON) vs no stimulation (OFF); (2) the µLED control group was Phox2b::ChR2 mice receiving green-light stimulation (527 nm, 20 Hz, 10 ms pulse, ON) vs no stimulation (OFF); (3)

the genetic control group was negative genotype littermates receiving blue-light stimulation (20 Hz, 10 ms pulse, ON) vs no stimulation (OFF).

Modulation of feeding behavior. For duodenal studies Cck::ChR2mice or negative controls were implanted with the soft gut fiber in the proximal duodenum. Mice were acclimated to the investigator handling and connection to the NeuroStack module. Mice were food deprived overnight (18 h) before connection to the NeuroStack module and receiving 30 minutes of wireless optical stimulation (20 Hz, 10 ms pulse). After 30-minutes of stimulation, mice were disconnected from the NeuroStack and given access to standard chow pellets (Purina 5001). Chow intake was measured each hour for 3 h. Mice had ad libitum access to water for the duration of the food restriction and testing. Each mouse received blue-light and green-light stimulation, randomized per condition. At least 48 h separated each test day. For ileal studies Pyy::ChR2 mice or negative controls were implanted with the soft gut fiber in the ileum. Mice were acclimated to experimenter handling and connection to the NeuroStack module. Mice were acclimated to Ensure (30%) solution for 6 hours following surgical recovery and at least 48 h before the first experimental session. Mice were food deprived overnight (18 h) before connection to the NeuroStack module. Mice received one-hour of wireless optical stimulation (20 Hz, 10 ms pulse), which began 10 minutes before getting access to the Ensure solution. Ensure (30 %) was loaded into 5 mL serological pipettes that were fashioned as sippers. Mice had access to the solution for 1 h and intake was measured every 5 minutes. Mice did not have access to food or water during the test sessions. Each mouse received blue-light and green-light simulation, randomized per condition. At least 48 h separated each test day. The feeding studies utilized the multiple independently addressable stimulation channels on the gut fiber. As such, these experiments were designed with within-subject controls. While the baseline food intake was lower in the control cohort of mice lacking ChR2, we attribute this to differences in individual body weight[167] and time of year of testing[168], which were unaccounted for in the within-subject design[169] of these studies.

Locomotor assays of brain and gut implanted mice. To test whether brain, gut or gut-brain dual implants coupled to the NeuroStack impacted locomotion, we evaluated locomotor behavior over 20 minutes. Open field test on naïve (un-operated) and implanted mice carrying NeuroStack were conducted in an open chamber (60 cm × 30 cm × 30 cm) for brain implantations and in the homecage for gut and gut-brain dual implantations over 20 min. Locomotor activity was recorded

as described in the real time place preference assay. The mouse position, distance traveled, and speed, were calculated.

Food and water intake of gut and gut-brain implanted mice. Animals were individually housed in a custom-built PhenoMaster behavioral phenotyping system (TSE Systems Inc. Chesterfield, MO). The PhenoMaster was programmed (software version 7.3.3) to automatically maintain a light cycle (03:00 lights on; 15:00 lights off), temperature (22 ºC), and humidity (50 %). Animals were provided with standard mouse chow (Purina 5001) and reverse osmosis water ad libitum. Food hopper and water bottle were attached to weight sensors (TSE) which were automatically sampled every 5 s to the nearest 0.01 g. For drinking measurements, a 10 s smoothing interval was used. For weight measurements, a 15 s smoothing interval with a 15 g threshold was used. Intake was measured every 5 s. Data were corrected for minor fluctuations by only permitting a monotonically increasing function for both food and water intake: values that represented negative food intake were replaced by the most recent value. For stability of intake measurements, the mean intake and water intake was calculated for two consecutive days for each individual mouse.

Immunohistochemical evaluation of foreign body response. Wild type mice (n=5 per group) bilaterally implanted in the VTA with microelectronics brain fibers or commercial silica waveguides (300 µm, FT300UMT Thorlabs) were anesthetized with isoflurane, injected intraperitoneally with fatal plus (100 mg kg^{-1}), and transcardially perfused with 50 mL of ice-cold PBS followed by 50 mL of ice-cold 4% paraformaldehyde (PFA) in PBS. The devices were carefully explanted and the brains were removed and additionally fixed in 4% PFA in PBS for 24 h at 4 °C, then stored in PBS afterward. Coronal slices (50 µm thickness) were prepared using a vibratome (Leica VT1000S) and a razor blade (Electron Microscopy Sciences, 72002) in ice-cold PBS. The slices were then stored in PBS at 4 °C in the dark until staining. Slices were permeabilized with 0.3% v/v Triton X-100 and blocked with 2.5% donkey serum in PBS for 30 min. Slices were incubated overnight at 4 °C in a solution of 2.5% donkey serum in PBS and a primary antibody (Iba1:Goat anti-Iba1, ab107159 Abcam, 1:500 dilution; GFAP: Goat anti-GFAP, ab53554 Abcam, 1:1000 dilution). Following incubation, slices were washed three times with PBS. The slices were then incubated with a secondary antibody (Donkey anti-Goat Alexa Fluor 488, A11055, 1:1000, Thermofischer) for 2 hr in room temperature on a shaker followed by additional three washes with PBS. Slices were then incubated with DAPI (4′6-diamidino-2-

phenylindole) (1:50 000) for another 20 min, and washed three times with PBS. Fluoromount-G (SouthernBiotech) was used for mounting slices onto glass microscope slides. A laser scanning confocal microscope (Fluoview FV1000, Olympus) was used for imaging with 20X objectives, with z-stack images across the slice thickness. Region of interest was chosen based on the implant location, imaging the immune response around the implant trace. FIJI (ImageJ 1.53g) was used to quantify the immune response as total integrated fluorescence intensity normalized to the image acquisition area.

Hematoxylin and eosin stain evaluation of foreign body response. Duodenal tissue from wild-type mice naïve (n=4) and implanted (n=4) to the duodenal implant was sliced and evaluated for hematoxylin and eosin (H&E) by the Duke Pathology Histology Lab. The villus height and crypt depths were measured using ImageJ 2 (1.5.3). For each mouse, the villus height and crypt depth were calculated as the average of 10 villi or crypts.

Statistics and Reproducibility. OriginPro 2021b, JMP Pro 15, or JMP Pro 16 software was used to assess the statistical significance of all comparison studies in this work. Power analyses for determining sample sizes for immunohistochemistry and behavior tests were not performed, instead the group sizes were chosen based on previous research conducted in the same brain circuit or intestinal region. This enabled direct comparison of our results with the prior work. In the statistical analysis of fiber characterization, one-way ANOVA followed by Tukey's post-hoc comparison test was used with thresholds of $*p < 0.05$, $**p < 0.01$, $***p < 0.001$. For the comparison between two groups in immunohistochemistry analyses, behavior assays, and hypothermia effect quantification *t*-test was used, and significance threshold was placed at $*p < 0.05$, $**p < 0.01$, $***p < 0.001$. For all parametric tests normality was determined using the Shapiro-Wilk method. Homognenity of variances was determined using the Levene's test wherever appropriate. All shaded areas and error bars represent standard deviation, data are presented as mean +/- s.d. Confocal micrographs of brain tissue were collected on at least 3 slices per brain to confirm reproducibility of results. Approriate fluorophores were evaluated in each opsin-expressing mouse included in the studies. Micrographs of gut tissue were collected on at least 3 tissue samples per animal to confirm reproducibility of results. Micrographs of fiber cross section were collected from 5 randomly selected regions of the draw to confirm reproducibility.

Other digital photographs such as those of the preform, fiber bundles, final devices, and implanted animals were collected once to serve as representative examples.

CHAPTER 4. CONCLUSIONS AND OUTLOOK

Overall outlook

I anticipate that the ideas, device designs, fabrication schemes, systems-level integration approaches, and in-vivo validation examples presented in this thesis will have broad utility in development of advanced bio-integrated interfaces for modulating neural circuits spanning multiple organs and the brain. The core ideas developed in this work can be pursued further in several potentially interesting directions. Below I present my perspectives on future directions for brain-organ neurotechnology and associated neurobiological questions that they may help answer.

Outlook on brain-organ neurotechnology

As highlighted in the introduction chapter, development of multifunctional devices for interfacing with the brain as well as the peripheral organs in preclinical rodent studies during free behavior is still in its infancy. While my work has successfully demonstrated cell-type specific neuromodulation of intestinal and central neural circuits through optogenetics, incorporation of wirelessly addressable physiological sensing modalities at both sites (central and peripheral) is still lacking. In this regard the functions that will be of immense value are wireless electrophysiological recording of single-unit neural activity and wireless photometric recording of cell-type specific calcium and neuromodulator/neurotransmitter dynamics. Successful implementation of these functions will require development of new wireless circuitry as well as entirely new brain-interfacing implantable front ends. The wireless electrophysiology function will benefit from higher density of electrodes in the brain fiber, whereas miniature and highly-sensitive photodiodes showing good spectral overlap with genetically encoded activity indicators (eg. GCaMP series, dLight series, GRAB series) will be crucial for successful implementation of wireless photometry function. Recording of gut physiology through accurate measurement of intestinal motility and pressure transients that help propel ingested matter can be valuable to study central neural control of gut motility as well in causally linking gut-motility to affective disorders such as anxiety and chronic stress. Sampling and recording of luminally secreted neurotransmitter is yet another unconquered frontier. Electrochemical detection of redox active gut-derived neurotransmitters such as serotonin has been recently shown in mice, but these studies were performed in acutely

implanted anesthetized animals. Developing robust catalytic electrodes with long-term stability and integrating them with a thermally drawn multifunctional fiber in a scalable fashion can address this unmet technological need in studying gut-brain neurobiology. In their current form, the microelectronic brain fibers do not lend themselves well for studying projection specific neural circuits. Similarly, the present design of intestinal fibers frustrates multi-region engagement with the intestine which has utility in studying intra-intestinal cross-talk and physiological feedback loops. To overcome these challenges, it will be crucial to integrate thermally drawn 3-D helical interconnects into both brain as well as gut probes which will provide the necessary strain relief mechanism for implanting devices in multiple regions in both the organs. Beyond the intestine, the soft, multifunctional microelectronic fibers can also be developed to interface with other tubular organ systems. One such example is that of peripheral vasculature. In this regard it is interesting to note that large bundles of peripheral nerves are often found to travel alongside major blood vessels (eg. splenic nerve and splenic artery), which make them strategically vital sites for bioelectronic interfacing. Moreover, other interesting vasculature such as the hepatic portal vein are known to be major detection sites of absorbed nutrients such as sugars, fats, and electrolyte contents. While intravascular fiber probes can be an appealing device design, a more practical way of achieving vascular interfacing can be with thermally drawn fiber-based soft elastomeric cuffs that are instrumented with a soft, microelectronic fiber probe.

Integrating multiple functions in probes that are implanted at multiple organs/sites in a rodent requires one to re-think the communication and powering backend. For seamless use of all, or a subset of embedded functions, it is impractical to rely on an externally tethered device. This design not only scales poorly with addition of more recording or stimulation channels, but also creates hurdles for conducting neuroscience experiments in socially interacting groups of animals as well as prevents group-housing. As such, creating devices that are wirelessly addressable as well as subdermally implantable will be the next logical step. Finally, successful integration of recording and stimulation functionalities in a brain-body bioelectronic device sets the stage for development of closed-loop control protocols, wherein physiologically or clinically relevant paradigms of stimulation can be programmed to be triggered in one organ by specific physiological changes recorded by the same device in the same or a different organ, while the animal performs complex behavior tasks in ethological settings.

APPENDIX A

Note: The material presented in this appendix was first published as M. Antonini, A. Sahasrabudhe* et. al. Adv. Funct. Mater.2021, 31, 2104857 (Ref. 29)*

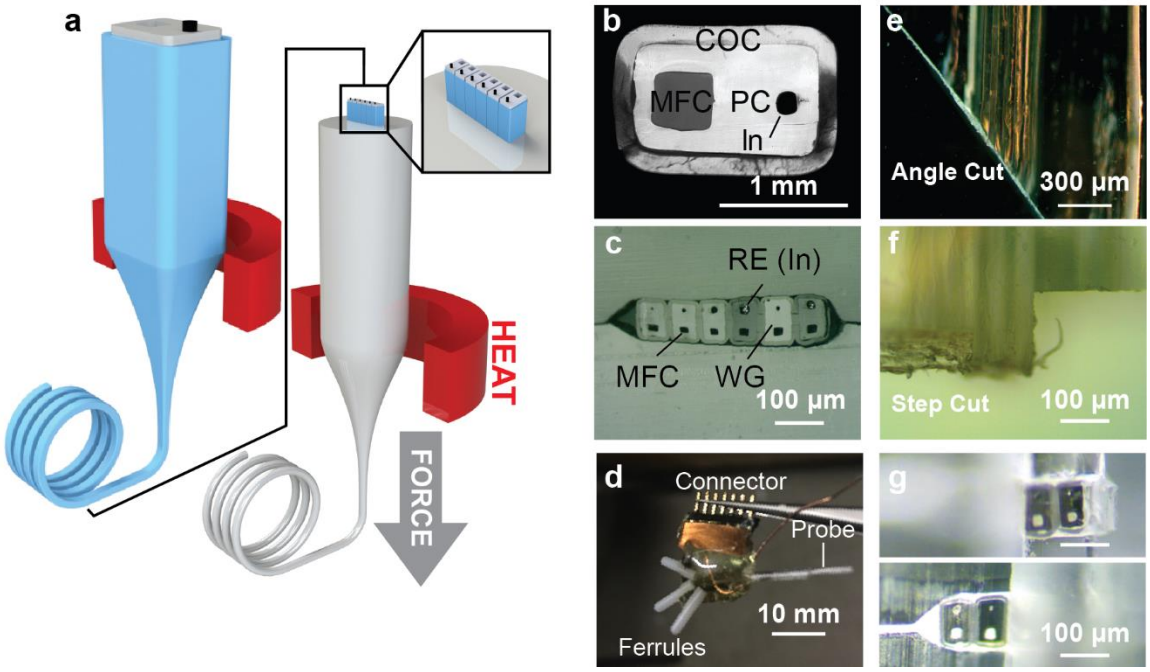

Fig. A1: Iterative thermal drawing for depth-specific neural probes. Using two-step thermal drawing process (a) a preform with a PC core and a COC cladding, a microfluidic channel and an indium electrode is drawn into mm-scale fiber (b). These are then stacked into another PC rod and drawn into microscale fiber (c). (d) illustrate a connectorized device. Each repeating unit featuring an optical waveguide, a microfluidic channel and a recording electrode. An angle (e) or a step-cut (f, g) of this device enable depth-specific neuromodulation.

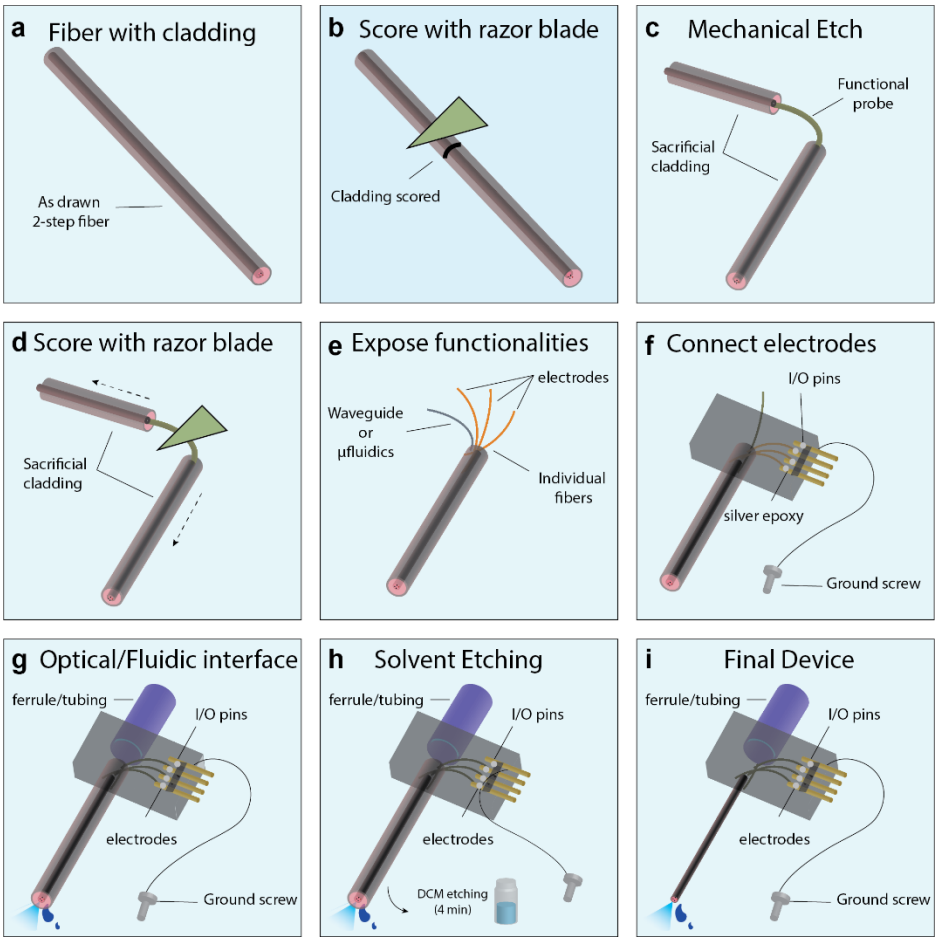

Fig. A2: two-step TDP enable rapid connectorization. (a-i) Connectorization procedure for probes fabricated using the two-step thermal drawing (a) The probe is drawn with a protective sacrificial cladding. (b) A razor blade is used to score the surface of the sacrificial cladding. (c) Gently bending and pulling the fiber frees the neural probe from its cladding. (d) Scoring and pulling of the outer COC layer of the probe allows for the individual components to split apart (e). (f) The individual electrodes can then be connected to pin headers using silver epoxy (f), while the optical wavefuide and microfluidic channel can be connected using UV epoxy to an optical ferrule and fluidic tubing, respectively (g). The distal end of the probe is inserted into dichloromethane (DMC) for 4min (h) to remove the sacrificial cladding and expose the functional fiber.

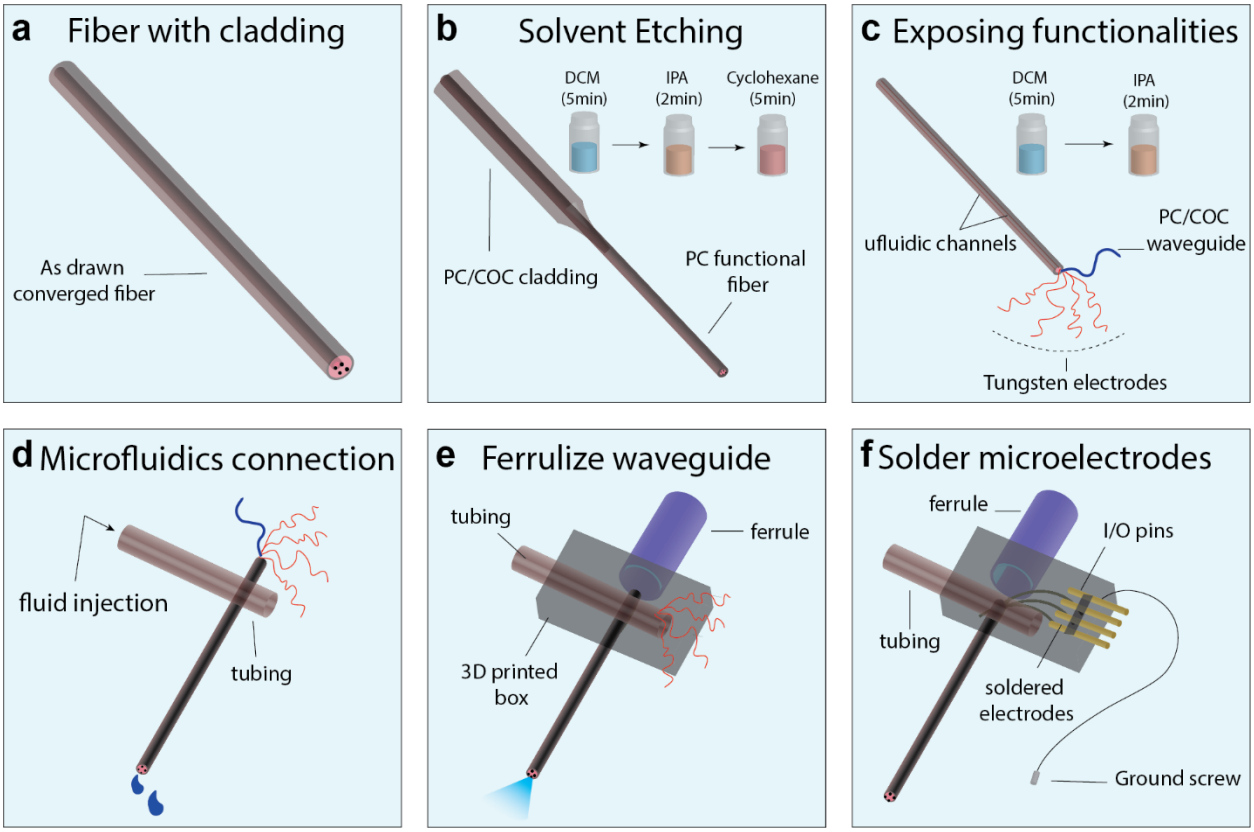

Fig. A3: Convergence TDP enable rapid connectorization. (a-f) Connectorization procedure for probes fabricated using the convergence TDP (a) The fiber is drawn with a protective sacrificial cladding. (b) The sacrificial cladding of PC and COC are etched using a simple solvent etching process that involves alternate cycles of DCM (5min), IPA(2min) and cyclohexane (5min) wash (c) The embedded functionalities of microwire electrodes and PC/COC waveguide are exposed by solvent etching using alternate wash cycles of DCM (5min) and IPA(2min). (d) The microfluidic channel is connected to external tubing using a T-connection. (e) The exposed waveguide from step (c) is coupled to a zirconia ferrule and subsequently polished (f). Finally, the exposed microwire electrodes from step (c) are soldered to header pins along with a ground screw bearing reference wire. All backend I/O interfaces are encapsulated in a 3D printed shuttle drive using UV curing epoxy in (e,f).

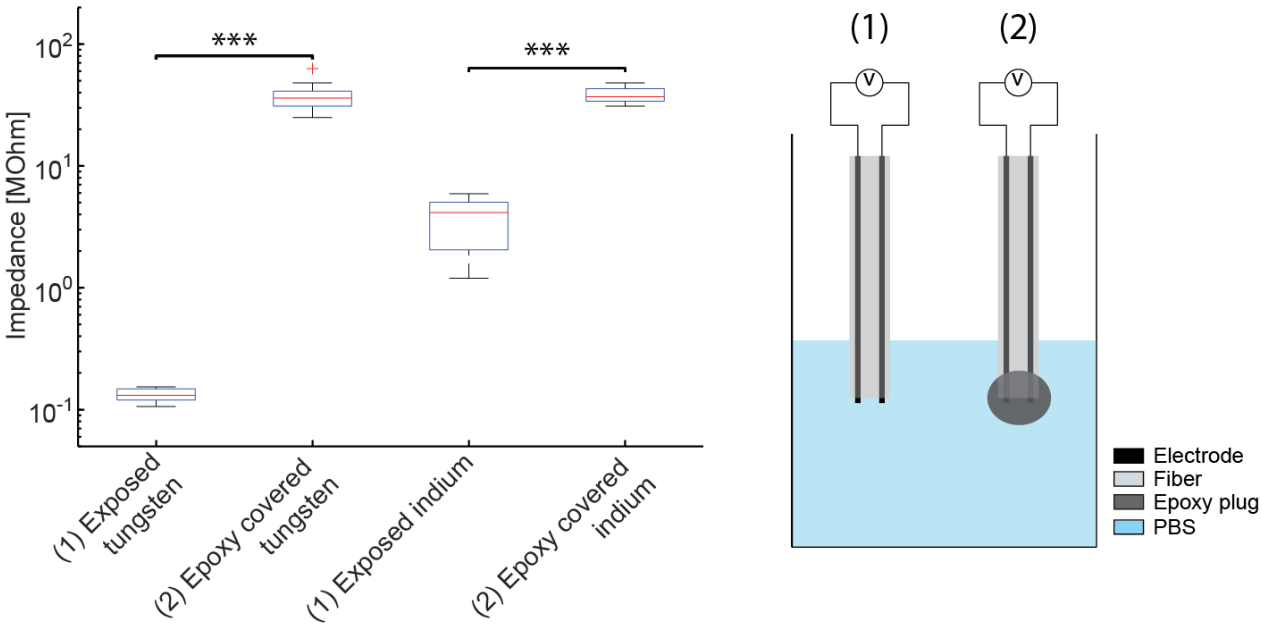

Fig. A4: Impedance across electrodes before and after covering the fiber tip with epoxy. Impedances at 1kHz across electrodes within the two-step fiber (indium) and converged fiber (tungsten). (1) Impedance measurement across exposed electrodes at the fiber tip in PBS, (2) open-circuit measurement of the epoxy-insulated fiber tip in PBS. (N=10 samples)

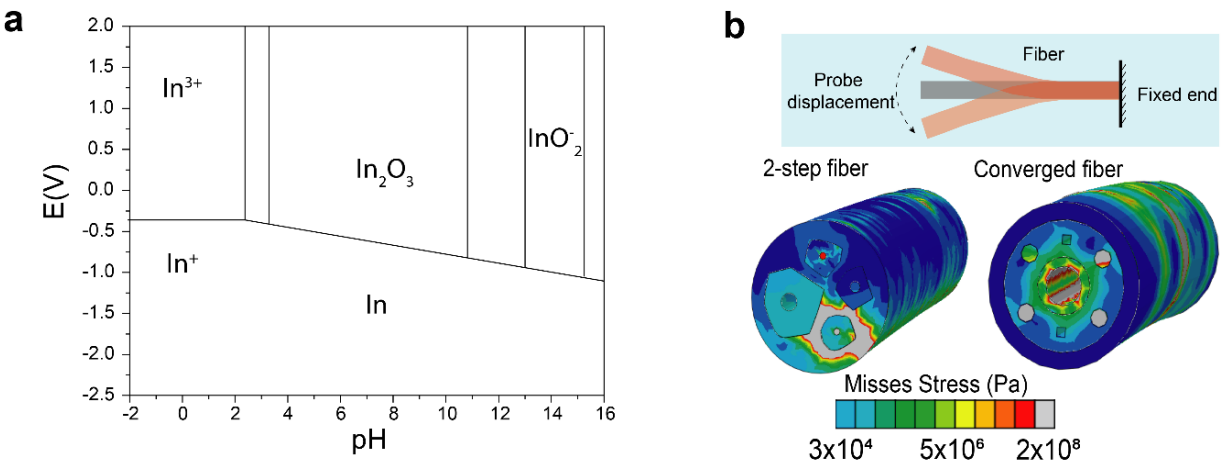

Fig. A5: (a) Pourbaix (E vs. pH diagram) for indium in water at 25 °C. This diagram was reproduced from ref. [170]; (b) Misses stress profile under bending deformation computed using finite element models for two-step (left) and converged fibers (right), respectively.

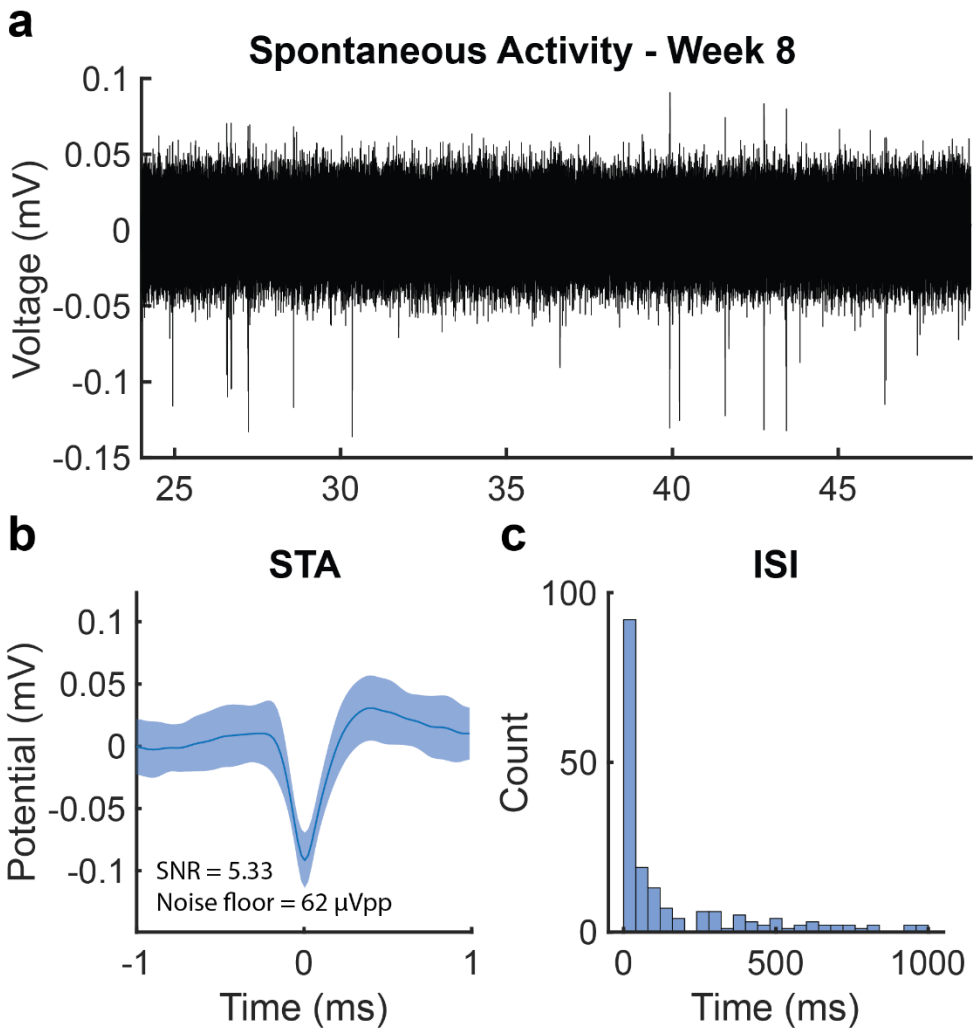

Fig. A6: Two-step indium fiber records single unit activity 8 weeks post-implantation.

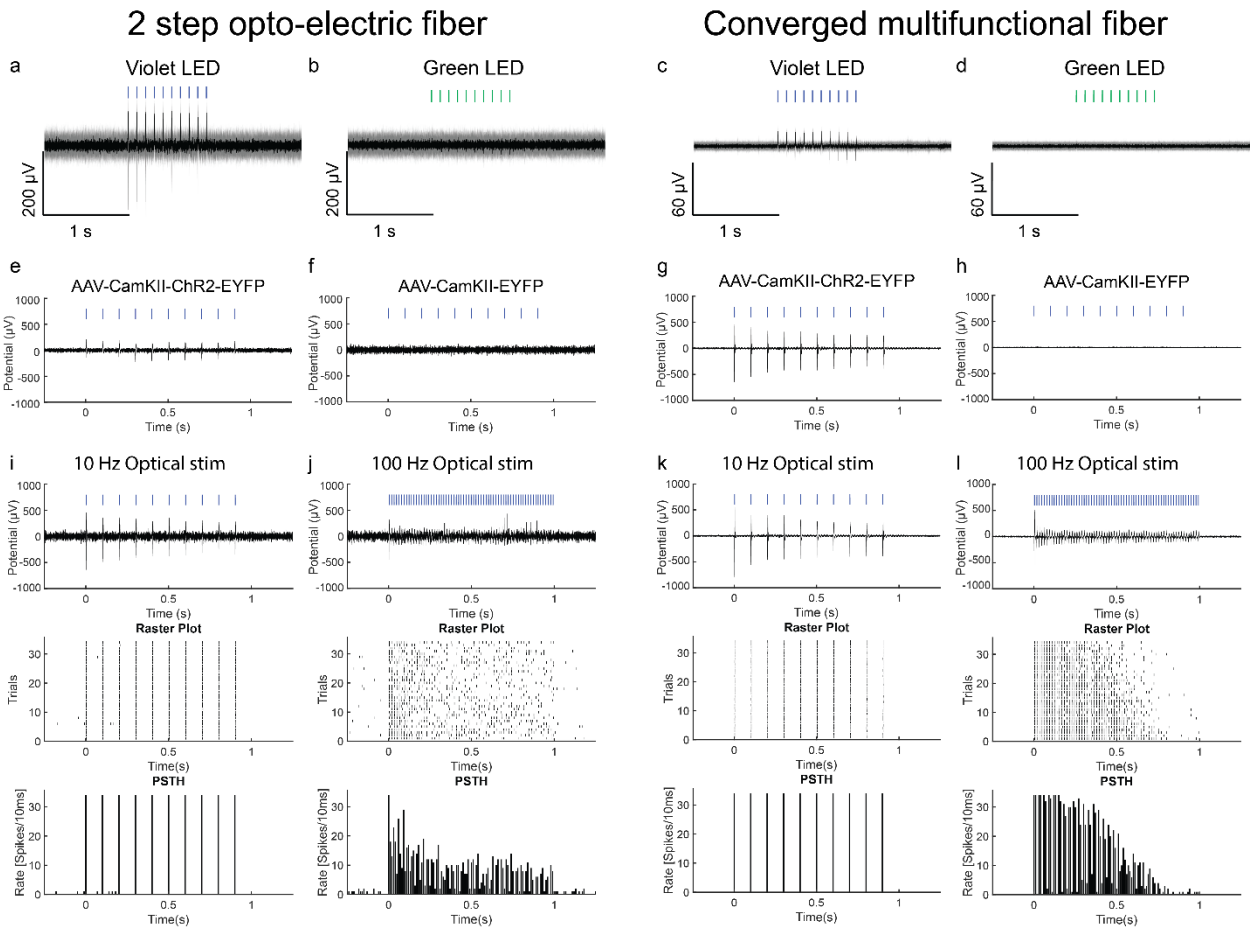

Fig. A7: Controls experiment for optically evoked activity using the two-step and converged fiber implanted in the mPFC. (a-d) Comparison of electrophysiological response to green LED (565 nm, 10 ms, 10 Hz, 4 mW/mm^2) and violet LED (420 nm, 10 ms, 10 Hz, 4 mW/ mm^2) light, for the two-step optoelectric and the converge multifunctional fiber (blue markers indicate laser onset). Only blue irradiation elicits electrophysiological activity. (e-h) Optically-evoked electrophysiological activity in mice transfected with AAV5-CaMKIIα::ChR2-EYFP (or control virus AAV5-CaMKIIα::EYFP). Neuronal activity is observed in mice transfected with ChR2, and not in control. (i,j) Comparison of optically evoked activity (473 nm, 10 ms, 10 mW/mm^2) at 10Hz and 100 Hz optical stimulation. Steady and correlated activity is observed at 10 Hz (i,k), as seen on the neural response (top), its associated raster plot (middle) and peri-stimulus time histogram (bottom). In comparison, 100 Hz stimuli elicited decaying and uncorrelated activity (j,l)

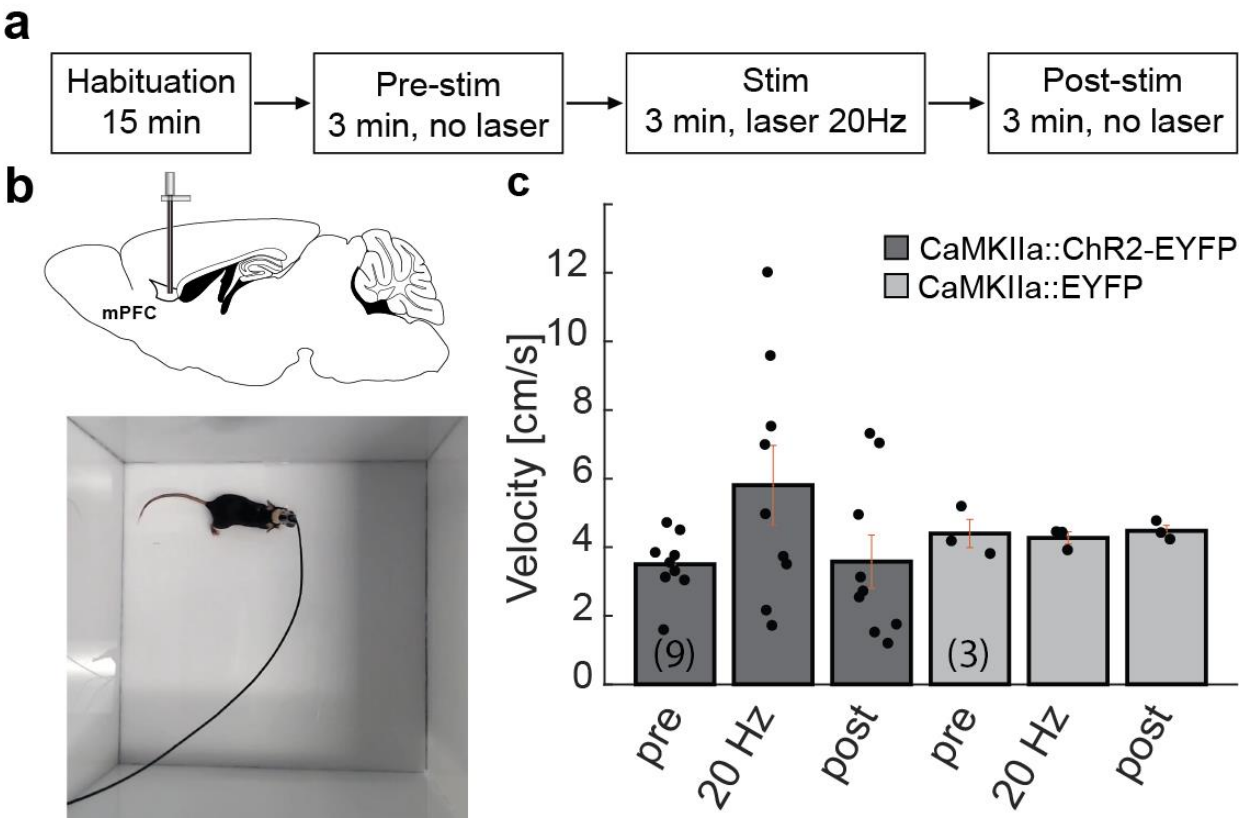

Fig. A8 – Behavioral assessment of mice implanted with converged and two-step fibers during optical stimulation. (a) Schematic depicting the Open Field Test paradigm. Animal that were implanted with the multifunctional converged or the two-step opto-electric fiber (b, top) were first left habituated to the behavioral chamber for 15 min (b, bottom), then recorded over a 9-min experiment, consisting of 3-min OFF epoch, 3-min ON epoch during which they were exposed to 20 Hz stimulation (5-ms pulse width), 3-min OFF epoch. (c) Average velocity recorded for WT mice transfected with AAV5-CaMKIIα::ChR2-EYFP (or control virus AAV5-CaMKIIα::EYFP), then implanted with two-step and converged neural probe in mPFC.

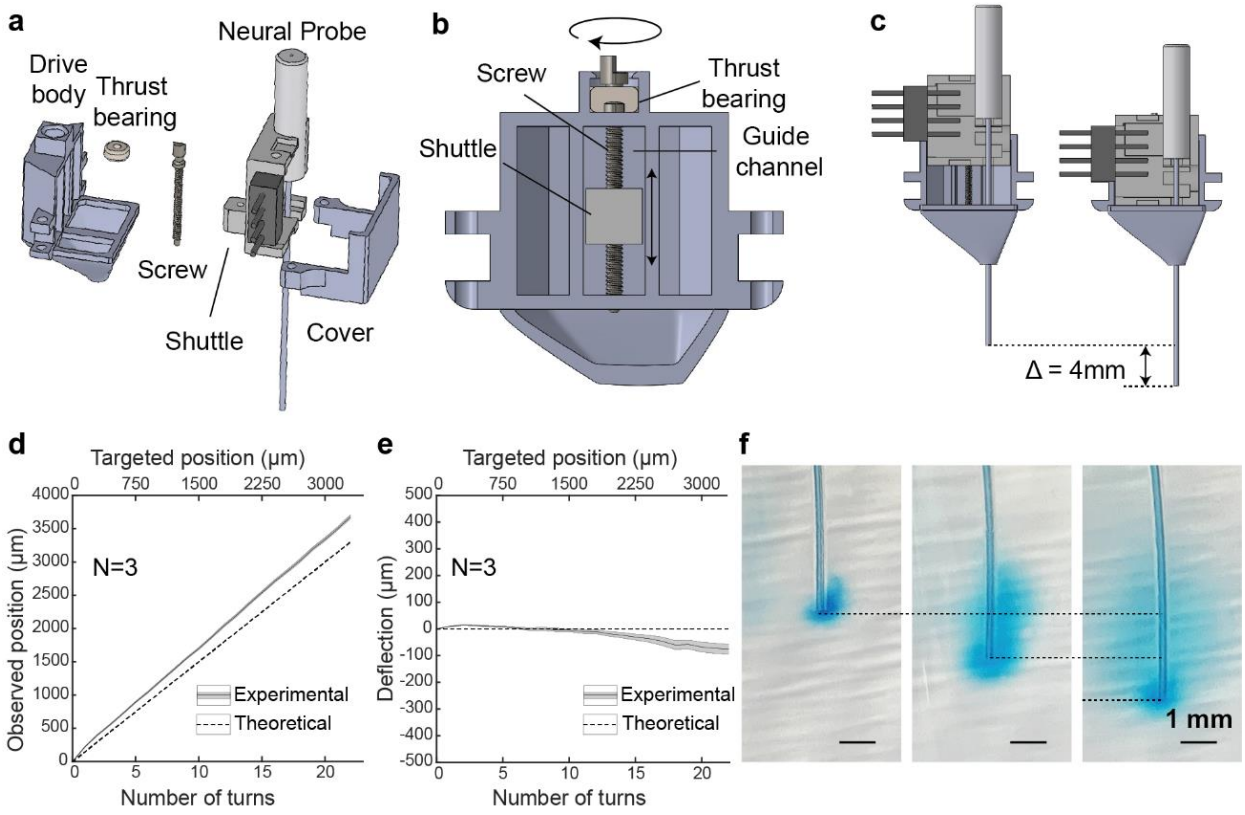

Fig. A9: Fabrication and characterization of a microdrive for post-implantation positioning of multifunctional neural probes. (a) Exploded view of the microdrive assembly composed of a 3d-printed drive body, a dental cement thrust bearing, a custom-made screw, a neural probe mounted on a shuttle, and a 3d-printed cover. (b) Schematic of the cross section of the microdrive illustrating the screw and shuttle system. The shuttle moves linearly via actuation of the screw, the screw rotate inside a guide channel and is held linearly by the light-cured cement. (c) Schematic of the shuttle in the upper drive and lower drive position, illustrating a range of 4mm. (d) Measurement of the probe depth relative to the number of screw turns relative to top position. (e) Lateral deflection of the probes relative to the number of screw turns. (N=3) (f) Injection of Evans Blue dye (2%; 500nl over 5 min) into a phantom brain (0.6% agarose gel) with the shuttle at 3 different position (0, -1mm, and -2mm).

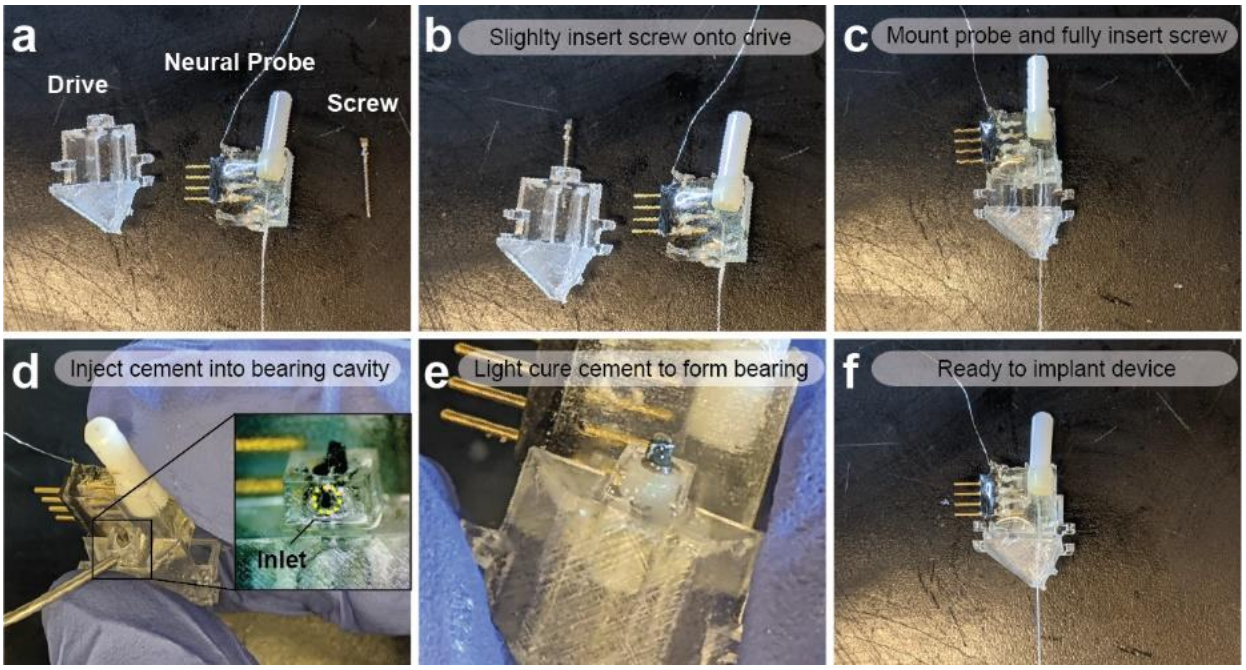

Fig. A10: Assembly procedure of the neural probe onto the microdrive. (a) The microdrive assembly is composed of the 3d printed drive, the neural probe and a custom-made screw. (b) First, insert the screw into the screw slot on the top of the drive. (c) Place the neural probe shuttle near the bottom position in the guide channel, with the screw hole aligned vertically, and insert the screw into the shuttle hole. (d) Inject light-cured cement into the bearing cavity at the top of the drive, and (e) cure-it around the screw collar to form a thrust bearing that prevents linear motion of the screw. (f) Rotate the screw slightly to separate the screw from the bearing, the device is ready to be implanted.

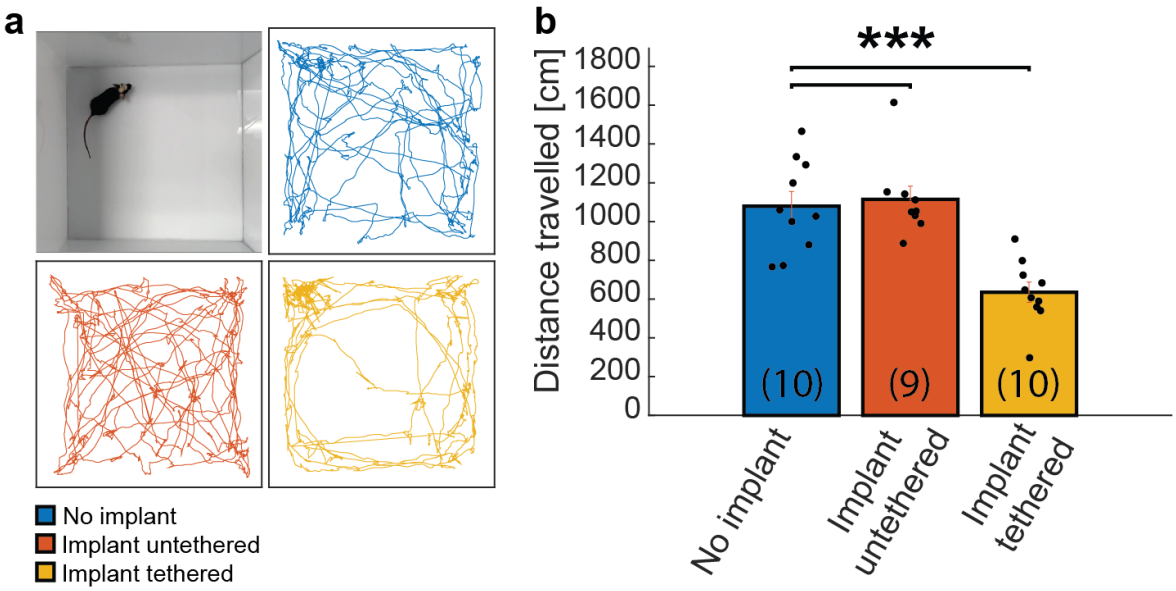

Fig. A11: Comparison of locomotor activity with and without the microdrive implant. (a) Picture of the open field test (top, left), and representative motion tracks of mice during a 3-min exploration session (top right, bottom left and right). (b) Total distance travelled over a 3-min exploration session indicates that the mice are not hindered by the implant, but exhibit decreased activity when the microdrive is tethered to external hardware (top, right). *** P<0.001.

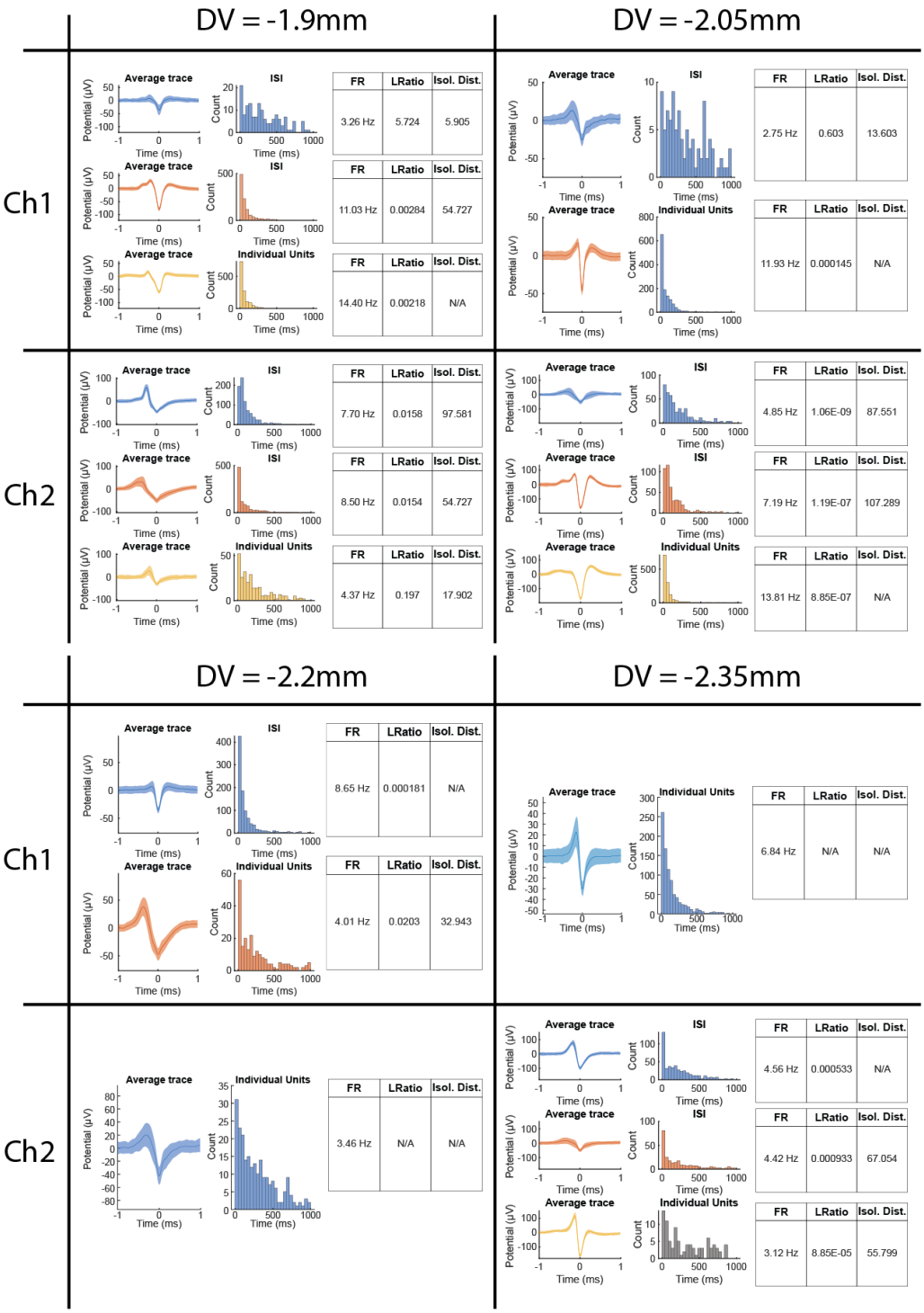

Fig. A12: Extended analysis of the endogenous neural activity recording from fig. 6. The neural probe (fig. 2b) was mounted onto the microdrive and implanted into the mPFC of C57BL/6 wild type mice.

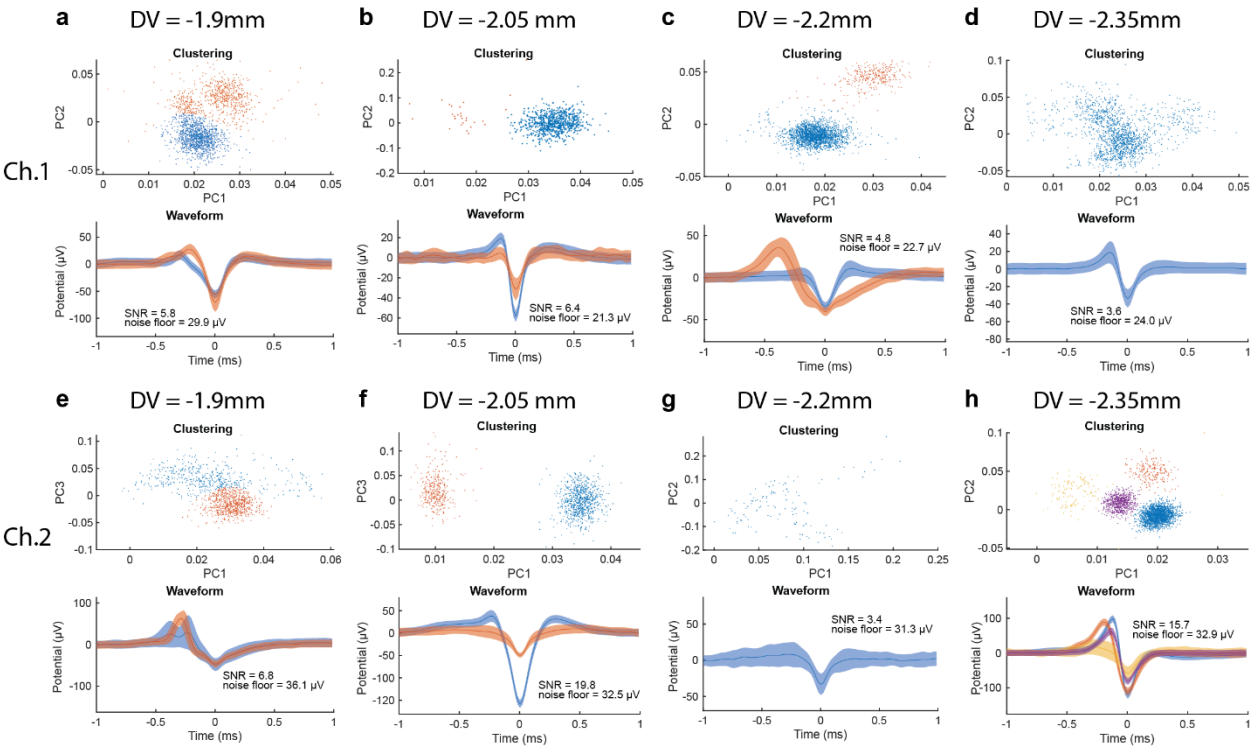

Fig. A13: Analysis of the endogenous neural activity recording from the same mouse of fig.6, while the animal was awake. Similar to fig. 6, The implant was placed slightly above the mPFC at AP= +1.7 mm, ML= 0.4 mm, DV= -1.9 mm during the first day, and was lowered by 150 μm (1 turn) every day for 3 days. Endogenous neural activity was successfully recorded at each depth for channel 1 (e-h) and 2 (i-l) and putative single unit activity were isolated by principal-component analysis (top), and the average trace illustrates the waveform of the separated units (bottom).

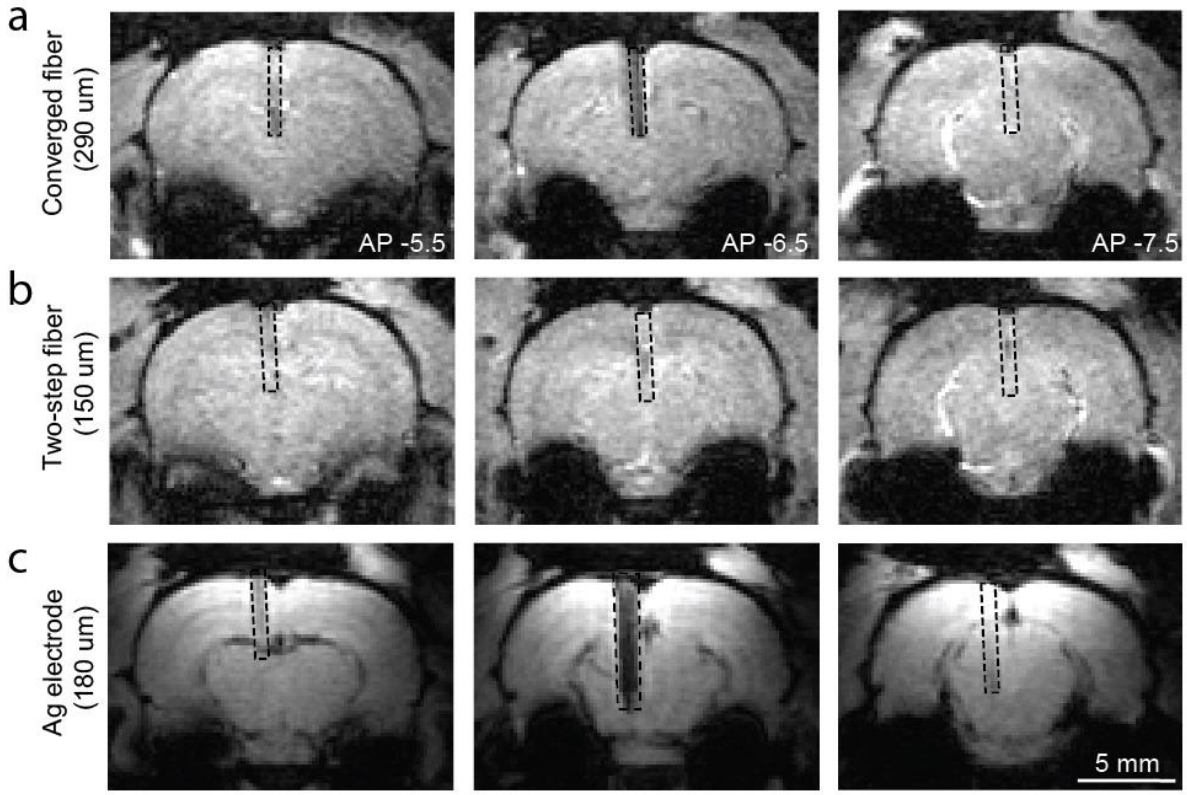

Fig. A14: **MRI image distortions caused by implants in comparison to silver wire which is routinely used for brain stimulation**. Three consecutive slices of a T1-weighted fast low angle shot sequence with 1mm distance from AP -5.5 to AP -7.5 for convergence fiber (A) and two-step fiber (B), compared to a silver wire electrode (C) implanted in the rat brain.

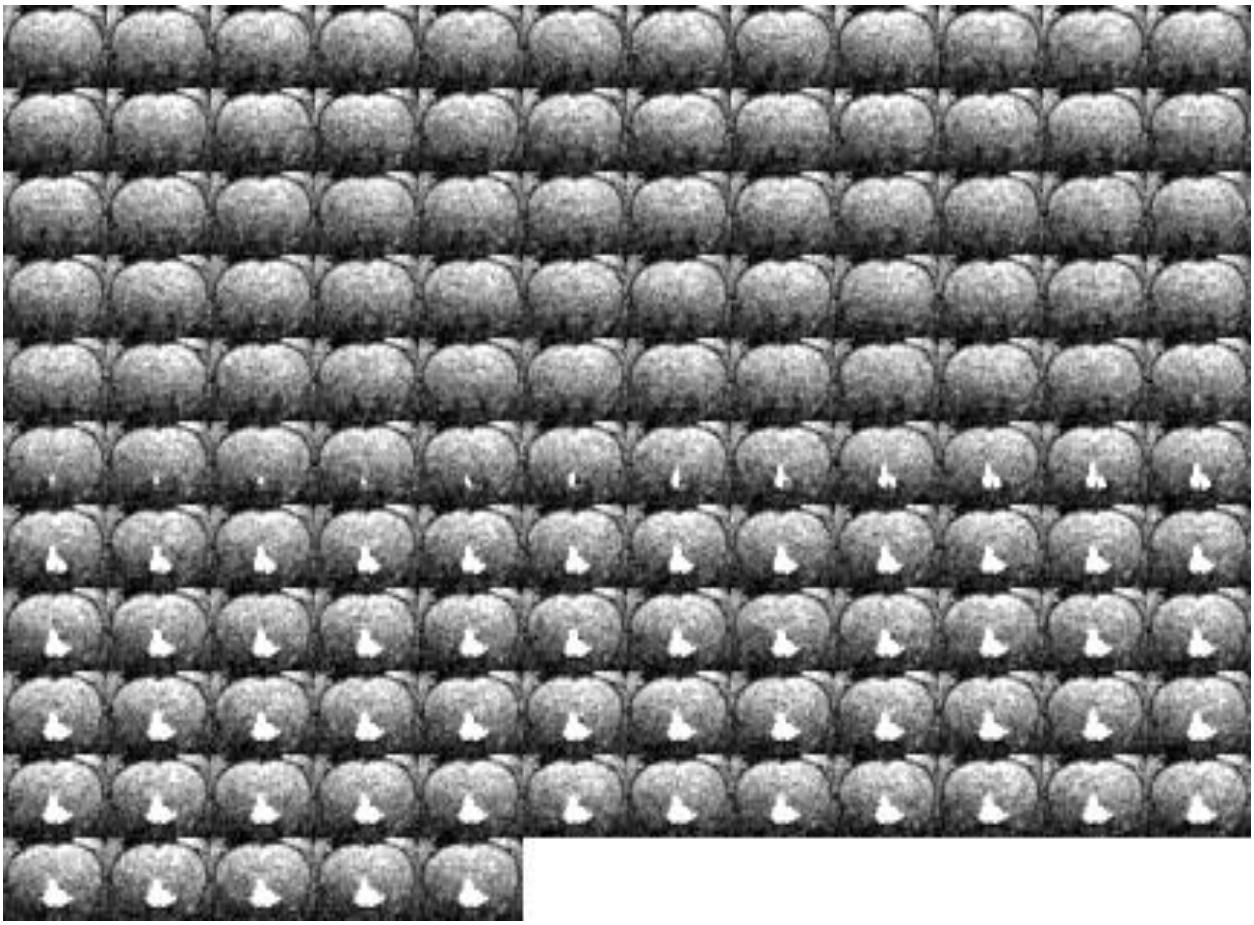

Figure A15: A portfolio of snapshots acquired after every 10s during a typical infusion session with a two-step fiber.

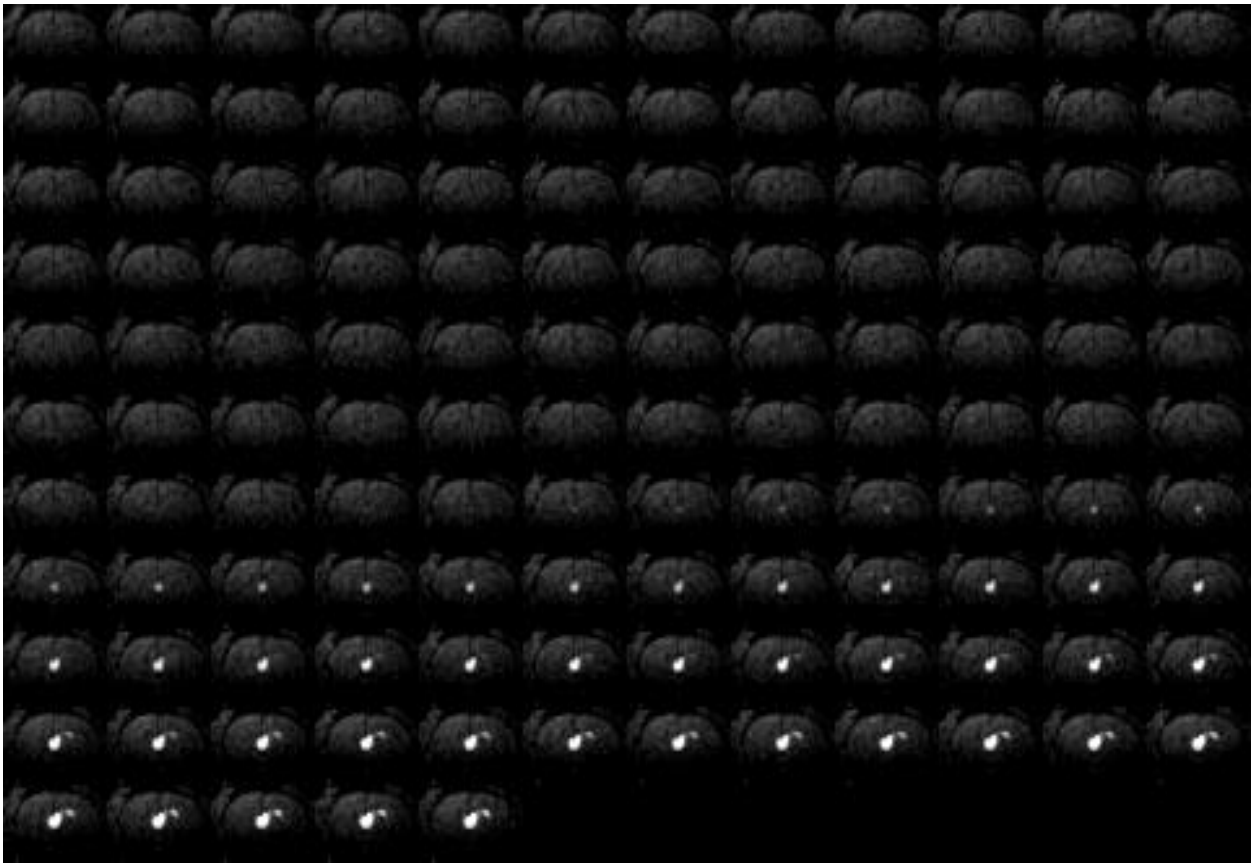

Figure A16: A portfolio of snapshots acquired after every 10s during a typical infusion session with a converged multifunctional fiber.

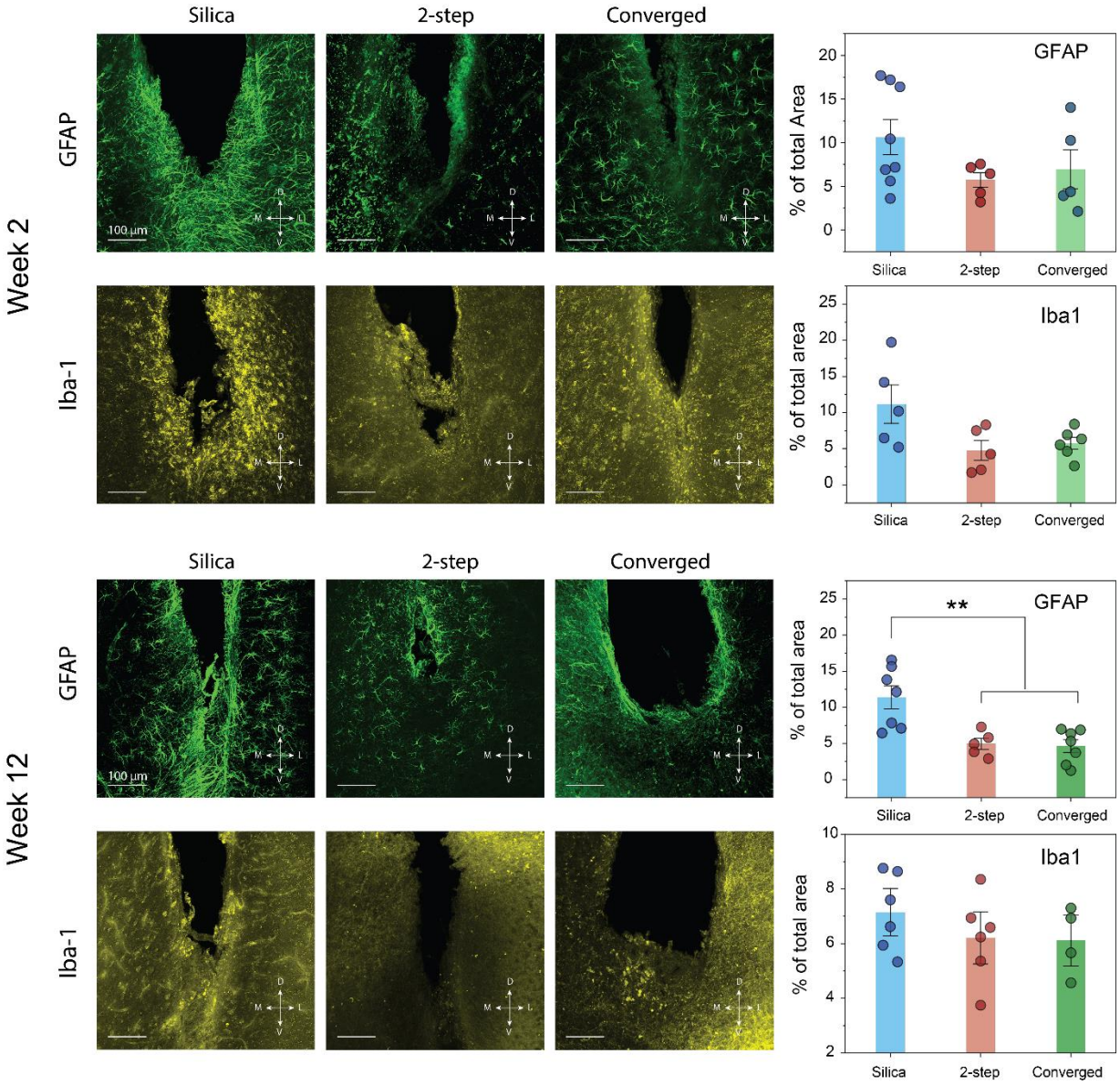

Figure A17: Immunohistochemical evaluation of the foreign body response at 2- and 12-weeks post implantation. Scale bar = 100 µm.

APPENDIX B

Note: The material presented in this appendix was first published as A. Sahasrabudhe, L. Rupprecht* et. al. (Ref. 31)*

Supplementary Methods

Fiber characterization. For cross-sectional imaging of the fibers, samples from different sections of the draw (n=5 randomly selected sections) were cold mounted into epoxy resin and polished on an automated grinding machine with series of sand papers of decreasing grain sizes (25N force, 300 rpm, 2 min for each sand paper with washing step in between). The polished epoxy blocks were imaged on a Nikon MA200 microscope. The electrode impedance for brain fiber (n=3 devices) was measured with a precision LCR meter (HP4284A, Agilent Technologies) with a sinusoidal input (10 mV bias, 20 Hz–10 kHz). The optical characterization of fiber integrated μLEDs (n=6 devices) was performed by powering them at different bias voltages and recording the light output with a photodetector (S121C, 400–1100 nm, 500 mW, Thorlabs) attached to a power meter (PM100D, Thorlabs). The I-V response of μLEDs was recorded with a potentiostat in a two-electrode configuration (Solartron 1280C and CorrWare 3.5i). The bending stiffness was measured with a dynamic mechanical analyzer (Q800, TA Instruments and Advantage v5.5). Different samples (n=3 fibers) of 1.2 cm lengths were mounted in a single cantilever clamp and tested with a frequency sweep (0.1–10 Hz) under controlled displacement of 20 μm at 37 °C. The cyclic bending tests (n=3 fibers) for soft gut fibers was performed with mechanical testing machine (Z2.5 with testXpert Ill Vl.11, Zwick/Roell) over 10^4 cycles, while recording the light output from μLEDs after every decade. The diode based thermal sensors were calibrated against a commercial thermocouple (NeuLog, NUL-203) by equilibrating the fiber and thermocouple in a hot water-bath or a hot plate at different temperatures and recording the current response from the diode at 2.2 V forward bias (n=4 devices). A fitted linear regression between the diode current and equilibrium thermocouple temperature yielded the standard curve for the sensor. The microfluidic capability of brain fibers (n=4) was evaluated by connecting the probes to an injection syringe (NanoFil) that was driven by an infusion pump (UMP-3, World Precision Instruments) and flowing a DI water bolus at different injection speeds. The injection output was

measured by weight and the injection rate was obtained upon dividing the injected volume by the time required to complete the injection. Identical procedure was employed for microfluidic characterization of gut fibers, by injecting a 0.2 ml bolus with a programmable pump (New Era Pump Systems) at rates commensurate with intraintestinal infusions.

Optical simulations. Finite-elements simulation implemented in COMSOL Multiphysics (Version 5.6) were used to model the optical field of the tissues. For absorbing-scattering media like biological tissues, the light transport equation was employed, where the light fluence rate at a given location in steady state $\Phi(r)$ obeys $D\nabla^2\Phi(r) - \mu_a\Phi(r) = 0$, where $D = \frac{1}{3}(\mu_a + \mu_s')$ is the diffusion constant, μ_a is the absorption coefficient of the medium, and μ_s' is the reduced scattering coefficient. The brain is modeled as a homogeneous medium [μ_a: 3.67 cm^{-1} (at 475 nm), 3.84 cm^{-1} (at 532 nm), μ_s': 51.15 cm-1 (at 475 nm), 46.3 cm-1 (at 532 nm)] with dimensions set such that the radiative power decays to zero before reaching to the boundary of the brain. To model the power of a μLED, an omnidirectional plane source is inserted at the center of the brain. The power of the source is defined to be two times the actual power to account for the emission directivity of the μLED. The intestine tissue [μ_a: 26.3 cm^{-1} (at 475 nm), μ_s': 33.25 cm^{-1} (at 475 nm)] is modeled as two coaxial cylinders filled with chyme, with the outer one corresponding to the serosal membrane (r = 1.8 mm) and the inner one corresponding to the mucosal membrane (r = 1.5 mm). The gut fiber is placed at the center of the coaxial structure and the region of the gut wall is employed for the light transport equation. The μLED emission profile is approximated by a power cosine function. Light emitted from the center of the μLED is propagated to the inner surface of the intestine to determine the fluence rate at the inner wall, which is used as a boundary source to calculate the power distribution in the intestine region. An optogenetic threshold of 0.1 mW/mm^2 is used to estimate the optical penetration depth and volume in all simulations[171–173].

Thermal simulations. Finite-element simulations via COMSOL Multiphysics (Version 5.6) were used to determine the temperature profile of tissues during μLED operation. The transient heat transport equation in a biological tissue can be expressed as $\rho C_p \frac{\partial T}{\partial t} + \rho C_p \boldsymbol{u} \cdot \nabla T - k\nabla^2 T = Q + Q_{bio}$, where $\rho, k\ C_p$, and $\boldsymbol{u}$ are the density, thermal conductivity, heat capacity, and fluid velocity, respectively. Q_{bio} represents a volumetric bioheat source term that can be further

expressed as $Q_{bio} = \rho_b C_{p,b} \omega_b (T_b - T_2) + Q_{met}$. T_b (310.15 K), $C_{p,b}$ (36000 J/kg.K), ω_b(0.008 s^{-1}), ρ_b (1057 kg/m^3), Q_{met} (9132 W/m^3) are the arterial blood temperature, specific heat of blood, blood perfusion rate, blood density, and the metabolic heat source, respectively. In addition to the metabolic heat source, there are two other sources of heat that originate from the μLED. The first heating source is due to the absorbance of optical power in the tissue, and the second is direct heat dissipation associated with μLED inefficiency. For modeling heat transport in the brain, the first term was introduced through coupling of the heat transfer module with the radiation in absorbing-scattering medium module in COMSOL, and the second term was introduced by defining a surface heat source at the μLED. The temperature profile in the gut was obtained without considering the optical absorption term due to the high light transmission through the chyme region. In addition, heat generated by blood perfusion was not considered in the intestinal tissue.

Mechanical simulations. The finite element modelling software, ABAQUS 2019 (Dassault systems), was used for simulating the stress distribution profiles in different fibers and the fiber displacement during brain tissue micromotion. The components that make up the fiber, such as the polymer cladding, and metal microwires, are represented with an 8-node 3D brick element in a HEX shape (C3D8H) with the corresponding mechanical properties. The biological tissue is represented as a 3D brick element with a TET shape (C3D10H). To simulate the relative motion of the brain fiber in the brain tissue, the tissue at the fiber tip was displaced by a fixed amplitude (0.01-0.1 mm) in a direction orthogonal to the fiber axis, while the other fiber end was held fixed to mimic skull-fixation in an implanted animal. A friction coefficient of 0.3 established contact interaction between the tissue and the fiber. The displacement of the fiber tip was quantified as a function of tissue micromotion. To simulate the stress distribution profiles in the gut fiber during surgical implantation process, the fiber was curved at different radii of curvature and the % strain in the copper interconnects was evaluated. To simulate the stress distribution profile as a function of polymer cladding stiffness, the gut fiber was held fixed at one while the other end was set free to deflect which mimics the implanted probe that is sutured to the stomach wall but is free to deflect in the gut lumen. Upon application of a small point load *F* at the free end, a deflection in the fiber was produced and the corresponding misses stress profile in various fiber components was captured.

Supplemental Note B1: Interconnects to support microelectronics in thermally drawn fibers

Incorporation of microelectronic chips in polymer fibers requires introduction of conducting interconnects that can robustly bond with the solid-state devices and power them without substantial resistive heating. However, achieving this with thermal drawing process is a challenge, as the technique imposes restrictions on the thermomechanical properties of constituent materials in a fiber that should have similar viscosity at the drawing temperature[24]. As such, possible material candidates that are compatible with fiber drawing and can function as interconnects are: 1) conducting composites, and 2) low melting point (T_m) metals. However, common conducting composites have conductivity that is 7-8 orders of magnitude lower than that of metals, which makes them unsuitable for use as interconnects[35,39]. The low T_m metals have sufficient conductivity but are more likely to exhibit fluid instabilities and undergo capillary breakup during fiber drawing[43,174]. To overcome these challenges, we leverage recently developed approach of convergence drawing[37,47]. During convergence drawing microwires of any material, irrespective of its thermomechanical properties, are fed into shrinking channels of a polymer preform. As the diameter of the channel approaches that of the microwire, the former is incorporated into the polymer cladding and is drawn by a combined effect of shear forces exerted by the viscous polymer and the pulling force of the capstan. We adapt this method to introduce microscale interconnects of Ag-Cu (40 μm) into multifunctional fibers (Video V1). To facilitate exposure of metal interconnects, the convergence process was carefully optimized such that the Ag-Cu microwires were positioned at a distance ≥15 μm from the top fiber surface.

Supplemental Note B2: Incorporation of semiconductor devices during fiber drawing

We demonstrate a self-assembly mechanism that enables robust *in-situ* electrical bonding of μLEDs as well as packages them in a layer of insulating polymer cladding at scale[47]. For this purpose, we assembled a multilayer poly(carbonate) (PC) preform (Fig. S3a) that consisted of two convergence layers (7 mm × 2.4 mm × 25 cm), a thin spacer layer (7 mm × 0.2 mm × 25 cm) and a central chip-containing layer (7 mm × 1.2 mm × 25 cm). Multiple microscale pockets (20 pockets, 300 μm × 300 μm × 50 μm) were machined within the central chip layer that

accommodated µLEDs (UT170, Cree). The µLEDs have metal bonding pads on either side of the $In_xGa_{1-x}N$ emissive layer, which facilitates *in-situ* interconnect bonding during the draw. The preform was consolidated along with the µLED chips at 185 ºC for 1 hr. We utilized a 2-step drawing process to obtain the resultant multifunctional fibers. In Step-1 (Fig. S3b) the preform was drawn along with the convergence of 40 µm Ag-Cu microwires that served as interconnects. To engineer *in-situ* bonding between chips and interconnects, we used a draw-down ratio of 25-30 that was higher than the predetermined value of 20, resulting in an "over-convergence" state. At this condition the microwires cut through the thin polymer spacer layer (~10 µm) and bond to the metal contact pads of µLEDs (Fig. S3b, Inset). The µLEDs themselves flow along with the viscous polymer due to shear forces during the draw. In Step-2 of the drawing process, we incorporated the microscale fiber produced in Step-1 through convergence inside an elastomeric cyclic olefin copolymer (ECOC) preform that also hosted a channel for microfluidic delivery and tungsten recording microelectrodes. The use of low T_g (90 ºC) ECOC preform for Step-2 of the drawing process ensured that the converging chip-embedded PC fibers did not thermally deform during the draw (T_g of PC = 150 ºC). Moreover, ECOC also provided moisture barrier properties serving as a packaging layer. Figure S3c shows a digital micrograph of a chip-loaded PC preform prior to thermal consolidation. Figure S3d shows the set-up for step-2 of the drawing process. The cross-sectional geometries of fibers from Steps 1 and 2 are conserved (Fig. S3 e-f). All integrated µLEDs across several meters of fibers from Steps 1 and 2 were functional and electrically connected (Fig. 3 g-i). Finally, the current-voltage (I-V, Fig. S3j) and light-output characterization (Fig. S3k) of several sections of as-drawn fibers confirmed the robustness of *in-situ* electrical bonding. Thus, like any other fiber functionality, microelectronic components are also amenable to scalable monolithic integration inside a multifunctional polymer fiber.

Supplemental Note B3: Comparison of NeuroStack module with battery-free technologies

Battery-free approaches for powering bioelectronic devices can be classified into radiative far-field and non-radiative near-field power transmission. The far-field approach leverages radio waves in the range of 400 MHz to 3 GHz that are straightforward to generate and provide relatively long transmission distances (~1 m). However, these frequencies also interfere with other telecommunication technologies such as WiFi (~2-5 GHz) and GPS (~1-2 GHz) which makes far-field radio waves susceptible to electromagnetic interference with these background

signals. Moreover, the high frequency radio waves can also interfere with themselves upon reflection or scattering from metal objects. On the other hand, the non-radiative near-field power delivery relies on induction of electromotive force in an electrical conductor due to a changing external magnetic field. In this approach the receiver coil is magnetically coupled to the transmitter coil at a target resonance frequency (100 kHz-100 MHz). While the near-field coupling is less susceptible to background interferences and reflections, its power harvesting efficiency varies as a cosine of the angle between the transmitting and receiving coil making this approach susceptible to angular variations during animal behavior. Moreover, both these approaches require design and tuning of transfer coils or resonant cavities for power transmission around behavioral arenas and large radiofrequency sources, which need optimization depending on the geometry and complexity of behavioral assays. This restricts the size of the behavior arena and limits long range operation in large complex spaces. The coupling of electrical power in battery-free devices is also restricted by volumetric and areal capacity of the implantation site[175,176] and limitations imposed by the maximum allowable specific absorption rate in small animals. For example, the size of an implantable receiving antenna mounted on the skull cannot exceed a diameter of 10-12 mm in mice[177]. Thus, it is challenging to support increasingly complex and power-hungry multifunctional devices with these approaches. Pioneering approaches that explore antennae implantation on the animal back have been demonstrated, however they require specialized surgical procedures and may experience misalignment induced by relative motion over extended experimental timescales[177,178].

Supplemental Note B4: Transient voltage pulse shaping removes capacitive artifacts

We hypothesized two possible sources of optical stimulation induced artifacts in our devices: 1) photoelectrochemical (PEC); 2) electromagnetic (EM). We quantified the PEC artifact at the electrode-electrolyte interface in a control experiment involving pulsed illumination of the tungsten electrodes with a 473 nm laser source in phosphate buffered saline (PBS) while simultaneously recording the electrode polarization versus a ground wire. No PEC artifacts were observed at a range of illumination intensities between 5-30 mW/mm^2. This is consistent with the large bandgap of native tungsten oxide layer (WO_3, 2.85 eV) which can function as a photoanode in presence of higher energy photons ($\lambda < 435$ nm)[179]. EM or capacitive artifacts are routinely observed in a device configuration that places high-voltage and fast-charging

interconnects in close proximity with signal carrying electrode lines connected to a high impedance load. In our fibers the recording tungsten microelectrodes and the Ag-Cu interconnects separated by a polymer dielectric form a pair of capacitors (Fig. S14a). The charging of these capacitors upon passage of µLED voltage signal produced robust artifacts that were time-locked to the start and end of the pulse with inverted polarities corresponding to charging and discharging currents. To minimize these artifacts, we utilized transient pulse shaping strategy that modified the rise/fall (r/f) times of voltage pulses. We observed a dramatic reduction of EM artifacts as the r/f times varied from 0.01 ms to 20 ms (Fig. S14 b-c). Notably this was observed for a range of optical intensities between 3-30 mW/mm^2 and pulse widths between 5-25 ms common in optogenetics studies. For pulses with r/f times >10 ms the generated artifact (10-20 µVpp) was found to be within the background noise level (~40 µVpp) and hence undetectable in the raw traces (Fig. S14 d-i). These findings were further corroborated with *in-vivo* opto-electrophysiology in the ventral tegmental area (VTA) of wild type (C57BL/6J) mice, wherein artifact-free traces were obtained for the trapezoidal shaped stimulation pulses (r/f time 10 ms) (Fig. S15 a-h). Thus, transient pulse shaping enabled artifact-free opto-electrophysiology with the microelectronics fibers.

Supplemental Note B5: Multisite, multifunctional fiber device enables simultaneous gut-brain implantation

We reasoned that developing and validating survival surgeries that allow multisite implantation of multifunctional fibers will motivate future studies of interoceptive neural circuits with these or similar multifunctional wireless devices. Given the miniature dimensions of research rodents, a multisite device should be controlled by a single wireless module connected to the common input/output (I/O) interface. However, this requirement prohibits mounting of the stiff brain fiber on a stereotaxic arm and restricts its motion in three dimensions. This, in turn, prevents accurate positioning of the fiber within a brain region of interest. To overcome these challenges, we developed a stretchable interconnect in the form of a helically coiled fiber with embedded metal microwires using thermal drawing. To produce such a fiber with broken axial symmetry we leveraged *in-situ* strain engineering achieved through the appropriate selection of the core and cladding polymers[180]. Strain engineering in thermally drawn fibers relies on accumulation of residual strain (pre-stretch) in an elastomeric core when it is drawn within a non-elastomeric

cladding material, originating from differences in viscosities at the draw temperature. This stored strain energy can produce out-of-plane buckling of the elastomeric core if it is composed of materials with differing Young's moduli and has a non-centrosymmetric cross-sectional geometry. Using these insights, we produced a conductive fiber-based stretchable interconnect composed of SEBS core with converged tungsten microwires inside a mechanically peelable poly(methyl methacrylate) (PMMA) cladding (Fig. S32 a-d). The dual-site gut-brain device that incorporates such a stretchable interconnect is shown in Fig. S32e. Stress-strain measurements on these interconnects showed that the constituent materials remain in the elastic response regime for uniaxial stretching exceeding 500%, which is over two orders of magnitude higher than the non-helical analogues (Fig. S32f). Current-voltage measurements of a μLED bonded to the interconnect at different levels of stretch (Fig. S32g) defined the functional threshold at which the interconnect transitions from an elastic to a plastic deformation, causing an open circuit (>200% strain). Electrical performance under continuous uniaxial cyclic stretching tests (10,000 cycles, 1 Hz, 50 and 100%) further highlighted their robust electromechanics, wherein a microscale surface-mount resistor bonded to the fiber was used as a signal read-out (Fig. S32h). As we demonstrate below, the typical mechanical deformation experienced by the interconnect during the surgical procedure remains well below their functional threshold value characterized here, thereby allowing us to freely extend the implantable fibers further out in space for precise stereotaxic implantation. Next, we developed a survival surgery with these multisite, multifunctional fiber devices by targeting implantation of the gut fiber in the proximal small intestine with concomitant implantation of the brain fiber in the VTA (Fig. S33a). The duodenal surgery was performed as previously described (see Methods section for details). Following the duodenal surgery, the brain fiber was implanted targeting the VTA. The free extension of the brain probe in three-dimensional space enabled by the stretchable helical fiber interconnect facilitated precise brain implantation (Fig. S33 b-d). Following one-week post-operative recovery, food intake, water intake, and locomotor behaviors were evaluated and compared to pre-operative values using a within-subject design. While food intake and water intake somewhat re-aligned between the dark and light cycles post-surgery, the surgery had no impact on overall food or water intake (Fig. S33 e-f). Moreover, there were no changes in locomotor activity in the implanted subjects (Fig. S33 g-h). These representative demonstrations exemplify use of wireless

microelectronics fiber technology in combined gut-brain or multi-organ studies in awake behaving mice.

Supplemental Note B6: State-of-the-art in multifunctional bioelectronic interfaces

As summarized in Table S1, existing approaches to produce multifunctional bio-integrated devices for brain or peripheral organs exclusively rely on cleanroom-based lithography techniques[128,132,181]. Such resource intensive approaches are unsuitable for rapid design customization or modifications to device layouts as they require design of new photomasks for each pattern and optimization of the accompanying processing steps[181]. The thin film nature of lithography also precludes single-step, monolithic integration of multiple functionalities in a bioelectronic device. Thus, all previously reported schemes require independent fabrication of individual device modalities (multi-step process by itself) followed by careful manual assembly of layers to yield the final device[23,132,182]. Moreover, limitations on device scalability and lengths due to the use of silicon wafers as supporting substrates pose additional challenges for deployment in anatomically hard-to-reach sites in peripheral organs. The field of bioelectronics lacked alternative routes that overcame these limitations to produce multifunctional implants at scale for brain and peripheral organs without compromising biocompatibility and functional sophistication. Through this work we introduce an entirely new class of multifunctional and wirelessly capable polymer-based microelectronic fibers that enable organ-specific interrogation of neuronal and non-neuronal cell-types that govern animal behavior. To accomplish this, we combine the scalability and design customization afforded by multimaterial thermal drawing[24] with the sophistication of semiconductor microelectronics. This approach allows us to deterministically tune the device mechanics to produce microscale wireless interfaces for the anatomically and functionally disparate organs such as the brain and the GI tract. In contrast to thin-film lithographic approaches, our method uniquely allows one-step, monolithic device fabrication in a manner that produces sub-km lengths of microstructured polymer filaments starting from a macroscale preform. This preform-to-device route also lends itself favorably for integrating solid-state microelectronic chips as demonstrated in Fig. S3 wherein we engineer electrical bonding of metal interconnects as well as *in-situ* packaging during the drawing process. This enables us to produce fully packaged and electrically pre-bonded multifunctional microelectronic fibers at scale.

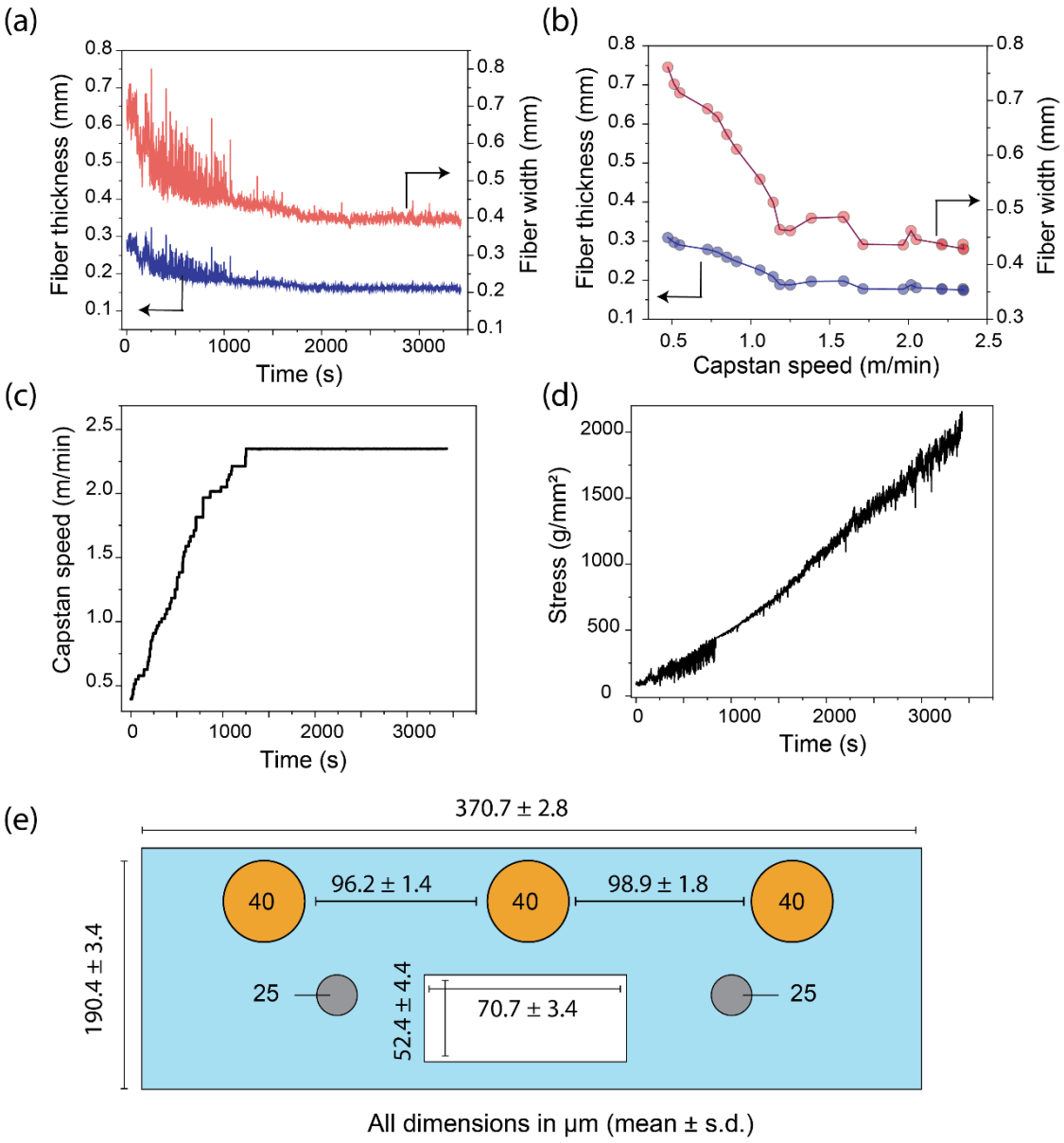

Figure B1. Thermal drawing data for the brain fibers

(a) Variation of fiber width (red trace) and thickness (blue trace) during the draw, where arrows indicate the corresponding y-axes for respective plots; **(b)** Variation of fiber width (red trace) and thickness (blue trace) with capstan speed at fixed preform feed-rate of 1 mm/min, where arrows indicate the corresponding y-axes for respective plots; **(c)** Variation of capstan speed during the

draw; **(d)** Variation of fiber stress during the draw; **(e)** Average dimensions of the fiber features over 5 randomly selected cross-sections.

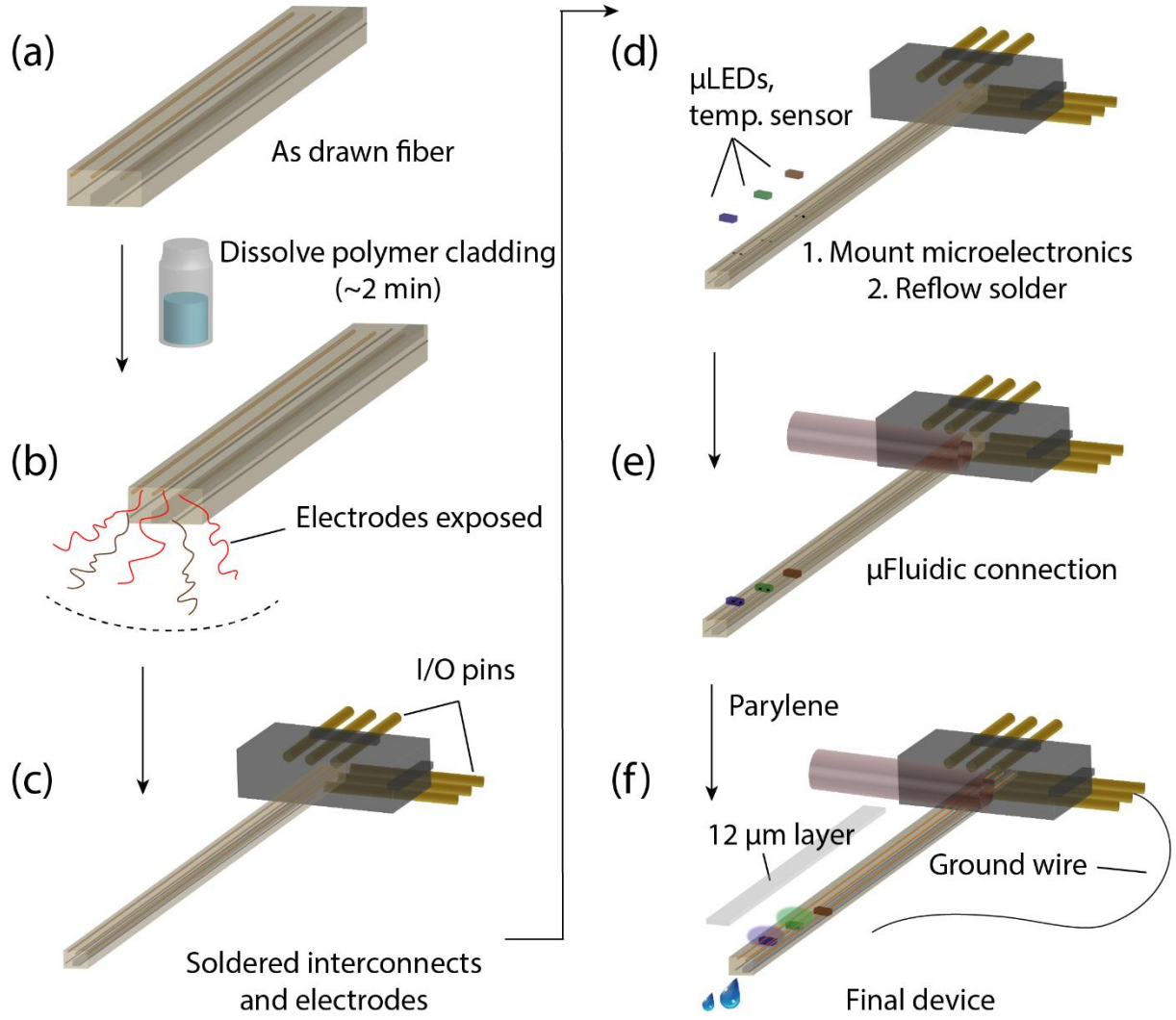

Figure B2. Process flow for fiber connectorization

(a) The PC or SEBS cladding is etched away in an organic solvent such as dichloromethane; **(b)** The embedded metal microwires are exposed and isolated; **(c)** The microwires are soldered to header pins; **(d)** The µLEDs and thermal sensors are mounted on the fiber surface with reflow soldering or thermally curable conductive silver epoxy; **(e)** The microfluidic channel is connected to external access tubing with a T-junction; **(f)** Finally, the ground wire is soldered onto a header pin and parylene-C is vapor deposited onto the fiber.

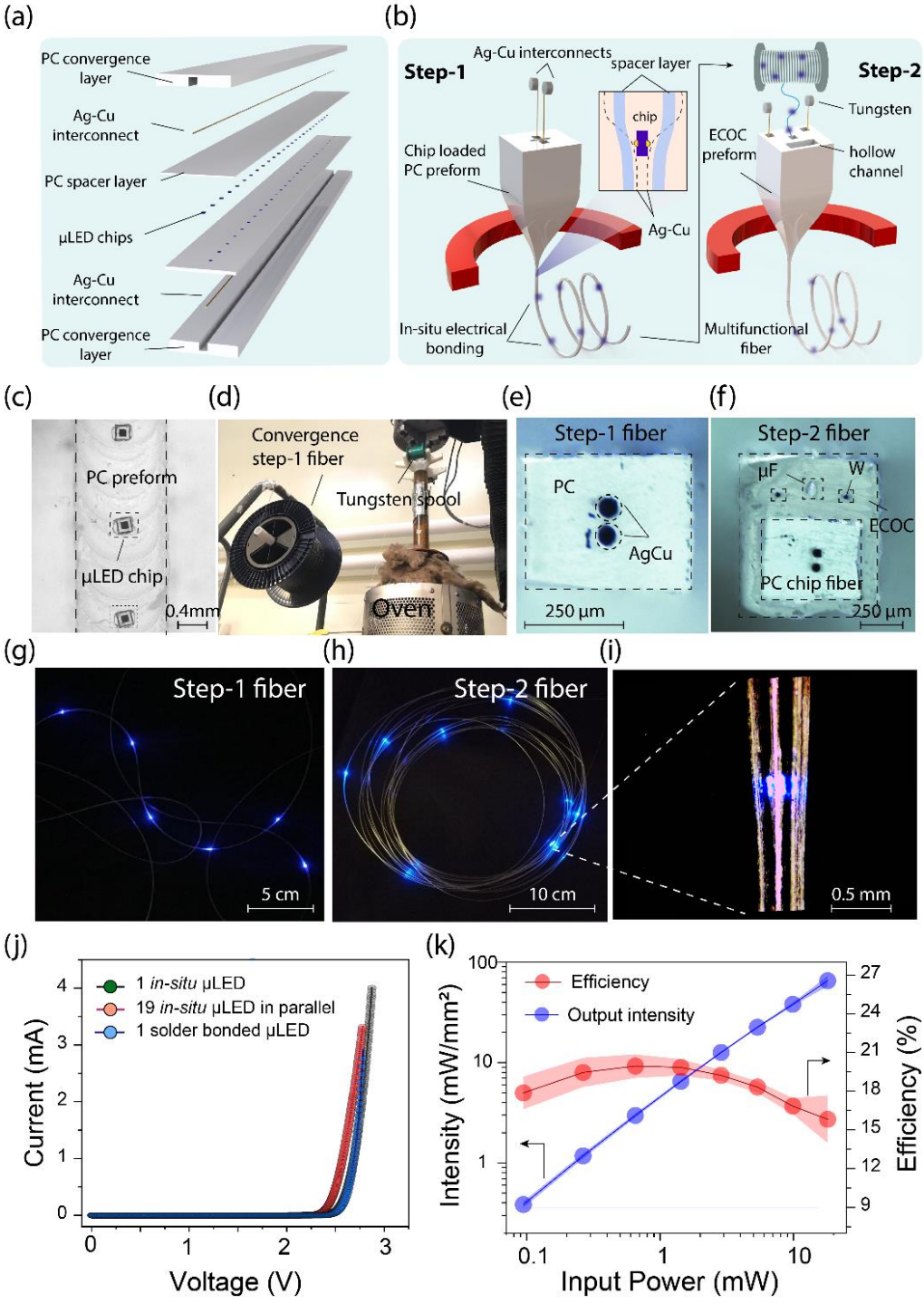

Figure B3. Integration of microelectronic devices at the preform stage permits *in-situ* electrical bonding and packaging in a multifunctional fiber

(a) Multilayered sandwiched configuration of the preform consisting of two convergence layers, two spacer layers, and a central chip layer; **(b)** (left) Step-1 involves drawing of the chip loaded preform with simultaneous feeding of Ag-Cu interconnects, inset shows the *in-situ* electrical bonding process during the draw, (right) Step-2 involves feeding the fiber obtained from Step-1 into another ECOC preform that can host tungsten microelectrodes and a microfluidic channel; **(c)** Optical micrograph of a μLED loaded central chip layer; **(d)** A photograph showing feeding of Step-1 fiber along with tungsten microwire spools in the ECOC preform; **(e)** Cross-sectional micrograph of Step-1 fiber; **(f)** Cross sectional micrograph of Step-2 fiber; representative photographs showing successful operation of several *in-situ* electrically bonded μLEDs from **(g)** Step-1 fiber and; **(h)** Step-2 fiber; **(i)** Optical micrograph of a fiber-integrated μLED fully packaged in a double layer insulating cladding of PC and ECOC; **(j)** I-V characteristics of *in-situ* fiber integrated blue μLEDs (green and red traces) after Step-2 showing robust electrical connection that is comparable to a reflow-soldered μLED (blue trace); **(k)** Light output and efficiency of *in-situ* integrated μLED as a function of input electrical power (n=4 random sections) where arrows indicate the corresponding y-axes for respective plots. Data are presented as mean values +/- s.d. All shaded areas and error bars represent s.d.

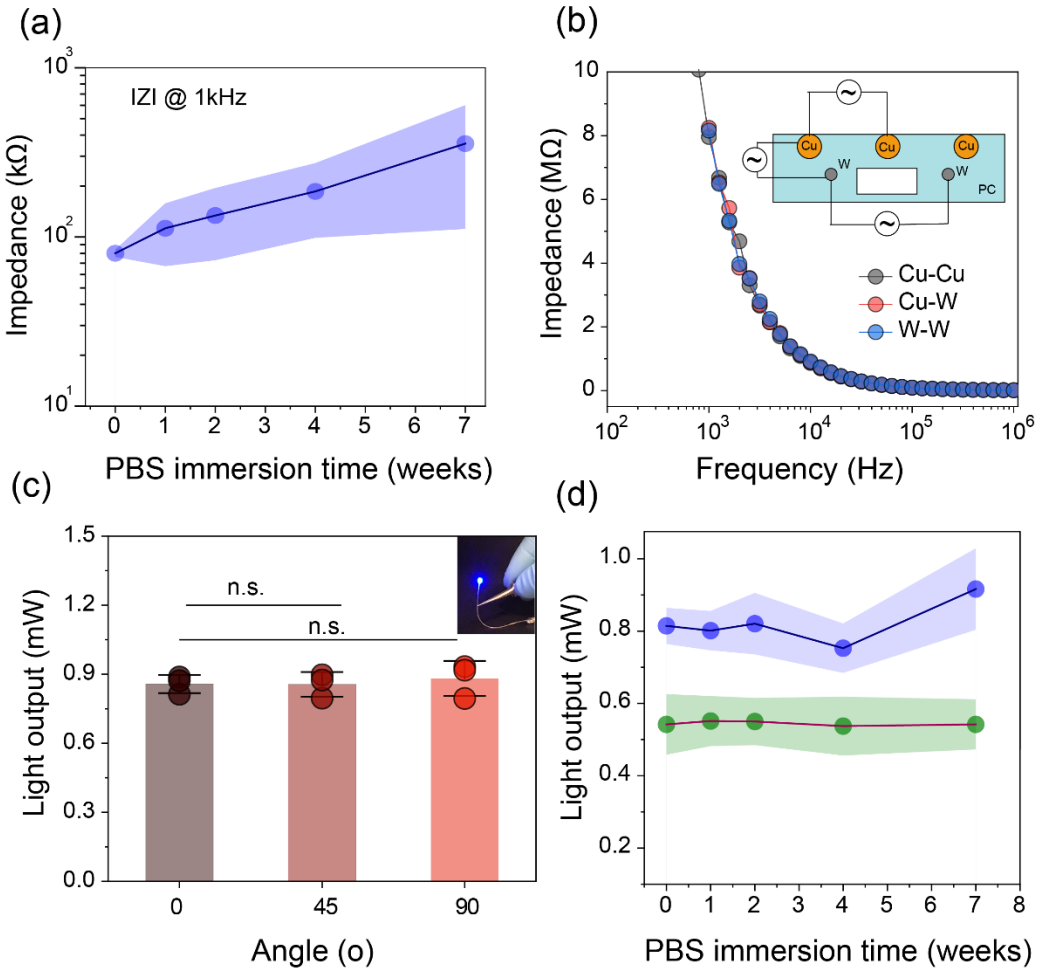

Figure B4. Electrical and optical characterization of the brain fibers

(a) Electrochemical impedance of tungsten microelectrodes at 1 kHz upon immersion in phosphate buffered saline (PBS) bath at 37 ºC over 7-weeks (n=6 devices); **(b)** Measurement of interwire impedance through the polymer cladding in a PBS electrolyte; **(c)** Light output from the fiber device bent at different angles; 45º: p = 0.97396, *F-value*: 0.00121; 90º: p = 0.64752, *F-value* = 0.24356 (n=3 fibers each, One-way ANOVA and Tukey's comparison test); **(d)** Light output from the fiber device that was immersed in PBS bath at 37 ºC over 7-weeks (blue trace, 470 nm µLED; green trace, 527 nm µLED, n=4 devices each). Data are presented as mean values +/- s.d. All shaded areas and error bars represent s.d.

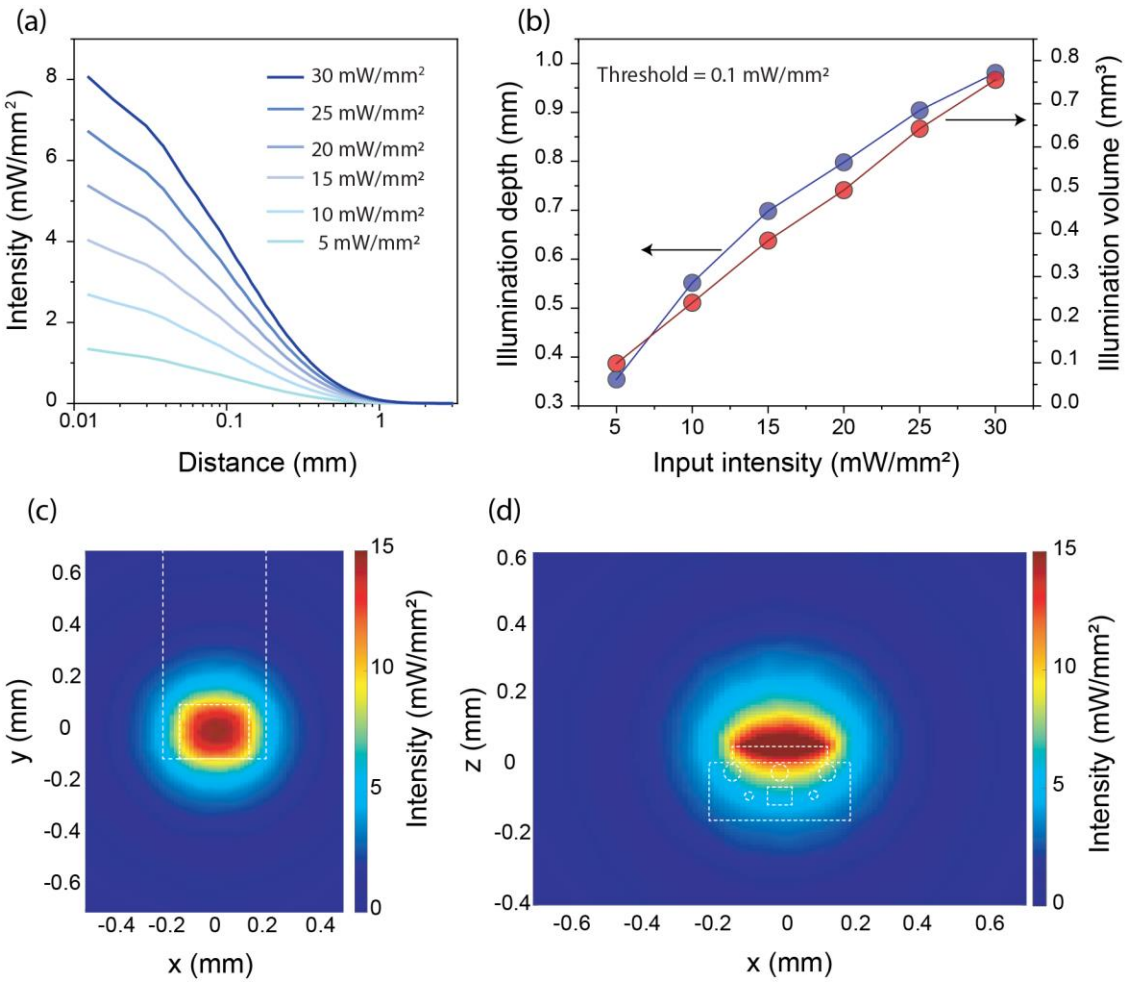

Figure B5. Optical FEM simulations of brain fibers in the brain tissue

(a) Variation of optical intensity with distance from surface of a fiber μLED (λ = 470 nm) at input intensities between 5-30 mW/mm^2; **(b)** Variation of illumination depth and volume with different input optical intensities (λ = 470 nm) where arrows indicate the corresponding y-axes for respective plots; **(c-d)** Spatial distribution of optical intensity at 30 mW/mm^2 around the fiber tip in the **(c)** x-y and; **(d)** x-z plane.

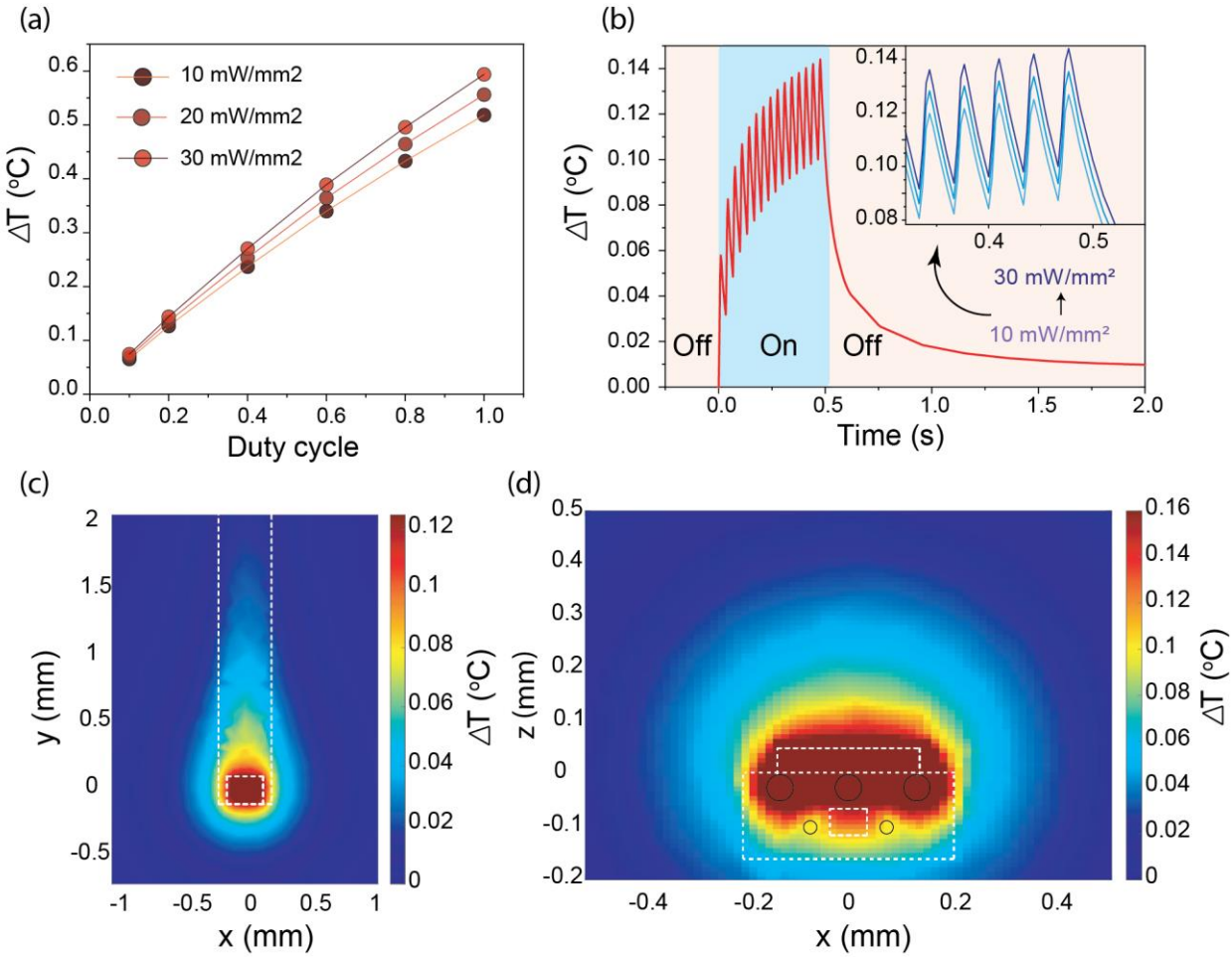

Figure B6. Thermal FEM simulation of brain fibers in the brain tissue

(a) Variation of local temperature at the surface of the fiber μLED (λ = 470 nm) as a function of duty cycle and optical intensity; **(b)** Temporal variation of temperature at the surface of fiber μLED at the end of a physiologically relevant optical stimulation pulse train (20 Hz, 20% duty cycle) and intensities of 10, 20, and 30 mW/mm^2; **(c, d)** Spatial distribution of temperature around the fiber tip at the end of an optical stimulation pulse train (30 mW/mm^2, 20 Hz, 20% duty cycle) in the **(c)** x-y and; **(d)** x-z plane.

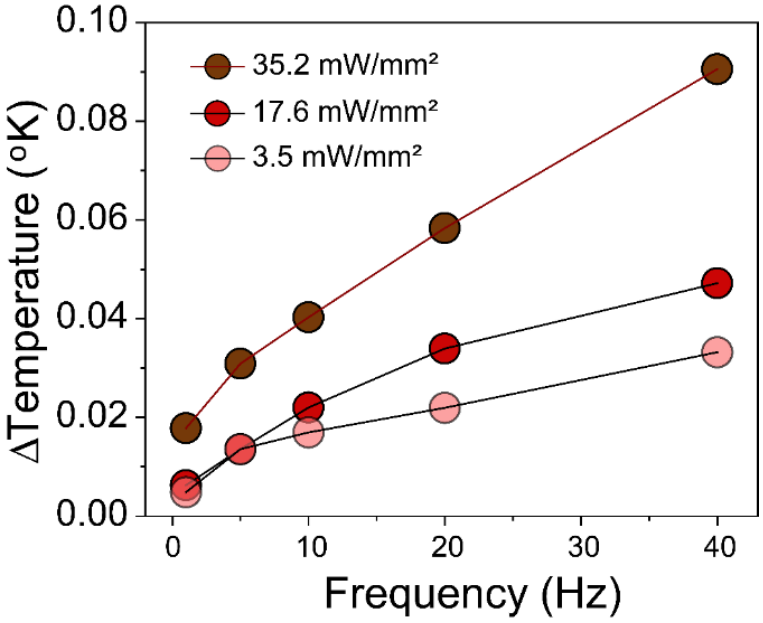

Figure B7. Characterization of thermal sensing modality of the brain fiber

Changes in local temperature around a fiber μLED (λ = 470 nm) detected by a co-located diode based thermal sensor while the μLED is operated at different optical stimulation frequencies and intensities.

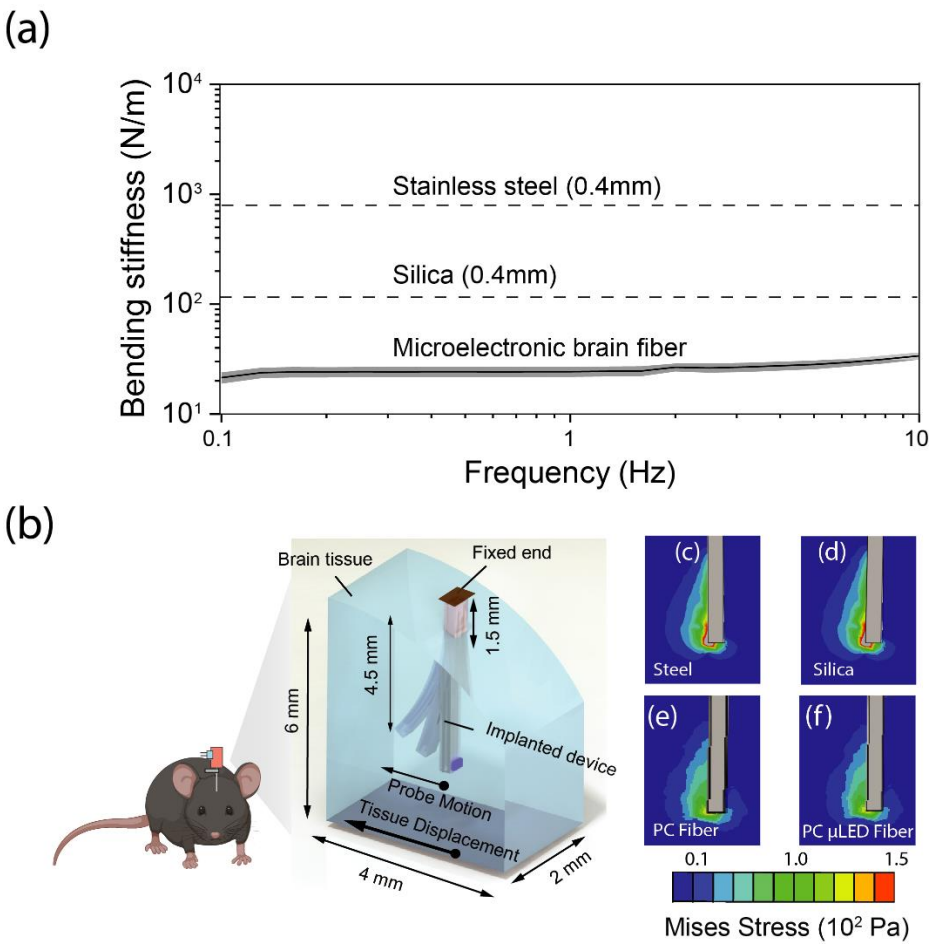

Figure B8. Mechanical FEM simulation of the brain fiber in the brain tissue

(a) Experimental bending stiffness measurement of PC brain fiber (n=3, length = ~1 cm) in a single cantilever mode with frequency sweep and the corresponding theoretical values for a silica waveguide (400 µm, length = 1 cm) and stainless steel wire (400 µm, length = 1cm); **(b)** 3D FEM model that captures the micromotion between fiber implant in brain tissue in the VTA, mimicking a single cantilever mode; **(c-f)** Spatial distribution of the misses stress around the implant tip at brain tissue displacement of 100 µm for **(c)** 400 µm steel wire; **(d)** 400 µm silica waveguide; **(e)** bare PC fiber and; **(f)** PC fiber with µLEDs. Data are presented as mean values +/- s.d. All shaded areas represent s.d.

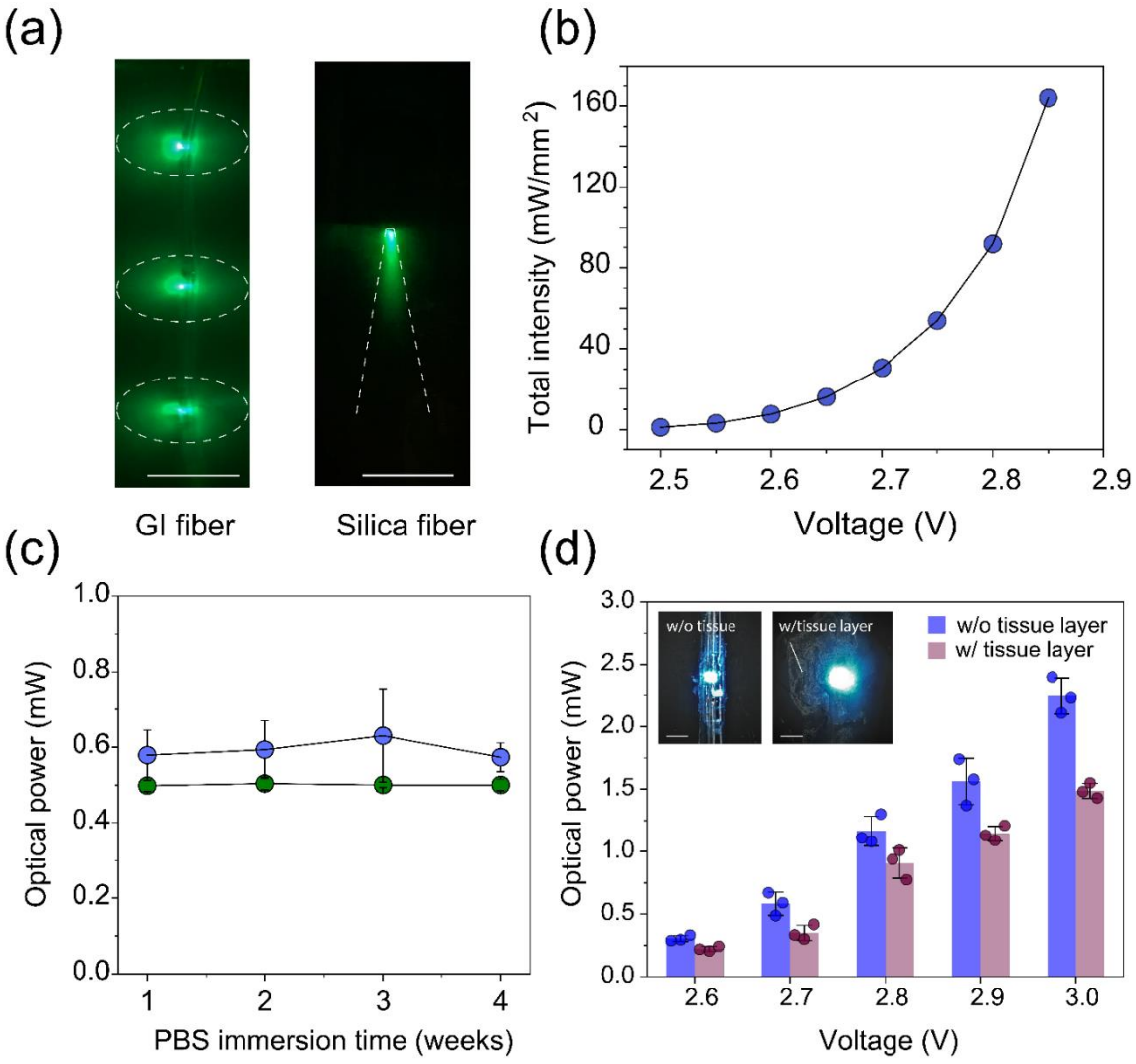

Figure B9. Optical characterization of soft gut fiber

(a) Lateral illumination profile from gut fiber (three 470 nm μLEDs, 10.6 mW/mm^2) as compared to dorsal-ventral oriented light cone from silica waveguide (right) in a 0.1 mM fluorescein solution (right), scale bar 1 cm; **(b)** Cumulative light output from three λ = 470 nm fiber μLEDs connected in parallel; **(c)** Light output from the gut fiber over the course of 4 weeks while being immersed in a PBS bath at 37 ºC for blue (n=3 independent samples) and green (n=3 independent samples) μLEDs; **(d)** Light output from the gut fiber with (n=3 independent samples) and without (n=3 independent samples) an overlaid layer of intestinal tissue. (Inset scale bar 0.5 mm). Data are presented as mean values +/- s.d. All error bars represent s.d.

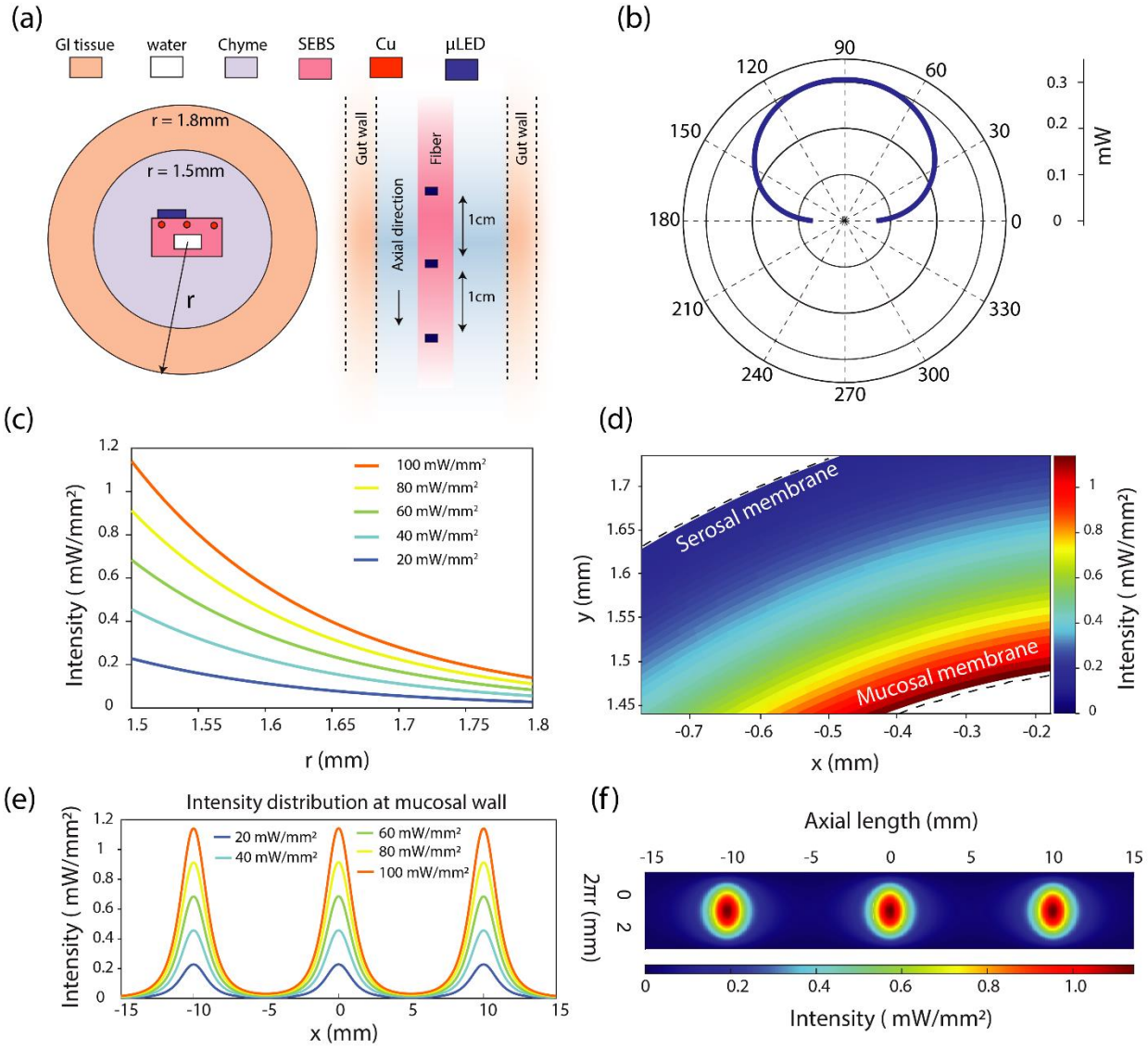

Figure B10. Optical FEM simulations of gut fiber in the intestinal lumen

(a) Schematic of the 3D optical FEM model showing the architecture of the gut fiber and dimensions of the small intestine (left: cross sectional view; right longitudinal view); **(b)** Fitted angular distribution of the µLED power emission profile (λ = 470 nm); **(c)** Radial light intensity distribution between the mucosal (r = 1.5 mm) and serosal membrane (r = 1.8 mm) as a function of µLED emission power; **(d)** Cross-sectional light intensity distribution between the mucosal and serosal membrane at µLED emission power of 100 mW/mm^2; **(e)** Axial light intensity profile at the mucosal wall as a function of µLED emission power; **(f)** Flattened light intensity

distribution profile projected onto the top half of the mucosal membrane plane at a µLED emission power of 100 mW/mm^2.

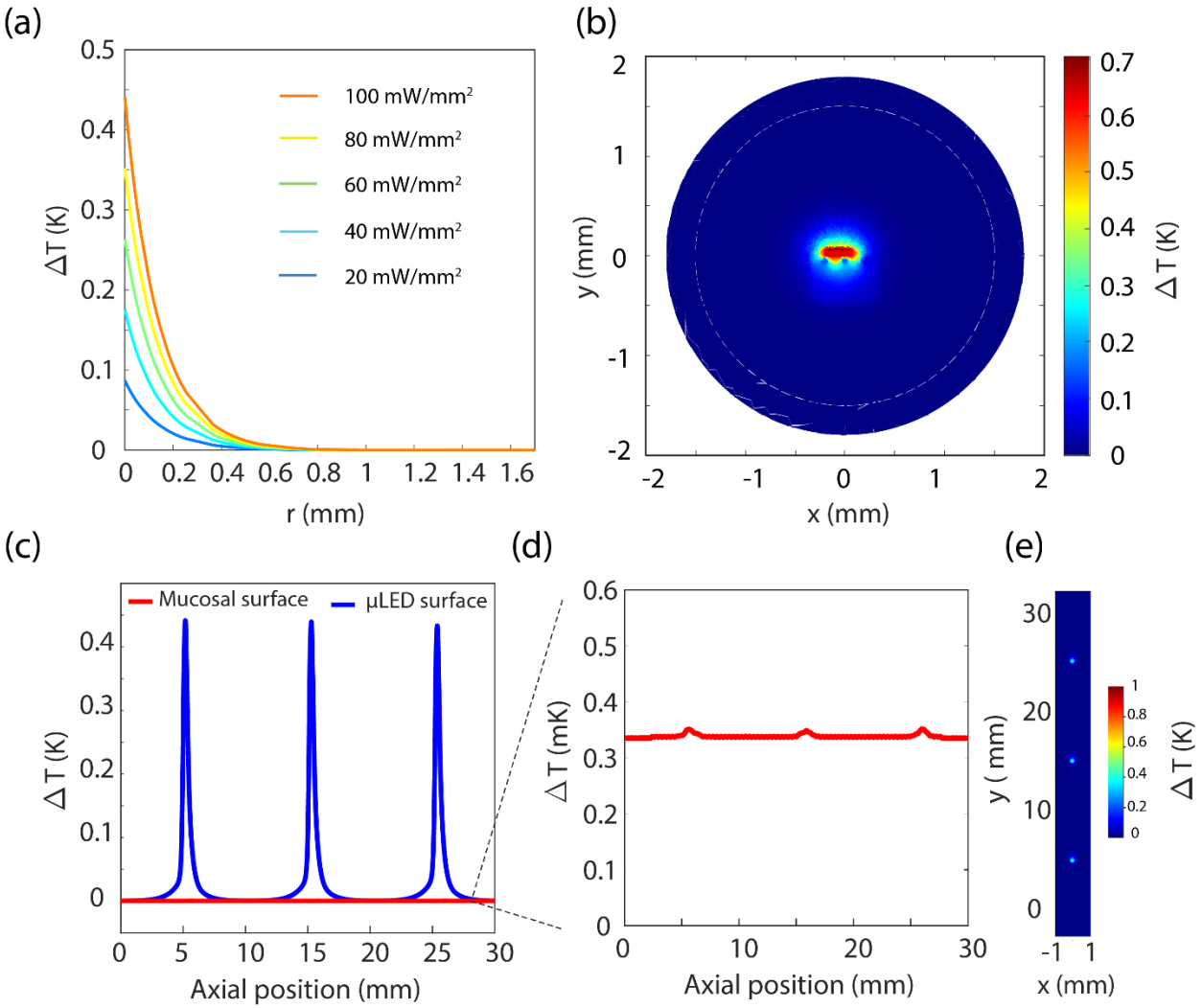

Figure B11. Thermal FEM simulation of the gut fiber in the small intestine lumen

(a) Radial profile of the change in temperature as a function of µLED emission power within the intestinal lumen; **(b)** Flattened profile of temperature change on the mucosal membrane at a µLED emission power of 100 mW/mm^2; **(c)** Axial profile of temperature change across the top µLED surface (blue) and on the mucosal surface (red) at an emission power of 100 mW/mm^2; **(d)** Enlarged axial profile from (c) of temperature change on the mucosal surface; **(e)** Planar cross-sectional profile of temperature change across the top µLED surface at an emission power of 100 mW/mm^2.

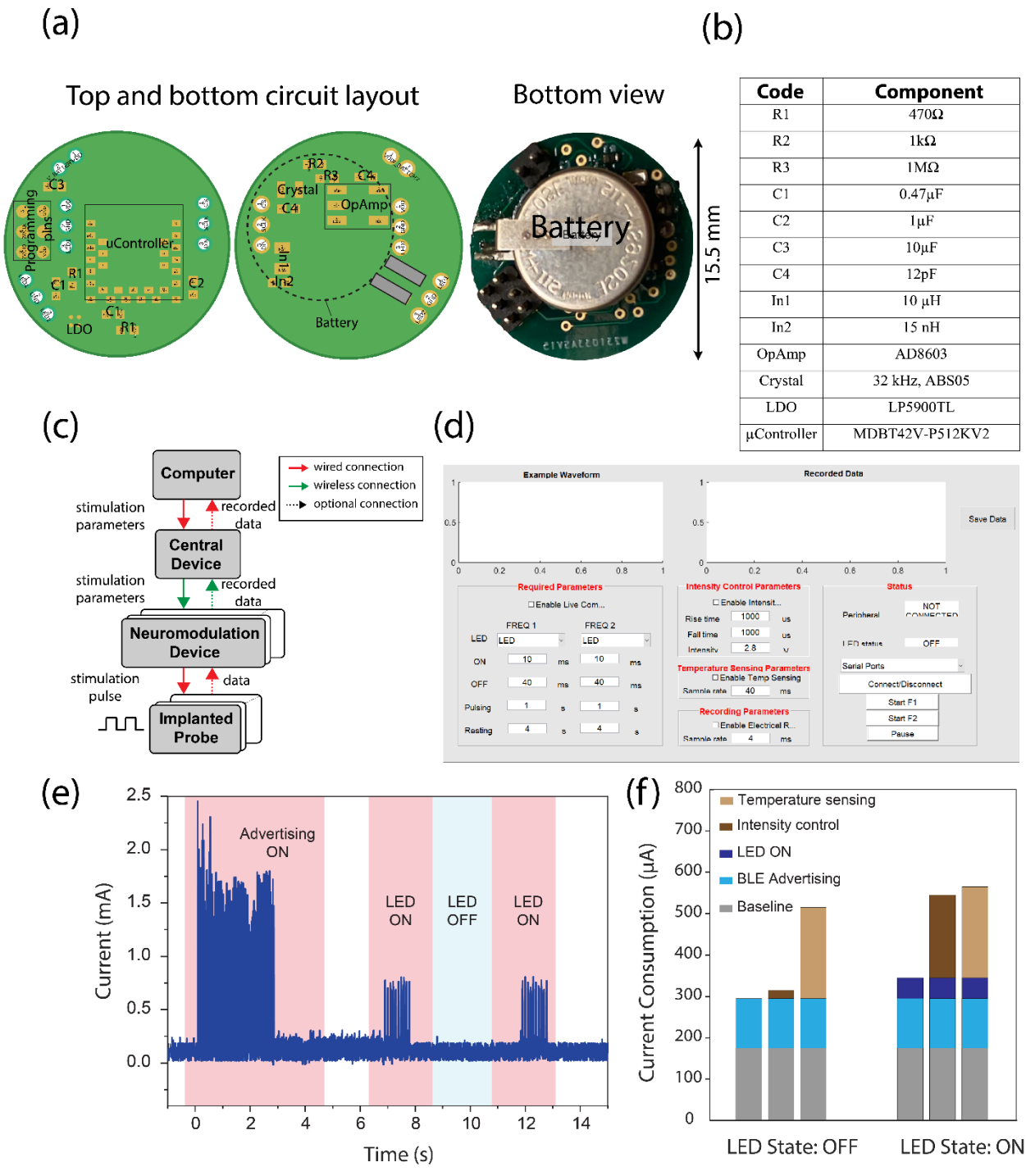

Code	Component
R1	470Ω
R2	1kΩ
R3	1MΩ
C1	0.47µF
C2	1µF
C3	10µF
C4	12pF
In1	10 µH
In2	15 nH
OpAmp	AD8603
Crystal	32 kHz, ABS05
LDO	LP5900TL
µController	MDBT42V-P512KV2

Figure B12. Circuit layout of NeuroStack primary module, graphical user interface (GUI), and power consumption profile across different modalities

(a) Top and bottom circuit layout along with a photograph showing the bottom view of the NeuroStack module which hosts a rechargeable battery; **(b)** Component details for NeuroStack module; **(c)** Flow of information between the neural probe and the base-station computer. The central board can control up to four neuromodulation devices mounted on different animals; **(d)** The GUI implemented in MATLAB to control and communicate with the neuromodulation device; **(e)** Dynamic and **(f)** steady-state power breakdown of the NeuroStack module where the total power consumption scales with other enabling functions such as temperature sensing and intensity control.

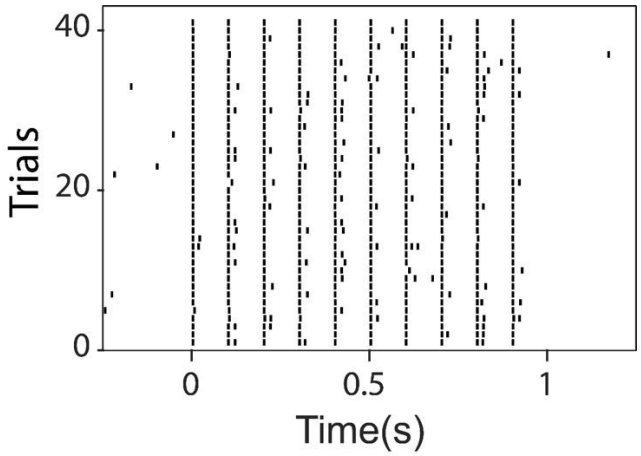

Figure B13. Extended data for figure 5d

Raster plot over 40 stimulation trials confirms reproducibility of the optically evoked electrical activity in mice expressing ChR2 in dopaminergic neurons on Day-20 following the combined viral injection and device implantation surgery.

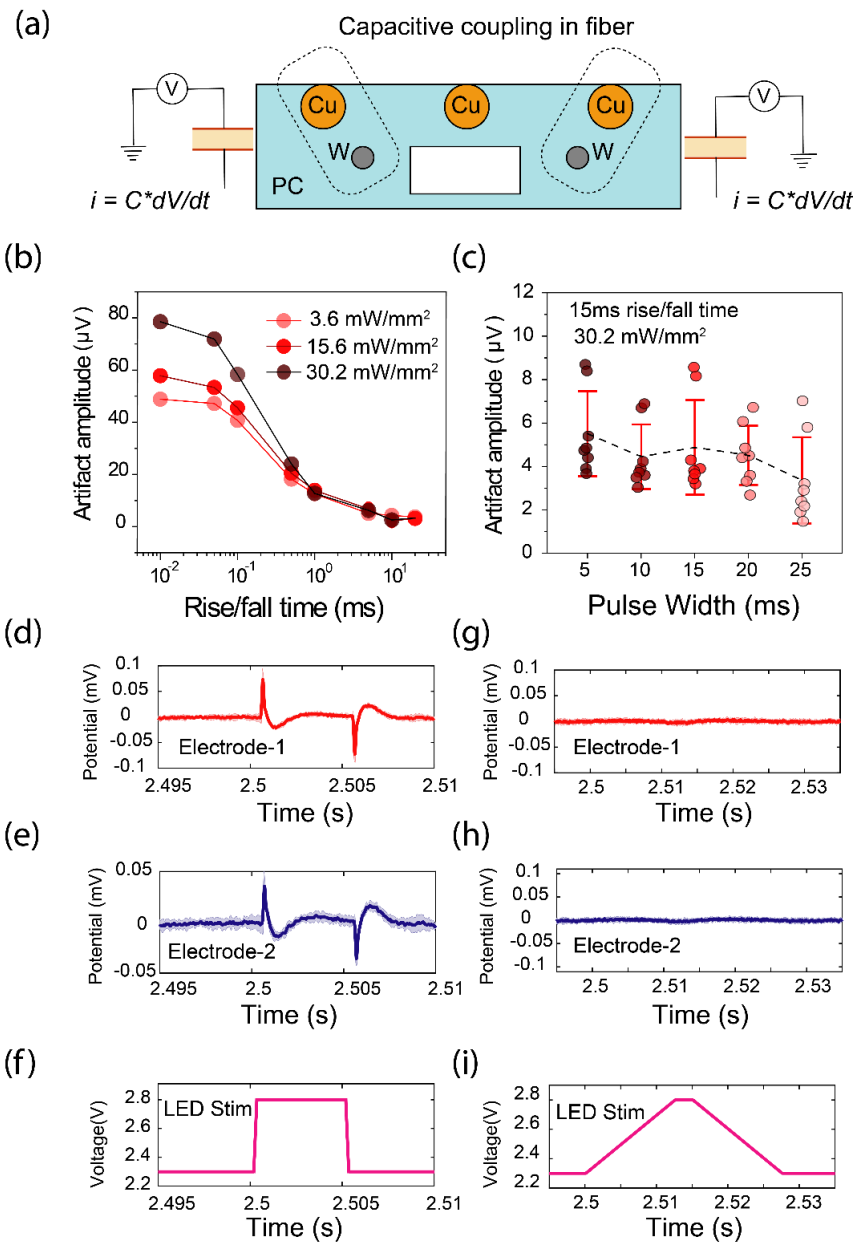

Figure B14. *In-vitro* quantification of capacitively coupled artifacts in brain fiber

(a) Schematic illustration of capacitive coupling between interconnect and electrode microwires separated by a polymer dielectric; **(b)** Artifactual signals recorded at the tungsten microelectrode in PBS vary with the rise /fall time of µLED optical stimulation pulses (5 ms pulse width, 10 Hz) at different intensities; **(c)** Artifact amplitude is invariant to changes in optical stimulation pulse width (n= 4 independent fiber samples, 2 electrodes per fiber); **(d-f)** signals recorded at both tungsten microelectrodes along with corresponding optical stimulation shape for square pulse

with 0.01 ms rise/fall time and; **(g-i)** trapezoidal pulse with 12.5 ms rise/fall time. Data are presented as mean values +/- s.d. All shaded areas and error bars represent s.d.

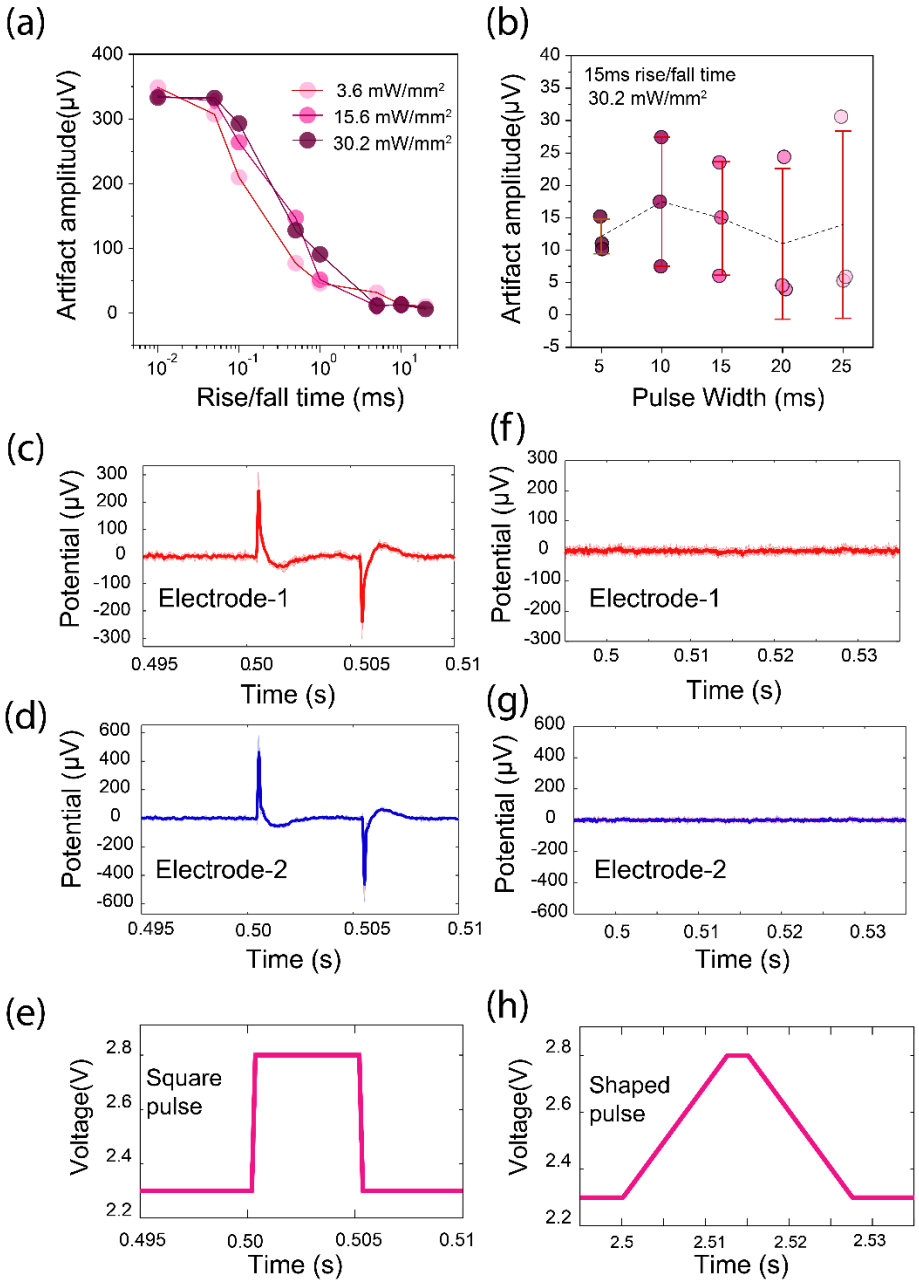

Figure B15. *In-vivo* quantification of capacitively coupled artifacts in brain fiber

(a) Artifact amplitude recorded at the tungsten microelectrode in ventral tegmental area (VTA) of C57BL/6J mice varies with the rise /fall time of μLED optical stimulation pulses at varying intensities; **(b)** Artifact amplitude is invariant to changes in optical stimulation pulse width (n=3 mice); **(c-e)** signals recorded at both tungsten microelectrodes along with corresponding optical stimulation shape for a square pulse with 0.01 ms rise/fall time and; **(f-h)** trapezoidal pulse with

12.5 ms rise/fall time. Data are presented as mean values +/- s.d. All shaded areas and error bars represent s.d.

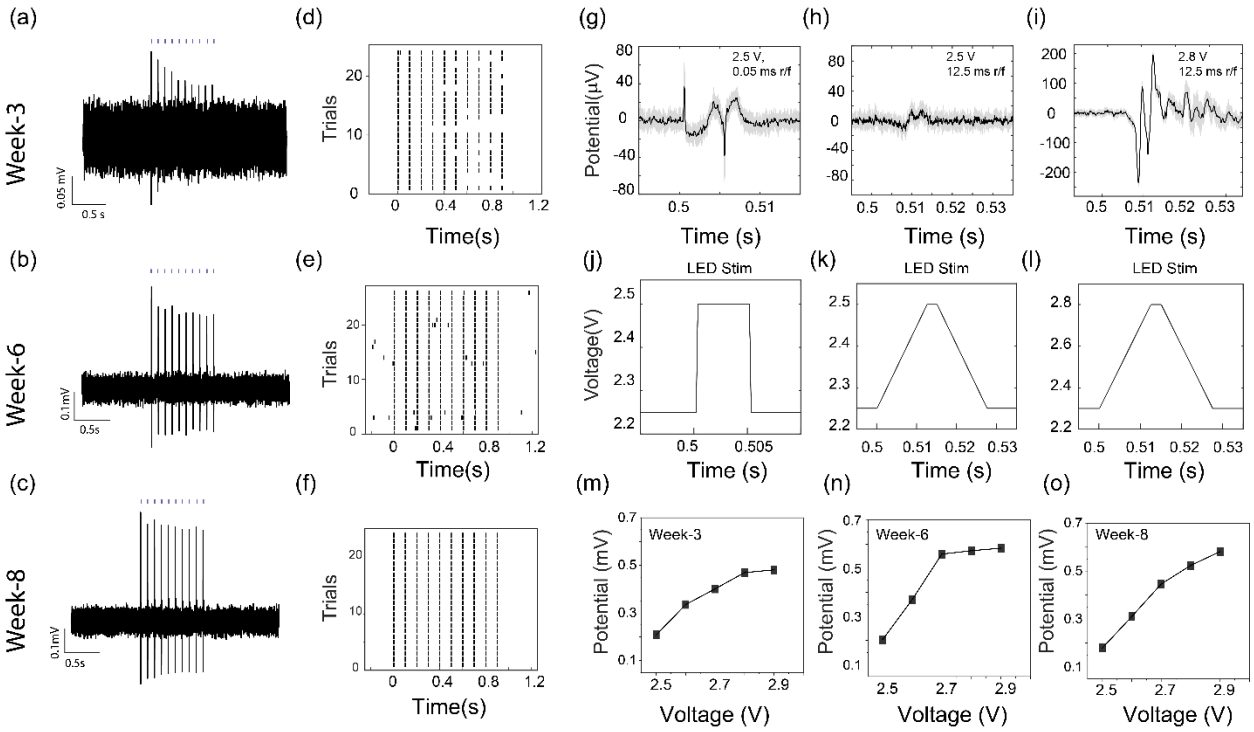

Figure B16. Chronic recordings of optically evoked electrical activity in mice transduced with ChR2 in dopaminergic (DA) neurons

Simultaneous optogenetic stimulation (470 nm, 10.3 mW/mm^2, 5 ms pulse width, 10 Hz, 1 s ON, 4 s OFF, blue markers indicate pulse onset) and recording of neural activity in the VTA of chronically implanted mice expressing ChR2 in DA neurons at **(a)** 3-weeks; **(b)** 6 weeks; **(c)** 8-weeks after viral transfection and fiber implantation surgery; **(d-f)** corresponding raster plots over >20 stimulation trials; **(g,j)** Optical stimulation with square pulse produces capacitively coupled artifacts; **(h,k)** Transient pulse shaping suppresses the capacitive artifact; **(i,l)** Multiunit activity recorded in response to shaped optical pulse (15.6 mW/mm^2, 12.5 ms r/f, 10 Hz); Amplitude of multiunit activity in response to optical stimulation (5 ms pulse width, 10 Hz, 1 s ON, 4 s OFF) increases with increasing stimulation intensity at **(m)** week-3; **(n)** week-6; and **(o)** week-8 time point post implantation for a representative animal. All shaded areas and error bars represent s.d.

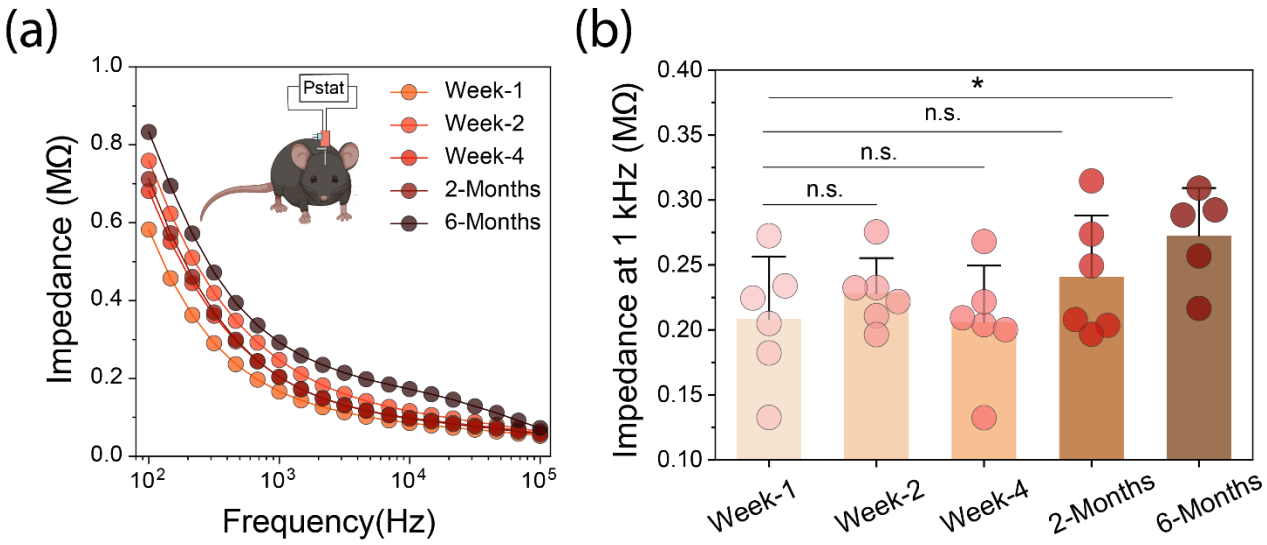

Figure B17. *In-vivo* stability of recording electrodes over 6 months

(a) Impedance spectra of a tungsten microelectrode in a chronically implanted brain fiber from week-1 to 6-months post implantation; **(b)** Corresponding values of the impedance modulus at 1 kHz. Week-2: p = 0.8292, 1-month: p = 0.98448, 2-month: p = 0.64561, 6-month: p = 0.02197 (n=3 mice, 2 electrodes per fiber, repeated measures one-way ANOVA followed by Tukey's post-hoc comparison test). Data are presented as mean values +/- s.d. All error bars represent s.d.

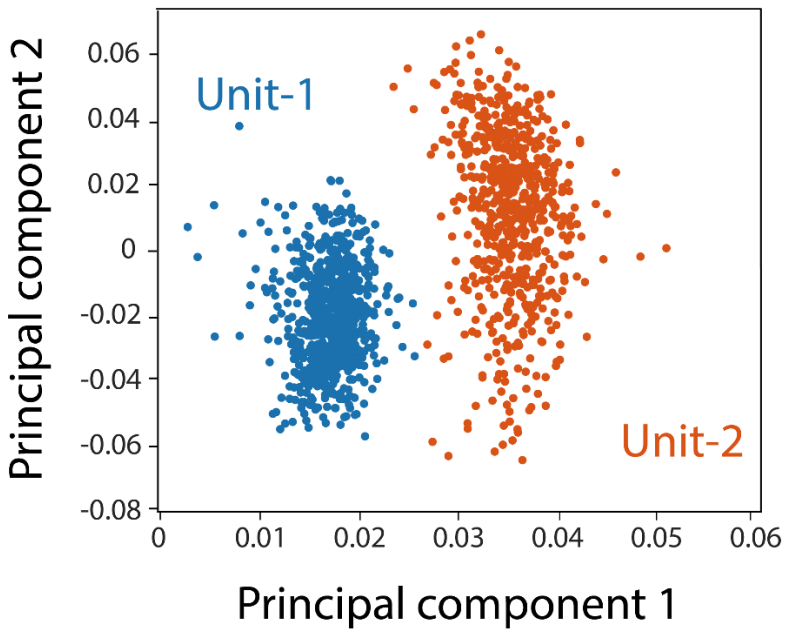

Figure B18. Extended data for figure 5e

Clusters revealed by principal component analysis of isolated action potentials at week-4 in the VTA.

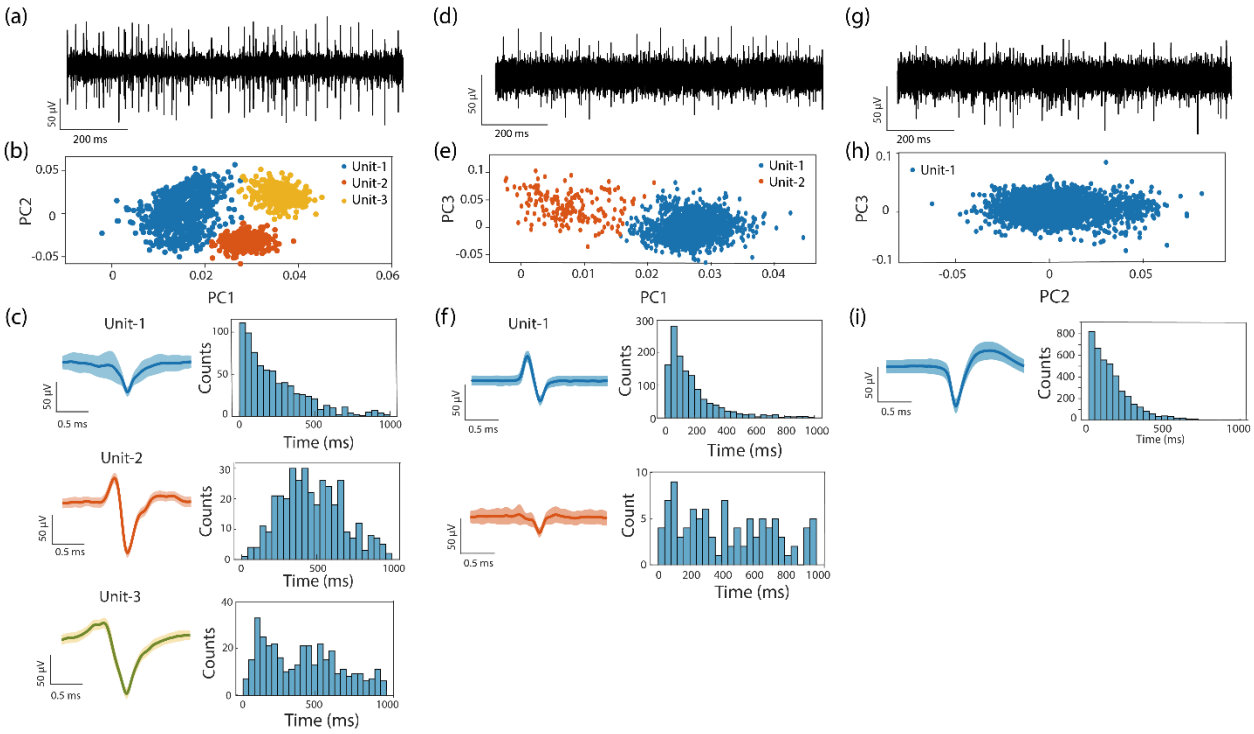

Figure B19. Chronic recording of single unit activity in the VTA at week-2 following implantation

(a,d,g) Raw traces of endogenous activity; **(b,e,h)** Clusters of single units revealed by principal component analysis; **(c,f,i)** Average spike waveforms (left column) corresponding to clustered units and their inter-spike-interval histograms (right column). Data from 3 separate animals. All shaded areas represent s.d., data are presented as mean values +/- s.d.

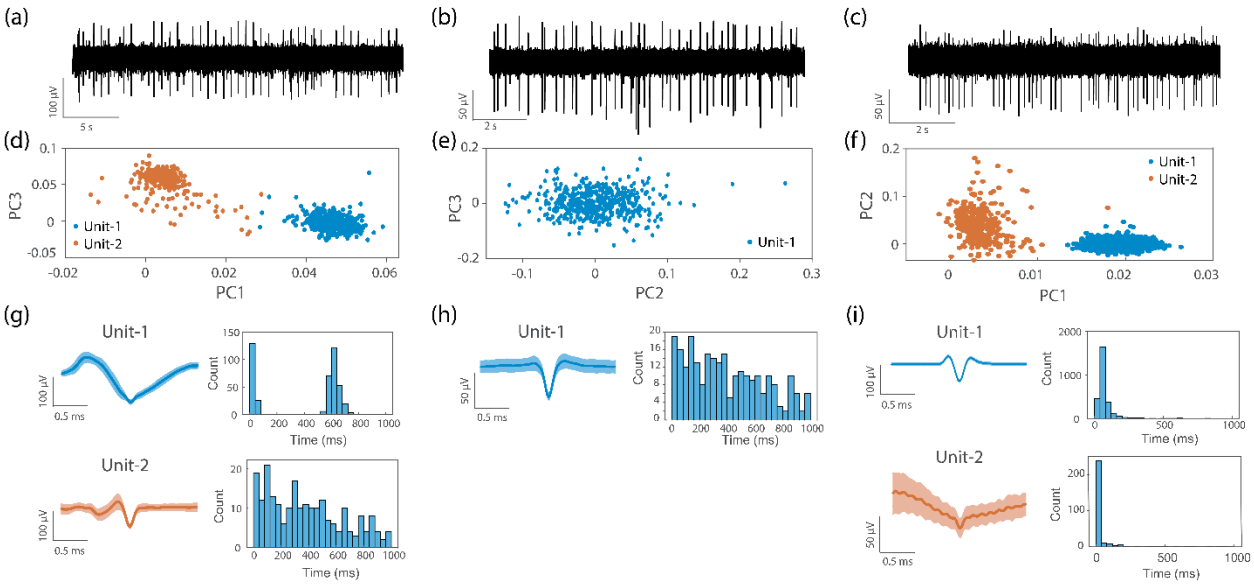

Figure B20. Chronic recording of single unit activity in the VTA at week-4 following implantation

(a-c) Raw trace of endogenous activity; **(d-f)** Clusters of single units revealed by principal component analysis; **(g-i)** Average spike waveforms corresponding to clustered units (left column) and their inter-spike-interval histograms (right column). Data from 3 separate animals. All shaded areas represent s.d., data are presented as mean values +/- s.d.

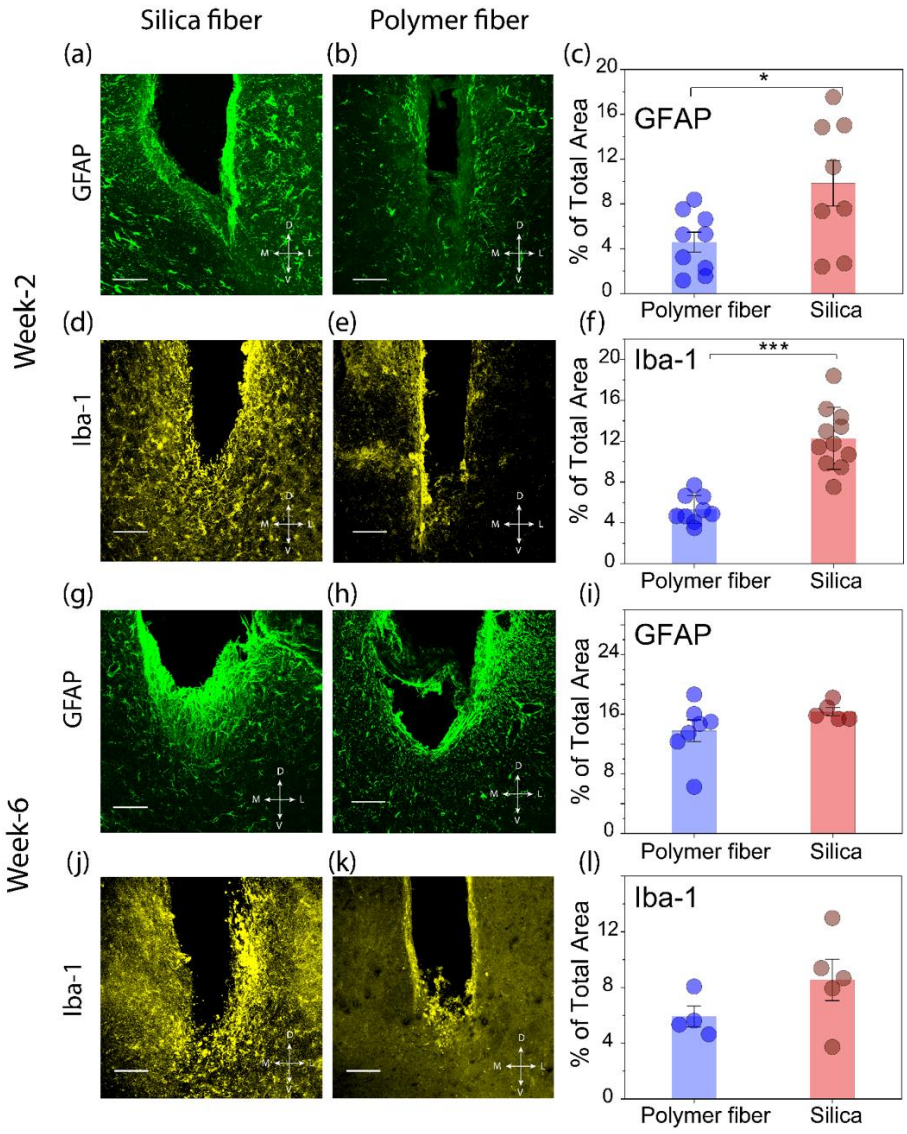

Figure B21. Immunohistochemical evaluation of biocompatibility of chronically implanted brain fiber

Astrocytic (GFAP) and microglia (Iba1) immunoreactivity surrounding a microelectronic polymer fiber and a 300 μm silica fiber, along with average fluorescence intensity quantifying the presence of Iba1 and GFAP at the implant tips at **(a-f)** week-2; and **(g-l)** week-6 time points post implantation (scale bar 100 μm). GFAP week-2; p = 0.04044, t = -2.36714 (n =9 polymer fiber traces and n=8 silica fiber traces, Welch's t-test); Iba1 week-2; $p = 5.68306\times10^{-6}$, t= -

6.33794 (n =9 polymer fiber traces and n=11 silica fiber traces, two-sample t-test). GFAP week-6; p = 0.18663, t = -1.41785 (n =7 polymer fiber traces and n=5 silica fiber traces, two sample t-test); Iba1 week-6; p = 0.18948, t = -1.4532 (n = 4 polymer fiber traces and n = 5 silica fiber traces, two sample t-test). Data are presented as mean values +/- s.d. All error bars represent s.d.

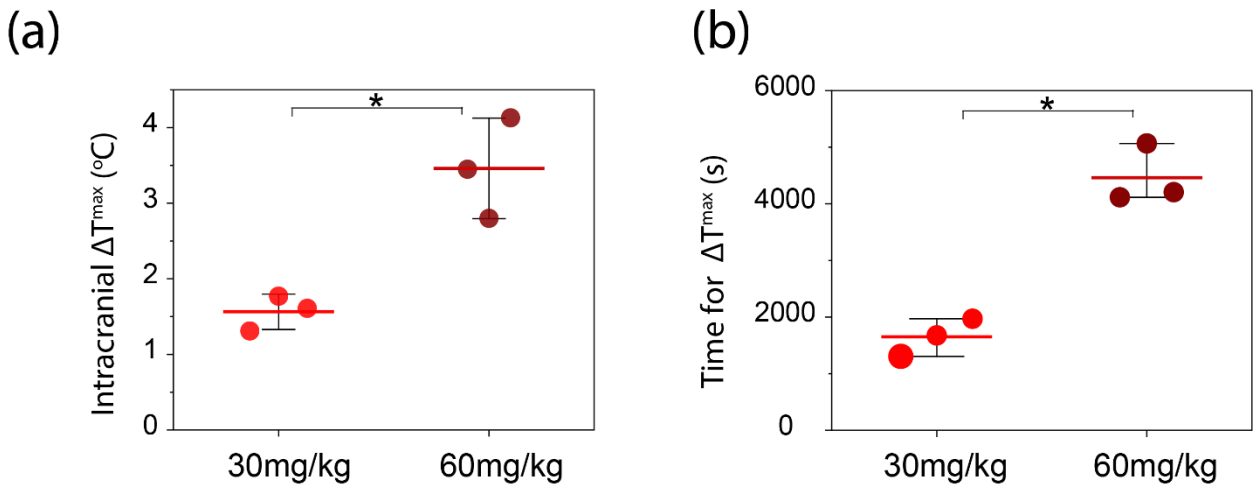

Figure B22. Temperature sensing modality in the fiber detects anesthesia-induced brain hypothermia in a dose dependent manner

(a) Anesthesia induced brain hypothermia recorded in the VTA by the thermal sensor within the fiber in response to an intraperitoneal injection of Ketamine/Xylazine mixture at 30 mg/kg (n=3 mice) and 60 mg/kg doses (n=3 mice) (p = 0.00958, t = -4.66065, two sample t-test); **(b)** corresponding time interval after which intracranial temperature begins to rise (n=3 mice for each condition, p = 0.00143, t = -7.83279, two sample t-test). Data are presented as mean values +/- s.d. All error bars represent s.d.

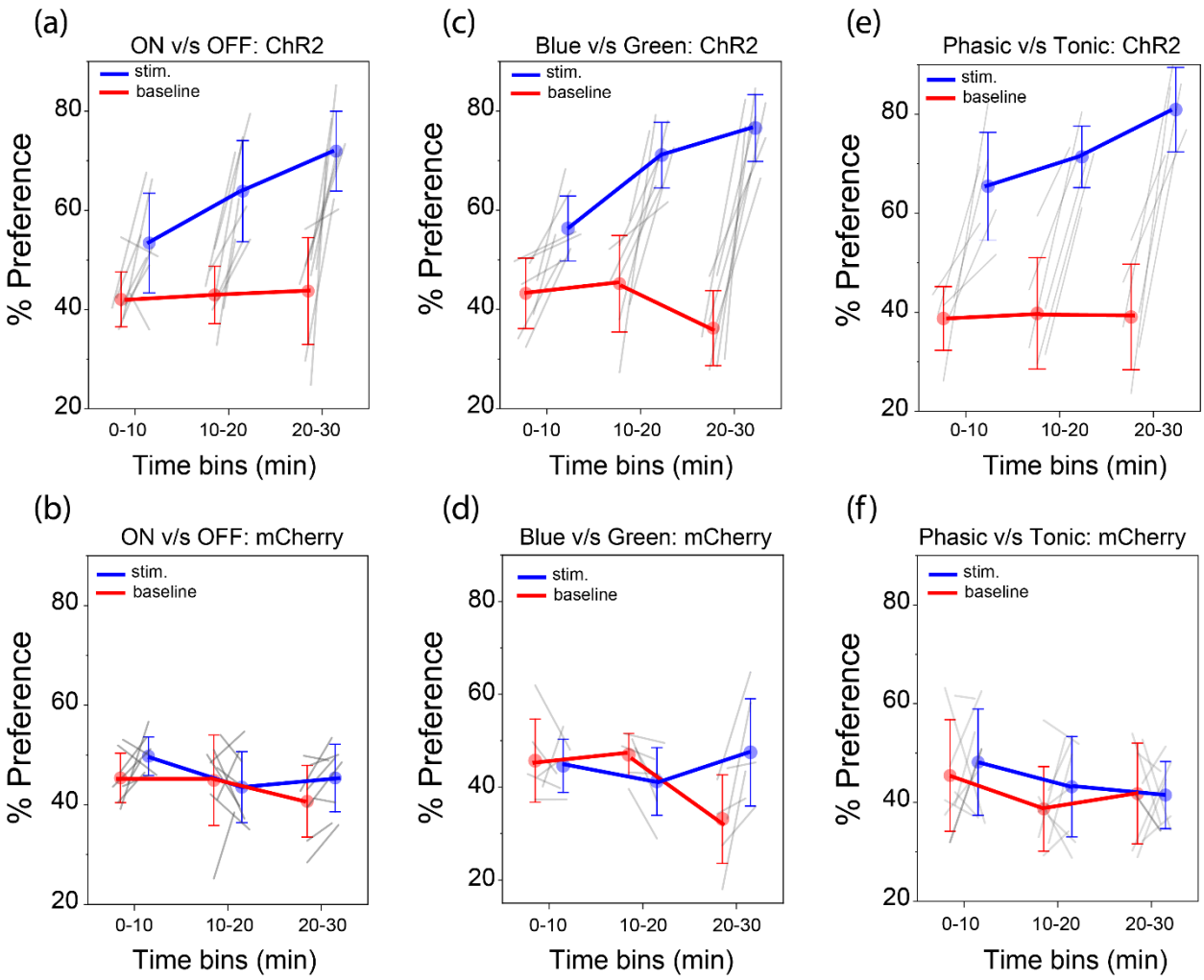

Figure B23. Wireless programmable optical stimulation of DA neurons in the VTA progressively imparts place preference

Preference (%) in a real-time place preference (RTPP) task binned at 10 min time intervals for **(a)** ChR2-mCherry mice in ON (λ = 470 nm, 25 Hz, 10 ms pulse, 1 s ON, 2 s OFF) v/s OFF condition (n=8 mice); **(b)** mCherry control mice in ON (λ = 470 nm, 25 Hz, 10 ms pulse, 1 s ON, 2 s OFF) v/s OFF condition (n=7 mice); **(c)** ChR2-mCherry mice in blue light (λ = 470 nm, 25 Hz, 10 ms pulse, 1 s ON, 2 s OFF) v/s green light stimulation (λ =527 nm, 25 Hz, 10 ms pulse, 1 s ON, 2 s OFF) condition (n=8 mice); **(d)** mCherry mice in blue light (λ = 470 nm, 25 Hz, 10 ms pulse, 1 s ON, 2 s OFF) v/s green light stimulation (λ =527 nm, 25 Hz, 10 ms pulse, 1 s ON, 2 s OFF) condition (n=6 mice); **(e)** ChR2-mCherry mice in Phasic bursting (λ = 470 nm, 40 Hz, 5ms pulse, 0.5 s ON, 4 s OFF) v/s tonic stimulation (λ = 470 nm, 5 Hz, 5 ms pulse) condition (n=6 mice); **(f)** mCherry mice in phasic bursting (λ = 470 nm, 40 Hz, 5ms pulse, 0.5 s ON, 4 s

OFF) v/s tonic stimulation (λ = 470 nm, 5 Hz, 5 ms pulse) condition (n=8 mice). Data are presented as mean values +/- s.d. All error bars represent s.d.

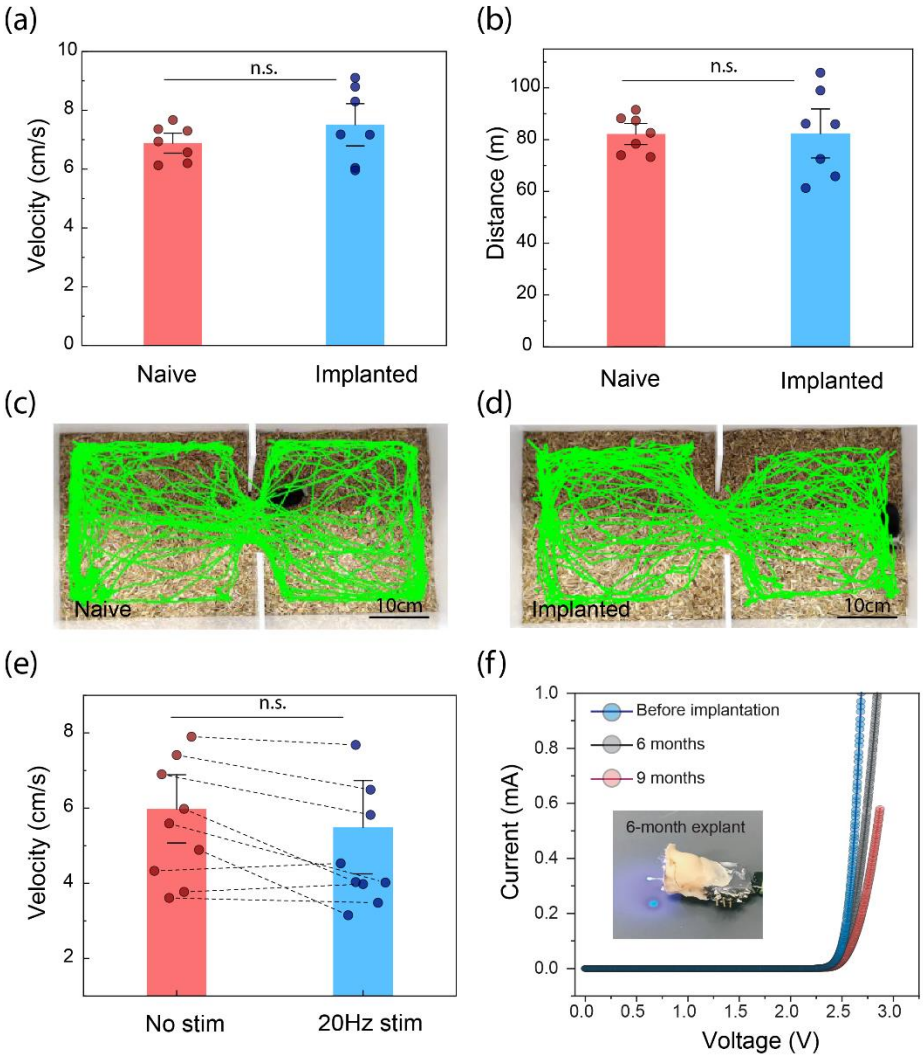

Figure B24. Control behavior experiments and characterization of explanted devices

Analysis of overall locomotor activity of brain implanted mice carrying NeuroStack module in the behavior chamber as compared to naïve controls: **(a)** Velocity; p = 0.26841, t = -1.1836, d.f. = 8.55636 (n=7 mice, Welch's t-test); and **(b)** distance travelled; p = 0.97869, t = - 0.02754, d.f = 8.16039 (n=7 mice, Welch's t-test); Position tracking in a representative run for **(c)** naïve subject; **(d)** module carrying implanted subject; **(e)** No significant changes in velocity of ChR2-mCherry mice was detected in response to 20 Hz stimulation (470 nm, 25 Hz, 10 ms pulse, 1 s ON, 2 s Off) as compared to without stimulation; p = 0.25085, t = 1.22729, d.f. = 8 (n=9 mice, two-tailed paired samples t-test); **(f)** Current-voltage characteristics of fiber µLED from devices that were explanted at 6 and 9 months as compared to pre-implantation. Data are presented as mean values +/- s.d. All error bars represent s.d.

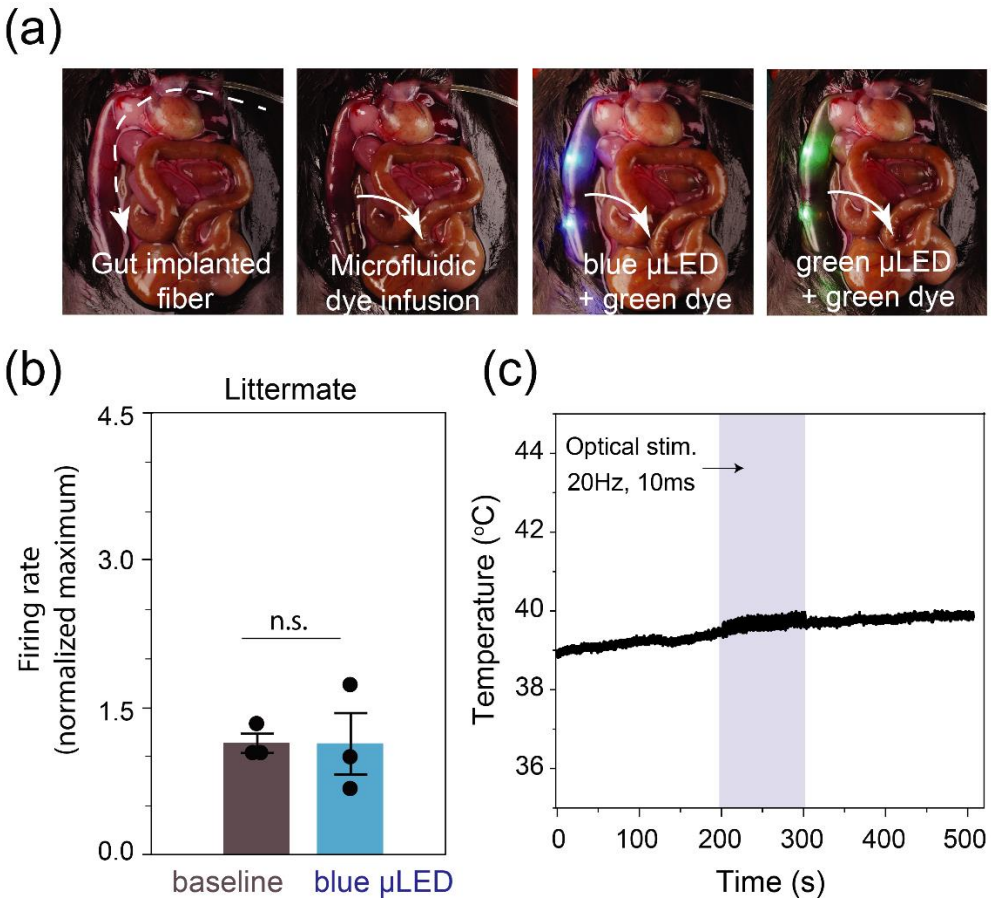

Figure B25. Optofluidic modality of gut fiber, control vagal recordings, and intraluminal gut temperature recording

(a) Dual optofluidic modality of a gut fiber implanted in the proximal small intestine, showing microfluidic infusion of a green dye solution, and simultaneous operation of blue and green µLEDs in the same fiber; **(b)** Quantification of vagal responses upon blue µLED stimulation in control littermates that lacked ChR2 in Cck cells (n=3 mice per group; *p = 0.6625 by Kruskal-Wallis test with non-parametric comparisons using Wilcoxon Method); **(c)** Intraluminal gut temperature recording in a chronically implanted animal before, during (shaded), and after optical stimulation epoch. Data are presented as mean values +/- s.em. All error bars represent s.e.m.

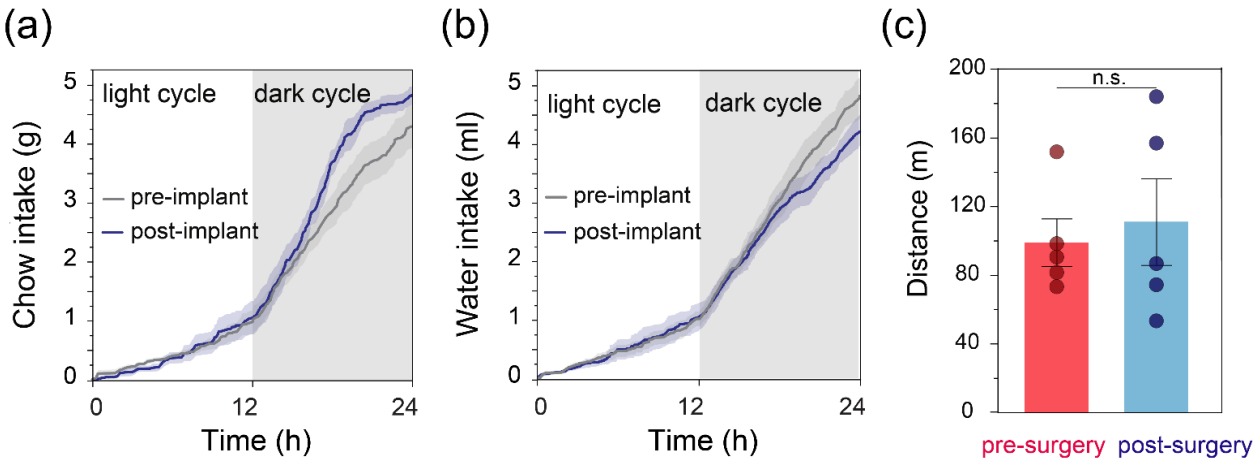

Figure B26. Feeding and locomotor behavior of mice chronically implanted with soft gut fiber in the proximal duodenum

(a) Feeding, and **(b)** drinking behavior is not affected by chronic implantation of the soft gut fibers in the small intestine; **(c)** Locomotor activity of mice in the homecage environment in the first 30 minutes of the dark cycle, pre- and post-implantation of gut fibers in the duodenum. Two-sided paired t-test, $p = 0.717$, $t = 0.389$, $d.f = 4$ (n=5 mice). Data are presented as mean values +/- s.e.m. All shaded areas and error bars represent s.e.m.

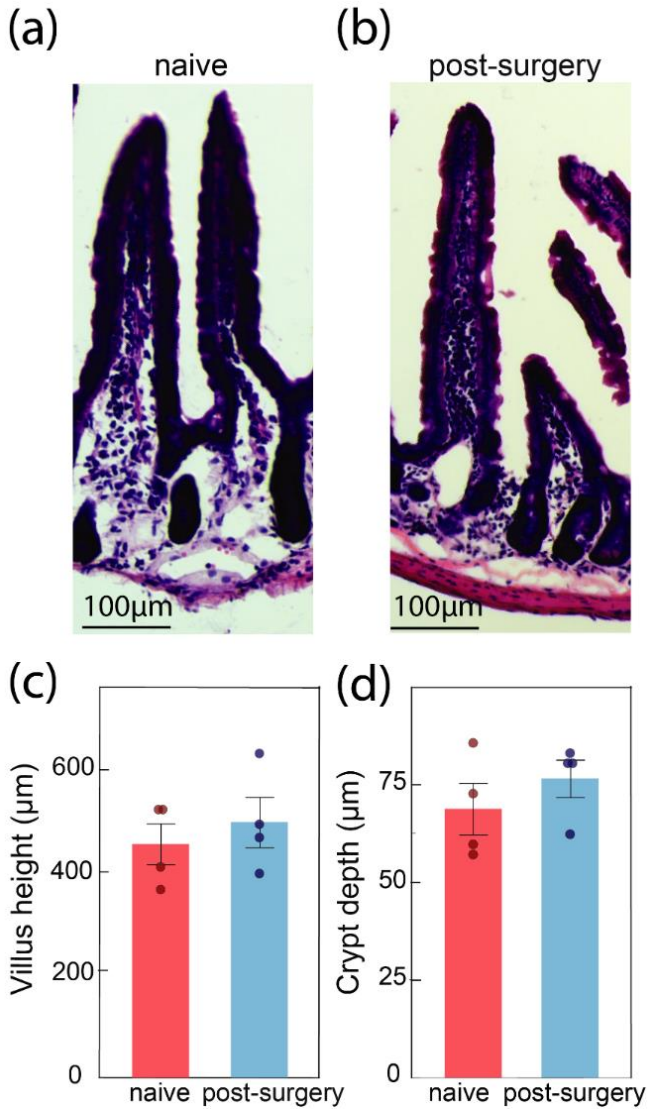

Figure B27. Histological assessment of biocompatibility of chronically implanted gut fibers

Optical micrographs of Hematoxylin and eosin (H&E) stained gut epithelial tissue from **(a)** naïve; and **(b)** gut implanted mice 1-week post-surgery; **(c)** Villi height (p = 0.5291, n=4 mice) and **(d)** crypt depth (p = 0.3789, n=4 mice) did not vary significantly for naïve and fiber-implanted mice as confirmed by two-sided t-test, indicating an intact and non-inflamed gut epithelium. Data are presented as mean values +/- s.e.m.

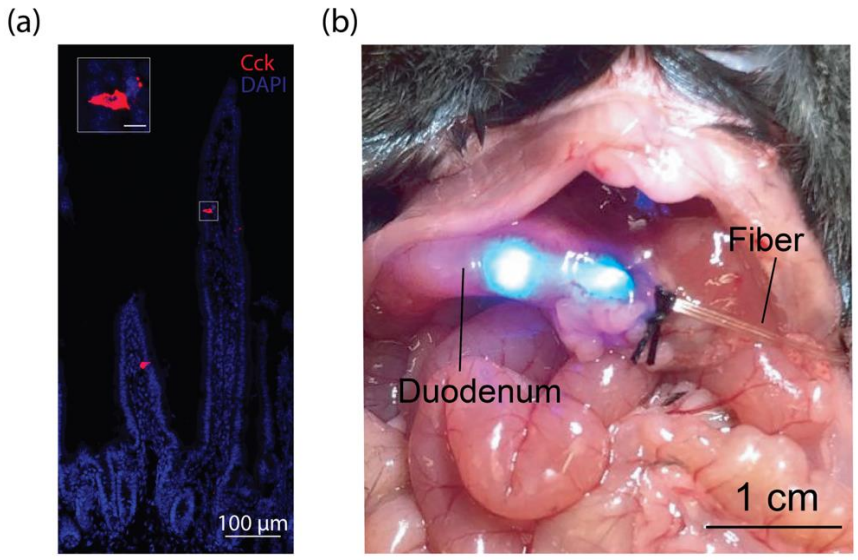

Figure B28. Visualization of the sparsely distributed cholecystokinin (Cck+) neuropod cells and the gut fiber during operation in the duodenum

(a) Confocal micrograph showing sparsely distributed Cck+ neuropod cells in the epithelial layer of the mouse duodenum. Inset shows Cck+ neuropod cell. Inset scale bar = 10 µm. Blue; DAPI; red; tdTomato; **(b)** Representative photograph of a chronically implanted gut fiber in the duodenum during blue µLED stimulation.

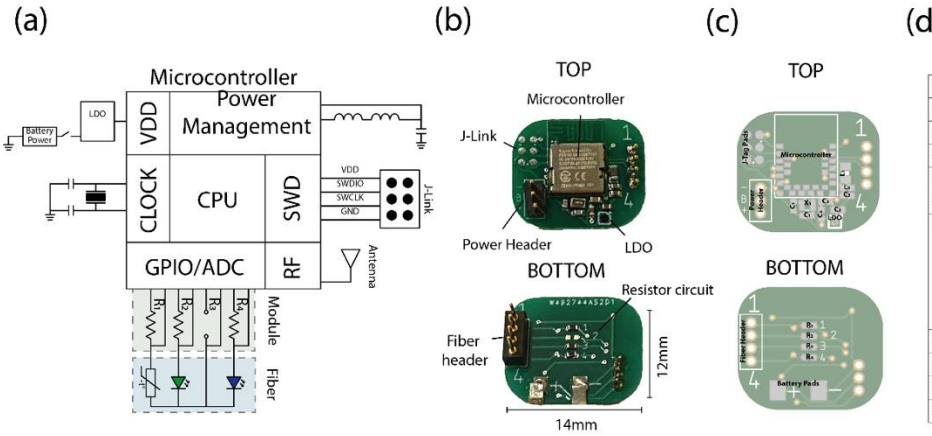

Code	Component
C_1	12pF
C_2	10µF
C_3	1µF
C_1	10µH
C_2	15nH
R_1, R_2, R_3, R_4	Depends on corresponding fiber components: • LED: 0Ω • NTC: 10kΩ • Ground: No Resistor
LDO	LP5907UVE 3.3V Linear Regulator
X1	ABS05W 32.768kHZ Crystal
Battery	GM470910/GM041215
Microcontroller	MDBTV-P512KV2

Figure B29. Modified wireless module that enables prolonged operation during feeding behavior

(a) Block diagram of the modified wireless module used for feeding experiments; **(b)** Top and bottom views of a fully functional module; **(c, d)** parts list for the module along with their positions on the circuit.

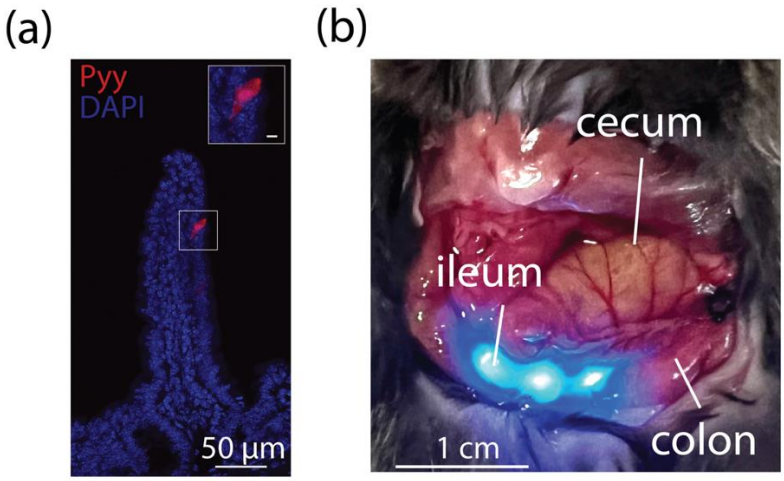

Figure B30. Visualization of the sparsely distributed Peptide YY (Pyy+) neuropod cells in gut epithelium and gut fiber in operation in the ileum

(a) Confocal micrographs of Pyy+ neuropod cells in the epithelial layer of the mouse ileum. Inset shows Pyy+ neuropod cell. Inset scale bar = 10 µm. Blue; DAPI; red; tdTomato; **(b)** Representative photograph of a chronically implanted gut fiber in the ileum during blue µLED stimulation.

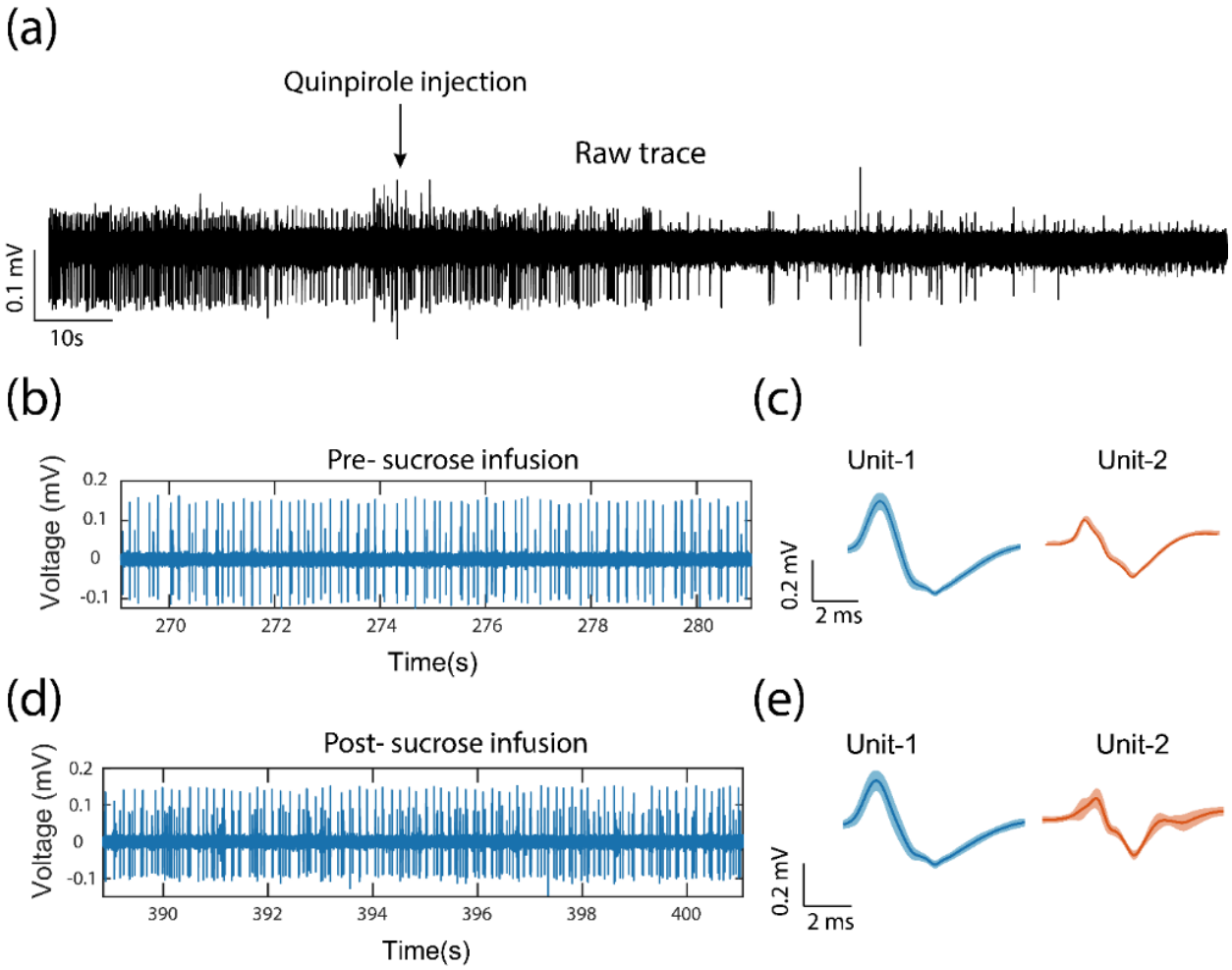

Figure B31. Electrophysiological recordings in the VTA via an implanted brain fiber pre- and post- sucrose infusion into the gut lumen via an implanted gut fiber

(a) Raw trace recorded from the VTA of a representative animal showing the sensitivity of recorded putative DA neuron to systemic injection of D2 autoreceptor agonist quinpirole; **(b)** Raw trace from a representative animal before intestinal sucrose infusion; **(c)** corresponding extracted units; **(d)** Raw trace from the same animal after intestinal sucrose infusion; **(e)** corresponding extracted units.

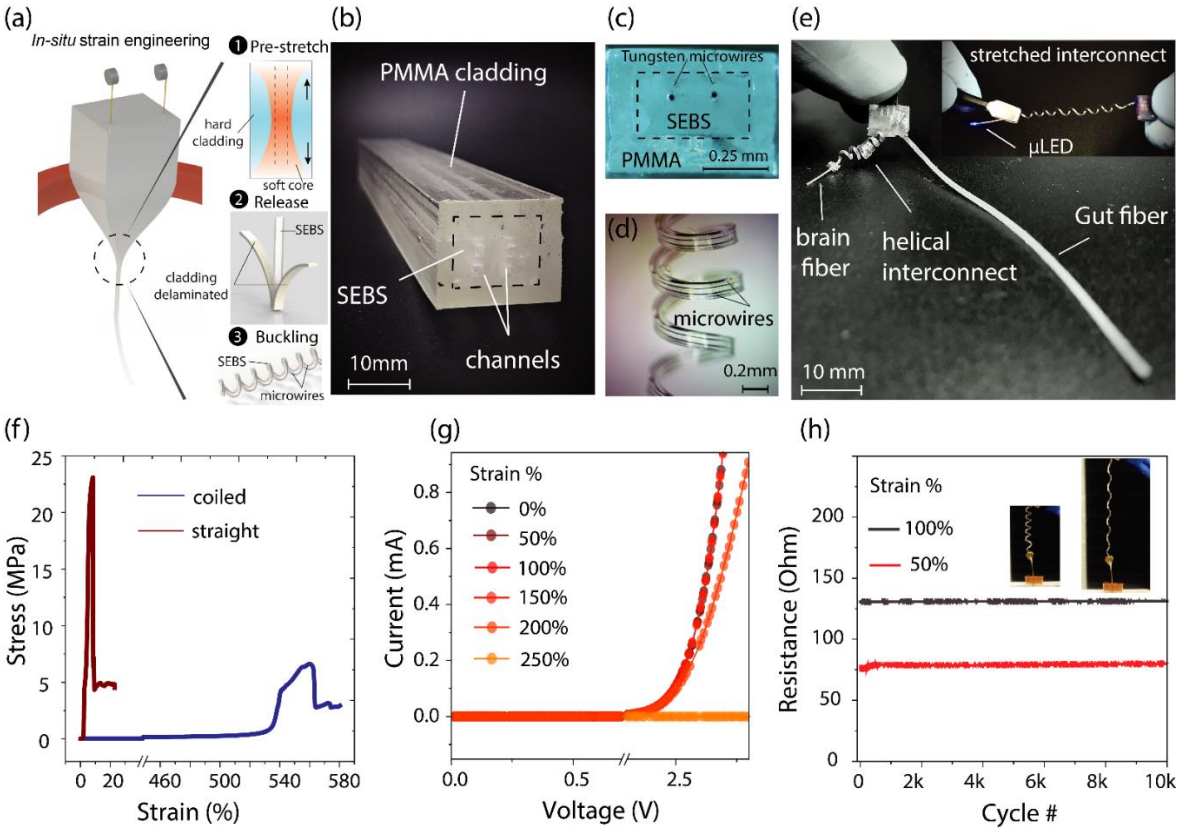

Figure B32. Thermally drawn stretchable interconnects enable multisite devices

(a) Schematic illustration of *in-situ* strain engineering during thermal drawing process that deterministically produces helically buckled fibers; **(b)** Preform geometry and composition; **(c)** cross-sectional micrograph of the drawn fiber with intact cladding; **(d)** optical micrograph of a helically coiled fiber upon cladding removal; **(e)** A photograph of a multisite, multifunctional gut-brain device. Inset shows the brain fiber with an operating µLED during uniaxial stretching of the interconnect; **(f)** Stress-strain plots for a helically coiled stretchable interconnect and a straight fiber instrumented with identical metal microwires; **(g)** Current-voltage characteristic of a blue µLED bonded to the stretchable interconnect at different values of uniaxial strain; **(h)** Cyclic stability of the stretchable interconnect over 10^4 cycles of continuous stretching to 50% and 100% strain while measuring the resistance from a micro resistor chip connected to the fiber.

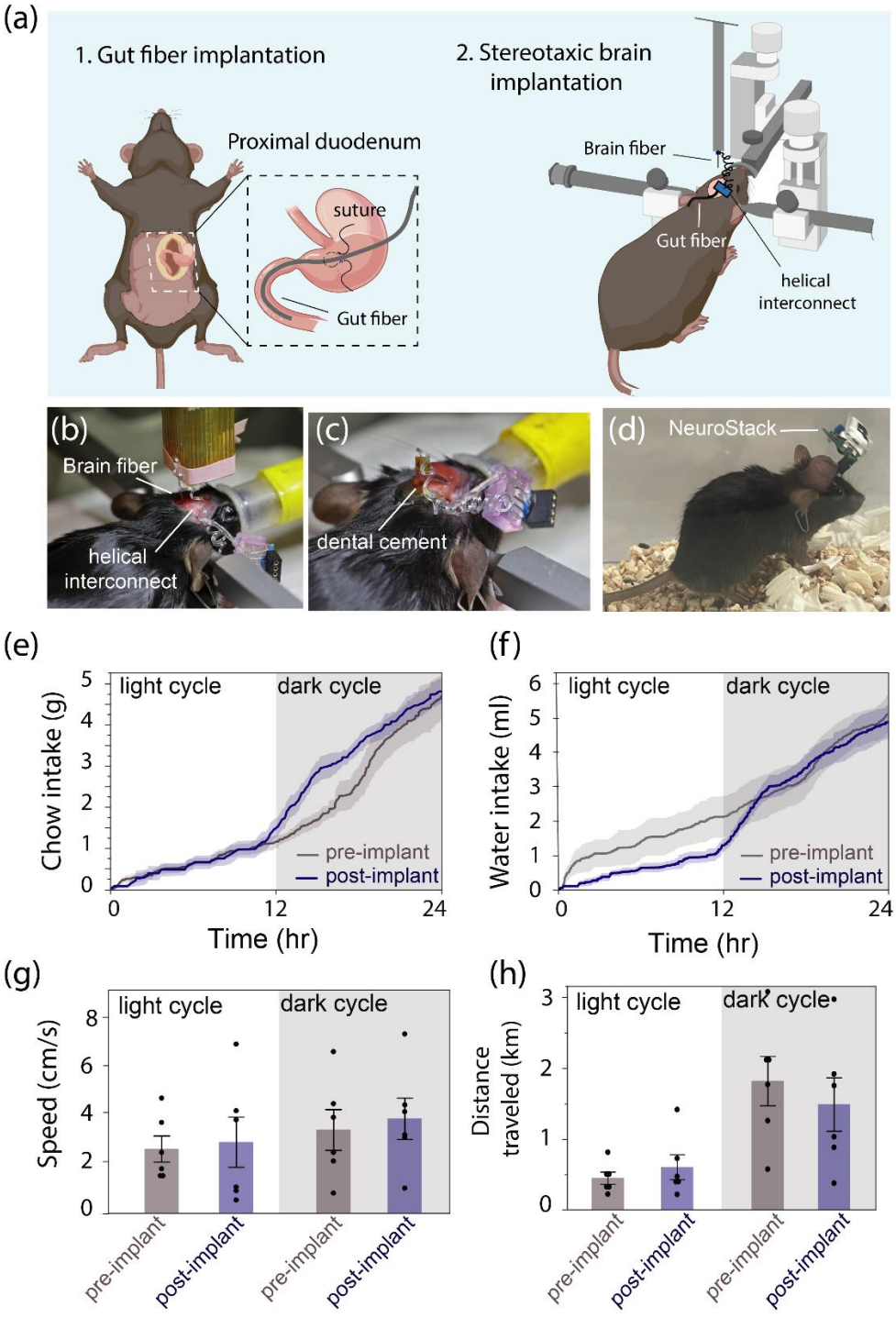

Figure B33. Compatibility of multisite devices with long-term implantation

(a) Schematic illustration of the surgical implantation procedure of a multisite, multifunctional microelectronic fiber device in the proximal small intestine and the VTA; **(b, c)** Corresponding

photographs showing the stretchable interconnect allowing stereotactic brain implantation; **(d)** A photograph of a fully recovered animal following multisite implantation surgery with the wireless module attached; **(e)** Food (p = 0.8940) and **(f)** water intake (p = 0.7849) of mice chronically implanted in the gut and brain (n=4) are unaffected compared to their values pre-surgery by two-sided paired t-test; the locomotor activity of the dually implanted mice (n=6) pre- and post-surgery remain unaffected as measured via **(g)** speed (p = 0.9106) and **(h)** distance travelled (p = 0.7511) over 24 h by two-sided t-test. Data are presented as mean values +/- s.e.m. All shaded areas and error bars represent s.e.m.

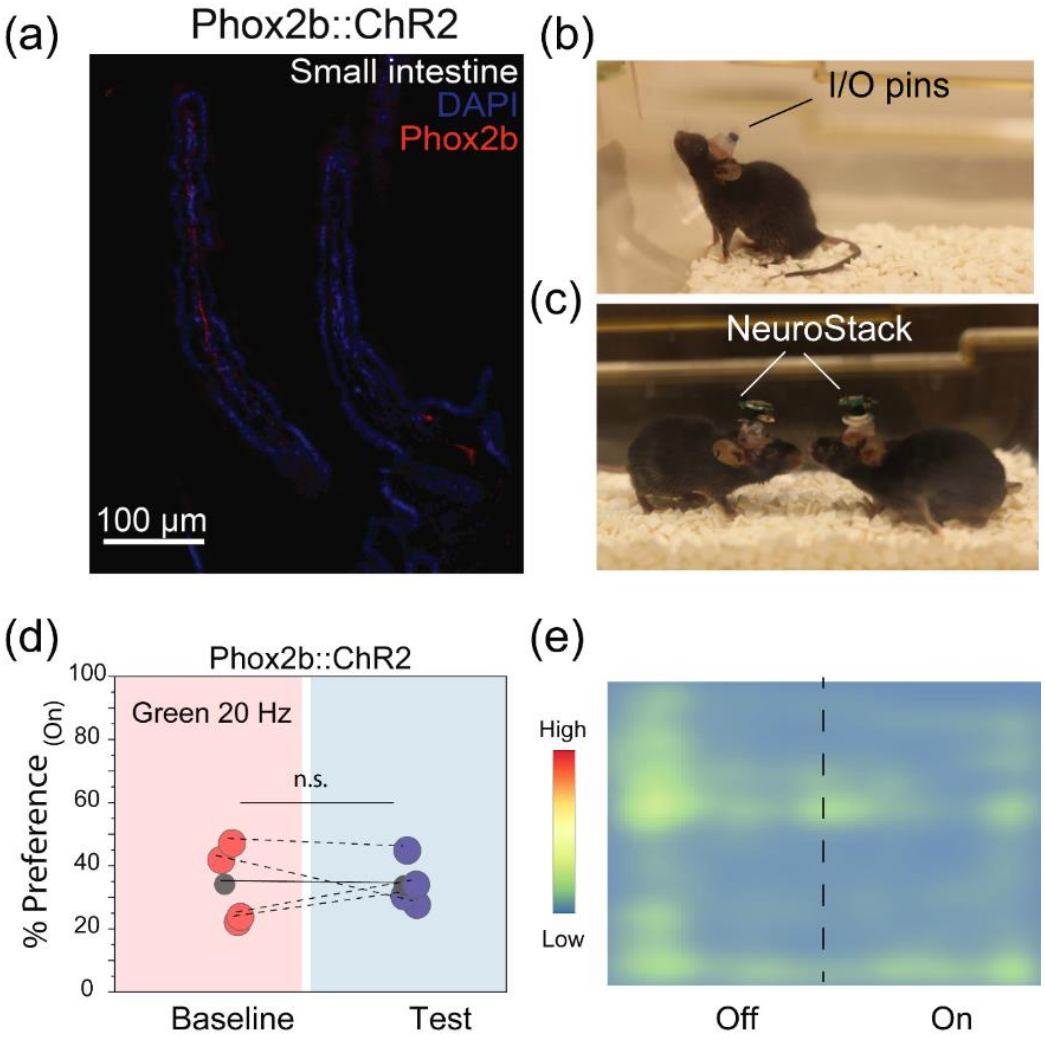

Figure B34. Visualization of Phox2b+ vagal afferents in the duodenum and place-preference behavior controls

(a) Confocal micrographs of Phox2b+ vagal afferents innervating the duodenal villi of a Phox2b::tdTomato mouse. Blue; DAPI; red; tdTomato; **(b)** A photograph of a mouse implanted with a gut fiber in the intestinal lumen during postoperative recovery in the home cage; **(c)** a pair of chronically implanted mice carrying NeuroStack modules; **(d)** Preference (%) in the chamber coupled to green µLED stimulation at baseline and on test-day for Phox2b::ChR2 mice (λ = 470 nm 20 Hz, 10 ms pulse, 0.5 s On duration, 1 s Off duration). Two-sided paired t-test, $p = 0.967$, $t = 0.045$, $d.f = 4$, **(e)** Corresponding representative activity heat map.

Table B1: Comparison of state-of-the-art wireless multifunctional bioelectronic interfaces.

Ref.	Fabrication method	Functions	CNS Organ	Visceral Organ	Powering scheme	Interfacing	Real-time Programming	Wireless data transfer
[128]	Photolithography	Optical stim Photo sensing Thermal sensing Electrophysiology	(Brain)	×	RF	Detachable plug-n-play		
[21]	Photolithography	Optical stim Strain sensing	×	(Bladder)	Inductive coupling	Subdermal implantation		
[183]	Photolithography	Optical stim Pharmacology	(Brain)	×	Battery powered	Head mounted		
[184]	Photolithography	Optical stim Pharmacology	×	(Sciatic nerve)	RF	Subdermal implantation		
[185]	Photolithography	Optical stim Pharmacology	(Brain)	×	Battery powered	Head mounted		
This work	Thermal drawing	Optical stim Pharmacology Electrophysiology Thermal sensing	(Brain)	(GI tract)	Battery powered	Detachable plug-n-play		

References

1. Azzalini, D., Rebollo, I. & Tallon-Baudry, C. Visceral Signals Shape Brain Dynamics and Cognition. *Trends Cogn. Sci.* **23**, 488–509 (2019).

2. Berntson, G. G. & Khalsa, S. S. Neural Circuits of Interoception. *Trends Neurosci.* **44**, 17 (2021).

3. Chen, W. G. *et al.* The Emerging Science of Interoception: Sensing, Integrating, Interpreting, and Regulating Signals within the Self. *Trends Neurosci.* **44**, 3–16 (2021).

4. Chen, W. G. *et al.* The Emerging Science of Interoception: Sensing, Integrating, Interpreting, and Regulating Signals within the Self. *Trends Neurosci.* **44**, 3–16 (2021).

5. Cao, Y., Li, R. & Bai, L. Vagal sensory pathway for the gut-brain communication. *Semin. Cell Dev. Biol.* **156**, 228–243 (2024).

6. Sun, M., Wan, Y., Shi, M., Meng, Z. X. & Zeng, W. Neural innervation in adipose tissue, gut, pancreas, and liver. *Life Metab.* **2**, 1–17 (2023).

7. Williams, E. K. K. *et al.* Sensory Neurons that Detect Stretch and Nutrients in the Digestive System. *Cell* **166**, 209–221 (2016).

8. Bai, L. *et al.* Genetic Identification of Vagal Sensory Neurons That Control Feeding. *Cell* **179**, 1129-1143.e23 (2019).

9. Sun, M., Wan, Y., Shi, M., Meng, Z. X. & Zeng, W. Neural innervation in adipose tissue, gut, pancreas, and liver. *Life Metab.* **2**, 1–17 (2023).

10. Payne, S. C., Furness, J. B. & Stebbing, M. J. Bioelectric neuromodulation for gastrointestinal disorders: effectiveness and mechanisms. *Nat. Rev. Gastroenterol. Hepatol. 2018 162* **16**, 89–105 (2018).

11. Bonaz, B. *et al.* Diseases, Disorders, and Comorbidities of Interoception. *Trends Neurosci.* **44**, 39–51 (2021).

12. Chen, R., Canales, A. & Anikeeva, P. Neural recording and modulation technologies. *Nat. Rev. Mater.* **2**, 16093 (2017).

13. Rivnay, J., Wang, H., Fenno, L., Deisseroth, K. & Malliaras, G. G. Next-generation probes, particles, and proteins for neural interfacing. *Sci. Adv.* **3**, e1601649 (2017).

14. Mirabella, P. N. & Fenselau, H. Advanced neurobiological tools to interrogate metabolism. *Nat. Rev. Endocrinol. 2023 1911* **19**, 639–654 (2023).

15. Shahriari, D., Rosenfeld, D. & Anikeeva, P. Emerging Frontier of Peripheral Nerve and Organ Interfaces. *Neuron* vol. 108 270–285 (2020).

16. Buchanan, K. L. *et al.* The preference for sugar over sweetener depends on a gut sensor cell. *Nat. Neurosci. 2022 252* **25**, 191–200 (2022).

17. Hong, G. & Lieber, C. M. Novel electrode technologies for neural recordings. *Nature Reviews Neuroscience* vol. 20 330–345 (2019).

18. Yang, X. *et al.* Bioinspired neuron-like electronics. *Nat. Mater.* **18**, 510–517 (2019).

19. Yizhar, O., Fenno, L. E., Davidson, T. J., Mogri, M. & Deisseroth, K. Optogenetics in Neural Systems. *Neuron* vol. 71 9–34 (2011).

20. Vázquez-Guardado, A., Yang, Y., Bandodkar, A. J. & Rogers, J. A. Recent advances in neurotechnologies with broad potential for neuroscience research. *Nature Neuroscience* vol. 23 1522–1536 (2020).

21. Mickle, A. D. *et al.* A wireless closed-loop system for optogenetic peripheral neuromodulation. *Nat. 2019 5657739* **565**, 361–365 (2019).

22. Madhvapathy, S. R. *et al.* Implantable bioelectronic systems for early detection of kidney transplant rejection. *Science (80-.).* **381**, 1105–1112 (2023).

23. McCall, J. G. *et al.* Fabrication and application of flexible, multimodal light-emitting devices for wireless optogenetics. *Nat. Protoc.* **8**, 2413–2428 (2013).

24. Canales, A., Park, S., Kilias, A. & Anikeeva, P. Multifunctional Fibers as Tools for Neuroscience and Neuroengineering. *Acc. Chem. Res.* **51**, 829–838 (2018).

25. Canales, A. *et al.* Multifunctional fibers for simultaneous optical, electrical and chemical interrogation of neural circuits in vivo. *Nat. Biotechnol.* **33**, 277–284 (2015).

26. Park, S. *et al.* One-step optogenetics with multifunctional flexible polymer fibers. *Nat. Neurosci.* **20**, 612–619 (2017).

27. Lu, C. *et al.* Flexible and stretchable nanowire-coated fibers for optoelectronic probing of spinal cord circuits. *Sci. Adv.* **3**, (2017).

28. Park, S. *et al.* Adaptive and multifunctional hydrogel hybrid probes for long-term sensing and modulation of neural activity. *Nat. Commun. 2021 121* **12**, 1–12 (2021).

29. Antonini, M.-J. *et al.* Customizing MRI-Compatible Multifunctional Neural Interfaces through Fiber Drawing. *Adv. Funct. Mater.* 2104857 (2021) doi:10.1002/ADFM.202104857.

30. Park, J. *et al.* In situ electrochemical generation of nitric oxide for neuronal modulation. *Nat. Nanotechnol.* **15**, 690–697 (2020).

31. Sahasrabudhe, A. *et al.* Multifunctional microelectronic fibers enable wireless modulation of gut and brain neural circuits. *Nat. Biotechnol. 2023* **13**, 1–13 (2023).

32. Frank, J. A., Antonini, M.-J. & Anikeeva, P. Next-generation interfaces for studying neural function. *Nat. Biotechnol.* (2019) doi:10.1038/s41587-019-0198-8.

33. Canales, A. *et al.* Multifunctional fibers for simultaneous optical, electrical and chemical interrogation of neural circuits in vivo. *Nat. Biotechnol.* **33**, 277–284 (2015).

34. Lu, C. *et al.* Flexible and stretchable nanowire-coated fibers for optoelectronic probing of spinal cord circuits. *Sci. Adv.* **3**, e1600955 (2017).

35. Park, S. *et al.* One-step optogenetics with multifunctional flexible polymer fibers. *Nat. Neurosci.* **20**, 612–619 (2017).

36. Tao, G., Stolyarov, A. M. & Abouraddy, A. F. Multimaterial Fibers. *Int. J. Appl. Glas. Sci.* **3**, 349–368 (2012).

37. Loke, G., Yan, W., Khudiyev, T., Noel, G. & Fink, Y. Recent Progress and Perspectives of Thermally Drawn Multimaterial Fiber Electronics. *Adv. Mater.* **32**, 1904911 (2020).

38. Shin, H. *et al.* Multifunctional multi-shank neural probe for investigating and modulating long-range neural circuits in vivo. *Nat. Commun.* **10**, 1–11 (2019).

39. Guo, Y. *et al.* Polymer Composite with Carbon Nanofibers Aligned during Thermal Drawing as a Microelectrode for Chronic Neural Interfaces. *ACS Nano* **11**, 6574–6585 (2017).

40. Logothetis, N. K., Pauls, J., Augath, M., Trinath, T. & Oeltermann, A. Neurophysiological investigation of the basis of the fMRI signal. *Nature* **412**, 150–157 (2001).

41. Zhao, S. *et al.* Graphene Encapsulated Copper Microwires as Highly MRI Compatible Neural Electrodes. *Nano Lett.* **16**, 7731–7738 (2016).

42. Zhao, S. *et al.* Full activation pattern mapping by simultaneous deep brain stimulation and fMRI with graphene fiber electrodes. *Nat. Commun.* **11**, 1–12 (2020).

43. Shabahang, S., Kaufman, J. J., Deng, D. S. & Abouraddy, A. F. Observation of the Plateau-Rayleigh capillary instability in multi-material optical fibers. *Appl. Phys. Lett.* **99**, 161909 (2011).

44. Yaman, M. *et al.* Arrays of indefinitely long uniform nanowires and nanotubes. *Nat. Mater.* **10**, 494–501 (2011).

45. Bayindir, M. *et al.* Metal-insulator-semiconductor optoelectronic fibres. *Nature* **431**, 826–829 (2004).

46. Frank, J. A. *et al.* In vivo photopharmacology enabled by multifunctional fibers. *ACS Chem. Neurosci.* **11**, 3813 (2020).

47. Rein, M. *et al.* Diode fibres for fabric-based optical communications. *Nature* **560**, 214–218 (2018).

48. Rios, G., Lubenov, E. V., Chi, D., Roukes, M. L. & Siapas, A. G. Nanofabricated Neural Probes for Dense 3-D Recordings of Brain Activity. *Nano Lett.* **16**, 6857–6862 (2016).

49. Rose, J. D. & Weishaar, D. J. Tapered tungsten fine-wire microelectrode for chronic single unit recording. *Brain Res. Bull.* **4**, 435–437 (1979).

50. Obaid, A. *et al.* Massively parallel microwire arrays integrated with CMOS chips for neural recording. *Sci. Adv.* **6**, eaay2789 (2020).

51. Protopopoff, E. & Marcus, P. Potential versus pH (Pourbaix) Diagrams. in *Corrosion: Fundamentals, Testing, and Protection* 17–30 (ASM International, 2018). doi:10.31399/asm.hb.v13a.a0003580.

52. Fang, H. *et al.* Capacitively coupled arrays of multiplexed flexible silicon transistors for long-term cardiac electrophysiology. *Nat. Biomed. Eng.* **1**, 38 (2017).

53. Jiang, S. *et al.* Spatially expandable fiber-based probes as a multifunctional deep brain interface. *Nat. Commun.* **11**, 1–14 (2020).

54. Lacour, S. P., Courtine, G. & Guck, J. Materials and technologies for soft implantable neuroprostheses. *Nature Reviews Materials* vol. 1 1–14 (2016).

55. Newby & R, J. Metals handbook, 9th edition. Volume 8: Mechanical testing. (1985).

56. Jasinska, A. J., Chen, B. T., Bonci, A. & Stein, E. A. Dorsal medial prefrontal cortex (MPFC) circuitry in rodent models of cocaine use: Implications for drug addiction therapies. *Addict. Biol.* **20**, 215–226 (2015).

57. Xu, P., Chen, A., Li, Y., Xing, X. & Lu, H. Medial prefrontal cortex in neurological diseases. *Physiological Genomics* vol. 51 432–442 (2019).

58. Euston, D. R., Gruber, A. J. & McNaughton, B. L. The Role of Medial Prefrontal Cortex in Memory and Decision Making. *Neuron* vol. 76 1057–1070 (2012).

59. Souza, B. C., Lopes-dos-Santos, V., Bacelo, J. & Tort, A. B. L. Spike sorting with Gaussian mixture models. *Sci. Rep.* **9**, 1–14 (2019).

60. Schmitzer-Torbert, N., Jackson, J., Henze, D., Harris, K. & Redish, A. D. Quantitative measures of cluster quality for use in extracellular recordings. *Neuroscience* **131**, 1–11 (2005).

61. Hill, D. N., Mehta, S. B. & Kleinfeld, D. Quality Metrics to Accompany Spike Sorting of Extracellular Signals. *J. Neurosci.* **31**, 8699–8705 (2011).

62. Lee, J. H. *et al.* Global and local fMRI signals driven by neurons defined optogenetically by type and wiring. *Nature* **465**, 788–792 (2010).

63. Kozai, T. D. Y. & Vazquez, A. L. Photoelectric artefact from optogenetics and imaging on microelectrodes and bioelectronics: new challenges and opportunities. *J. Mater. Chem. B* **3**, 4965–4978 (2015).

64. Boyden, E. S., Zhang, F., Bamberg, E., Nagel, G. & Deisseroth, K. Millisecond-timescale, genetically targeted optical control of neural activity. *Nat. Neurosci.* **8**, 1263–1268 (2005).

65. Anikeeva, P. *et al.* Optetrode: a multichannel readout for optogenetic control in freely moving mice. *Nat. Neurosci.* **15**, 163–70 (2011).

66. Lee, D. *et al.* Characterization of tetrodes coated with Au nanoparticles (AuNPs) and PEDOT and their application to thalamic neural signal detection in vivo. *Exp. Neurobiol.* **27**, 593–604 (2018).

67. Voigts, J., Newman, J. P., Wilson, M. A. & Harnett, M. T. An easy-to-assemble, robust, and lightweight drive implant for chronic tetrode recordings in freely moving animals. *J. Neural Eng.* **17**, (2020).

68. Paxinos, G. & Franklin, K. *The mouse brain in stereotaxic coordinates, 2nd edition*. (Academic Press, 2001).

69. Rey, H. G., Pedreira, C. & Quian Quiroga, R. Past, present and future of spike sorting

techniques. *Brain Res. Bull.* **119**, 106–117 (2015).

70. Harris, K. D., Quiroga, R. Q., Freeman, J. & Smith, S. L. Improving data quality in neuronal population recordings. *Nat. Neurosci.* **19**, 1165–1174 (2016).

71. Foltynie, T. *et al.* MRI-guided STN DBS in Parkinson's disease without microelectrode recording: Efficacy and safety. *J. Neurol. Neurosurg. Psychiatry* **82**, 358–363 (2011).

72. Li, N. & Jasanoff, A. Local and global consequences of reward-evoked striatal dopamine release. *Nature* **580**, 239–244 (2020).

73. Fiallos, A. M. *et al.* Reward magnitude tracking by neural populations in ventral striatum. *Neuroimage* **146**, 1003–1015 (2017).

74. Bricault, S. *et al.* Image-guided neural activity manipulation with a paramagnetic drug. *Nat. Commun.* **11**, 1–6 (2020).

75. Lind, G., Linsmeier, C. E. & Schouenborg, J. The density difference between tissue and neural probes is a key factor for glial scarring. *Sci. Rep.* **3**, 1–7 (2013).

76. Saxena, T. *et al.* The impact of chronic blood–brain barrier breach on intracortical electrode function. *Biomaterials* **34**, 4703–4713 (2013).

77. Bredt, D. S. & Snyder, S. H. NITRIC OXIDE: A Physiologic Messenger Molecule. *Annu. Rev. Biochem.* **63**, 175–195 (1994).

78. Mustafa, A. K., Gadalla, M. M. & Snyder, S. H. Signaling by gasotransmitters. *Sci. Signal.* **2**, (2009).

79. Yoshida, T. *et al.* Nitric oxide activates TRP channels by cysteine S-nitrosylation. *Nat. Chem. Biol.* **2**, 596–607 (2006).

80. Lundberg, J. O., Weitzberg, E. & Gladwin, M. T. The nitrate-nitrite-nitric oxide pathway in physiology and therapeutics. *Nat. Rev. Drug Discov.* **7**, 156–167 (2008).

81. Iverson, N. M. *et al.* In vivo biosensing via tissue-localizable near-infrared-fluorescent single-walled carbon nanotubes. *Nat. Nanotechnol.* **8**, 873 (2013).

82. Calabrese, V. *et al.* Nitric oxide in the central nervous system: neuroprotection versus neurotoxicity. *Nat. Rev. Neurosci.* **8**, 766 (2007).

83. Huang, Z. *et al.* Effects of cerebral ischemia in mice deficient in neuronal nitric oxide synthase. *Science (80-.).* **265**, 1883 LP – 1885 (1994).

84. Liu, V. W. T. & Huang, P. L. Cardiovascular roles of nitric oxide: A review of insights from nitric oxide synthase gene disrupted mice†. *Cardiovasc. Res.* **77**, 19–29 (2008).

85. Yoshida, T., Limmroth, V., Irikura, K. & Moskowitz, M. A. The NOS Inhibitor, 7-Nitroindazole, Decreases Focal Infarct Volume but Not the Response to Topical Acetylcholine in Pial Vessels. *J. Cereb. Blood Flow Metab.* **14**, 924–929 (1994).

86. Wang, P. G. *et al.* Nitric Oxide Donors: Chemical Activities and Biological Applications. *Chem. Rev.* **102**, 1091–1134 (2002).

87. Jen, M. C., Serrano, M. C., Van Lith, R. & Ameer, G. A. Polymer-based nitric oxide therapies: Recent insights for biomedical applications. *Adv. Funct. Mater.* **22**, 239–260 (2012).

88. Xiang, H. J., Guo, M. & Liu, J. G. Transition-Metal Nitrosyls for Photocontrolled Nitric Oxide Delivery. *Eur. J. Inorg. Chem.* **2017**, 1586–1595 (2017).

89. Feelisch, M. The use of nitric oxide donors in pharmacological studies. *Naunyn. Schmiedebergs. Arch. Pharmacol.* **358**, 113–122 (1998).

90. Miller, M. R. & Megson, I. L. Recent developments in nitric oxide donor drugs. *Br. J. Pharmacol.* **151**, 305–321 (2007).

91. Zhou, E. Y. *et al.* Near-Infrared Photoactivatable Nitric Oxide Donors with Integrated Photoacoustic Monitoring. *J. Am. Chem. Soc.* **140**, 11686–11697 (2018).

92. Suchyta, D. J. & Schoenfisch, M. H. Controlled Release of Nitric Oxide from Liposomes. *ACS Biomater. Sci. Eng.* **3**, 2136–2143 (2017).

93. Rosca, V., Duca, M., de Groot, M. T. & Koper, M. T. M. ChemInform Abstract: Nitrogen Cycle Electrocatalysis. *ChemInform* **40**, 2209–2244 (2009).

94. Stoychev, D., Papoutsis, A., Kelaidopoulou, A., Kokkinidis, G. & Milchev, A. Electrodeposition of platinum on metallic and nonmetallic substrates - Selection of experimental conditions. *Mater. Chem. Phys.* **72**, 360–365 (2001).

95. Lammel, S. *et al.* Input-specific control of reward and aversion in the ventral tegmental area. *Nature* **491**, 212 (2012).

96. Chen, R., Romero, G., Christiansen, M. G., Mohr, A. & Anikeeva, P. Wireless magnetothermal deep brain stimulation. *Science (80-.).* 1261821 (2015) doi:10.1126/science.1261821.

97. Gunaydin, L. A. *et al.* Natural Neural Projection Dynamics Underlying Social Behavior. *Cell* **157**, 1535–1551 (2014).

98. Nugent, F. S., Penick, E. C. & Kauer, J. A. Opioids block long-term potentiation of inhibitory synapses. *Nature* **446**, 1086 (2007).

99. Iravani, M. M., Kashefi, K., Mander, P., Rose, S. & Jenner, P. Involvement of inducible nitric oxide synthase in inflammation-induced dopaminergic neurodegeneration. *Neuroscience* **110**, 49–58 (2002).

100. Sagar, S. M., Sharp, F. R. & Curran, T. Expression of c-fos protein in brain: metabolic mapping at the cellular level. *Science (80-.).* **240**, 1328 LP – 1331 (1988).

101. Christoph, G. R., Leonzio, R. J. & Wilcox, K. S. Stimulation of the lateral habenula inhibits dopamine-containing neurons in the substantia nigra and ventral tegmental area of the rat. *J. Neurosci.* **6**, 613 LP – 619 (1986).

102. Monai, H. *et al.* Calcium imaging reveals glial involvement in transcranial direct current stimulation-induced plasticity in mouse brain. *Nat. Commun.* **7**, 11100 (2016).

103. Thomas, D. D., Liu, X., Kantrow, S. P. & Lancaster, J. R. The biological lifetime of nitric oxide: Implications for the perivascular dynamics of NO and O₂ *Proc. Natl. Acad. Sci.* **98**, 355 LP – 360 (2001).

104. Franklin, K. B. J. & Paxinos, G. *The mouse brain in stereotaxic coordinates*. vol. 3 (Academic press New York:, 2008).

105. Damak, S. *et al.* Detection of sweet and umami taste in the absence of taste receptor T1r3. *Science (80-.).* **301**, 850–853 (2003).

106. Ren, X. *et al.* Nutrient Selection in the Absence of Taste Receptor Signaling. *J. Neurosci.* **30**, 8012–8023 (2010).

107. Sclafani, A. & Ackroff, K. Flavor preferences conditioned by intragastric glucose but not fructose or galactose in C57BL/6J mice. *Physiol. Behav.* **106**, 457–461 (2012).

108. Sclafani, A., Cardieri, C., Tucker, K., Blusk, D. & Ackroff, K. Intragastric glucose but not fructose conditions robust flavor preferences in rats. *https://doi.org/10.1152/ajpregu.1993.265.2.R320* **265**, (1993).

109. Zukerman, S., Ackroff, K. & Sclafani, A. Rapid post-oral stimulation of intake and flavor conditioning by glucose and fat in the mouse. *Am. J. Physiol. - Regul. Integr. Comp. Physiol.* **301**, 1635–1647 (2011).

110. Han, W. *et al.* Striatal Dopamine Links Gastrointestinal Rerouting to Altered Sweet Appetite. *Cell Metab.* **23**, 103–112 (2016).

111. Kaelberer, M. M., Rupprecht, L. E., Liu, W. W., Weng, P. & Bohorquez, D. V. Neuropod Cells: The Emerging Biology of Gut-Brain Sensory Transduction. *https://doi.org/10.1146/annurev-neuro-091619-022657* **43**, 337–353 (2020).

112. Kaelberer, M. M. & Bohórquez, D. V. The now and then of gut-brain signaling. *Brain Research* vol. 1693 192–196 (2018).

113. Kaelberer, M. M. *et al.* A gut-brain neural circuit for nutrient sensory transduction. *Science (80-.).* **361**, (2018).

114. Critchley, H. D. & Harrison, N. A. Visceral Influences on Brain and Behavior. *Neuron* vol. 77 624–638 (2013).

115. Heijtz, R. D. *et al.* Normal gut microbiota modulates brain development and behavior. *Proc. Natl. Acad. Sci. U. S. A.* **108**, 3047–3052 (2011).

116. Bercik, P. *et al.* Chronic gastrointestinal inflammation induces anxiety-like behavior and alters central nervous system biochemistry in mice. *Gastroenterology* **139**, 2102–2112 (2010).

117. Han, W. *et al.* A Neural Circuit for Gut-Induced Reward. *Cell* (2018) doi:10.1016/j.cell.2018.08.049.

118. Birmingham, K. *et al.* Bioelectronic medicines: a research roadmap. *Nat. Rev. Drug Discov. 2014 136* **13**, 399–400 (2014).

119. Pavlov, V. A. & Tracey, K. J. Bioelectronic medicine: Preclinical insights and clinical advances. *Neuron* **110**, 3627–3644 (2022).

120. Jun, J. J. *et al.* Fully integrated silicon probes for high-density recording of neural activity. *Nature* **551**, 232–236 (2017).

121. Hunt, D. L. *et al.* Multimodal in vivo brain electrophysiology with integrated glass microelectrodes. *Nat. Biomed. Eng. 2019 39* **3**, 741–753 (2019).

122. Lechasseur, Y. *et al.* A microprobe for parallel optical and electrical recordings from single neurons in vivo. *Nat. Methods 2011 84* **8**, 319–325 (2011).

123. Steinmetz, N. A. *et al.* Neuropixels 2.0: A miniaturized high-density probe for stable, long-term brain recordings. *Science (80-.).* **372**, (2021).

124. Kampasi, K. *et al.* Efficient assembly of multi-color fiberless optoelectrodes with on-board light sources for neural stimulation and recording. *Proc. Annu. Int. Conf. IEEE Eng. Med. Biol. Soc. EMBS* **2016-October**, 4479–4482 (2016).

125. Vöröslakos, M. *et al.* HectoSTAR μLED Optoelectrodes for Large-Scale, High-Precision In Vivo Opto-Electrophysiology. *Adv. Sci.* **9**, 2105414 (2022).

126. Wu, F. *et al.* Monolithically Integrated μLEDs on Silicon Neural Probes for High-Resolution Optogenetic Studies in Behaving Animals. *Neuron* **88**, 1136–1148 (2015).

127. Minev, I. R. *et al.* Electronic dura mater for long-term multimodal neural interfaces. *Science (80-.).* **347**, 159–163 (2015).

128. Kim, T. -i. *et al.* Injectable, Cellular-Scale Optoelectronics with Applications for Wireless Optogenetics. *Science (80-.).* **340**, 211–216 (2013).

129. Kim, W. S. *et al.* Organ-specific, multimodal, wireless optoelectronics for high-throughput phenotyping of peripheral neural pathways. *Nat. Commun. 2021 121* **12**, 1–10 (2021).

130. Kathe, C. *et al.* Wireless closed-loop optogenetics across the entire dorsoventral spinal cord in mice. *Nat. Biotechnol.* (2021) doi:10.1038/s41587-021-01019-x.

131. Park, S. Il *et al.* Soft, stretchable, fully implantable miniaturized optoelectronic systems for wireless optogenetics. *Nat. Biotechnol.* **33**, 1280–1286 (2015).

132. McCall, J. G. *et al.* Preparation and implementation of optofluidic neural probes for in vivo wireless pharmacology and optogenetics. *Nat. Protoc.* **12**, 219–237 (2017).

133. Loke, G., Yan, W., Khudiyev, T., Noel, G. & Fink, Y. Recent Progress and Perspectives of Thermally Drawn Multimaterial Fiber Electronics. *Advanced Materials* vol. 32 1904911 (2020).

134. Orguc, S., Sands, J., Sahasrabudhe, A., Anikeeva, P. & Chandrakasan, A. P. Modular Optoelectronic System for Wireless, Programmable Neuromodulation during Free Behavior. in *Proceedings of the Annual International Conference of the IEEE Engineering in Medicine and Biology Society, EMBS* vols 2020-July 4322–4325 (Institute of Electrical and Electronics Engineers Inc., 2020).

135. Yizhar, O., Fenno, L. E., Davidson, T. J., Mogri, M. & Deisseroth, K. Optogenetics in Neural Systems. *Neuron* vol. 71 9–34 (2011).

136. Fenno, L., Yizhar, O. & Deisseroth, K. The Development and Application of Optogenetics. *Annu. Rev. Neurosci.* **34**, 389–412 (2011).

137. Webb, R. C. *et al.* Ultrathin conformal devices for precise and continuous thermal characterization of human skin. *Nat. Mater.* **12**, 938–944 (2013).

138. Elwassif, M. M., Kong, Q., Vazquez, M. & Bikson, M. Bio-heat transfer model of deep brain stimulation-induced temperature changes. *J. Neural Eng.* **3**, (2006).

139. Lacour, S. P., Courtine, G. & Guck, J. Materials and technologies for soft implantable neuroprostheses. *Nat. Rev. Mater.* **1**, 16063 (2016).

140. Bowcutt, R. *et al.* Heterogeneity across the murine small and large intestine. *World J. Gastroenterol.* **20**, 15216 (2014).

141. Qu, Y. *et al.* Superelastic Multimaterial Electronic and Photonic Fibers and Devices via Thermal Drawing. *Adv. Mater.* **30**, 1707251 (2018).

142. Brookes, S. J. H., Spencer, N. J., Costa, M. & Zagorodnyuk, V. P. Extrinsic primary afferent signalling in the gut. *Nature Reviews Gastroenterology and Hepatology* vol. 10 286–296 (2013).

143. Tsai, H. C. *et al.* Phasic firing in dopaminergic neurons is sufficient for behavioral conditioning. *Science (80-.).* **324**, 1080–1084 (2009).

144. Kozai, T. D. Y. & Vazquez, A. L. Photoelectric artefact from optogenetics and imaging on microelectrodes and bioelectronics: new challenges and opportunities. *J. Mater. Chem. B* **3**, 4965–4978 (2015).

145. Lenhardt, R. The effect of anesthesia on body temperature control. *Front. Biosci. - Sch.* **2 S**, 1145–1154 (2010).

146. Akeju, O. *et al.* Electroencephalogram signatures of ketamine anesthesia-induced unconsciousness. *Clin. Neurophysiol.* **127**, 2414–2422 (2016).

147. Kaelberer, M. M. *et al.* A gut-brain neural circuit for nutrient sensory transduction. *Science (80-.).* (2018) doi:10.1126/science.aat5236.

148. Kaelberer, M. M., Rupprecht, L. E., Liu, W. W., Weng, P. & Bohórquez, D. V. Neuropod Cells: The Emerging Biology of Gut-Brain Sensory Transduction. *Annu. Rev. Neurosci.* **43**, 337–353 (2020).

149. Bohórquez, D. V. *et al.* Neuroepithelial circuit formed by innervation of sensory enteroendocrine cells. *J. Clin. Invest.* **125**, 782–786 (2015).

150. Bai, L. *et al.* Enteroendocrine cell types that drive food reward and aversion. *Elife* **11**, (2022).

151. Holzer, P. TRPV1 and the gut: from a tasty receptor for a painful vanilloid to a key player in hyperalgesia. *Eur. J. Pharmacol.* **500**, 231–241 (2004).

152. Adriaenssens, A. E., Reimann, F. & Gribble, F. M. Distribution and Stimulus Secretion Coupling of Enteroendocrine Cells along the Intestinal Tract. *Compr. Physiol.* **8**, 1603–1638 (2018).

153. Rust, V. A. & Crosby, K. M. Cholecystokinin acts in the dorsomedial hypothalamus of young male rats to suppress appetite in a nitric oxide-dependent manner. *Neurosci. Lett.* **764**, 136295 (2021).

154. Moran, T. H. & McHugh, P. R. Cholecystokinin suppresses food intake by inhibiting gastric emptying. *https://doi.org/10.1152/ajpregu.1982.242.5.R491* **11**, (1982).

155. Moran, T. H. & Kinzig, K. P. Gastrointestinal satiety signals. II. Cholecystokinin. *Am. J. Physiol. - Gastrointest. Liver Physiol.* **286**, (2004).

156. Maljaars, P. W. J., Peters, H. P. F., Mela, D. J. & Masclee, A. A. M. Ileal brake: a sensible food target for appetite control. A review. *Physiol. Behav.* **95**, 271–281 (2008).

157. Schirra, J. & Göke, B. The physiological role of GLP-1 in human: incretin, ileal brake or more? *Regul. Pept.* **128**, 109–115 (2005).

158. Koda, S. *et al.* The Role of the Vagal Nerve in Peripheral PYY3–36-Induced Feeding Reduction in Rats. *Endocrinology* **146**, 2369–2375 (2005).

159. Welch, I., Saunders, K. & Read, N. W. Effect of ileal and intravenous infusions of fat emulsions on feeding and satiety in human volunteers. *Gastroenterology* **89**, 1293–1297 (1985).

160. El-Salhy, M., Mazzawi, T., Gundersen, D., Hatlebakk, J. G. & Hausken, T. The role of peptide YY in gastrointestinal diseases anddisorders. *Int. J. Mol. Med.* **31**, 275 (2013).

161. Latorre, R., Sternini, C., De Giorgio, R. & Greenwood-Van Meerveld, B. Enteroendocrine Cells: A Review of Their Role In Brain-Gut Communication. *Neurogastroenterol. Motil.* **28**, 620 (2016).

162. Alhadeff, A. L. Monitoring In Vivo Neural Activity to Understand Gut–Brain Signaling. *Endocrinology* **162**, 1–12 (2021).

163. Beutler, L. R. *et al.* Dynamics of Gut-Brain Communication Underlying Hunger. *Neuron* **96**, 461-475.e5 (2017).

164. Han, W. *et al.* A Neural Circuit for Gut-Induced Reward. *Cell* **175**, 665-678.e23 (2018).

165. Kupari, J., Häring, M., Agirre, E., Castelo-Branco, G. & Ernfors, P. An Atlas of Vagal Sensory Neurons and Their Molecular Specialization. *Cell Rep.* **27**, 2508-2523.e4 (2019).

166. Hibberd, T. J. *et al.* Optogenetic Induction of Colonic Motility in Mice. *Gastroenterology* **155**, 514-528.e6 (2018).

167. Body Weight Information for C57BL/6J | The Jackson Laboratory. https://www.jax.org/jax-mice-and-services/strain-data-sheet-pages/body-weight-chart-000664.

168. Campbell, H. L. SEASONAL CHANGES IN FOOD CONSUMPTION AND RATE OF

GROWTH OF THE ALBINO RAT. *https://doi.org/10.1152/ajplegacy.1945.143.3.428* **143**, 428–433 (1945).

169. Ellacott, K. L. J., Morton, G. J., Woods, S. C., Tso, P. & Schwartz, M. W. Assessment of Feeding Behavior in Laboratory Mice. *Cell Metab.* **12**, 10–17 (2010).

170. Pourbaix, M. *Atlas of Electrochemical Equilibria in-Aqueous Solutions*.

171. Klapoetke, N. C. *et al.* Independent optical excitation of distinct neural populations. *Nat. Methods* **11**, 338–346 (2014).

172. Mattis, J. *et al.* Principles for applying optogenetic tools derived from direct comparative analysis of microbial opsins. *Nat. Methods* **9**, 159–172 (2012).

173. Yang, Y. *et al.* Wireless multilateral devices for optogenetic studies of individual and social behaviors. *Nat. Neurosci. 2021 247* **24**, 1035–1045 (2021).

174. Rein, M. *et al.* Self-assembled fibre optoelectronics with discrete translational symmetry. *Nat. Commun.* **7**, 12807 (2016).

175. Yoo, S. *et al.* Wireless Power Transfer and Telemetry for Implantable Bioelectronics. *Adv. Healthc. Mater.* **10**, 2100614 (2021).

176. Singer, A. & Robinson, J. T. Wireless Power Delivery Techniques for Miniature Implantable Bioelectronics. *Adv. Healthc. Mater.* **10**, 2100664 (2021).

177. Shin, G. *et al.* Flexible Near-Field Wireless Optoelectronics as Subdermal Implants for Broad Applications in Optogenetics. *Neuron* **93**, 509-521.e3 (2017).

178. Gutruf, P. *et al.* Fully implantable optoelectronic systems for battery-free, multimodal operation in neuroscience research. *Nat. Electron. 2018 112* **1**, 652–660 (2018).

179. Hossain, M. F. & Takahashi, T. Effect of annealing temperature on nanostructured WO3 films on P-Si substrate. in *Procedia Engineering* vol. 56 702–706 (Elsevier Ltd, 2013).

180. Kanik, M. *et al.* Strain-programmable fiber-based artificial muscle. *Science (80-.).* **365**, 145–150 (2019).

181. McCall, J. G. *et al.* Fabrication and application of flexible, multimodal light-emitting devices for wireless optogenetics. *Nat. Protoc.* **8**, 2413–2428 (2013).

182. Seymour, J. P., Wu, F., Wise, K. D. & Yoon, E. State-of-the-art mems and microsystem tools for brain research. *Microsystems Nanoeng.* **3**, 1–16 (2017).

183. Jeong, J.-W., Mccall, J. G., Huang, Y., Bruchas, M. R. & Rogers, J. A. Wireless Optofluidic Systems for Programmable In Vivo Pharmacology and Optogenetics. *Cell* **162**, 662–674 (2015).

184. Zhang, Y. *et al.* Battery-free, fully implantable optofluidic cuff system for wireless optogenetic and pharmacological neuromodulation of peripheral nerves. *Sci. Adv.* **5**, eaaw5296 (2019).

185. Qazi, R. *et al.* Wireless optofluidic brain probes for chronic neuropharmacology and photostimulation. *Nat. Biomed. Eng. 2019 38* **3**, 655–669 (2019).